Phenomenology of the LHC and flavour factories

VNIVERSITAT DE VALÈNCIA

Tesi doctoral
Programa de Doctorat en Física
Juliol 2020

Ana Peñuelas Martínez
IFIC, Universitat de València - CSIC
Departament de Física Teòrica

Director de tesi:
Antonio Pich Zardoya

Als meus pares
i al meu germà

Antonio Pich Zardoya, catedràtic de la Universitat de València,

certifica:

Que la present memòria "Phenomenology of the LHC and flavour factories" ha sigut realitzada sota la seua direcció a l'Institut de Física Corpuscular, centre mixt de la Universitat de València i del CSIC, per **Ana Peñuelas Martínez** i constitueix la seua Tesi per a optar al grau de Doctora en Física.

I perquè així conste, en compliment de la legislació vigent, presenta en el Departament de Física Teòrica de la Universitat de València la referida Tesi Doctoral, i firma el present certificat.

València, a 9 de juliol de 2020.

Antonio Pich Zardoya

Contents

Preface

The forces and particle content of nature are described by the Standard Model (SM) of particle physics. This model was developed in the later half of the 20th century thanks to the progress at the theoretical aspects and the confirmation of the predicted particles at experiments and colliders. The discovery of the Higgs boson in 2012 represented a crucial confirmation of the model and initiated an age of exploration at the Large Hadron Collider (LHC). Even though the success of the SM was confirmed, some theoretical and experimental issues seem to indicate that this cannot be the ultimate theory. In this thesis, some of the paths indicating deviations from the SM will be followed.

After a general overview of the SM in Chapter 1, a set of simple extensions of the scalar sector of the SM will be presented in Chapter 2, namely the N-Higgs doublet models (NHDMs), containing N Higgs doublets with the same quantum numbers as the SM one. These models present non-diagonal Yukawa couplings, which cannot be accommodated experimentally and therefore need to be suppressed. The most general way for suppressing such non-diagonal interactions is tree-level alignment in flavour space, described in Chapter 2. Flavour alignment is broken at loop level, due to quantum corrections. This is studied in Chapter 6, where we show that models are phenomenologically safe after including these corrections. Then, in Chapter 7 a global fit of a CP-conserving NHDM with $N = 2$ doublets will be performed, including several theoretical, electroweak, flavour and Higgs observables. The fit will be performed with the code `HEPfit`, presented in Chapter 5.

The second path that will be explored are the charged B-anomalies. These anomalies are deviations with respect to the SM predictions in $b \to c$ transitions, with the ones appearing in the ratios $\mathcal{R}_D$ and $\mathcal{R}_{D^*}$ being the most interesting. After a general overview of the transitions and relevant observables in Chapter 4, two different effective field theory (EFT) fits will be performed in Chapter 8. In the first one, the most general Hamiltonian containing dimensions-six operators is considered, working with a minimal set of assumptions: new physics is only present in the third generation of leptons, the CP-conserving limit is taken, there are no light right-handed neutrinos and electroweak symmetry breaking is linearly realized. Later, the last two assumptions are relaxed, and fits are extended to include operators appearing from non-linear symmetry breaking and operators describing right-handed neutrinos. The EFT approach, followed in the fits, is described in Chapter 3.

Finally, the electroweak top and bottom quark couplings will be studied in Chapter 9. In this chapter, we will present a global fit to the relevant effective electroweak dimension-six operators, performed using `HEPfit`. Bounds will be discussed for these operators using LEP/SLC and LHC data. In addition, prospects on future colliders such as the high-luminosity phase of the LHC and ILC have been set. The top-quark Yukawa coupling will be studied in detail, which leads to a percent-level determination.

Chapter 1

The Standard Model

The Standard Model [1–4] is the best and simplest theory we have to describe elementary particles and their interactions. It is built under symmetry assumptions, so its particle content, the fields of the SM can be classified into 1/2 spin representations *fermions* (*quarks* and *leptons*), and *bosons* corresponding either to spin 0 (*Higgs boson*) or to spin 1 (*weak bosons* $W^{\pm}, Z^0$, *photon* γ and *gluons* g). The SM is a local or gauge theory under the group $SU(3)_C \otimes SU(2)_L \otimes U(1)_Y$, and therefore the nature of the different weak, strong and electromagnetic interactions is related to the symmetry principles of this group. For a review of the SM read [5, 6].

1.1 Quantum Chromodynamics

Quantum Chromodynamics (QCD) [1] is a non-Abelian gauge theory based on the symmetry group $SU(3)_C$ [8–11] that describes the interaction between the quarks and the gauge bosons of the theory, the gluons. Quarks can carry six different flavours (*up*, *down*, *charm*, *strange*, *top* and *bottom*) and $N_C = 3$ possible colour charges.

[1] See [7] for futher details about QCD.

The free Lagrangian of QCD will take the form,

$$\mathcal{L}_0 = \sum_f \bar{q}_f (i\gamma^\mu \partial_\mu - m_f) q_f \,, \tag{1.1.1}$$

where q_f^α represents the field of a quark with colour α and flavour f and we have adopted a vector notation in colour space $q_f^T \equiv (q_f^1, q_f^2, q_f^3)$. The Lagrangian in Eq. (1.1.1) is invariant under a global $SU(3)_C$ transformation,

$$q_f^\alpha \xrightarrow{SU(3)} (q_f^\alpha)' = U_\beta^\alpha q_f^\beta \,, \qquad U U^\dagger = U^\dagger U = 1 \,, \qquad \det U = 1 \,, \tag{1.1.2}$$

where U represents a $SU(3)_C$ matrix,

$$U = \exp\left\{ i \frac{\lambda_a}{2} \theta_a \right\} \,, \tag{1.1.3}$$

and λ^a, $a = (1, ...8)$ are the Gell-Mann matrices, which are the generators of the group in the fundamental representation. They are traceless, $\mathrm{Tr}(\lambda_a) = 0$, and satisfy the commutation relations,

$$\left[\frac{\lambda_a}{2}, \frac{\lambda_b}{2} \right] = i f^{abc} \frac{\lambda_c}{2} \,, \tag{1.1.4}$$

where f^{abc} are totally antisymmetric structure constants of $SU(3)_C$ and θ_a are arbitrary parameters. Requiring the QCD Lagrangian to be invariant under *local* $SU(3)_C$ transformations, i.e $\theta_a = \theta_a(x)$, the quark fields are transformed as,

$$q_f^\alpha \xrightarrow{SU(3)_C} \left(q_f^\alpha \right)' = U_\beta^\alpha q_f^\beta \approx q_f^\alpha + i \Big(\frac{\lambda_a}{2} \Big)_{\alpha\beta} \delta\theta_a \, q_f^\beta \,. \tag{1.1.5}$$

To keep the invariance under $SU(3)_C$ the gauge principle must be applied and new terms must be added to the Lagrangian of Eq. (1.1.1). These new pieces come from the replacement of the usual derivatives by covariant derivatives,

$$D^\mu q_f = \Big[\partial_\mu + i g_s \frac{\lambda_a}{2} G_a^\mu(x) \Big] q_f \equiv \Big[\partial_\mu + i g_s G^\mu(x) \Big] q_f \,, \tag{1.1.6}$$

and from the $N_C^2 - 1 = 8$ new gauge bosons, the gluons, G_a^μ, carrying colour a.

The infinitesimal transformations of the quark fields are given by Eq. (1.1.5) while for gluon fields,

$$G_a^\mu \xrightarrow{SU(3)_C} (G_a^\mu)' = G_a^\mu - \frac{1}{g_s}\partial^\mu(\delta\theta_a) - f^{abc}\,\delta\theta_b G_c^\mu\,. \tag{1.1.7}$$

Now one can rewrite the corresponding gauge-invariant kinetic term,

$$\mathcal{L}_{QCD} = -\frac{1}{4}G_a^{\mu\nu}G^a_{\mu\nu} + \sum_f \overline{q}_f(i\gamma^\mu D_\mu - m_f)q_f\,, \tag{1.1.8}$$

where $G_a^{\mu\nu}$ are the fields strengths,

$$G^{\mu\nu}(x) \equiv -\frac{i}{g_s}[D_\mu, D_\nu] = \partial^\mu G^\nu - \partial^\nu G^\mu + ig_s[G^\mu, G^\nu] \equiv \frac{\lambda_a}{2}G_a^{\mu\nu}(x)\,, \tag{1.1.9}$$
$$G_a^{\mu\nu}(x) = \partial^\mu G_a^\nu - \partial^\nu G_a^\mu - g_s f^{abc}G_b^\mu G_c^\nu\,,$$

transforming as

$$G^{\mu\nu} \xrightarrow{SU(3)_C} (G^{\mu\nu})' = UG^{\mu\nu}U^\dagger\,. \tag{1.1.10}$$

Since gauge invariance forbids adding a mass term for the gluon fields, they will remain as massless spin-1 particles. Expanding the Lagrangian of Eq. (1.1.8),

$$\begin{aligned}\mathcal{L}_{QCD} = \; & -\frac{1}{4}(\partial^\mu G_a^\nu - \partial^\nu G_a^\mu)(\partial_\mu G^a_\nu - \partial_\nu G^a_\mu) + \sum_f \bar{q}_f^\alpha(i\gamma^\mu\partial_\mu - m_f)\,q_f^\alpha \\ & - g_s\,G_a^\mu \sum_f \bar{q}_f^\alpha\gamma^\mu\left(\frac{\lambda_a}{2}\right)_{\alpha\beta} q_f^\beta \\ & + \frac{g_s}{2}f^{abc}\,(\partial^\mu G_a^\nu - \partial^\nu G_a^\mu)\,G_\mu^b G_\nu^c - \frac{g_s^2}{4}f^{abc}f_{ade}G_b^\mu G_c^\nu G_\mu^d G_\nu^e\,,\end{aligned} \tag{1.1.11}$$

one can identify quadratic terms giving the propagators, the interaction terms between gluons and quarks and the gluon self interactions, appearing due to the non-Abelian character of the theory. Such interactions are summarized in Fig. 1.1.

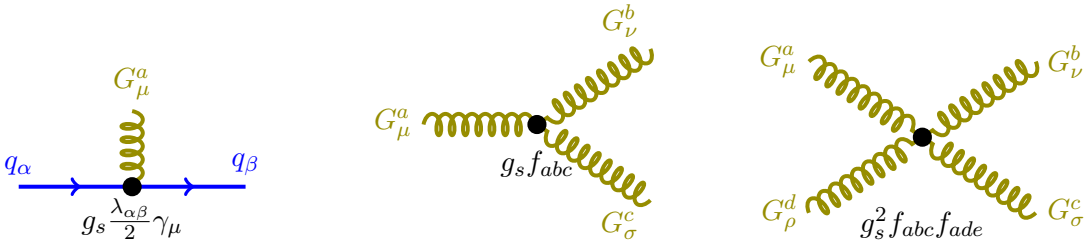

Figure 1.1: Cubic and quartic interaction vertices of the QCD Lagrangian. Gluons and quarks are denoted as green and blue lines respectively.

1.2 Electroweak unification

Weak interactions are described by the Electroweak Standard Model (EWSM), based on the symmetry group $G \equiv SU(2)_L \otimes U(1)_Y$ [1–3]. The EWSM contains left and right-handed fields interacting through spin-1 mediators: massless *photon*, γ, and massive *weak bosons*, $W^\pm$ and Z^0.

The fermionic sector of the SM consists of three families of quarks and leptons that only differs in their masses and flavour quantum numbers,

$$\textit{1st generation:}\ \begin{bmatrix} \nu_e & u \\ e^- & d' \end{bmatrix}, \qquad \textit{2nd generation:}\ \begin{bmatrix} \nu_\mu & c \\ \mu^- & s' \end{bmatrix}, \qquad \textit{3rd generation:}\ \begin{bmatrix} \nu_\tau & t \\ \tau^- & b' \end{bmatrix}.$$

In this notation the left column of a given matrix represents the lepton sector of each generation. The first elements are the *neutrinos* and the second ones are the *charged leptons*. The right column represents the quark sector with *up quarks* as first elements and *down quarks* as second ones. Taking any of these families for quarks we have,

$$Q_1(x) = \begin{bmatrix} q_u \\ q_d \end{bmatrix}_L, \qquad Q_2(x) = q_{u\,R}\,, \qquad Q_3(x) = q_{d\,R}\,, \tag{1.2.12}$$

and for leptons,

$$L_1(x) = \begin{bmatrix} \nu_\ell \\ \ell^- \end{bmatrix}_L, \qquad L_2(x) = \ell^-_R\,. \tag{1.2.13}$$

The quantum numbers of these fields under $SU(3)_C \otimes SU(2)_L \otimes U(1)_Y$ are,

$$\begin{aligned} Q_1(x) &= (3,2,+1/6)\,, \quad Q_2(x) = (3,1,+2/3)\,, \quad Q_3(x) = (3,1,-1/3)\,, \\ L_1(x) &= (1,2,-1/2)\,, \quad L_2(x) = (1,1,-1)\,. \end{aligned} \tag{1.2.14}$$

The free Lagrangian,

$$\mathcal{L}_0 = i\sum_{j=1}^{3} \bar{Q}_j(x)\gamma^\mu \partial_\mu Q_j(x) + i\sum_{j=1}^{2} \bar{L}_j(x)\gamma^\mu \partial_\mu L_j(x)\,, \tag{1.2.15}$$

is invariant under global G transformations of the fields,

$$\begin{aligned} Q_1(x) &\xrightarrow{G} Q_1'(x) \equiv \exp\{iy_1^q\beta\}\, U_L Q_1(x)\,, \\ Q_{2,3}(x) &\xrightarrow{G} Q_{2,3}'(x) \equiv \exp\{iy_{2,3}^q\beta\}\, Q_{2,3}(x)\,, \\ L_1(x) &\xrightarrow{G} Q_1'(x) \equiv \exp\{iy_1^\ell\beta\}\, U_L L_1(x)\,, \\ L_2(x) &\xrightarrow{G} L_2'(x) \equiv \exp\{iy_2^\ell\beta\}\, L_2(x)\,, \end{aligned} \tag{1.2.16}$$

where the exponential part of Eq. (1.2.16) represents the transformation under the group $U(1)_Y$ and the parameters $y_i^{q,\ell}$ are the hypercharges. The part corresponding to the $SU(2)_L$ group is related to the non-abelian matrix transformation U_L,

$$U_L \equiv \exp\{i\frac{\sigma_i}{2}\alpha^i\}\,, \tag{1.2.17}$$

where σ_i are the Pauli matrices and U_L only acts on the left-handed components. Requiring the Lagrangian to be also invariant under local transformations, $\alpha^i = \alpha^i(x)$ and $\beta^i = \beta^i(x)$ there will appear four vector bosons: three W_μ^i (one for each $SU(2)_L$ generator) and B_μ for the $U(1)_Y$ generator. The following covariant derivatives need to be introduced,

$$\begin{aligned} D_\mu Q_1(x) &\equiv \left[\partial_\mu + ig\widetilde{W}_\mu(x) + ig' y_1^q B_\mu(x)\right] Q_1(x)\,, \\ D_\mu Q_{2,3}(x) &\equiv \left[\partial_\mu + ig' y_{2,3}^q B_\mu(x)\right] Q_{2,3}(x)\,, \\ D_\mu L_1(x) &\equiv \left[\partial_\mu + ig\widetilde{W}_\mu(x) + ig' y_1^\ell B_\mu(x)\right] L_1(x)\,, \\ D_\mu L_2(x) &\equiv \left[\partial_\mu + ig' y_2^\ell B_\mu(x)\right] L_2(x)\,, \end{aligned} \tag{1.2.18}$$

where $\widetilde{W}_\mu(x) \equiv \frac{\sigma_i}{2} W^i_\mu(x)$.

The covariant derivative fixes the transformation of the gauge fields,

$$\begin{aligned} B_\mu(x) &\xrightarrow{G} B'_\mu(x) \equiv B_\mu(x) - \frac{1}{g'}\partial_\mu \beta(x)\,, \\ \widetilde{W}_\mu(x) &\xrightarrow{G} \widetilde{W}'_\mu(x) \equiv U_L \widetilde{W}_\mu(x) U_L^\dagger + \frac{i}{g}\partial_\mu U_L(x) U_L(x)^\dagger\,. \end{aligned} \tag{1.2.19}$$

Finally one should add the kinetic term for gauge bosons,

$$\mathcal{L}_{\rm kin} = -\frac{1}{4} B_{\mu\nu} B^{\mu\nu} - \frac{1}{2}{\rm Tr}\left[\widetilde{W}_{\mu\nu}\widetilde{W}^{\mu\nu}\right] = -\frac{1}{4} B_{\mu\nu} B^{\mu\nu} - \frac{1}{4} W^i_{\mu\nu} W_i^{\mu\nu}\,, \tag{1.2.20}$$

where the field strengths have been introduced,

$$\begin{aligned} B_{\mu\nu} &\equiv \partial_\mu B_\nu - \partial_\nu B_\mu\,, \\ \widetilde{W}_{\mu\nu} &\equiv -\frac{i}{g}\left[\left(\partial_\mu + ig\widetilde{W}_\mu\right)\left(\partial_\nu + ig\widetilde{W}_\nu\right)\right] = \partial_\mu \widetilde{W}_\nu - \partial_\nu \widetilde{W}_\mu + ig[\widetilde{W}_\mu, \widetilde{W}_\nu]\,, \\ \widetilde{W}_{\mu\nu} &\equiv \frac{\sigma_i}{2} W^i_{\mu\nu}\,, \\ W^i_{\mu\nu} &= \partial_\mu W^i_\nu - \partial_\nu W^i_\mu - g\epsilon^{ijk} W^j_\mu W^k_\nu\,. \end{aligned} \tag{1.2.21}$$

The field strengths transform as,

$$B_{\mu\nu} \xrightarrow{G} B_{\mu\nu}\,, \qquad \widetilde{W}_{\mu\nu} \xrightarrow{G} U_L \widetilde{W}_{\mu\nu} U_L^\dagger\,. \tag{1.2.22}$$

Since the field strengths of Eq.(1.2.20) contain quadratic pieces, $\mathcal{L}_{\rm kin}$ will contain cubic and quartic self-interactions between the gauge bosons. Mass terms for bosons are forbidden, since they would break gauge symmetry. Fermion mass terms would imply interaction between left and right-handed fields, with different transformation properties and therefore are also forbidden.

The EWSM Lagrangian takes the form,

$$\mathcal{L}_{\rm EWSM} = -\frac{1}{4} B_{\mu\nu} B^{\mu\nu} - \frac{1}{4} W^i_{\mu\nu} W_i^{\mu\nu} + i\sum_j \left(\bar{Q}_j \not{D} Q_j + \bar{L}_j \not{D} L_j\right), \tag{1.2.23}$$

and contains charged, neutral and self-interactions that will be described in the following sections.

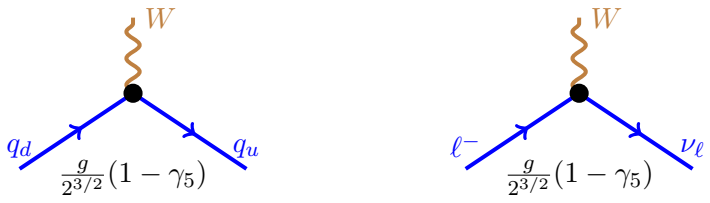

Figure 1.2: Charged-current interaction vertices for quarks (left panel) and leptons (right panel) described in Eq. (1.2.26). Fermions and bosons are described as solid blue and brown wavy lines respectively.

1.2.1 Charged-current interactions

The EWSM contains terms that allow the interaction between fermions and bosons,

$$\begin{aligned}\mathcal{L}_{\text{EWSM}} \subset \; & - \; g\, Q_1(x)\gamma^\mu \widetilde{W}_\mu Q_1(x) - g'\, B_\mu \sum_{j=1}^{3} Q_j(x)\gamma^\mu Q_j(x) \\ & - \; g\, L_1(x)\gamma^\mu \widetilde{W}_\mu L_1(x) - g'\, B_\mu \sum_{j=1}^{3} L_j(x)\gamma^\mu L_j(x)\,. \end{aligned} \tag{1.2.24}$$

These interactions can be classified into charged and neutral currents by expanding the $\widetilde{W}_\mu$ terms,

$$\widetilde{W}_\mu = \frac{\sigma^i}{2} W_\mu^i = \frac{1}{2}\begin{bmatrix} W_\mu^3 & \sqrt{2}W_\mu^\dagger \\ \sqrt{2}W_\mu & -W_\mu^3 \end{bmatrix}, \tag{1.2.25}$$

where the charged-current contribution will be due to the term $W_\mu^\dagger \equiv (W_\mu^1 - iW_\mu^2)/\sqrt{2}$, and W_μ^3 will contribute to the neutral currents, as we will see in the next section. The Lagrangian of the charged currents, for any family of quarks and leptons is,

$$\mathcal{L}_{\text{CC}} = -\frac{g}{2\sqrt{2}}\left\{W_\mu^\dagger[\bar{u}\gamma^\mu(1-\gamma_5)d + \nu_\ell\gamma^\mu(1-\gamma_5)\ell^-] + \text{h.c.}\right\}. \tag{1.2.26}$$

and it will give rise to the vertices of Fig. 1.2.

1.2.2 Neutral-current interactions

The Lagrangian of Eq. (1.2.24) also contains neutral current interactions, that will come both from the interactions with W^3_μ and B_μ.

Given that the photon interacts in the same way with both fermion chiralities, the field B_μ cannot be equal to the electromagnetic field. It should be an arbitrary combination of W^3_μ and B_μ,

$$\begin{bmatrix} W^3_\mu \\ B_\mu \end{bmatrix} = \begin{bmatrix} \cos\theta_W & \sin\theta_W \\ -\sin\theta_W & \cos\theta_W \end{bmatrix} \begin{bmatrix} Z_\mu \\ A_\mu \end{bmatrix} , \tag{1.2.27}$$

and the neutral-current Lagrangian can be expressed in terms of these fields,

$$\begin{aligned} \mathcal{L}_{NC} = \; & - \sum_j \bar{Q}_j(x) \left\{ \not{A} \left[g\frac{\sigma_3}{2}\mathrm{s}_{\theta_W} + g' y^q_j \mathrm{c}_{\theta_W} \right] + \not{Z} \left[g\frac{\sigma_3}{2}\mathrm{c}_{\theta_W} - g' y^q_j \mathrm{s}_{\theta_W} \right] \right\} Q_j \\ & - \sum_j \bar{L}_j(x) \left\{ \not{A} \left[g\frac{\sigma_3}{2}\mathrm{s}_{\theta_W} + g' y^\ell_j \mathrm{c}_{\theta_W} \right] + \not{Z} \left[g\frac{\sigma_3}{2}\mathrm{c}_{\theta_W} - g' y^\ell_j \mathrm{s}_{\theta_W} \right] \right\} L_j \, . \end{aligned} \tag{1.2.28}$$

where $\mathrm{c}_{\theta_W} \equiv \cos\theta_W$ and $\mathrm{s}_{\theta_W} \equiv \sin\theta_W$.

To recover the Quantum Electrodynamics (QED) Lagrangian from the A_μ piece one must impose,

$$g \sin\theta_W = g' \cos\theta_W = e \, , \qquad Y = Q - T_3 \, , \tag{1.2.29}$$

where the electromagnetic charge operator, Q, is expressed as:

$$Q_1 = \begin{bmatrix} Q_{u/\nu} & 0 \\ 0 & Q_{d/e} \end{bmatrix} , \qquad Q_2 = Q_{u/\nu} \, , \qquad Q_3 = Q_{d/e} \, , \tag{1.2.30}$$

and $T_3 \equiv \frac{\sigma_3}{2}$.

The form of the hypercharge, Y, is derived from the fact that it should be a linear combination of Q and T_3 and the requirement that it commutes with the involved operators. The relation of Eq. (1.2.29) fixes the hypercharge of the fermions:

$$\begin{aligned} &\textit{Quarks:} \quad y_1^q = Q_u - \tfrac{1}{2} = Q_d + \tfrac{1}{2} = +\tfrac{1}{6}, \quad y_2^q = Q_u = +\tfrac{2}{3}, \quad y_3^q = Q_d = -\tfrac{1}{3}, \\ &\textit{Leptons:} \quad y_1^\ell = Q_\nu - \tfrac{1}{2} = Q_e + \tfrac{1}{2} = -\tfrac{1}{2}, \quad y_2^\ell = Q_\nu = 0, \qquad y_3^\ell = Q_e = -1. \end{aligned}$$

The neutral-current Lagrangian, containing the interactions of Fig. 1.3 reads,

$$\mathcal{L}_{\rm NC} = \mathcal{L}_{QED} + \mathcal{L}_{NC}^Z \,, \tag{1.2.31}$$

where the first term is the QED Lagrangian,

$$\mathcal{L}_{\rm QED} = -e\, A_\mu \sum_j \bar{\psi}_j \gamma^\mu Q_j \psi_j \equiv -e A_\mu J_{\rm em}^\mu \,, \tag{1.2.32}$$

and the second one the Lagrangian describing the interactions between the Z-boson and the quarks,

$$\begin{aligned} \mathcal{L}_{NC}^Z &= -\frac{e}{2\sin\theta_W \cos\theta_W} J_Z^\mu Z_\mu \,, \\ J_Z^\mu &\equiv \sum_j \bar{\psi}_j \gamma^\mu (\sigma_3 - 2\sin^2\theta_W Q_j)\psi_j = J_3^\mu - 2\sin^2\theta_W J_{\rm em}^\mu \,. \end{aligned} \tag{1.2.33}$$

The former can be rewritten in terms of the fermion fields

$$\mathcal{L}_{NC}^Z = -\frac{2}{2\sin\theta_W \cos\theta_W} Z_\mu \sum_f \bar{f}\gamma^\mu (v_f - a_f\gamma_5) f \,, \tag{1.2.34}$$

where $a_f = T_3^f$ and $v_f = T_3^f(1 - 4|Q_f|\sin^2\theta_W)$.

1.2.3 Gauge self-interactions

The Lagrangian of Eq. (1.2.20) also contains cubic and quartic self-interactions between the gauge bosons,

$$\begin{aligned} \mathcal{L}_3 &= ie\Big\{\cot\theta_W \Big[(\partial^\mu W^\nu - \partial^\nu W^\mu) W_\mu^\dagger Z_\nu - (\partial^\mu W^{\nu\dagger} - \partial^\nu W^{\mu\dagger}) W_\mu Z_\nu + W_\mu W_\nu^\dagger (\partial^\mu Z^\nu - \partial^\nu Z^\mu)\Big] \\ &+ (\partial^\mu W^\nu - \partial^\nu W^\mu) W_\mu^\dagger A_\nu - (\partial^\mu W^{\nu\dagger} - \partial^\nu W^{\mu\dagger}) W_\mu A_\nu + W_\mu W_\nu^\dagger (\partial^\mu A^\nu - \partial^\nu A^\mu)\Big\} \,, \end{aligned} \tag{1.2.35}$$

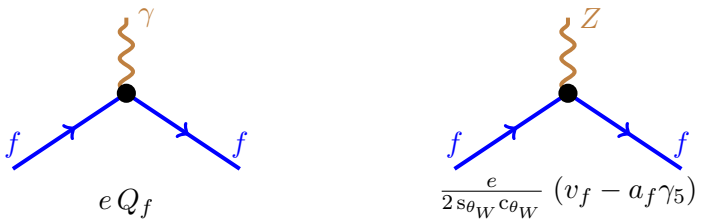

Figure 1.3: Neutral-current interaction vertices for quarks (left panel) and leptons (right panel) described in Eq. (1.2.34). Fermions and bosons are described as solid blue and brown wavy lines respectively.

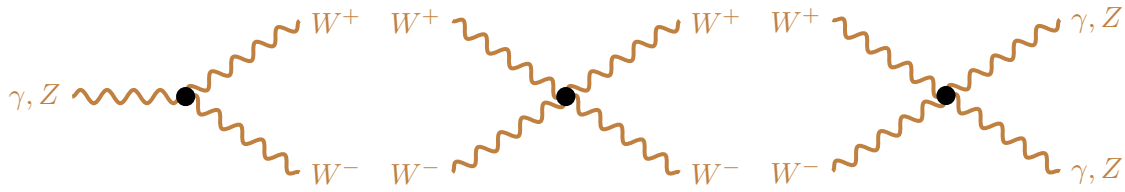

Figure 1.4: Self-interaction vertices of the gauge bosons described in the Lagrangians of Eq. (1.2.35) and (1.2.36). Bosons are described as brown wavy lines.

and

$$\begin{aligned}\mathcal{L}_4 &= -e^2\left\{\frac{1}{2\sin^2\theta_W}\left[\left(W_\mu^\dagger W^\mu\right)^2 - W_\mu^\dagger W^{\mu\dagger} W_\nu W^\nu\right] + \cot^2\theta_W\left[W_\mu^\dagger W^\mu Z_\nu Z^\nu - W_\mu^\dagger Z^\mu W_\nu Z^\nu\right]\right. \\ &+ \cot\theta_W\left[2W_\mu^\dagger W^\mu Z_\nu A^\nu - W_\mu^\dagger Z^\mu W_\nu A^\nu - W_\mu^\dagger A^\mu W_\nu Z^\nu\right] \\ &+ \left.\left[W_\mu^\dagger W^\mu A_\nu A^\nu - W_\mu^\dagger A^\mu W_\nu A^\nu\right]\right\}. \qquad (1.2.36)\end{aligned}$$

Such interactions generate cubic and quartic vertices as summarized in Fig. 1.4.

1.3 Spontaneous Symmetry Breaking

In our description of Electroweak unification gauge bosons are massless particles, while experimental results show that $W^\pm$ and Z should be massive bosons.

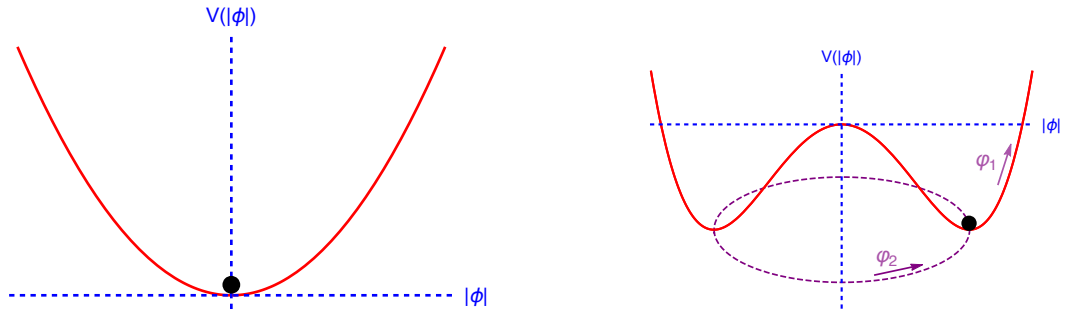

Figure 1.5: Potential for the two different values of μ^2. The left panel shows the case in which the potential has only one minimum, while in the right panel there is an infinite number of degenerate minima. In the last case φ_1 and φ_2 are the fields parametrizing excitations over the ground state.

To generate masses, we need to break gauge symmetry through *spontaneous symmetry breaking* (SSB) [12–16]. In this process the Lagrangian is invariant under a group of transformations that has a degenerate set of states with minimal energy. The fact of selecting one of these states as the ground state will spontaneously break the symmetry, leading to the appearance of new spin-0 massless particles, the *Goldstone bosons* that then will give mass to our vector bosons through the *Higgs mechanism*.

1.3.0.1 Goldstone Theorem

To illustrate the main idea of the Goldstone theorem, let's consider a complex scalar field, $\phi(x)$, and the following Lagrangian,

$$\mathcal{L} = \partial_\mu \phi^\dagger(x) \partial^\mu \phi(x) - V(\phi)\,, \qquad V(\phi) = \mu^2 \phi^\dagger \phi + h(\phi^\dagger \phi)^2\,, \tag{1.3.37}$$

where $\mathcal{L}$ is invariant under a global phase transformation,

$$\phi(x) \to \phi'(x) = e^{i\theta}\,\phi(x)\,. \tag{1.3.38}$$

The parameter h should be positive for the potential to be bounded from below. Depending on the sign of μ^2 two different possibilities will arise, as it can be seen in Fig. 1.5:

- **1.** $\mu^2 > 0$**:** The only minimum of $V(\phi)$ is $\phi = 0$.
- **2.** $\mu^2 < 0$**:** There is an infinity set of degenerate minima ($\phi_0(x)$) satisfying the condition $|\phi_0(x)| = \sqrt{\frac{-\mu^2}{2h}} = \frac{v}{\sqrt{2}}$.

We will focus in case **2**, in which there is a degenerate set of minima. If we choose one of these minima, for instance, $\phi_0(x) = \frac{v}{\sqrt{2}}$, the symmetry gets spontaneously broken. The field $\phi(x)$ can be parametrized as excitations over the ground state,

$$\phi(x) = \frac{1}{\sqrt{2}}\Big(v + \varphi_1(x) + i\,\varphi_2(x)\Big)\,, \tag{1.3.39}$$

where φ_1 and φ_2 are real fields.

Parametrizing the potential in this way it reads,

$$V(\phi) = V(\phi_0) - \mu^2\,\varphi_1^2 + h\,v\varphi_1\,(\varphi_1^2 + \varphi_2^2) + \frac{h}{4}(\varphi_1^2 + \varphi_2^2)^2\,, \tag{1.3.40}$$

where φ_1 describes a state with mass $m_{\varphi_1}^2 = -2\mu^2$, and φ_2 is massless and describes excitations around the flat direction of the potential with same energy (ground state). This is a general result, known as *Goldstone Theorem* [16, 17]:

*If a Lagrangian is invariant under a continuous symmetry group G, but the vacuum is only invariant under a subgroup $H \subset G$, then there must exist as many massless spin-0 particles (Nambu-Goldstone bosons) as broken generators (*i.e. *generators of G which don't belong to H) .*

1.3.0.2 Higgs Boson

The process of SSB described in the previous section seems to be useless to generate masses for the gauge bosons. However, once one studies the SSB of a local theory the problem is

solved. Let's start building a scalar Lagrangian. The simplest way to do this is to consider a $SU(2)_L$ doublet of complex scalar fields,

$$\phi(x) = \begin{bmatrix} \phi^{(+)}(x) \\ \phi^{(0)}(x) \end{bmatrix}, \tag{1.3.41}$$

and a gauged scalar Lagrangian invariant under $SU(2)_L \otimes U(1)_Y$ transformations,

$$\begin{aligned} \mathcal{L}_s &= (D_\mu\phi)^\dagger D^\mu\phi - \mu^2\phi^\dagger\phi - h(\phi^\dagger\phi)^2\,, \qquad (h>0, \mu^2<0)\,, \\ D^\mu\phi &= \left\{\partial^\mu + ig\widetilde{W}^\mu + ig' y_\phi B^\mu\right\}\phi\,, \qquad y_\phi = Q_\phi - T_3 = \frac{1}{2}\,. \end{aligned} \tag{1.3.42}$$

The coupling between $\phi(x)$ and $A^\mu(x)$ fixes the value of the hypercharge.

Looking for the minimum of the potential,

$$\frac{\partial V}{\partial|\phi|} = 0 \rightarrow |\phi_0(x)| = \sqrt{\frac{-\mu^2}{2h}}\,. \tag{1.3.43}$$

Only the neutral component of the doublet will acquire a vacuum expectation value (vev),

$$|\,\langle 0|\,\phi\,|0\rangle\,| = \begin{bmatrix} 0 \\ |\,\langle 0|\,\phi^{(0)}\,|0\rangle\,| \end{bmatrix} = \begin{bmatrix} 0 \\ \sqrt{\frac{-\mu^2}{2h}} \end{bmatrix}. \tag{1.3.44}$$

Eq. (1.3.44) is satisfied by an infinite set of states differing by a phase. Once a particular ground state is chosen,

$$\langle 0|\,\phi^{(0)}\,|0\rangle = \sqrt{\frac{-\mu^2}{2h}} \equiv \frac{v}{\sqrt{2}}\,, \tag{1.3.45}$$

the $SU(2)_L \otimes U(1)_Y$ symmetry gets broken to the electromagnetic group $U(1)_Q$, which remains a symmetry of the vacuum.

The four generators of G are the three generators for $SU(2)_L$, $\frac{\sigma_i}{2}$ and the generator of $U(1)_Y, Y$. The generator of the group $U(1)_Q$ into which G gets broken is Q. A generator is broken if $T_a\,\langle 0|\,\phi^{(0)}\,|0\rangle \neq 0$,

$$
\begin{aligned}
T_1 \langle 0|\, \phi^{(0)}\, |0\rangle &= \frac{\sigma_1}{2} \langle 0|\, \phi^{(0)}\, |0\rangle = \frac{1}{2\sqrt{2}} \begin{bmatrix} v \\ 0 \end{bmatrix} \neq 0\,, \\
T_2 \langle 0|\, \phi^{(0)}\, |0\rangle &= \frac{\sigma_2}{2} \langle 0|\, \phi^{(0)}\, |0\rangle = -\frac{i}{2\sqrt{2}} \begin{bmatrix} v \\ 0 \end{bmatrix} \neq 0\,, \\
T_3 \langle 0|\, \phi^{(0)}\, |0\rangle &= \frac{\sigma_3}{2} \langle 0|\, \phi^{(0)}\, |0\rangle = \frac{1}{2\sqrt{2}} \begin{bmatrix} 0 \\ -v \end{bmatrix} \neq 0\,, \\
Y \langle 0|\, \phi^{(0)}\, |0\rangle &= \frac{I}{2} \langle 0|\, \phi^{(0)}\, |0\rangle = \frac{1}{2\sqrt{2}} \begin{bmatrix} 0 \\ v \end{bmatrix} \neq 0\,, \\
Q \langle 0|\, \phi^{(0)}\, |0\rangle &= (Y + T_3) \langle 0|\, \phi^{(0)}\, |0\rangle = \begin{bmatrix} 0 \\ 0 \end{bmatrix}\,.
\end{aligned} \tag{1.3.46}
$$

The Goldstone Theorem would imply the existence of three massless particles, the Goldstone bosons. However, if we parametrize our doublet considering excitations over the physical vacuum,

$$
\phi(x) = \exp\left\{ i \frac{\sigma_i}{2} \theta^i(x) \right\} \begin{bmatrix} 0 \\ \frac{v + H(x)}{\sqrt{2}} \end{bmatrix}\,, \tag{1.3.47}
$$

and then using local $SU(2)_L$ invariance we choose a particular gauge for which $\theta^i(x) = 0$, the Goldstone bosons $\theta_i(x)$ disappear. Consequently, the three massless Goldstone bosons are eliminated from the Lagrangian by a local gauge transformation and their three degrees of freedom become the longitudinal polarization of the gauge bosons $W^{\pm}$ and Z, which acquire mass as it can be seen at the kinetic part of the Lagrangian,

$$
\mathcal{L}_{\text{kin}} = \frac{1}{2} \left\{ (\partial_\mu H)(\partial^\mu H) + (v + H)^2 \Big(\frac{g^2}{4} W_\mu^\dagger W_\mu + \frac{g^2}{8 \cos^2 \theta_W} Z_\mu Z^\mu \Big) \right\}\,. \tag{1.3.48}
$$

In the Lagrangian of Eq. (1.3.48) the Goldstone bosons have already been eliminated. This particular choice of the gauge $\theta^i(x) = 0$ is known as the unitary gauge. The vev of the neutral scalar doublet has generated a mass term for the gauge bosons $W^{\pm}$ and Z,

$$M_Z \cos\theta_W = M_W = \frac{1}{2} v g \,, \tag{1.3.49}$$

Since Q is an unbroken generator, the photon remain massless, and there is a new scalar particle: the *Higgs boson*.

It is often said that the Goldstone bosons have been "eaten" by the gauge bosons, meaning that the degrees of freedom of the Goldstones have been eliminated and gauge bosons have acquired a new degree of freedom, the longitudinal mode.

The Lagrangian that describes this new particle, the Higgs boson is:

$$\mathcal{L}_S = \frac{1}{4} h v^4 + \mathcal{L}_H + \mathcal{L}_{HG^2} \,, \tag{1.3.50}$$

where

$$\begin{aligned} \mathcal{L}_H &= \frac{1}{2}\partial_\mu H \partial^\mu H - \frac{1}{2} M_H^2 H^2 - \frac{M_H^2}{2v} H^3 - \frac{M_H^2}{8v^2} H^4 \,, \\ \mathcal{L}_{HG^2} &= M_W^2 W_\mu^\dagger W^\mu \left\{ 1 + \frac{2}{v} H + \frac{H^2}{v^2} \right\} + \frac{1}{2} M_Z^2 Z_\mu Z^\mu \left\{ 1 + \frac{2}{v} H + \frac{H^2}{v^2} \right\} . \end{aligned} \tag{1.3.51}$$

Eq. (1.3.51) determines the Higgs mass,

$$M_H = \sqrt{-2\mu^2} = \sqrt{2h}\, v \,. \tag{1.3.52}$$

and the couplings that can be seen in Fig. 1.6.

1.3.0.3 Yukawa sector

Once we have introduced the Higgs doublet the right structures to give mass to the fermions can be formed. The forbidden structures by gauge invariance, that would give mass are of the form $\overline{\psi}\psi = \overline{\psi}_L \psi_R + \overline{\psi}_R \psi_L$, with quantum numbers under $(SU(3)_C, SU(2)_L, U(1)_Y)$,

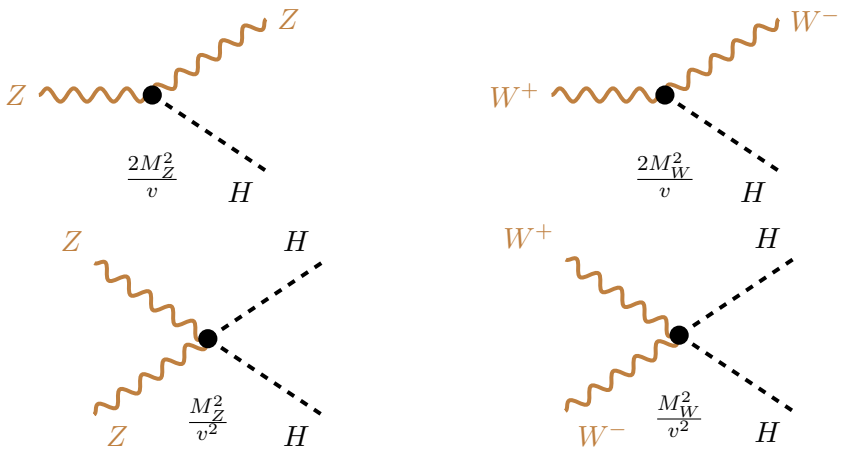

Figure 1.6: Coupling between the Higgs boson (black dashed lines) and the gauge bosons (brown wavy lines). The vertices can be obtained from Eqs. 1.3.51.

$$
\begin{aligned}
L_L &= \left(1, 2, -\frac{1}{2}\right), \qquad e_R = (1, 1, -1), \qquad u_R = \left(3, 1, +\frac{2}{3}\right), \\
Q_L &= \left(3, 2, -\frac{1}{6}\right), \qquad \nu_{eR} = (1, 1, 0), \qquad d_R = \left(3, 1, -\frac{1}{3}\right).
\end{aligned} \tag{1.3.53}
$$

Combing these fields with the Higgs doublet with quantum numbers $\phi = \left(1, 2, \frac{1}{2}\right)$ the gauge-invariant structures can be formed (assuming the non-existence of right-handed neutrinos, nu_{eR}),

$$
\mathcal{L}_Y = -\left\{c_1 \bar{Q}_L \, \phi \, d_R - c_2 \, \bar{Q}_L \, \phi^c \, u_R - c_3 \bar{L}_L \, \phi \, e_R\right\} + \text{h.c.}\,, \tag{1.3.54}
$$

where c_i are arbitrary parameters and the second term contains the $\mathcal{C}$-conjugate scalar field, $\phi^c \equiv i\sigma_2 \phi^*$, which in the unitary gauge takes the form,

$$
\phi^c = \frac{1}{\sqrt{2}} \begin{bmatrix} v + H(x) \\ 0 \end{bmatrix}. \tag{1.3.55}
$$

The mass of the fermions is generated through the vev of the Higgs doublet,

$$
\mathcal{L}_Y = -\left\{\frac{1}{\sqrt{2}}(v + H)(c_1 \, \bar{d}\, d + c_2 \, \bar{u}\, u + c_3 \, \bar{e}\, e)\right\} = -\left(1 + \frac{H}{v}\right)(m_d \, \bar{d}\, d + m_u \, \bar{u}\, u + m_e \, \bar{e}\, e)\,. \tag{1.3.56}
$$

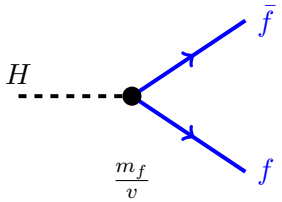

Figure 1.7: Higgs coupling (black dashed line) to the fermions (blue solid line). The couplings are related to the masses through the vev.

where

$$m_d = c_1 \frac{v}{\sqrt{2}}\,, \qquad m_u = c_2 \frac{v}{\sqrt{2}}\,, \qquad m_e = c_3 \frac{v}{\sqrt{2}}\,. \tag{1.3.57}$$

The values of c_i are arbitrary, and the couplings of the fermions with the Higgs boson are fixed by the masses, as we can see in Fig. 1.7 and Eq. (1.3.57).

1.3.0.4 Yukawa coupling for three generations

The existence of six quark flavours (u, d, c, s, t, b), three charged leptons (e, μ, τ) and their corresponding neutrinos $(\nu_e, \nu_\mu, \nu_\tau)$ is an experimental and well-proved fact. These particles are often classified into first (u, d, e, ν_e), second (c, s, μ, ν_μ) and third generation (t, b, τ, ν_τ). Since the particles of the second and third generation have the same quantum numbers and only differ in their masses, we can add more terms to the Lagrangian of Eq. (1.3.57),

$$\mathcal{L}_Y = -\left(\bar{\mathbf{Q}}'_L \mathbf{M}'_d \,\phi\, \mathbf{d}'_R + \bar{\mathbf{Q}}'_L \,\mathbf{M}'_u \,\phi^c\, \mathbf{u}'_R + \bar{\mathbf{L}}'_L \mathbf{M}'_\ell \,\phi\, \ell'_R\right) + \text{h.c}\,, \tag{1.3.58}$$

where $\mathbf{d}'_R$, $\mathbf{u}'_R$, ℓ'_R, $\bar{\mathbf{Q}}'_L$ and $\bar{\mathbf{L}}'_L$ are vectors in the 3-dimensional flavour space, and $\mathbf{M}'_d$, $\mathbf{M}'_u$ and $\mathbf{M}'_\ell$ are arbitrary matrices. These non-diagonal mass matrices introduce a total of 54 parameters, in addition to the non-conservation of lepton number. Since the Lagrangian (but $\mathcal{L}_Y$) is invariant under $U(3)_{Q_L} \otimes U(3)_{u_R} \otimes U(3)_{d_R} \otimes U(3)_{L_L} \otimes U(3)_{\ell_R}$ (often called Weak Basis Transformation) we can perform transformations in the fermionic fields to reduce the number of parameters,

$$\mathbf{Q}'_L \to \mathbf{U}_Q\,\mathbf{Q}'_L \equiv \mathbf{Q}_L\,, \quad \mathbf{L}'_L \to \mathbf{U}_\ell\,\mathbf{L}'_L \equiv \mathbf{L}_L\,,$$
$$\mathbf{d}'_R \to \mathbf{U}_d\,\mathbf{d}'_R \equiv \mathbf{d}_R\,, \quad \mathbf{u}'_R \to \mathbf{U}_u\,\mathbf{u}'_R \equiv \mathbf{u}_R\,, \quad \ell'_R \to \mathbf{U}_R\,\ell'_R \equiv \ell_R\,.$$

It is convenient to choose a transformation such that the maximum number of parameters of the matrices is reduced, i.e, making them diagonal.

$$\begin{aligned}\frac{v}{\sqrt{2}}\mathbf{U}_Q^\dagger \mathbf{M}'_d \mathbf{U}_d &= \mathbf{M}_d\,,\\ \frac{v}{\sqrt{2}}\mathbf{U}_Q^\dagger \mathbf{M}'_u \mathbf{U}_d &= \mathcal{M}_u\,,\\ \frac{v}{\sqrt{2}}\mathbf{U}_L^\dagger \mathbf{M}'_\ell \mathbf{U}_R &= \mathcal{M}_\ell\,,\end{aligned}$$

where $\mathcal{M}_u$ and $\mathcal{M}_\ell$ are diagonal, positive defined matrices and $\mathbf{M}_d$ is an hermitian and positive defined matrix. The latter will contain non-diagonal elements responsible of the mixture between left-handed up and down quarks in the weak interaction. To diagonalize this matrix we can perform an $SU(3)$ transformation,

$$d_R \to \mathrm{V_{CKM}}\,d_R\,, \qquad d_L \to \mathrm{V_{CKM}}\,d_L. \tag{1.3.59}$$

The resulting mass matrices of our Yukawa Lagrangian will be diagonal

$$\mathcal{L}_Y = -\left(1+\frac{H}{v}\right)\left(\overline{\mathbf{d}}_\mathbf{L}\mathcal{M}_d\mathbf{d}_R + \overline{\mathbf{u}}_\mathbf{L}\mathcal{M}_u\mathbf{u}_R + \bar{\ell}_L\mathcal{M}_\ell\ell_R + \mathrm{h.c}\right). \tag{1.3.60}$$

The neutral current Lagrangian, described in Eq. (1.2.31) will remain flavour invariant at tree level, while charged current interactions will change flavour,

$$\mathcal{L}_{CC} = -\frac{g}{\sqrt{2}}\left\{W_\mu^\dagger\left[\sum_{i,j}\bar{u}_i\gamma^\mu(1-\gamma_5)V_{ij}d_j + \sum_\ell \bar{\nu}_\ell\gamma^\mu(1-\gamma_5)\ell\right] + \mathrm{h.c.}\right\}. \tag{1.3.61}$$

The resulting charged current Lagrangian contains the so-called Cabibbo-Kobayashi-Maskawa (CKM) matrix, $\mathrm{V_{CKM}}$,

$$\mathrm{V_{CKM}} = \begin{bmatrix} V_{ud} & V_{us} & V_{ub}\\ V_{cd} & V_{cs} & V_{cb}\\ V_{td} & V_{ts} & V_{tb}\end{bmatrix}. \tag{1.3.62}$$

which describes the flavour mixing in charged currents.

Chapter 2

The aligned N-Higgs doublet model

The existence of a Higgs-like boson with mass around 125 GeV was proven by the ATLAS and CMS collaborations of the LHC [18, 19] in 2012. This particle was already predicted by the SM and therefore it is well explained within the theory [12–14]. However one can go beyond the minimal content of the SM and enlarge the scalar sector adding extra Higgs-like particles. Extended models of perturbative EWSM containing scalar fields transforming as singlets or doublets under the $SU(2)_L$ group with $Y = 1/2$ satisfy the successful mass relation $M_W = M_Z \cos\theta_W$ and can fulfil all electroweak precision tests.

Singlets under $SU(2)_L$ have been previously studied and constrained by direct searches, electroweak precision observables (EWPO) and theoretical constriaints [20, 21]. Doublets give rise to more interesting phenomenological consequences. In addition to the three electroweak Goldstone bosons the scalar spectrum contains N doublets with $N-1$ charged and $2N-1$ neutral scalars, which in general can be complex and generate CP-violating phases. By adding new doublets there is a rich variety of possible new interactions, which include Yukawa couplings that are not diagonal in flavour space, giving rise to phenomenologically constrained flavour-changing-neutral-currents (FCNC).

In this chapter we will describe the basic ingredients of this model, the N-Higgs doublet model (N2HDM), *i.e.* the scalar potential and the process of SSB. Later, we will see how the alignment in flavour space is required in order to avoid FCNCs and the consequences of this alignment in flavour space.

2.1 Multi-Higgs-doublet models

Let us consider an electroweak model with the SM fermion content and gauge group, and an extended scalar sector involving N doublets with hypercharge $Y = \frac{1}{2}$,

$$\phi_a \,=\, \mathrm{e}^{i\theta_a} \begin{bmatrix} \phi_a^+ \\ \frac{1}{\sqrt{2}}\,(v_a + \rho_a + i\,\eta_a) \end{bmatrix} . \tag{2.1.1}$$

The neutral components of the doublets ϕ_a acquire a vev $\langle \phi_a^0 \rangle = \mathrm{e}^{i\theta_a}\, v_a/\sqrt{2}$, which in general can be complex ($v_a \geq 0$). Since one global phase can always be rotated away through a $U(1)_Y$ transformation we choose $\theta_1 = 0$, leaving the relative phases $\tilde{\theta}_a = \theta_a - \theta_1$.

2.1.1 Scalar potential

It is convenient to perform a global $SU(N)$ transformation in the space of scalar fields,

$$\Phi_a \,=\, \sum_{b=1}^{N} \Omega_{ab}\, \mathrm{e}^{-i\tilde{\theta}_b}\, \phi_b \,, \qquad\qquad \phi_b \,=\, \mathrm{e}^{i\tilde{\theta}_b} \sum_{a=1}^{N} \Omega_{ab}\, \Phi_a \,, \qquad\qquad \Omega \cdot \Omega^T \,=\, \Omega^T \cdot \Omega \,=\, 1 \,, \tag{2.1.2}$$

such that only the first doublet acquires a vev. This transformation is characterized by the condition $\Omega_{1a} = v_a/v$, with $v = \left(\sum_a v_a^2\right)^{1/2} > 0$, and defines the Higgs basis,

$$\Phi_1 \,=\, \begin{bmatrix} G^+ \\ \frac{1}{\sqrt{2}}\,(v + S_1^0 + i\,G^0) \end{bmatrix} , \qquad\qquad \Phi_{a>1} \,=\, \begin{bmatrix} S_a^+ \\ \frac{1}{\sqrt{2}}\,(S_a^0 + i\,P_a^0) \end{bmatrix} . \tag{2.1.3}$$

The electroweak symmetry breaking (EWSB) is then fully associated to the doublet Φ_1, which contains the electroweak Goldstone fields G^0 and G^+, and plays the role of the SM Higgs doublet.

The potential takes the form,

$$V = Y_{ab}\left(\Phi_a^\dagger \Phi_b\right) + Z_{abcd}\left(\Phi_a^\dagger \Phi_b\right)\left(\Phi_c^\dagger \Phi_d\right) , \tag{2.1.4}$$

with

$$Y_{ab} = Y_{ba}^* , \qquad Z_{abcd} = Z_{cdab} , \qquad Z_{abcd} = Z_{badc}^* . \tag{2.1.5}$$

Since the potential is hermitic we have a total of $N^2(N^2+3)/2$ independent real parameters. One can minimize the potential and find the following relations in the Higgs basis,

$$\begin{aligned} \tfrac{\partial V}{\partial \Phi_1} &= 0 \rightarrow\ Y_{11} = -Z_{1111}\, v^2 , \\ \tfrac{\partial V}{\partial \Phi_{i\neq 1}} &= 0 \rightarrow\ \ Y_{1i} = -Z_{111i}\, v^2 . \end{aligned} \tag{2.1.6}$$

The potential of Eq. (2.1.5) can be decomposed into a linear, a quadratic a cubic and a quartic term,

$$V = -\frac{1}{4} Z_{1111} v^4 + V_2 + V_3 + V_4 . \tag{2.1.7}$$

In this decomposition V_2 contains the mass terms,

$$V_2 = S_i^+ \mathcal{M}_{ij}^+ S_j^+ + \frac{1}{2} \mathcal{S}_i^0 \mathcal{M}_{ij}^0 \mathcal{S}_j^0 , \tag{2.1.8}$$

where $\mathcal{M}^+(\mathcal{M}^0)$ are the corresponding charged (neutral) non-diagonal mass matrices, that will depend on the parameters of the potential. The $2N-1$ neutral scalar mass eigenstates, $\varphi_i^0 = \mathcal{R}_{ij}\mathcal{S}_j^0$, are related to the scalar-doublet field components $\mathcal{S}_i^0 = \{S_1^0, S_2^0, P_2^0, \cdots, S_N^0, P_N^0\}$ through an orthogonal transformation $\mathcal{R}$ which depends on the parameters of the scalar potential. CP-violating mixes the CP-even (S_a^0) and CP-odd (P_a^0) scalar particles and the resulting mass eigenstates do not have, in general, definite CP quantum numbers. Similarly, the $N-1$ charged fields $\mathcal{S}_i^+ = \{S_2^+, S_3^+, \cdots, S_N^+\}$ mix among themselves giving rise

to the charged mass eigenstates $\varphi_i^+ = \mathcal{R}_{ij}^{(+)}\mathcal{S}_j^+$, with $\mathcal{R}^{(+)}$ a $(N-1)\times(N-1)$ orthogonal matrix.

The cubic term of the potential can be written as,

$$\begin{aligned} V_3 &= v\left[\mathcal{R}\mathrm{e}\left(Z_{1bcd}\right)\left(P_b^0P_c^0S_d^0 - P_b^0P_d^0S_c^0 + P_c^0P_d^0S_b^0 + S_b^0S_c^0S_d^0 + S_b^0\left(S_c^-S_d^+ + S_c^+S_d^-\right)\right)\right. \\ &- \left.\mathcal{I}\mathrm{m}\left(Z_{1bcd}\right)\left(P_b^0P_c^0P_d^0 + P_b^0S_c^0S_d^0 + P_b^0\left(S_c^+S_d^- - S_c^-S_d^+\right) - P_c^0S_b^0S_d^0 + P_d^0S_b^0S_c^0\right)\right], \end{aligned} \tag{2.1.9}$$

and the quartic part,

$$\begin{aligned} V_4 &= Z_{abcd}\left\{S_a^-S_b^+S_c^-S_d^+ + \frac{1}{2}\left(S_a^-S_b^+S_c^0S_d^0 + S_a^0S_b^0S_c^-S_d^+\right)\right. \\ &+ \frac{1}{2}\left(S_a^-S_b^+P_c^0P_d^0 + P_a^0P_b^0S_c^-S_d^+\right) + \frac{i}{2}\left[S_a^-S_b^+\left(S_c^0P_d^0 - P_c^0S_d^0\right)\right. \\ &+ \left.\left(S_a^0P_b^0 - P_a^0S_b^0\right)S_c^-S_d^+\right] + \frac{1}{4}\left[S_a^0S_b^0S_c^0S_d^0 + S_a^0S_b^0P_c^0P_d^0\right. \\ &+ P_a^0P_b^0S_c^0S_d^0 + iS_a^0S_b^0\left(S_c^0P_d^0 - P_c^0S_d^0\right) + i\left(S_a^0P_b^0 - P_a^0S_b^0\right)S_c^0S_d^0 \\ &+ P_a^0P_b^0P_c^0P_d^0 + iP_a^0P_b^0\left(S_c^0P_d^0 - P_c^0S_d^0\right) + i\left(S_a^0P_b^0 - P_a^0S_b^0\right)P_c^0P_d^0 \\ &- \left.\left.\left(S_a^0P_b^0S_c^0P_d^0 - S_a^0P_b^0P_c^0S_d^0 - P_a^0S_b^0S_c^0P_d^0 + P_a^0S_b^0P_c^0S_d^0\right)\right]\right\} \end{aligned} \tag{2.1.10}$$

2.1.2 Gauge sector

Once symmetry breaking has undergone, interaction terms between the scalar fields, the Goldstone fields $G^\pm$ and G^0 and the gauge bosons $W_\mu^\pm, Z_\mu, A_\mu$ will arise. These terms come from the covariant derivative, $D_\mu = \partial_\mu + i\,e\,QA_\mu - i\frac{g}{\cos\theta_\mathrm{w}}Z_\mu(T_3 - Q\sin^2\theta_\mathrm{w}) - i\,g[T_+W_\mu^\dagger + T_-W_\mu]$ with $T_\pm = \frac{1}{\sqrt{2}}\left(T_1 \pm iT_2\right)$,

$$\mathcal{L}_\mathrm{kin} + \sum_{a=1}^{N} D_\mu\Phi_a^\dagger D^\mu\Phi_a + \mathcal{L}_{GF} = \mathcal{L}_{V^2} + \mathcal{L}_{\phi^2} + \mathcal{L}_{\phi V} + \mathcal{L}_{\phi^2 V} + \mathcal{L}_{\phi V^2} + \mathcal{L}_{\phi^2V^2}\,. \tag{2.1.11}$$

The term $\mathcal{L}_{\rm GF}$ needs to be introduced to fix the gauge and cancel the quadratic terms mixing the gauge and the Goldstone bosons. Adopting the Feynman-'t Hooft gauge, R_ϵ ($\varepsilon = 1$),

$$\mathcal{L}_{\rm GF} = -\frac{1}{2}(\partial_\mu A^\mu)^2 - \frac{1}{2}(\partial_\mu Z^\mu + M_Z G^0)^2 - (\partial^\mu W^\dagger_\mu + iM_W G^+)(\partial_\nu W^\nu - iM_W G^-)\,. \quad (2.1.12)$$

Once the gauge is fixed the Goldstone bosons masses $M_{G^\pm} = M_W = gv/2$ and $M_{G^0} = M_Z = M_W/\cos\theta_{\rm w}$ are determined. Expanding Eq. (2.1.11) one can distinguish quadratic terms,

$$\mathcal{L}_{V^2} = -\frac{1}{2}(\partial_\mu A^\mu)^2 - \frac{1}{2}(\partial_\mu Z^\mu)^2 + \frac{1}{2}M_Z^2 Z_\mu Z^\mu - (\partial^\mu W^\dagger_\mu)(\partial_\nu W^\nu) + M_W^2 W^\dagger_\mu W^\mu\,, \quad (2.1.13)$$

and,

$$\begin{aligned}\mathcal{L}_{\phi^2} &= \frac{1}{2}\partial_\mu S_1^0 \partial^\mu S_1^0 + \sum_{a=2}^{N}\frac{1}{2}\left[\partial_\mu S_a^0 \partial^\mu S_a^0 + \partial_\mu P_a^0 \partial^\mu P_a^0\right] + \partial_\mu S_a^+ \partial^\mu S_a^- \\ &+ \frac{1}{2}\partial_\mu G^0 \partial^\mu G^0 - \frac{1}{2}M_Z^2 (G_0)^2 + \partial_\mu G^+ \partial^\mu G^- - M_W^2 G^+ G^-\,, \end{aligned} \quad (2.1.14)$$

cubic interactions between two scalars and one vector boson,

$$\begin{aligned}\mathcal{L}_{\phi^2 V} = \sum_{a=2}^{N}\Bigg\{ & ie[\,A^\mu + \cot(2\theta_{\rm w})Z^\mu]\left[(S_a^+ \overleftrightarrow{\partial_\mu} S_a^-) + (G^+ \overleftrightarrow{\partial_\mu} G^-)\right] \\ & + \frac{e}{\sin(2\theta_{\rm w})}Z^\mu\left[(G^0 \overleftrightarrow{\partial_\mu} S_1^0) + (P_a^0 \overleftrightarrow{\partial_\mu} S_a^0)\right] \\ & + \frac{g}{2}W^{\mu\dagger}\left[(S_a^- \overleftrightarrow{\partial_\mu} P_a^0) - i(S_a^- \overleftrightarrow{\partial_\mu} S_a^0) + (G^- \overleftrightarrow{\partial_\mu} G^0) - i(G^- \overleftrightarrow{\partial_\mu} S_1^0)\right] \\ & + \frac{g}{2}W^{\mu}\left[(S_a^+ \overleftrightarrow{\partial_\mu} P_a^0) + i(S_a^+ \overleftrightarrow{\partial_\mu} S_a^0) + (G^+ \overleftrightarrow{\partial_\mu} G^0) + i(G^+ \overleftrightarrow{\partial_\mu} S_1^0)\right]\Bigg\}\,, \end{aligned} \quad (2.1.15)$$

cubic interactions between one scalar and two vector bosons,

$$\begin{aligned}\mathcal{L}_{\phi V^2} = & \left\{\frac{2}{v}S_1\left[\frac{1}{2}M_Z^2 Z_\mu Z^\mu + M_W^2 W^\dagger_\mu W^\mu\right]\right. \\ & \left. + \ (eM_W A^\mu - gM_Z \sin^2\theta_{\rm w} Z^\mu)(G^+ W_\mu + G^- W^+_\mu)\right\}\,, \end{aligned} \quad (2.1.16)$$

and quartic interactions between two scalars and two vector bosons,

$$\begin{aligned}\mathcal{L}_{\phi^2V^2} = & \sum_{a=2}^{N}\Big\{\frac{1}{v^2}\left[\frac{1}{2}M_Z^2 Z_\mu Z^\mu + M_W^2 W_\mu^\dagger W^\mu\right][(S_1^0)^2+(S_a^0)^2+(P_a^0)^2+(G^0)^2] \\ & + \left\{e^2[A^\mu+\cot(2\theta_{\rm w})Z^\mu]^2+\frac{g^2}{2}W_\mu^\dagger W^\mu\right\}(G^+G^-+S_a^+S_a^-) \\ & + \frac{eg}{2}(A^\mu-\tan\theta_{\rm w}Z^\mu)[S_1(G^+W_\mu+G^-W_\mu^\dagger)+S_a^0(S_a^+W_\mu+S_a^-W_\mu) \\ & + iP_a^0(S_a^-W_\mu^\dagger-S_a^+W_\mu)+iG_0(G^-W_\mu^\dagger-G^+W_\mu)]\Big\}\,, \end{aligned} \tag{2.1.17}$$

with $A\overset{\leftrightarrow}{\partial_\mu}B \equiv A(\partial_\mu B)-(\partial_\mu A)B$.

As it can be seen from Eq. (2.1.17) the couplings between the scalar particles and vector bosons ($g_{\varphi_i^0 VV}$) are related to the ones of the SM,

$$g_{\varphi_a^0 VV} = \mathcal{R}_{i1}\, g_{hVV}^{SM}\,, \tag{2.1.18}$$

with $VV = ZZ, WW$. This implies,

$$\sum_{a=1}^{N} g_{\varphi_a^0 VV}^2 = (g_{hVV}^{SM})^2\,, \tag{2.1.19}$$

and indicates that the scalar coupling to weak bosons cannot be enhanced over the SM value and must obey custodial symmetry, *i.e.* $g_{\varphi_a^0 WW}^2 = g_{\varphi_a^0 ZZ}^2$.

2.1.3 Yukawa sector

Yukawa interactions take the generic form,

$$\mathcal{L}_Y \;=\; -\sum_{a=1}^{N}\Big\{\bar{Q}'_L\,(\Gamma_a\phi_a\,d'_R+\Delta_a\phi_a^c\,u'_R)+\bar{L}'_L\,\Pi_a\phi_a\,\ell'_R+\text{h.c.}\Big\}\,, \tag{2.1.20}$$

where Q'_L and L'_L are the left-handed quark and lepton doublets, and d'_R, u'_R, ℓ'_R the corresponding right-handed fermion singlets. All fermion fields denote $N_G = 3$ vectors in flavour space; for instance, $d'_R = (d'_R, s'_R, b'_R)^T$. The Yukawa couplings Γ_a, Δ_a and Π_a are $N_G \times N_G$ complex flavour matrices.

In the Higgs basis the Yukawa structures of Eq. (2.1.20) take the form

$$\sum_{a=1}^{N} \Gamma_a \phi_a \,=\, \sum_{b=1}^{N} \hat{\Gamma}_b \Phi_b \,, \qquad\qquad \sum_{a=1}^{N} \Delta_a \tilde{\phi}_a \,=\, \sum_{b=1}^{N} \hat{\Delta}_b \tilde{\Phi}_b \,, \qquad\qquad \sum_{a=1}^{N} \Pi_a \phi_a \,=\, \sum_{b=1}^{N} \hat{\Pi}_b \Phi_b \,, \tag{2.1.21}$$

with

$$\hat{\Gamma}_b \,=\, \sum_{a=1}^{N} \Omega_{ba}\, \mathrm{e}^{i\tilde{\theta}_a}\, \Gamma_a \,, \qquad\qquad \hat{\Delta}_b \,=\, \sum_{a=1}^{N} \Omega_{ba}\, \mathrm{e}^{-i\tilde{\theta}_a}\, \Delta_a \,, \qquad\qquad \hat{\Pi}_b \,=\, \sum_{a=1}^{N} \Omega_{ba}\, \mathrm{e}^{i\tilde{\theta}_a}\, \Pi_a \,. \tag{2.1.22}$$

The EWSB mechanism generates the mass matrices

$$M'_d \,=\, \frac{v}{\sqrt{2}}\, \hat{\Gamma}_1 \,, \qquad\qquad M'_u \,=\, \frac{v}{\sqrt{2}}\, \hat{\Delta}_1 \,, \qquad\qquad M'_\ell \,=\, \frac{v}{\sqrt{2}}\, \hat{\Pi}_1 \,, \tag{2.1.23}$$

which only involve the Yukawa structures associated with the doublet field Φ_1. Their diagonalization determines the fermion mass eigenstates

$$U_L^{f\dagger}\, M'_f\, U_R^f \,=\, M_f \,, \qquad\qquad f'_L \,=\, U_L^f\, f_L \,, \qquad\qquad f'_R \,=\, U_R^f\, f_R \,, \tag{2.1.24}$$

and the fermion masses

$$M_d \,=\, \mathrm{diag}(m_d, m_s, m_b) \,, \qquad\qquad M_u \,=\, \mathrm{diag}(m_u, m_c, m_t) \,, \qquad\qquad M_\ell \,=\, \mathrm{diag}(m_e, m_\mu, m_\tau) \,. \tag{2.1.25}$$

Neutrinos remain massless because the model does not include ν_R fields.

In terms of the fermion mass eigenstates, the Yukawa Lagrangian is given by

$$\begin{aligned} \mathcal{L}_Y \;\;=\;\; & -\left(1 + \frac{S_1^0}{v}\right) \Big\{ \bar{d}_L M_d d_R + \bar{u}_L M_u u_R + \bar{\ell}_L M_\ell \ell_R \Big\} \\ & - \frac{1}{v} \sum_{a=2}^{N} \Big(S_a^0 + i\, P_a^0 \Big) \Big\{ \bar{d}_L Y_d^{(a)} d_R + \bar{u}_R Y_u^{(a)\dagger} u_L + \bar{\ell}_L Y_\ell^{(a)} \ell_R \Big\} \\ & - \frac{\sqrt{2}}{v} \sum_{a=2}^{N} S_a^+ \Big\{ \bar{u}_L V_{\mathrm{CKM}} Y_d^{(a)} d_R - \bar{u}_R Y_u^{(a)\dagger} V_{\mathrm{CKM}} d_L + \bar{\nu}_L Y_\ell^{(a)} \ell_R \Big\} + \mathrm{h.c.} \,, \end{aligned} \tag{2.1.26}$$

where $V_{\mathrm{CKM}} = U_L^{u\dagger} U_L^d$ is the usual CKM quark-mixing matrix [22, 23]. The analogous mixing matrix in the charged-current leptonic Yukawa, $V_{\mathrm{L}} = U_L^{\nu\dagger} U_L^\ell$, has been reabsorbed through a redefinition of the massless neutrino fields, $\bar{\nu}_L \cdot V_{\mathrm{L}} \to \bar{\nu}_L$, so that the leptonic

$W^\pm$ interactions are flavour diagonal. For $a \neq 1$, the Yukawa structures

$$Y_d^{(a)} \,=\, \frac{v}{\sqrt{2}}\, U_L^{d\dagger}\, \hat{\Gamma}_a\, U_R^d\,, \qquad Y_u^{(a)} \,=\, \frac{v}{\sqrt{2}}\, U_L^{u\dagger}\, \hat{\Delta}_a\, U_R^u\,, \qquad Y_\ell^{(a)} \,=\, \frac{v}{\sqrt{2}}\, U_L^{\ell\dagger}\, \hat{\Pi}_a\, U_R^\ell\,, \tag{2.1.27}$$

are not related to the mass matrices and their elements could take arbitrary complex values. In general, they remain non-diagonal in the fermion mass-eigenstate basis, giving rise to unwanted flavour-changing couplings of the neutral scalar fields.

2.1.4 Natural flavour conservation

The simplest way to avoid flavour non-diagonal Yukawa matrices $Y_f^{(a)}$ is minimizing drastically the number of flavour structures in the Lagrangian (2.1.20) so that, for a given type of right-handed fermion f'_R, only one single scalar doublet ϕ_{a_f} is allowed to have non-zero Yukawa coupling. A given choice of three fields $\{\phi_{a_d}, \phi_{a_u}, \phi_{a_\ell}\}$ defines a particular model with $\Gamma_a = \delta_{a_d a}\, \Gamma_{a_d}$, $\Delta_a = \delta_{a_u a}\, \Delta_{a_u}$ and $\Pi_a = \delta_{a_\ell a}\, \Pi_{a_\ell}$.

In the Higgs basis, this implies

$$\hat{\Gamma}_a \,=\, \Omega_{aa_d}\, \mathrm{e}^{i\tilde{\theta}_{a_d}}\, \Gamma_{a_d}\,, \qquad \hat{\Delta}_a \,=\, \Omega_{aa_u}\, \mathrm{e}^{-i\tilde{\theta}_{a_u}}\, \Delta_{a_u}\,, \qquad \hat{\Pi}_a \,=\, \Omega_{aa_\ell}\, \mathrm{e}^{i\tilde{\theta}_{a_\ell}}\, \Pi_{a_\ell}\,. \tag{2.1.28}$$

Since there are only three flavour structures, one for each type of fermion, the diagonalization of the mass matrices $\hat{\Gamma}_1$, $\hat{\Delta}_1$ and $\hat{\Pi}_1$ also diagonalizes all Yukawas with $a \neq 1$ [24,25]. One obtains:

$$Y_f^{(a)} \,=\, \varsigma_f^{(a)}\, M_f\,, \qquad\qquad \varsigma_f^{(a)} \,=\, \frac{\Omega_{aa_f}}{\Omega_{1a_f}}\,. \tag{2.1.29}$$

This particular form of the Yukawa Lagrangian could be enforced through a discrete symmetry $\mathcal{Z}_2^d \otimes \mathcal{Z}_2^u \otimes \mathcal{Z}_2^\ell$, where each separate $\mathcal{Z}_2^f$ transformation is defined so that f'_R and ϕ_{a_f} reverse sign,

$$\mathcal{Z}_2^f: \quad f'_R \,\to\, -f'_R\,, \qquad\qquad \phi_{a_f} \,\to\, -\phi_{a_f}\,, \tag{2.1.30}$$

while all other fields remain unchanged [26]. The symmetry guarantees that the resulting flavour structure is stable under quantum corrections, ensuring that FCNC local interactions cannot reappear at higher orders. Notice that the assumption of natural flavour

conservation singles out a particular basis of scalar fields where the discrete symmetry is defined.

For $N = 2$, one can choose four different inequivalent options for $\{a_d, a_u, a_\ell\}$, where a_f labels the doublet to which the fermion f'_R is coupled (the remaining possibilities amount to a permutation of ϕ_1 and ϕ_2), which are usually taken as

$$\begin{aligned}
&\text{Type I}: \quad \{2,2,2\}\,, && \varsigma_d = \varsigma_u = \varsigma_\ell = \cot\beta\,,\\
&\text{Type II}: \quad \{1,2,1\}\,, && \varsigma_d = \varsigma_\ell = -\tan\beta\,, \qquad \varsigma_u = \cot\beta\,,\\
&\text{Type X}: \quad \{2,2,1\}\,, && \varsigma_d = \varsigma_u = \cot\beta\,, \qquad \varsigma_\ell = -\tan\beta\,,\\
&\text{Type Y}: \quad \{1,2,2\}\,, && \varsigma_d = -\tan\beta\,, \qquad \varsigma_u = \varsigma_\ell = \cot\beta\,,
\end{aligned} \tag{2.1.31}$$

with $\varsigma_f \equiv \varsigma_f^{(2)}$ and $\tan\beta \equiv v_2/v_1$. A single $\mathcal{Z}_2$ transformation is enough in this case to define the model: ϕ_1 is odd, while ϕ_2, Q'_L, L'_L and u'_R are all even. The four different types of models are obtained defining different transformations of the d'_R and ℓ'_R fields under $\mathcal{Z}_2$. In type I the two fields are even [27, 28], they are both odd in type II [28, 29] $d'_R \to d'_R$ and $\ell'_R \to -\ell'_R$ in type X [30], and $d'_R \to -d'_R$ and $\ell'_R \to \ell'_R$ in type Y [30]. If the $\mathcal{Z}_2$ symmetry is imposed in the Higgs basis, all fermions must couple to Φ_1 in order to get their masses and the doublet Φ_2 necessarily decouples from the fermion sector. One gets then a type-I structure (exchanging the labels 1 and 2) with $\varsigma_f = 0$, known as the inert two-Higgs-doublet model [31].

With $N = 3$ there are five inequivalent possibilities, up to permutations of the three scalar-field labels, which we define through the following choices of $\{a_d, a_u, a_\ell\}$:

$$\begin{aligned}
&\text{Type A}: \quad \{1,1,1\}\,, && \varsigma_d^{(a)} = \varsigma_u^{(a)} = \varsigma_\ell^{(a)} = \Omega_{a1}/\Omega_{11}\\
&\text{Type B}: \quad \{1,2,1\}\,, && \varsigma_d^{(a)} = \varsigma_\ell^{(a)} = \Omega_{a1}/\Omega_{11}\,, \qquad \varsigma_u^{(a)} = \Omega_{a2}/\Omega_{12}\,,\\
&\text{Type C}: \quad \{1,1,2\}\,, && \varsigma_d^{(a)} = \varsigma_u^{(a)} = \Omega_{a1}/\Omega_{11}\,, \qquad \varsigma_\ell^{(a)} = \Omega_{a2}/\Omega_{12}\,,\\
&\text{Type D}: \quad \{1,2,2\}\,, && \varsigma_d^{(a)} = \Omega_{a1}/\Omega_{11}\,, \qquad \varsigma_u^{(a)} = \varsigma_\ell^{(a)} = \Omega_{a2}/\Omega_{12}\,,\\
&\text{Type E}: \quad \{1,2,3\}\,. && \varsigma_d^{(a)} = \Omega_{a1}/\Omega_{11}\,, \qquad \varsigma_u^{(a)} = \Omega_{a2}/\Omega_{12}\,, \qquad \varsigma_\ell^{(a)} = \Omega_{a3}/\Omega_{13}\,.
\end{aligned} \tag{2.1.32}$$

One can easily check that each one of these structures can be enforced by using only two $\mathcal{Z}_2$ symmetries.

For $N > 3$, natural flavour conservation implies that three scalar doublets, which can always be chosen as $\phi_{1,2,3}$, couple to the fermions following one of the five allowed $N = 3$ types, while the remaining $N - 3$ doublets decouple.

2.1.5 Flavour alignment

Natural flavour conservation is a very strong assumption, which for $N > 3$ involves $N - 3$ fermiophobic scalar doublets (in the scalar basis where the $\mathcal{Z}_2^f$ symmetries are imposed). In order to avoid FCNC interacting vertices in $\mathcal{L}_Y$, what is really needed is that only a single flavour structure is present for each f_R type, *i.e.*, the alignment condition [24, 25]:

$$\Gamma_a \,=\, \mathrm{e}^{-i\tilde{\theta}_a}\,\xi_d^{(a)}\,\Gamma_1\,, \qquad \Delta_a \,=\, \mathrm{e}^{i\tilde{\theta}_a}\,\xi_u^{(a)\dagger}\,\Delta_1\,, \qquad \Pi_a \,=\, \mathrm{e}^{-i\tilde{\theta}_a}\,\xi_\ell^{(a)}\,\Pi_1\,, \tag{2.1.33}$$

where $\xi_f^{(1)} = 1$ while $\xi_f^{(a\neq 1)}$ can be arbitrary complex parameters. All Yukawa matrices are then simultaneously diagonalized in the fermion mass-eigenstate basis, with the result

$$Y_{d,\ell}^{(a)} \,=\, \varsigma_{d,\ell}^{(a)}\,M_{d,\ell}\,, \qquad\qquad Y_u^{(a)} \,=\, \varsigma_u^{(a)\dagger}\,M_u\,, \tag{2.1.34}$$

where the alignment proportionality parameters are given by

$$\varsigma_f^{(a)} \,=\, \frac{\sum_{b=1}^N \Omega_{ab}\,\xi_f^{(b)}}{\sum_{b=1}^N \Omega_{1b}\,\xi_f^{(b)}}\,. \tag{2.1.35}$$

Natural flavour conservation corresponds to the particular cases where the alignment parameters $\xi_f^{(b\neq 1)}$ are either all zero ($\varsigma_f^{(a)} = \Omega_{a1}/\Omega_{11}$) or one of them, $\xi_f^{(a_f)}$, takes an infinite value ($\varsigma_f^{(a)} = \Omega_{aa_f}/\Omega_{1a_f}$).

The hypothesis of flavour alignment leads to a very appealing structure for the Yukawa Lagrangian in Eq. (2.1.26): i) all fermion-scalar interactions are proportional to the corresponding fermion mass matrices, ii) FCNCs vertices are absent at tree level, and iii) the only source of flavour-changing transitions is the charged-current quark mixing matrix V_{CKM}, which appears in the $W^\pm$ and $H^\pm$ fermionic couplings. In addition to the fermion masses, the only new parameters introduced by the Yukawa interactions are the $3(N-1)$ complex alignment factors $\varsigma_f^{(a)}$ ($a \neq 1$), which provide additional sources of CP violation beyond the SM quark-mixing phase.

The flavour-alignment condition does not exhaust all possibilities for a tree-level Lagrangian without FCNC interactions. The most general structure is obtained with a set of N simultaneously-diagonalizable matrices $Y_f^{\prime(a)}$, for each type of fermion f. One can also describe this generic possibility with the parametrization (2.1.34) through the alignment matrices

$$\varsigma_{d,\ell}^{(a)} \equiv Y_{d,\ell}^{(a)}\, M_{d,\ell}^{-1}\,, \qquad\qquad \varsigma_u^{(a)\dagger} \equiv Y_u^{(a)}\, M_u^{-1}\,. \tag{2.1.36}$$

These expressions are completely general because all charged fermion masses are known to be non vanishing; therefore, $\det M_f \neq 0$ and M_f^{-1} is well defined. Since all $Y_f^{(a)}$ matrices are assumed to be diagonal, the alignment factors become now diagonal matrices (in the fermion mass-eigenstate basis):

$$\varsigma_d^{(a)} = \mathrm{diag}(\varsigma_d^{(a)},\varsigma_s^{(a)},\varsigma_b^{(a)})\,, \qquad \varsigma_u^{(a)} = \mathrm{diag}(\varsigma_u^{(a)},\varsigma_c^{(a)},\varsigma_t^{(a)})\,, \qquad \varsigma_\ell^{(a)} = \mathrm{diag}(\varsigma_e^{(a)},\varsigma_\mu^{(a)},\varsigma_\tau^{(a)})\,. \tag{2.1.37}$$

The structure of the resulting Yukawa Lagrangian in Eq. (2.1.26) is formally the same than for normal alignment (provided one takes care of not commuting the matrix factors $\varsigma_f^{(a)}$ and V_{CKM}). However, one loses the hierarchies dictated by the fermion mass spectrum because there is really no connection between the numerical values of the Yukawa couplings and the corresponding masses. Small (large) values of m_f can be compensated with large (small) $\varsigma_f^{(a)}$ factors so that $y_f^{(a)} = \varsigma_f^{(a)} m_f$ have acceptable magnitudes in the perturbative regime.

In the fermion weak-eigenstate basis, the relation between the Yukawa matrices $Y_f^{\prime(a)}$ and $M_f^{\prime}$ involves the alignment factors

$$\varsigma_f^{\prime(a)} = U_L^f\, \varsigma_f^{(a)}\, U_L^{f\dagger}\,, \tag{2.1.38}$$

which, in general, are no-longer diagonal. Therefore, $Y_f^{\prime(a)}$ and $M_f^{\prime}$ do not necessarily commute. The absence of FCNC interactions only requires this commutator to be zero in the fermion mass-eigenstate basis.

2.1.6 The two Higgs doublet model

The simplest non-trivial NHDM is the so-called two-Higgs doublet model (2HDM) in which an extra doublet is added. Despite its simplicity the model contains interesting features.

In the case of $N = 2$ the potential of Eq. (2.1.4) is usually written,

$$\begin{aligned} V &= \mu_1^2(\Phi_1^\dagger\Phi_1) + \mu_2^2(\Phi_2^\dagger\Phi_2) + [\mu_3\Phi_1^\dagger\Phi_2 + \mu_3^*\Phi_2^\dagger\Phi_1] \\ &+\lambda_1(\Phi_1^\dagger\Phi_1)^2 + \lambda_2(\Phi_2^\dagger\Phi_2)^2 + \lambda_3(\Phi_1^\dagger\Phi_1)(\Phi_2^\dagger\Phi_2) + \lambda_4(\Phi_1^\dagger\Phi_2)(\Phi_2^\dagger\Phi_1) \\ &+\Big[(\lambda_5\Phi_1^\dagger\Phi_2 + \lambda_6\Phi_1^\dagger\Phi_1 + \lambda_7\Phi_2^\dagger\Phi_2)(\Phi_1^\dagger\Phi_2) + \text{h.c.}\Big]\,. \end{aligned} \tag{2.1.39}$$

where the connexion with Eq. (2.1.4) reads,

$$\begin{aligned} \lambda_1 &= Z_{1111}, & \lambda_2 &= Z_{2222}, & \lambda_3 &= Z_{1122} + Z_{2211} = 2\,Z_{1122}, \\ \lambda_4 &= Z_{1221} + Z_{2112} = 2\,Z_{1221}, & \lambda_5 &= Z_{1212}, \\ \lambda_6 &= Z_{1112} + Z_{1211} = 2\,Z_{1112}, & \lambda_7 &= Z_{2212} + Z_{1222} = 2\,Z_{2212}. \end{aligned} \tag{2.1.40}$$

The quadratic term Eq. (2.1.8) can be written as,

$$V_2 = M_{H^\pm}^2 H^+H^- + \frac{1}{2}\begin{bmatrix} S_1^0, & S_2^0, & P_2^0 \end{bmatrix} \mathcal{M} \begin{bmatrix} S_1^0 \\ S_2^0 \\ P_2^0 \end{bmatrix}, \tag{2.1.41}$$

where $M_{H^\pm}^2$ is a function of the parameters of the potential and the mass matrix of the neutral scalar fields is non-diagonal,

$$M_{H^\pm}^2 = \mu_2^2 + \frac{1}{2}\lambda_3 v^2\,, \tag{2.1.42}$$

$$\mathcal{M} = \begin{bmatrix} 2\lambda_1 v^2 & v^2\lambda_6^R & -v^2\lambda_6^I \\ v^2\lambda_6^R & M_{H^\pm}^2 + v^2\left(\frac{\lambda_4}{2} + \lambda_5^R\right) & -v^2\lambda_5^I \\ -v^2\lambda_6^I & -v^2\lambda_5^I & M_{H^\pm}^2 + v^2\left(\frac{\lambda_4}{2} - \lambda_5^R\right) \end{bmatrix}. \tag{2.1.43}$$

with $\lambda_i^R = \mathcal{R}\mathrm{e}(\lambda_i)$ and $\lambda_i^I = \mathcal{I}\mathrm{m}(\lambda_i)$.

The matrix $\mathcal{M}$ is diagonalized by an orthogonal rotation, $\mathcal{R}$ that relates the fields $\{S_1^0, S_2^0, P_2^0\}$ with the mass eigenstates $\varphi_i^0 = \{h, H, A\}$:

$$\mathcal{M} = \mathcal{R}^T \begin{bmatrix} M_h^2 & 0 & 0 \\ 0 & M_H^2 & 0 \\ 0 & 0 & M_A^2 \end{bmatrix} \mathcal{R}\,, \qquad \begin{bmatrix} h \\ H \\ A \end{bmatrix} = \mathcal{R} \begin{bmatrix} S_1^0 \\ S_2^0 \\ P_2^0 \end{bmatrix}\,. \tag{2.1.44}$$

Matching the traces of (2.1.43) and (2.1.44),

$$M_h^2 + M_H^2 + M_A^2 = 2M_{H^\pm}^2 + v^2(2\lambda_1 + \lambda_4)\,. \tag{2.1.45}$$

In the CP conserving limit ($\lambda_5^I = \lambda_6^I = \lambda_7^I = 0$) the CP admixture disappears and P_2^0 does not mix with other neutral fields. The scalar spectrum contains a CP-odd field, $A = P_2^0$, and two CP-even fields, h and H, which are a mixture of S_1^0 and S_2^0,

$$\begin{bmatrix} h \\ H \end{bmatrix} = \begin{bmatrix} \cos\tilde{\alpha} & \sin\tilde{\alpha} \\ -\sin\tilde{\alpha} & \cos\tilde{\alpha} \end{bmatrix} \begin{bmatrix} S_1^0 \\ S_2^0 \end{bmatrix}\,. \tag{2.1.46}$$

The Yukawa couplings take the simple form,

$$\begin{aligned} y_{d,\ell}^h &= \cos\tilde{\alpha} + \sin\tilde{\alpha}\,\varsigma_{d,\ell}\,, & y_{d,\ell}^H &= -\sin\tilde{\alpha} + \cos\tilde{\alpha}\,\varsigma_{d,\ell}\,, & y_{d,\ell}^A &= i\,\varsigma_{d,\ell}\,, \\ y_u^h &= \cos\tilde{\alpha} + \sin\tilde{\alpha}\,\varsigma_u^*\,, & y_u^H &= -\sin\tilde{\alpha} + \cos\tilde{\alpha}\,\varsigma_u^*\,, & y_u^A &= -i\,\varsigma_u^*\,. \end{aligned} \tag{2.1.47}$$

We choose the convention $M_h \leq M_H$ and $0 \leq \tilde{\alpha} \leq \pi$, so that $\sin\tilde{\alpha}$ is positive.

In this case, the masses of the scalar fields are:

$$M_h^2 = \frac{1}{2}(\Sigma - \Delta)\,, \quad M_H^2 = \frac{1}{2}(\Sigma + \Delta)\,, \quad M_A^2 = M_{H^\pm}^2 + v^2\Big(\frac{\lambda_4}{2} - \lambda_5^R\Big)\,, \tag{2.1.48}$$

with

$$\Sigma = M_{H^\pm}^2 + v^2\left(2\lambda_1 + \frac{\lambda_4}{2} + \lambda_5^R\right), \tag{2.1.49}$$

$$\Delta = \sqrt{\left[M_{H^\pm}^2 + v^2(-2\lambda_1 + \frac{\lambda_4}{2} + \lambda_5^R)\right]^2 + 4v^2(\lambda_6^R)^2}\,,$$

$$\tan\tilde{\alpha} = \frac{M_h^2 - 2\lambda_1 v^2}{\lambda_6^R v^2}\,.$$

Chapter 3

Effective Field Theory

Effective field theory is a useful tool to describe physical problems involving different energy scales [32–37]. In an EFT approach one uses the appropriate *degrees of freedom* (d.o.f.) to describe physical systems, *i.e.* one isolates the d.o.f. that give relevant effects for the studied model or process. The main idea is based in the *decoupling theorem* [38]:

The contribution to physical amplitudes of the heavy d.o.f. are suppressed by inverse powers of mass up to logarithmic corrections.

This means that the dynamics of a system at low energies cannot depend on the details at high energies. Referring to high and low energies implies that both an energy scale and a range of validity has to be set.

The SM has succeed in reproducing many electroweak tests with an extreme precision, which seems to be a strong confirmation of the model. However, one can also find deviations from the SM predictions (flavour anomalies, $(g-2)_\mu$...), that can be interpreted as new physics (NP). This apparent incompatibility is understood once we introduce the EFT formalism. Within this formalism the effect of NP lying in high energy scales is suppressed at the electroweak scale. Therefore, the SM is recovered at low energies.

EFT allow us to identify these NP effects though small deviations of the low-energy parameters of a given effective Lagrangian from the SM ones. Such deviations are accessible though high-precision low-energy experiments.

3.1 Operator product expansion

Let's consider a theory whose particle content is a heavy scalar field, Φ_H with mass M and a light field Φ_L with mass m,

$$\mathcal{L} = \mathcal{L}_{\text{kin}}^{\Phi_H} + \mathcal{L}_{\text{kin}}^{\Phi_L} + J\Phi_H \,, \tag{3.1.1}$$

where the first two terms are the kinetic terms of the fields,

$$\mathcal{L}_{\text{kin}}^{\Phi_{H,L}} = -\frac{1}{2}\Phi_{H,L}\left(\Box + m^2_{\Phi_{H,L}}\right)\Phi_{H,L} \,, \tag{3.1.2}$$

with $\Box = \partial_\mu \partial^\mu$. The last term of Eq. (3.1.1) is the source of Φ_H. Note there is not a similar term for Φ_L because we are obtaining an effective Lagrangian whose functional is,

$$Z_{\text{eff}}[J] = \int [\mathcal{D}\,\Phi_L] \exp\left[i \int d^4x (\mathcal{L}_{\text{eff}} + J_L \Phi_L)\right] . \tag{3.1.3}$$

Our purpose is to study some phenomenological effect of these fields at a given scale $E \ll M$. The normalized generating functional is,

$$Z[J] \equiv \frac{\int [\mathcal{D}\,\Phi_L][\mathcal{D}\,\Phi_H] \mathrm{e}^{iS[\Phi_L,\Phi_H,J]}}{\int [\mathcal{D}\,\Phi_L][\mathcal{D}\,\Phi_H] \mathrm{e}^{iS[\Phi_L,\Phi_H,0]}} \,, \tag{3.1.4}$$

where $S[\Phi_L, \Phi_H, J] \equiv \int d^D x\, \mathcal{L}$ is the action of $\mathcal{L}$ and D is the dimension of spacetime.

The field Φ_H does not satisfy the equation of motion, but one can rewrite it in terms of an auxiliary field Φ_0 defined as $\Phi_H = \tilde{\Phi} + \Phi_0$ that does satisfy such equation,

$$\left(\Box + m^2_{\Phi_H}\right)\Phi_0 = J(x) \,. \tag{3.1.5}$$

The solution of Eq. (3.1.5) is,

$$\Phi_0(x) = -\int d^D y\, \Delta_F(x-y)\, J(y)\,, \tag{3.1.6}$$

where $\Delta_F(x-y)$ is the Feynman propagator,

$$\Delta_F(x-y) \equiv \int \frac{d^D k}{(2\pi)^D} \frac{\mathrm{e}^{-ik\cdot(x-y)}}{k^2 - M^2 - i\epsilon}\,. \tag{3.1.7}$$

The Lagrangian of Eq. (3.1.1) can be written in terms of Φ_0,

$$\begin{aligned}
\mathcal{L}[\Phi_L, \Phi_H] &= \mathcal{L}[\Phi_L, \tilde{\Phi}, \Phi_0] = \mathcal{L}^{\Phi_L}_{\rm kin} + \mathcal{L}^{\Phi_0}_{\rm kin} + \mathcal{L}^{\tilde{\Phi}}_{\rm kin} - \frac{1}{2}\Phi_0\left(\Box + M^2\right)\tilde{\Phi} \\
&- \frac{1}{2}\tilde{\Phi}\left(\Box + M^2\right)\Phi_0 + J\left(\tilde{\Phi} + \Phi_0\right) \\
&= \mathcal{L}^{\Phi_L}_{\rm kin} + \mathcal{L}^{\tilde{\Phi}}_{\rm kin} + \frac{1}{2}J\,\Phi_0 - \frac{1}{2}\partial_\mu\left(\Phi_0\partial^\mu\tilde{\Phi} - \tilde{\Phi}\partial^\mu\Phi_0\right)\,,
\end{aligned} \tag{3.1.8}$$

where we have applied the identity

$$\Phi_0\Box\tilde{\Phi} - \tilde{\Phi}\Box\Phi_0 = \partial_\mu\left(\Phi_0\partial^\mu\tilde{\Phi} - \tilde{\Phi}\partial^\mu\Phi_0\right)\,, \tag{3.1.9}$$

and the equation of motion of Eq.(3.1.5).

The action can be expressed as,

$$S[\Phi_L, \tilde{\Phi}, \Phi_0, J] = \int d^D x\left(\mathcal{L}^{\Phi_L}_{\rm kin} + \mathcal{L}^{\tilde{\Phi}}_{\rm kin} + \frac{1}{2}J\,\Phi_0\right)\,, \tag{3.1.10}$$

where the last term of Eq. (3.1.10) has been eliminated using Gauss' law. Using Eq. (3.1.6),

$$S[\Phi_L, \tilde{\Phi}, \Phi_0, J] = \int d^D x\left(\mathcal{L}^{\Phi_L}_{\rm kin} + \mathcal{L}^{\tilde{\Phi}}_{\rm kin}\right) - \frac{1}{2}\int d^D x\, d^D y\, J(x)\,\Delta_F(x-y)J(y)\,, \tag{3.1.11}$$

the generating functional can be written as,

$$Z[J] = \exp\left(-\frac{i}{2}\int d^D x\, d^D y\, J(x)\,\Delta_F(x-y)J(y)\right)\,. \tag{3.1.12}$$

This generating function can be obtained from a non-local Lagrangian,

$$\mathcal{L} = -\frac{1}{2}\int d^D y\, J(x)\, \Delta_F(x-y)\, J(y)\,, \tag{3.1.13}$$

and thus we have obtained the same functional with a simpler Lagrangian than the one of Eq. (3.1.8). The dependence on the heavy field Φ_H has been cancelled out with the normalization $Z[0]$. We say that the heavy field has been *integrated out*.

Now we can consider $x \approx y$ and perform a Taylor expansion,

$$J(y) = \lim_{N\to\infty} \sum_{n=0}^{N} \frac{(-1)^n}{n!} \hat{J}_{\mu_1\ldots\mu_n}(x)(x-y)^{\mu_1}\ldots(x-y)^{\mu_n}\,, \tag{3.1.14}$$

where $\hat{J}_{\mu_1\ldots\mu_n}(x) \equiv \left(\partial^z_{\mu_1}\ldots\partial^z_{\mu_n}\right) J(z)\Big|_{z=x}$. Then using Eq. (3.1.7),

$$\begin{aligned}
\mathcal{L} &= -\frac{1}{2}\lim_{N\to\infty}\sum_{n=0}^{N}\frac{(-1)^n}{n!}J(x)\,\hat{J}_{\mu_1\ldots\mu_n}(x)\cdot\int\frac{d^Dk}{(2\pi)^D}\frac{1}{k^2-M^2}\cdot\int d^Dy\,(x-y)^{\mu_1}\ldots(x-y)^{\mu_n}\,\mathrm{e}^{-ik\cdot(x-y)}\\
&= -\frac{1}{2}\lim_{N\to\infty}\sum_{n=0}^{N}\frac{(-i)^n}{n!}J(x)\,\hat{J}_{\mu_1\ldots\mu_n}(x)\cdot\int\frac{d^Dk}{(2\pi)^D}\frac{1}{k^2-M^2}\cdot\int d^Dy\,\partial_k^{\mu_1}\ldots\partial_k^{\mu_n}\,\mathrm{e}^{-ik\cdot(x-y)}\\
&= \frac{1}{2}\frac{1}{M^2}\lim_{N\to\infty}\sum_{n=0}^{\frac{N}{2}}J(x)\left(-\frac{\Box}{M^2}\right)^n J(x)\,,
\end{aligned} \tag{3.1.15}$$

where we have used the Dirac Delta $\int d^Dz\mathrm{e}^{ikz} = (2\pi)^D\delta^{(D)}(k)$ and,

$$\partial_k^{\mu_1}\ldots\partial_k^{\mu_n}\,\mathrm{e}^{-ik\cdot(x-y)} = (-i)^n(x-y)^{\mu_1}\ldots(x-y)^{\mu_n}\mathrm{e}^{ik(x-y)}. \tag{3.1.16}$$

We obtain a series of local operators depending on the source $J(x)$. Truncating the series of Eq. (3.1.15),

$$\mathcal{L}_{\text{eff}} \approx \frac{1}{2}\frac{1}{M^2}\sum_{n=0}^{N/2}J(x)\left(-\frac{\Box}{M^2}\right)^n J(x), \tag{3.1.17}$$

Since $E/M < 1$, the $N+1$ missing corrections are always smaller than the included ones, assuring the convergence of the series. This is called the operator product expansion (OPE).

3.2 Effective Lagrangian

As we have seen an effective Lagrangian can be expressed in terms of a sum of local operators [39],

$$\mathcal{L}_{\text{eff}} = \sum_{i,j} \frac{c_i^{(j)}}{\Lambda^{d_i-4}} \mathcal{O}_i^{(j)} = \sum_{i,j} C_i^{(j)} \mathcal{O}_i^{(j)} \,, \tag{3.2.18}$$

where $\mathcal{O}_i^{(j)}$ are the *operators* of dimension d_i, constructed from the light fields and $C_i^{(j)}$ are the so-called *Wilson coefficients* which contain information about the couplings with the heavy degrees of freedom. Λ is the scale where the heavy fields become relevant, *i.e.* the NP scale. The sum over j accounts for all the different operators with the same dimension.

Depending on the dimension of the operators they can be classified into three different types,

- $d_i < 4$: *Relevant operators.* They are important at low energies. Usually they are forbidden by symmetries. They are superrenormalizable operators.
- $d_i = 4$: *Marginal operators.* Their effects are not suppressed by powers of the ratio E/Λ. (they can only receive small logarithmic corrections $\ln E/\Lambda$). They are renormalizable operators.
- $d_i > 4$: *Irrelevant operators.* They are suppressed at low energies. Non-renormalizable operators.

$\mathcal{L}_{\text{eff}}$ contains an infinite number of terms (power series in Λ). Therefore, we say it is non-renormalizable in the usual sense, since we would need an infinite number of counterterms to renormalize it. However, the effective Lagrangian is usually truncanted at some dimension N, and, therefore, only a finite number of counterterms are needed [35].

3.3 Renormalization group equations

Let's consider the Lagrangian of Eq. (3.2.18) expressed in terms of the bare operators and Wilson coefficients,

$$\begin{aligned}\mathcal{L}_{\text{eff}} &= \sum_i \left(\sum_j \mathcal{C}_i^{(j)\,B} \mathcal{O}_i^{(j)\,B} \right) = \sum_i \left(\sum_j \mathcal{C}_i^{(j)\,B} \sum_a^n Z_{ia}^{(j)}(\mu)\, \mathcal{O}_a^{(j)}(\mu) \right) \\ &= \sum_i \left(\sum_j \mathcal{C}_i^{(j)}(\mu)\, \mathcal{O}_i^{(j)}(\mu) \right) \equiv \sum_i \left(\boldsymbol{\mathcal{C}}_i^T(\mu)\, \boldsymbol{\mathcal{O}}_i(\mu) \right) , \end{aligned} \tag{3.3.19}$$

where $\boldsymbol{\mathcal{O}}_i$ are 1-column vectors and $\boldsymbol{\mathcal{C}}_i^T$ are 1-row vectors of dimension d_i. The matrices $Z_{ia}^{(j)}$ are the renormalization constants. In general different operators of the same dimension mix under renormalization,

$$\mathcal{O}_i^{(j)\,B} = \sum_a^n Z_{ia}^{(j)}(\mu)\, \mathcal{O}_a^{(j)}(\mu) \;\rightarrow\; \mathcal{C}_i^{(j)\,B} = \sum_a^n \left(Z^{(j)} \right)^{-1}_{ai} (\mu)\, \mathcal{C}_a^{(j)}(\mu) \,. \tag{3.3.20}$$

Or in matrix notation,

$$\boldsymbol{\mathcal{O}}^{(j)\,B} = \mathbf{Z}^{(j)}(\mu)\, \boldsymbol{\mathcal{O}}^{(j)}(\mu) \;\rightarrow\; \boldsymbol{\mathcal{C}}^{(j)\,B} = \left(\left(\mathbf{Z}^{(j)} \right)^{-1} \right)^T (\mu)\, \boldsymbol{\mathcal{C}}^{(j)}(\mu) \,. \tag{3.3.21}$$

Loop corrections and hence the μ-dependence is included in the Wilson coefficients so that the renormalized $\mathcal{L}_{\text{eff}}$ is scale independent. The renormalization group equations (RGEs) will give us the μ-dependence for $\boldsymbol{\mathcal{C}}$ and $\boldsymbol{\mathcal{O}}$. Since the bare operators do not depend on the scale one can take their derivative with respect to the scale μ,

$$\mu \frac{d\boldsymbol{\mathcal{O}}^{(j)\,B}(\mu)}{d\mu} = 0 = \mu\, \frac{d\mathbf{Z}^{(j)}}{d\mu} \boldsymbol{\mathcal{O}}^{(j)} + \mu\, \mathbf{Z}^{(j)} \frac{d\boldsymbol{\mathcal{O}}^{(j)}}{d\mu} \,. \tag{3.3.22}$$

This can be written in a more compact way defining the gamma function of $\boldsymbol{\mathcal{O}}^{(j)}$,

$$\gamma_{\mathcal{O}}^{(j)} = \left(\mathbf{Z}^{(j)} \right)^{-1} \mu\, \frac{d}{d\mu} \mathbf{Z}^{(j)} = \gamma_{\mathcal{O}}^{(j)\,(1)} \left(\frac{\alpha}{\pi} \right) + \gamma_{\mathcal{O}}^{(j)\,(2)} \left(\frac{\alpha}{\pi} \right)^2 + \dots \,, \tag{3.3.23}$$

where α is the expansion parameter. From Eq. (3.3.22) the RGEs can be written as,

$$\left(\mu\,\frac{d}{d\mu}+\gamma_{\mathcal{O}}^{(j)}\right)\boldsymbol{\mathcal{O}}(\mu)=0\,,\;\rightarrow\;\left(\mu\,\frac{d}{d\mu}-\left(\gamma_{\mathcal{O}}^{(j)}\right)^{T}\right)\boldsymbol{\mathcal{C}}(\mu)=0\,. \tag{3.3.24}$$

To solve Eq. (3.3.24) one must find a matrix $\mathbf{U}^{(j)}$ that diagonalizes $\gamma_{\mathcal{O}}^{(j)}$,

$$\left(\mathbf{U}^{(j)}\right)^{-1}\left(\gamma_{\mathcal{O}}^{(j)}\right)^{T}\mathbf{U}=\widetilde{\gamma}_{\mathcal{O}}^{(j)}\,, \tag{3.3.25}$$

where $\widetilde{\gamma}_{\mathcal{O}}^{(j)}$ is a diagonal matrix. Inserting Eq. (3.3.25) at (3.3.24),

$$\left(\mathbf{U}^{(j)}\,\left(\mathbf{U}^{(j)}\right)^{-1}\,\mu\,\frac{d}{d\mu}-\mathbf{U}^{(j)}\,\widetilde{\gamma}_{\mathcal{O}}^{(j)}\,\left(\mathbf{U}^{(j)}\right)^{-1}\right)\boldsymbol{\mathcal{C}}^{(j)}(\mu)=0\,, \tag{3.3.26}$$

and defining $\tilde{\boldsymbol{\mathcal{C}}}\equiv\mathbf{U}^{-1}\boldsymbol{\mathcal{C}}$ we can write Eq. (3.3.24) in diagonal form,

$$\left(\mu\,\frac{d}{d\mu}-\widetilde{\gamma}_{\mathcal{O}}^{(j)}\right)\tilde{\boldsymbol{\mathcal{C}}}^{(j)}(\mu)=0\,. \tag{3.3.27}$$

Now the coefficients $\mathcal{C}_i^{(j)}(\mu)$ obey unmixed RGEs,

$$\left(\mu\,\frac{d}{d\mu}-\widetilde{\gamma}_{\mathcal{O},i}^{(j)}\right)\tilde{\mathcal{C}}_i^{(j)}(\mu)=0\,, \tag{3.3.28}$$

where $\widetilde{\gamma}_{\mathcal{O},i}^{(j)}$ are the diagonal terms of $\widetilde{\gamma}_{\mathcal{O}}^{(j)}$. The solution of this equation is,

$$\tilde{\mathcal{C}}_i^{(j)}(\mu)=\tilde{\mathcal{C}}_i^{(j)}(\mu_0)\exp\left\{\int_{\alpha(\mu_0)}^{\alpha(\mu)}\frac{d\alpha}{\alpha}\frac{\widetilde{\gamma}_{\mathcal{O},i}^{(j)}(\alpha)}{\beta(\alpha)}\right\}\,. \tag{3.3.29}$$

where

$$\beta\left(\alpha\right)\equiv-\frac{\mu}{Z_\alpha}\frac{dZ_\alpha}{d\mu}\,, \tag{3.3.30}$$

and Z_α is the renormalization constant relating the bare parameter α_0 to α *i.e.*, $\alpha_0=Z_\alpha\,\alpha$.

β is the *anomalous dimension of the coupling* and it can be perturbatively expanded as,

$$\beta(\alpha)=\beta_1\left(\frac{\alpha}{\pi}\right)+\beta_2\left(\frac{\alpha}{\pi}\right)^2+...=\sum_i\beta_i\left(\frac{\alpha}{\pi}\right)^i\,. \tag{3.3.31}$$

Finally, changing the basis we can write the solution of the RGEs in terms of our original, mixed coefficients,

$$\mathcal{C}_i^{(j)}(\mu) = \sum_{a,k} \mathbf{U}_{ia} \exp\left\{ \int_{\alpha(\mu_0)}^{\alpha(\mu)} \frac{d\alpha}{\alpha} \frac{\gamma^{(j)}_{\mathcal{O},\,a}(\alpha)}{\beta(\alpha)} \right\} \left(\left(\mathbf{U}^{(j)} \right)^{-1} \right)_{ak} \mathcal{C}_k^{(j)}(\mu_0)\,. \tag{3.3.32}$$

Chapter 4

Flavour observables in $q_u \to q_d \ell \bar{\nu}$ transitions

A huge effort has been made to build particle colliders that allow us to access regions of parameter space where deviations from the SM could lie. At present, the most important experiments operate at the LHC at CERN. This is a *pp* collider containing different particle detectors (ATLAS, CMS, ALICE and LHCb). It has been running since 2008, with energies up to 13 TeV and has collected a luminosity of 140 fb^{-1} in Run 2. In general, one can distinguish two different directions that can be followed to access to NP information at colliders.

First of all, one can try to detect heavy particles through *direct searches*. A collision will produce particles that are not described by the SM and could be interpreted as NP, *i.e.* in processes such as $pp \to X_{\text{NP}}$. These direct searches have not resulted in the observation of relevant states up to energy scales of approximately 1 TeV, but have been very useful to set upper bounds on the masses of particles predicted in different NP models.[1] The other promising way to observe NP at particle colliders is through *precision physics*. As described in Chapter 3, deviations from the SM can be observed in precision low-energy

[1] For a small set of direct searches see Refs. [40–43].

parameters from an EFT approach. As an example of that, the so-called *flavour anomalies* have driven the attention of the particle physics community. They are deviations of flavour observables from their SM predictions. These flavour anomalies include discrepancies between the inclusive and exclusive determinations of CKM elements [44], anomalies in neutral semileptonic decays $b \to s\ell\ell$ transitions [45–47] and charged-current anomalies in $b \to c\tau\nu$ transitions [48]. The latter will be the ones studied in this thesis. Their basic features and interest will be described in the following sections. The analysis of the anomalies with the current data can be found in Chapter 8.

To study them, let's start by considering the effective Hamiltonian of $q_u \to q_d \ell \bar{\nu}$ transitions containing both left- and right-handed neutrinos at the electroweak scale,

$$\mathcal{H}_{\text{eff}} = \frac{4 G_F V_{q_u\, q_d}}{\sqrt{2}} \left(\mathcal{O}^V_{LL} + \sum_{\substack{X=S,V,T \\ A,B=L,R}} C^X_{AB}\, \mathcal{O}^X_{AB} \right), \tag{4.0.1}$$

with the ten four-fermion operators:

$$\begin{aligned} \mathcal{O}^V_{AB} &\equiv (\bar{q}_u\, \gamma^\mu P_A q_d) \left(\bar{\ell} \gamma_\mu P_B \nu \right), \\ \mathcal{O}^S_{AB} &\equiv (\bar{q}_u\, P_A q_d) \left(\bar{\ell} P_B \nu \right), \\ \mathcal{O}^T_{AB} &\equiv \delta_{AB}\ (\bar{q}_u\, \sigma^{\mu\nu} P_A q_d) \left(\bar{\ell} \sigma_{\mu\nu} P_A \nu \right), \end{aligned} \tag{4.0.2}$$

which are invariant under $SU(3)_C \otimes U(1)_{\text{em}}$. Tensor operators with different lepton and quark chiralities vanish identically.[2]

In absence of NP, the only non-zero operator comes from the W_μ mediator, contributing to the SM Wilson operator $\mathcal{O}^V_{LL}$. These dimension-six operators mediate transitions involving one up and one down quarks, a charged lepton and its corresponding neutrino. They can be interpreted in terms of NP mediators lying at a high energy scale and described in different UV models (see Sections 8.2.3 and 8.3.3.1). The relation between the

[2] This is a direct consequence of the Dirac-algebra identity $\sigma^{\mu\nu} = \frac{i}{2}\, \varepsilon^{\mu\nu\alpha\beta} \sigma_{\alpha\beta}$, which implies $\sigma_{\mu\nu} \otimes \sigma^{\mu\nu}\gamma_5 = \sigma_{\mu\nu}\gamma_5 \otimes \sigma^{\mu\nu}$ and $\sigma_{\mu\nu}\gamma_5 \otimes \sigma^{\mu\nu}\gamma_5 = \sigma_{\mu\nu} \otimes \sigma^{\mu\nu}$. We use the convention $\varepsilon^{0123} = -\varepsilon^{0123} = -1$.

corresponding Wilson coefficients at a high-energy scale and the observables lying at the electroweak scale is given by the RGEs as it is illustrated in Section 8.2.3.

The Hamiltonian of Eq. (4.0.1) allows us to study both leptonic and semileptonic decays of pseudoscalar mesons and to build observables that have been already measured or could be accessed experimentally in the near future. The discrepancies between some of these observables and their SM predictions are promising hints of NP that will be studied in Chapter 8. The set of observables that can be built, but have not been measured yet can help us to disentangle several of the possible NP solutions.

In the case of leptonic decays, the non-perturbative QCD part is the *meson decay constant* calculated from *lattice QCD* (LQCD). For the semileptonic decays, one has to control several form factors (FFs) depending on the dilepton momentum squared q^2.

In the following sections, leptonic and semileptonic decays as well as the relevant observables that can be built will be briefly described. For the former, the helicity formalism, typically used to describe semileptonic transitions keeping the polarization of the involved particles will be summarized.

4.1 Leptonic decays

We will calculate the leptonic decay $P^-(q) \to \ell(p_1)\bar{\nu}_\ell(p_2)$. P^- is a pseudoscalar meson $J^P = 0^-$ formed by $\bar{q}_u$ and q_d. Some examples of these pseudoscalar mesons are $K^- = \bar{u}s, D^- = \bar{c}d$ or $B^- = \bar{u}b$.

To study observables related to these transitions, the corresponding hadronic currents are needed. One can write the hadronic parts of Eq. (4.0.1) in terms of vector, axial, scalar, pseudoscalar and tensor currents,

$$
\begin{aligned}
V^\mu(x) &= \bar{q}_u(x)\gamma^\mu q_d(x) = \bar{q}_u(x)\gamma^\mu q_{d\,R}(x) + \bar{q}_u(x)\gamma^\mu q_{d\,L}(x) \\
A^\mu(x) &= \bar{q}_u(x)\gamma^\mu\gamma^5 q_d(x) = \bar{q}_u(x)\gamma^\mu q_{d\,R}(x) - \bar{q}_u(x) q_{d\,L}(x)\,, \\
S(x) &= \bar{q}_u(x) q_d(x) = \bar{q}_u(x) q_{d\,R}(x) + \bar{q}_u(x) q_{d\,L}(x) \\
P(x) &= \bar{q}_u(x)\gamma^5 q_d(x) = \bar{q}_u(x)\gamma^5 q_{d\,R}(x) - \bar{q}_u(x)\gamma^5 q_{d\,L}(x), \\
T^{\mu\nu}(x) &= \bar{q}_u(x)\sigma^{\mu\nu} q_d(x) = \bar{q}_u(x)\,\sigma^{\mu\nu} q_{d\,R}(x) + \bar{q}_u(x)\,\sigma^{\mu\nu} q_{d\,L}(x), \\
T_5^{\mu\nu}(x) &= \bar{q}_u(x)\sigma^{\mu\nu}\gamma^5 q_d(x) = \bar{q}_u(x)\,\sigma^{\mu\nu} q_{d\,R}(x) - \bar{q}_u(x)\,\sigma^{\mu\nu} q_{d\,L}(x). \qquad (4.1.3)
\end{aligned}
$$

Due to parity conservation and Lorentz invariance, the vector, scalar and tensor currents will not contribute to the decay amplitude.[3] For the axial current, the matrix element is parametrized as,

$$\langle 0|\, A^\mu(x)\, |P(q)\rangle = i\mathrm{e}^{-iqx} f_P\, q^\mu\,, \qquad (4.1.4)$$

where f_P is the so-called decay constant. Decay constants are well determined from LQCD and can be found at Refs. [49, 50]. Applying the QCD equation of motion at Eq. (4.1.4) one gets the pseudoscalar matrix element,

$$\langle 0|\, P(x)\, |P(q)\rangle = -\frac{i\mathrm{e}^{-iqx}\, f_P\, M_P^2}{m_{q_u} + m_{q_d}}\,. \qquad (4.1.5)$$

Then, the matrix elements $\mathcal{M}_{L,R}$ corresponding to the decay into left- and right-handed neutrinos, respectively, are given by

[3] Note that a pseudoscalar meson is odd under parity. Therefore only the axial and the pseudoscalar will contribute to leptonic decays.

$$\begin{aligned}\mathcal{M}_L &= i\sqrt{2}G_F V_{q_u\,q_d}\, f_P\, \bar{u}(p_1)\left[\left(1+C_{RL}^V-C_{LL}^V\right)\,\gamma^\mu\, P_L\, q_\mu\right.\\ &- \left.\left(C_{RL}^S-C_{LL}^S\right)\,P_L\,\frac{m_P^2}{m_{q_u}+m_{q_d}}\right]v(p_2)\,, \qquad (4.1.6)\\ \mathcal{M}_R &= i\sqrt{2}G_F V_{q_u\,q_d}\, f_P\, \bar{u}(p_1)\left[\left(C_{RR}^V-C_{LR}^V\right)\,\gamma^\mu\, P_R\, q_\mu\right.\\ &- \left.\left(C_{RR}^S-C_{LR}^S\right)\,P_R\,\frac{m_P^2}{m_{q_u}+m_{q_d}}\right]v(p_2)\,, \qquad (4.1.7)\end{aligned}$$

and the branching ratio reads,

$$\begin{aligned}\mathcal{B}\left(P^-\to\ell\bar{\nu}_\ell\right) &= \frac{G_F^2\,|V_{q_u\,q_d}|^2\,m_P\,m_\ell^2}{8\,\pi}\,f_P^2\,\tau_P\left(1-\frac{m_\ell^2}{m_P^2}\right)^2\\ &\left|1+C_{LL}^V-C_{RL}^V+\frac{m_P^2}{m_\ell\,(m_{q_u}+m_{q_d})}\left(C_{RL}^S-C_{LL}^S\right)\right|^2\\ &+\left|C_{RR}^V-C_{LR}^V+\frac{m_P^2}{m_\ell\,(m_{q_u}+m_{q_d})}\left(C_{LR}^S-C_{LR}^S\right)\right|^2\,, \qquad (4.1.8)\end{aligned}$$

where τ_P is the lifetime of the pseudoscalar meson. As expected, the contributions of left- and right-handed neutrinos are symmetric under the interchanges $\left(1+C_{LL}^V-C_{RL}^V\right)\leftrightarrow\left(C_{LR}^V-C_{RR}^V\right)$ and $\left(C_{RL}^S-C_{LL}^S\right)\leftrightarrow\left(C_{RR}^S-C_{LR}^S\right)$. One can also note that the parts involving different neutrino polarizations do not mix. To finish, just recall that since the non-perturbative content of leptonic decays depend on a single parameter (the leptonic decay constant), and they are determined with a precision below the percent level [49], they are extremely clean observables.

4.2 Semileptonic decays

Let us consider the semileptonic decay of a "mother" meson into a "daughter" one, $M(p_M)\to M'(p_{M'},\lambda_{M'})\ell(p_\ell,\lambda_\ell)\bar{\nu}_\ell(p_\nu,\lambda_\nu)$, where M is a pseudoscalar meson $\left(J^M=0^-\right)$ and M' is either a pseudoscalar meson $P\left(J^P=0^-\right)$ with no polarization (we will de-

note it as $\lambda_P = s$) or vector meson $V\left(J^V = 1^-\right)$ with polarizations $\lambda_V = 0, \pm$. The four-momentum transfer is defined as $q = p_M - p'_M$.

Decays into one pseudoscalar meson require minimum input from non-perturbative QCD. As we did for leptonic decays, applying Lorentz invariance and parity conservation one can note that only the vector $V^\mu(x)$, the scalar $S(x)$ and the tensor currents $T^{\mu\nu}_{(5)}(x)$ contribute,

$$\begin{aligned}
\langle P(p_P)|V^\mu(x)|M(p_M)\rangle &= \left[(p_M+p_P)^\mu - \frac{m_M^2-m_P^2}{q^2}q^\mu\right]F_1(q^2) + q^\mu\frac{m_M^2-m_P^2}{q^2}F_0(q^2),\\
\langle P(p_P)|S(x)|M(p_M)\rangle &= \frac{m_M^2-m_P^2}{m_{q_d}-m_{q_u}}F_0(q^2),\\
\langle P(p_P)|A^\mu(x)|M(p_M)\rangle &= \langle P(p_P)|P|M(p_M)\rangle = 0,\\
\langle P(p_P)|T^{\mu\nu}(x)|M(p_M)\rangle &= -i(p_M^\mu p_P^\nu - p_P^\mu p_M^\nu)\frac{2F_T(q^2)}{m_M+m_P},\\
\langle P(p_P)|T_5^{\mu\nu}(x)|M(p_M)\rangle &= -\epsilon^{\mu\nu\alpha\beta}\,p_{M\alpha}p_{P\beta}\,\frac{2F_T(q^2)}{m_M+m_P},
\end{aligned} \tag{4.2.9}$$

where the polarization of the P meson has been omitted since there is no polarization.

Decays into vector mesons require a larger input form LQCD. They depend on more FFs which are more difficult to study in LQCD. The hadronic matrix elements can be parametrized as,

$$
\begin{aligned}
\langle V(p_V,\lambda_V)|V^\mu(x)|M(p_M)\rangle &= -i\,\epsilon^{\mu\nu\rho\sigma}\,\epsilon_{\nu *}(\lambda_V)\,p_{M\rho}p_{V\sigma}\frac{2\,V(q^2)}{m_M+m_V},\\
\langle V(p_V,\lambda_V)|A^\mu(x)|M(p_M)\rangle &= (m_M+m_V)A_1(q^2)\left(\epsilon^{\mu *}(\lambda_M)-q^\mu\frac{(\epsilon^*(\lambda_M)\cdot q)}{q^2}\right)\\
&\quad +q^\mu(\epsilon^*(\lambda_M)\cdot q)\frac{2m_V}{q^2}A_0(q^2)\\
&\quad -\frac{\epsilon^*(\lambda_M)\cdot q}{m_M+m_V}A_2(q^2)\left((p_M+p_V)_\mu-q^\mu\frac{m_M^2-m_V^2}{q^2}\right),\\
\langle V(p_V,\lambda_V)|S(x)|M(p_M)\rangle &= 0,\\
\langle V(p_V,\lambda_V)|P(x)|M(p_M)\rangle &= -(\epsilon^*(\lambda_M)\cdot q)\frac{2m_V}{m_{q_d}+m_{q_u}}A_0(q^2),\\
\langle V(p_V,\lambda_V)|T^{\mu\nu}(x)|M(p_M)\rangle &= \epsilon^{\mu\nu\rho\sigma}\Big\{-\epsilon_{\rho *}(\lambda_M)(p_M+p_V)_\sigma T_1(q^2)\\
&\quad +2\frac{(\epsilon^*(\lambda_M)\cdot q)}{q^2}p_{M\rho}p_{D^*\sigma}\left(T_1(q^2)-T_2(q^2)-\frac{q^2}{m_M^2-m_V^2}T_3(q^2)\right)\\
&\quad +\epsilon^{*\rho}(\lambda_M)q^\sigma\frac{m_B^2-m_V^2}{q^2}(T_1(q^2)-T_2(q^2))\Big\}. \qquad (4.2.10)
\end{aligned}
$$

The FFs depend on the channel studied. For the particular case of $\bar{B}\to D^{(*)}\tau\bar{\nu}$ transitions they can be found at Refs. [51,52]. The FFs of these transitions are summarized in Appendix A.

4.2.1 Helicity formalism

The matrix elements,

$$
\mathcal{M}^{\lambda_{M'},\lambda_\ell}_{\lambda_\nu}\propto\langle M'(\lambda_{M'})|\,J^\alpha_{\rm had}\,|M\rangle\,\langle\ell(\lambda_\ell)\bar{\nu}_\ell(\lambda_\nu)|\,J_{\alpha\,\rm lep}\,|0\rangle\ , \qquad (4.2.11)
$$

with $\alpha=1,\mu,\mu\nu$ for scalar, vector, and tensor couplings respectively, are needed to calculate the relevant observables of semileptonic transitions and will be calculated using the helicity formalism [53–55], which is based in factorizing the amplitudes of Eq. (4.2.11) into hadronic and leptonic amplitudes by considering an intermediate off-shell virtual

boson V^* with polarization λ_{V^*}. Using the completeness relation for the polarization vectors $\epsilon_\mu(\lambda)$,

$$\sum_\lambda \delta_\lambda \, \epsilon^*_\mu(\lambda)\, \epsilon_\nu(\lambda) \, = \, g_{\mu\nu} \qquad \text{with} \qquad \delta_0 = \delta_\pm = -\delta_t = -1\,, \tag{4.2.12}$$

we can write the matrix element as the product of leptonic and hadronic amplitudes,

$$\begin{aligned}
\mathcal{M}[M \to M'(\lambda'_M)\, \ell(\lambda_\ell)\, \bar{\nu}_X] \;&=\; \frac{G_F}{\sqrt{2}}\, V_{q_u\, q_d} \sum_{A=L,R} \Bigg\{ \Big(\delta_{AL}\delta_{XL} + C^V_{AX}\Big) \sum_\lambda \delta_\lambda \, H^{\lambda_D}_{V_A,\lambda}\, L^{\lambda_\ell, X}_{V\mp A,\lambda} \\
&\qquad + \, C^S_{AX}\; H^{\lambda_D}_{S_A}\, L^{\lambda_\ell, X}_{S\mp P} \, + \, C^T_{AX} \sum_{\lambda,\lambda'} \delta_\lambda\, \delta_{\lambda'}\, H^{\lambda_D}_{T_A,\lambda\lambda'}\, L^{\lambda_\ell, X}_{T\mp T5,\lambda\lambda'} \Bigg\} \\
&\equiv \; \frac{G_F}{\sqrt{2}}\, V_{q_u\, q_d}\, \mathcal{M}^{\lambda_D,\lambda_\ell}_{L,R}\,.
\end{aligned} \tag{4.2.13}$$

where $X = L, R$ denotes the neutrino helicity, λ_ℓ the lepton helicity and $\lambda_{M'}$ is the previously defined daughter meson helicity. This formalism is useful to calculate observables that distinguish the helicities of the process. Note that the terms proportional to C^T_{LR} and C^T_{RL} vanish identically.

The problem is then reduced to calculate the leptonic $L^{\lambda_\ell, X}_Y$ and hadronic $H^{\lambda_D}_Y$ amplitudes with $Y = V \mp A, \lambda$ for vector amplitudes, $Y = S \mp P$ for scalar and pseudoscalar amplitudes and $Y = T \mp T5, \lambda\lambda'$ for tensor amplitudes. The kinematics of the processes, including the polarization spinors is summarized in Appendix B.

4.2.1.1 Leptonic amplitudes

The leptonic helicity amplitudes are defined as,

$$\begin{aligned}
L^{\lambda_\ell, \overset{L}{R}}_{V\mp A,\lambda}(q^2, \theta_\ell, \phi) \;&=\; \epsilon_\mu(\lambda)\, \langle \ell(\lambda_\ell)\bar{\nu}(\lambda_\nu)|\bar{\ell}\gamma^\mu(1\mp\gamma_5)\nu|0\rangle\,, \\
L^{\lambda_\ell, \overset{L}{R}}_{S\mp P}(q^2, \theta_\ell, \phi) \;&=\; \langle \ell(\lambda_\ell)\bar{\nu}(\lambda_\nu)|\bar{\ell}(1\mp\gamma_5)\nu|0\rangle\,, \\
L^{\lambda_\ell, \overset{L}{R}}_{T\mp T5,\lambda,\lambda'}(q^2, \theta_\ell, \phi) \;&=\; -L^{\lambda_\ell, \overset{L}{R}}_{T\mp T5,\lambda',\lambda} \, = \, -i\, \epsilon_\mu(\lambda)\, \epsilon_\nu(\lambda')\, \langle \ell(\lambda_\ell)\bar{\nu}(\lambda_\nu)|\bar{\ell}\sigma^{\mu\nu}(1\mp\gamma_5)\nu|0\rangle\,,
\end{aligned} \tag{4.2.14}$$

where $\epsilon_\mu(\lambda)$ are the polarization vectors of the intermediate virtual boson ($\lambda = t, 0, \pm$) in its rest frame defined in Appendix B. Notice that the helicity of the neutrino is explicitly

given in the above equation with the symbols L ($\lambda_\nu = -1/2$) and R ($\lambda_\nu = +1/2$) for left-handed and right-handed neutrinos.

The vectorial leptonic amplitudes for left-handed neutrinos (LHN) are given by:

$$\begin{aligned}
L^{+,L}_{V-A,+}(q^2,\theta_\ell,\phi) &= \sqrt{2}\, m_\ell \beta_\ell \,\sin\theta_\ell \,\mathrm{e}^{-2i\phi}\,, \\
L^{+,L}_{V-A,-}(q^2,\theta_\ell,\phi) &= -\sqrt{2}\, m_\ell \beta_\ell \,\sin\theta_\ell\,, \\
L^{+,L}_{V-A,0}(q^2,\theta_\ell,\phi) &= 2\, m_\ell \beta_\ell \,\cos\theta_\ell \,\mathrm{e}^{-i\phi}\,, \\
L^{+,L}_{V-A,t}(q^2,\theta_\ell,\phi) &= -2\, m_\ell \beta_\ell \,\mathrm{e}^{-i\phi}\,, \\
L^{-,L}_{V-A,\pm}(q^2,\theta_v,\phi) &= \sqrt{2q^2}\,\beta_\ell\,(1 \pm \cos\theta_\ell)\,\mathrm{e}^{\mp i\phi}\,, \\
L^{-,L}_{V-A,0}(q^2,\theta_\ell,\phi) &= -2\,\sqrt{q^2}\,\beta_\ell \,\sin\theta_\ell\,, \\
L^{-,L}_{V-A,t}(q^2,\theta_\ell,\phi) &= 0\,,
\end{aligned} \tag{4.2.15}$$

where $\beta_\ell = \sqrt{1 - m_\ell^2/q^2}$. The scalar leptonic amplitudes for LHNs are:

$$\begin{aligned}
L^{+,L}_{S-P}(q^2,\theta_\ell,\phi) &= -2\sqrt{q^2}\beta_\ell\,\mathrm{e}^{-i\phi}\,, \\
L^{-,L}_{S-P}(q^2,\theta_\ell,\phi) &= 0\,.
\end{aligned} \tag{4.2.16}$$

The tensor leptonic amplitudes for LHNs take the form:

$$\begin{aligned}
L^{+,L}_{T-T5,+0}(q^2,\theta_\ell,\phi) &= \sqrt{2q^2}\beta_\ell \,\sin\theta_\ell\,\mathrm{e}^{-2i\phi}\,, \\
L^{+,L}_{T-T5,-0}(q^2,\theta_\ell,\phi) &= \sqrt{2q^2}\beta_\ell \,\sin\theta_\ell\,, \\
L^{+,L}_{T-T5,+-}(q^2,\theta_\ell,\phi) &= -L^{+,L}_{T-T5,0t} \,=\, 2\sqrt{q^2}\beta_\tau \,\cos\theta_\ell\,\mathrm{e}^{-i\phi}\,, \\
L^{+,L}_{T-T5,+t}(q^2,\theta_\ell,\phi) &= -\sqrt{2q^2}\beta_\ell \,\sin\theta_\ell\,\mathrm{e}^{-2i\phi}\,, \\
L^{+,L}_{T-T5,-t}(q^2,\theta_\ell,\phi) &= \sqrt{2q^2}\beta_\ell \,\sin\theta_\ell\,, \\
L^{-,L}_{T-T5,\pm 0}(q^2,\theta_\ell,\phi) &= \pm\sqrt{2} m_\ell\beta_\ell\,(1 \pm \cos\theta_\ell)\,\mathrm{e}^{\mp i\phi}\,, \\
L^{-,L}_{T-T5,+-}(q^2,\theta_\ell,\phi) &= -L^{-,L}_{T-T5,0t} \,=\, -2m_\ell\beta_\ell \,\sin\theta_\ell\,, \\
L^{-,L}_{T-T5,\pm t}(q^2,\theta_\ell,\phi) &= -\sqrt{2} m_\ell\beta_\ell\,(1 \pm \cos\theta_\ell)\,\mathrm{e}^{\mp i\phi}\,.
\end{aligned} \tag{4.2.17}$$

The right-handed vectorial leptonic amplitudes are given by:

$$\begin{aligned}
L^{+,R}_{V+A,\pm}(q^2,\theta_\ell,\phi) &= \sqrt{2q^2}\beta_\ell\,(1\mp\cos\theta_\ell)\,\mathrm{e}^{\mp i\phi}\,,\\
L^{+,R}_{V+A,0}(q^2,\theta_\ell,\phi) &= 2\sqrt{q^2}\beta_\ell\,\sin\theta_\ell\,,\\
L^{+,R}_{V+A,t}(q^2,\theta_\ell,\phi) &= 0\,,\\
L^{-,R}_{V+A,+}(q^2,\theta_\ell,\phi) &= \sqrt{2}m_\ell\beta_\ell\,\sin\theta_\ell\,,\\
L^{-,R}_{V+A,-}(q^2,\theta_\ell,\phi) &= -\sqrt{2}m_\ell\beta_\ell\,\sin\theta_\ell\,\mathrm{e}^{2i\phi}\,,\\
L^{-,R}_{V+A,0}(q^2,\theta_\ell,\phi) &= 2m_\ell\beta_\ell\,\cos\theta_\ell\,\mathrm{e}^{i\phi}\,,\\
L^{-,R}_{V+A,t}(q^2,\theta_\ell,\phi) &= -2m_\ell\beta_\ell\,\mathrm{e}^{i\phi}\,.
\end{aligned} \tag{4.2.18}$$

The scalar leptonic amplitudes for right-handed neutrinos (RHNs) are:

$$\begin{aligned}
L^{+,R}_{S+P}(q^2,\theta_\ell,\phi) &= 0\,,\\
L^{-,R}_{S+P}(q^2,\theta_\ell,\phi) &= -2\sqrt{q^2}\beta_\ell\,\mathrm{e}^{i\phi}\,.
\end{aligned} \tag{4.2.19}$$

Finally, the tensor leptonic amplitudes for RHNs are:

$$\begin{aligned}
L^{+,R}_{T+T5,\pm 0}(q^2,\theta_\ell,\phi) &= \mp\sqrt{2}m_\ell\beta_\ell\,(1\mp\cos\theta_\ell)\,\mathrm{e}^{\mp i\phi}\,,\\
L^{+,R}_{T+T5,+-}(q^2,\theta_\ell,\phi) &= L^{+,R}_{T+T5,0t} = -2m_\ell\beta_\ell\,\sin\theta_\ell\,,\\
L^{+,R}_{T+T5,\pm t}(q^2,\theta_\ell,\phi) &= -\sqrt{2}m_\ell\beta_\ell\,(1\mp\cos\theta_\ell)\,\mathrm{e}^{\mp i\phi}\,,\\
L^{-,R}_{T+T5,+0}(q^2,\theta_\ell,\phi) &= -\sqrt{2q^2}\beta_\ell\,\sin\theta_\ell\,,\\
L^{-,R}_{T+T5,+-}q^2,\theta_\ell,\phi) &= L^{-,R}_{T+T5,0t} = -2\sqrt{q^2}\beta_\ell\,\cos\theta_\ell\,\mathrm{e}^{i\phi}\,,\\
L^{-,R}_{T+T5,+t}(q^2,\theta_\ell,\phi) &= -\sqrt{2q^2}\beta_\ell\,\sin\theta_\ell\,,\\
L^{-,R}_{T+T5,-0}(q^2,\theta_\ell,\phi) &= -\sqrt{2q^2}\beta_\ell\,\sin\theta_\ell\,\mathrm{e}^{2i\phi}\,,\\
L^{-,R}_{T+T5,-t}(q^2,\theta_\ell,\phi) &= \sqrt{2q^2}\beta_\ell\,\sin\theta_\ell\,\mathrm{e}^{2i\phi}\,.
\end{aligned} \tag{4.2.20}$$

4.2.1.2 Hadronic amplitudes

Combining leptonic and helicity amplitudes as in Eq. (4.2.11) the amplitudes for $M \to P$ transitions are:

$$\begin{aligned}
H^s_{V,0}(q^2) &\equiv H^s_{V_L,0}(q^2) = H^s_{V_R,0}(q^2) = \sqrt{\frac{\lambda_P(q^2)}{q^2}}\, F_1(q^2)\,, \\
H^s_{V,t}(q^2) &\equiv H^s_{V_L,t}(q^2) = H^s_{V_R,t}(q^2) = \frac{m_M^2 - m_P^2}{\sqrt{q^2}}\, F_0(q^2)\,, \\
H^s_{S}(q^2) &\equiv H^s_{S_L}(q^2) = H^s_{S_R}(q^2) \simeq \frac{m_M^2 - m_P^2}{m_{q_d} - m_{q_u}}\, F_0(q^2)\,, \\
H^s_{T}(q^2) &= H^s_{T_L+-} = H^s_{T_L 0t} = -H^s_{T_R+-} = H^s_{T_R 0t} = -\frac{\sqrt{\lambda_P(q^2)}}{m_M + m_P}\, F_T(q^2)\,,
\end{aligned} \tag{4.2.21}$$

where λ_P is the Källén function,

$$\lambda_{M'}(q^2) \equiv \lambda(m_M^2, m_{M'}^2, q^2) = m_M^4 + m_{M'}^4 + q^4 - 2m_M m_{M'} - 2m_M q^2 - 2m_{M'}^2 q^2\,, \tag{4.2.22}$$

with $M' = P$.

For $M \to V$:

$$\begin{aligned}
H_{V,\pm}(q^2) &\equiv H^{\pm}_{V_L,\pm}(q^2) = -H^{\mp}_{V_R,\mp}(q^2) = (m_M + m_V)\, A_1(q^2) \mp \frac{\sqrt{\lambda_V(q^2)}}{m_M + m_V}\, V(q^2)\,, \\
H_{V,0}(q^2) &\equiv H^0_{V_L,0}(q^2) = -H^0_{V_R,0}(q^2) \\
&= \frac{m_M + m_V}{2m_V\sqrt{q^2}} \left[-(m_M^2 - m_V^2 - q^2)\, A_1(q^2) + \frac{\lambda_V(q^2)}{(m_M + m_V)^2}\, A_2(q^2) \right], \\
H_{V,t}(q^2) &\equiv H^0_{V_L,t}(q^2) = -H^0_{V_R,t}(q^2) = -\sqrt{\frac{\lambda_V(q^2)}{q^2}}\, A_0(q^2)\,, \\
H_{S}(q^2) &\equiv H^0_{S_R}(q^2) = -H^0_{S_L}(q^2) \simeq -\frac{\sqrt{\lambda_V(q^2)}}{m_{q_d} + m_{q_u}}\, A_0(q^2)\,, \\
H_{T,0}(q^2) &\equiv H^0_{T_L 0t}(q^2) = H^0_{T_L+-}(q^2) = -H^0_{T_R 0t}(q^2) = H^0_{T_R+-}(q^2) \\
&= \frac{1}{2m_V} \left[-(m_M^2 + 3\, m_V^2 - q^2)\, T_2(q^2) + \frac{\lambda_V(q^2)}{m_M^2 - m_V^2}\, T_3(q^2) \right], \\
H_{T\pm}(q^2) &\equiv H^{\pm}_{T_L \pm 0}(q^2) = \pm H^{\pm}_{T_L \pm t}(q^2) = \mp H^{\mp}_{T_R \mp t}(q^2) = -H^{\mp}_{T_R \mp 0}(q^2) \\
&= \frac{1}{\sqrt{q^2}} \left[\pm (m_M^2 - m_V^2)\, T_2(q^2) + \sqrt{\lambda_V}\, T_1(q^2) \right].
\end{aligned} \tag{4.2.23}$$

where λ_V is the Källén function of Eq. (4.2.22) with $M' = V$.

4.3 $b \to c\tau\bar{\nu}$ observables

Recently, several deviations from the SM in observables involving $b \to c\tau\bar{\nu}$ transitions have been experimentally measured [56–58]. The most important ones are the ratios $\mathcal{R}_{D^{(*)}}$ defined as,

$$\mathcal{R}_{D^{(*)}} = \frac{\mathcal{B}\left(B \to D^{(*)}\tau\bar{\nu}_\tau\right)}{\mathcal{B}\left(B \to D^{(*)}\ell\bar{\nu}_\ell\right)}\,, \tag{4.3.24}$$

where $\ell = e, \mu$ denotes a *light* lepton. The latest word averages, performed by the Heavy Flavour Averaging Group (HFLAV) collaboration [48],

$$\mathcal{R}_D^{\text{ave}} = 0.340 \pm 0.027 \pm 0.013 \qquad \text{and} \qquad \mathcal{R}_{D^*}^{\text{ave}} = 0.295 \pm 0.011 \pm 0.008\,, \tag{4.3.25}$$

deviate at the 3.1σ level (considering their correlation of -0.38) from the arithmetic average of SM predictions [59–62] quoted also by HFLAV [48],

$$\mathcal{R}_D^{\text{SM}} = 0.299 \pm 0.003\ (1.4\sigma) \qquad \text{and} \qquad \mathcal{R}_{D^*}^{\text{SM}} = 0.258 \pm 0.005\ (2.5\sigma). \tag{4.3.26}$$

$\mathcal{R}_D$ and $\mathcal{R}_{D^*}$ have the advantage of being clean observables: many uncertainties coming from the FFs and the CKM element V_{cb} cancel in the ratios of Eq.(4.3.24). This implies that the discrepancy with respect to the SM prediction is translated into a large violation of tree-level lepton universality, which cannot be accommodated in the SM.

The HFLAV averages quoted in Eq. (4.3.25) are calculated combining measurements from several experiments. The ones presenting a stronger discrepancy are the 2012 and 2013 BaBar measurements [63,64], while the most recent experimental values of Belle [65–67] and LHCb [68–70] are closer to the SM predictions. [4] The q^2 differential distributions

[4] Note that the LHCb measurements only use semimuonic models as normalization channels. Also, while kinematics are completely known at B-meson factories, momenta of the LHC colliding partons are unknown.

of $B \to D$ and $B \to D^*$ have also been measured by Belle [65] and BaBar [64], restricting large deviations from the SM. Another observable related to $B \to D^*$ transitons, the integrated longitudinal polarization $\bar{F}_L^{D^*}$ recently measured by Belle presents a 1.6σ [71] discrepancy and it is difficult to accommodate within its 1σ uncertainty. A more detailed overview of the different $\mathcal{R}_{D^{(*)}}$ measurements and how averages have changed through time will be given in Chapter 8. Besides anomalies in the ratios of $B \to D^{(*)}$ transitions, the observable,

$$\mathcal{R}(J/\psi) \equiv \frac{\mathcal{B}(B_c \to J/\psi\, \tau\bar{\nu})}{\mathcal{B}(B_c \to J/\psi\, \mu\, \bar{\nu})}\,, \tag{4.3.27}$$

measured by LHCb [72] presents a 1.7σ deviation with respect to the SM prediction. In this case the τ^+ decays leptonically to $\mu^+\bar{\nu}_\mu\nu_\tau$ and theoretical uncertainties from FFs governing $B_c \to J/\psi$ transitions result in large error bands for the SM predictions. Finally, combining the inclusive measurement $\mathcal{B}\left(B_c \to X_c\tau\bar{\nu}\right)/\mathcal{B}\left(B_c \to X_c e\bar{\nu}\right)$ [73], which is independent of any FFs, with the exclusive measurements $\mathcal{B}\left(\bar{B} \to D\tau\bar{\nu}\right) + \mathcal{B}\left(\bar{B} \to D^*\tau\bar{\nu}\right)$ there is no room for other $\bar{B}$ channels such as D^{**} (the four lightest orbitally excited D meson states), which should contribute at a 0.5% [74]. [5]

The study of these anomalies related to $b \to c\tau\bar{\nu}$ observables can be performed through an EFT approach using the Hamiltonian of Eq. (4.0.1). Different analyses without light right-handed neutrinos and with these particles will be done Chapter 8. In this Section we give the list of the relevant observables involving these $b \to c\tau\bar{\nu}$ transitions that will be used for the following analyses.

[5] The SM prediction of the ratio for inclusive decay rates, $R(X_c)$, can be computed using the OPE and found to be $R(X_c) = 0.222 \pm 0.007$ [75]. Combining it with the most recent world average $\mathcal{B}(B^- \to X_c e\bar{\nu}) = (10.92 \pm 0.16)\,\%$ [76, 77] yields to the SM prediction $\mathcal{B}(B^- \to X_c\tau\bar{\nu}) = (2.42 \pm 0.05)\,\%$. On the other hand, using Ref. [78] and taking it into account for the theoretical description of these decays, one finds $\mathcal{B}\left(\bar{B} \to D\tau\bar{\nu}\right)\mathcal{B}\left(\bar{B} \to D^*\tau\bar{\nu}\right) + \mathcal{B}\left(\bar{B} \to D^{**}\tau\bar{\nu}\right) \sim 3\%$, presenting an important tension with the SM prediction.

4.3.1 $B \to D\tau\bar{\nu}$

The differential distribution of the decay $B \to D\tau\bar{\nu}$ can be written as

$$\frac{d\Gamma(B \to D\tau\bar{\nu})}{dq^2\, d\cos\theta_\tau} = \frac{G_F^2 V_{cb}^2}{256\, m_B^3 \pi^3}\, q^2\, \lambda_D^{1/2}(q^2) \left(1 - \frac{m_\tau^2}{q^2}\right)^2 \Big\{ J_0(q^2) + J_1(q^2)\, \cos\theta_\tau + J_2(q^2)\, \cos^2\theta_\tau \Big\}, \tag{4.3.28}$$

where $q^2 = (p_\tau + p_{\bar{\nu}})^2$, θ_τ is the polar angle of the τ momentum in the rest frame of the $\tau\bar{\nu}$ pair, with respect to the z-axis defined by the momentum of the D meson in the B rest frame, and $\lambda_{D^{(*)}}(q^2)$ is the Källen function of Eq. (4.2.22) with $M = B$ and $M' = D$.

The coefficient functions of the different angular dependences are given by

$$\begin{aligned}
J_0(q^2) &= \left|\tilde{\mathcal{A}}_0^L - \frac{2m_\tau}{\sqrt{q^2}}\, \tilde{\mathcal{A}}_T^L\right|^2 + \frac{m_\tau^2}{q^2} \left|\tilde{\mathcal{A}}_t^L + \frac{\sqrt{q^2}}{m_\tau}\, \tilde{\mathcal{A}}_S^L\right|^2 + (L \leftrightarrow R)\,, \\
J_1(q^2) &= \frac{2m_\tau^2}{q^2}\, \mathcal{R}\mathrm{e}\left[\left(\tilde{\mathcal{A}}_0^L - \frac{2\sqrt{q^2}}{m_\tau}\, \tilde{\mathcal{A}}_T^L\right)\left(\tilde{\mathcal{A}}_t^{L*} + \frac{\sqrt{q^2}}{m_\tau}\, \tilde{\mathcal{A}}_S^{L*}\right)\right] + (L \leftrightarrow R)\,, \\
J_2(q^2) &= -\left(1 - \frac{m_\tau^2}{q^2}\right) \left(|\tilde{\mathcal{A}}_0^L|^2 - 4\,|\tilde{\mathcal{A}}_T^L|^2\right) + (L \leftrightarrow R)\,,
\end{aligned} \tag{4.3.29}$$

where

$$\begin{aligned}
\tilde{\mathcal{A}}_0^L &= \left(1 + C_{LL}^V + C_{RL}^V\right) H_{V,0}^s\,, & \tilde{\mathcal{A}}_0^R &= \left(C_{LR}^V + C_{RR}^V\right) H_{V,0}^s\,, \\
\tilde{\mathcal{A}}_t^L &= \left(1 + C_{LL}^V + C_{RL}^V\right) H_{V,t}^s\,, & \tilde{\mathcal{A}}_t^R &= \left(C_{LR}^V + C_{RR}^V\right) H_{V,t}^s\,, \\
\tilde{\mathcal{A}}_S^L &= \left(C_{RL}^S + C_{LL}^S\right) H_S^s\,, & \tilde{\mathcal{A}}_S^R &= \left(C_{RR}^S + C_{LR}^S\right) H_S^s\,, \\
\tilde{\mathcal{A}}_T^L &= 2\, C_{LL}^S\, H_T^s\,, & \tilde{\mathcal{A}}_T^R &= 2\, C_{RR}^T\, H_T^s\,.
\end{aligned} \tag{4.3.30}$$

The hadronic helicity amplitudes $H_{V,0}^s$, $H_{V,t}^s$, H_S^s and H_T^s are functions of q^2, and their explicit expressions are given in Section 4.2.1.2 with the FFs of Appendix A. The LHN contributions to Eq. (4.3.29) are in full agreement with Ref. [79]. Notice that the vector and scalar Wilson coefficients only appear in the combinations $C_{LX}^V + C_{RX}^V$ and $C_{LX}^S + C_{RX}^S$, regardless of the neutrino chirality X.

The helicity amplitudes for the transition $B \to D\tau\nu$ are defined as

$$\mathcal{M}[B \to D\,\tau(\lambda_\tau)\,\nu_{L,R}] \equiv -\sqrt{2}\, G_F\, V_{cb}\, \mathcal{M}_{L,R}^{\lambda_\tau}\,, \tag{4.3.31}$$

where $\lambda_\tau = \pm\frac{1}{2}$ denotes the τ helicity in the rest frame of the $\tau\bar{\nu}$ pair. The four reduced amplitudes $\mathcal{M}_{L,R}^{\lambda_\tau}$ are given by:

$$\begin{aligned}
\mathcal{M}_L^{+\frac{1}{2}} &= -2\sqrt{q^2}\,\beta_\tau\,\mathrm{e}^{-i\phi}\left\{\frac{m_\tau}{\sqrt{q^2}}\left[\tilde{\mathcal{A}}_t^L + \cos\theta_\tau\,\tilde{\mathcal{A}}_0^L\right] + \tilde{\mathcal{A}}_S^L - 2\,\cos\theta_\tau\,\tilde{\mathcal{A}}_T^L\right\},\\
\mathcal{M}_L^{-\frac{1}{2}} &= 2\sqrt{q^2}\,\beta_\tau\,\sin\theta_\tau\left\{\tilde{\mathcal{A}}_0^L - \frac{2m_\tau}{\sqrt{q^2}}\,\tilde{\mathcal{A}}_T^L\right\},\\
\mathcal{M}_R^{+\frac{1}{2}} &= -2\sqrt{q^2}\,\beta_\tau\,\sin\theta_\tau\left\{\tilde{\mathcal{A}}_0^R - \frac{2m_\tau}{\sqrt{q^2}}\,\tilde{\mathcal{A}}_T^R\right\},\\
\mathcal{M}_R^{-\frac{1}{2}} &= -2\sqrt{q^2}\,\beta_\tau\,\mathrm{e}^{i\phi}\left\{\frac{m_\tau}{\sqrt{q^2}}\left[\tilde{\mathcal{A}}_t^R + \cos\theta_\tau\,\tilde{\mathcal{A}}_0^R\right] + \tilde{\mathcal{A}}_S^R - 2\,\cos\theta_\tau\,\tilde{\mathcal{A}}_T^R\right\}. \quad (4.3.32)
\end{aligned}$$

Integrating Eq. (4.3.28) over $\cos\theta_\tau$, one obtains [80]

$$\begin{aligned}
\frac{d\Gamma}{dq^2}(B\to D\tau\bar{\nu}) &= \frac{G_F^2 V_{cb}^2}{192 m_B^3\pi^3}\,q^2\,\lambda_D^{1/2}(q^2)\left(1-\frac{m_\tau^2}{q^2}\right)^2\\
&\times\left\{\left(|1+C_{LL}^V+C_{RL}^V|^2+|C_{LR}^V+C_{RR}^V|^2\right)\left[(H_{V,0}^s)^2\left(\frac{m_\tau^2}{2q^2}+1\right)+\frac{3m_\tau^2}{2q^2}(H_{V,t}^s)^2\right]\right.\\
&+\frac{3}{2}(H_S^s)^2\left(|C_{RL}^S+C_{LL}^S|^2+|C_{RR}^S+C_{LR}^S|^2\right)+8\left(|C_{LL}^T|^2+|C_{RR}^T|^2\right)(H_T^s)^2\left(1+\frac{2m_\tau^2}{q^2}\right)\\
&+3\,\mathcal{R}\mathrm{e}\left[(1+C_{LL}^V+C_{RL}^V)(C_{RL}^S+C_{LL}^S)^*+(C_{LR}^V+C_{RR}^V)(C_{RR}^S+C_{LR}^S)^*\right]\frac{m_\tau}{\sqrt{q^2}}H_S^s H_{V,t}^s\\
&\left.-12\,\mathcal{R}\mathrm{e}\left[(1+C_{LL}^V+C_{RL}^V)\,C_{LL}^{T*}+(C_{RR}^V+C_{LR}^V)\,C_{RR}^{T*}\right]\frac{m_\tau}{\sqrt{q^2}}H_T^s H_{V,0}^s\right\}. \quad (4.3.33)
\end{aligned}$$

The linear term in the θ_τ distribution given in Eq. (4.3.28) can be accessed via the forward-backward asymmetry, traditionally defined as

$$\mathcal{A}_{FB}^D = \frac{1}{d\Gamma/dq^2}\left[\int_0^1 - \int_{-1}^0\right] d\cos\theta_\tau\,\frac{d^2\Gamma}{dq^2 d\cos\theta_\tau} = \frac{1}{2}\frac{J_1(q^2)}{J_0(q^2)+\frac{1}{3}J_3(q^2)}, \quad (4.3.34)$$

and the τ polarization asymmetry can be constructed as

$$\mathcal{P}_\tau^D = \frac{d\Gamma_{\lambda_\tau=1/2}/dq^2 - d\Gamma_{\lambda_\tau=-1/2}/dq^2}{d\Gamma/dq^2}, \quad (4.3.35)$$

where the decomposition of the amplitude in τ helicity states is given in Eqs. (4.3.31) and (4.3.32).

4.3.2 $B \to D^* \tau \bar{\nu}$

The vector meson D^* in the final state provides additional observables compared to the previous case. The angular analysis of a four-body final state, namely $B \to D^*(\to D\,\pi)\tau\bar{\nu}$, further allows us to construct a multitude of observables that can be extracted from data [79, 81–87]. The differential decay distribution of the transition process $B(p_B) \to D^*(p_{D^*})\,\tau(p_\tau)\,\bar{\nu}(p_{\bar{\nu}})$, with $D^*(p_{D^*}) \to D(p_D)\,\pi(p_\pi)$ on the mass shell, can be expressed in the form [79]:

$$\begin{aligned}
\frac{d^4\Gamma(B \to D^*\tau\bar{\nu})}{dq^2\, d\cos\theta_\tau\, d\cos\theta_D\, d\phi} \;&\equiv\; I(q^2, \theta_\tau, \theta_D, \phi) \\
&= \frac{9}{32\pi}\Big\{ I_1^s \sin^2\theta_D + I_1^c \cos^2\theta_D + \Big(I_2^s \sin^2\theta_D + I_2^c \cos^2\theta_D\Big)\cos 2\theta_\tau \\
&\quad + (I_3 \cos 2\phi + I_9 \sin 2\phi)\sin^2\theta_D \sin^2\theta_\tau + (I_4 \cos\phi + I_8 \sin\phi)\sin 2\theta_D \sin 2\theta_\tau \\
&\quad + (I_5 \cos\phi + I_7 \sin\phi)\sin 2\theta_D \sin\theta_\tau + \Big(I_6^s \sin^2\theta_D + I_6^c \cos^2\theta_D\Big)\cos\theta_\tau \Big\}\,.
\end{aligned} \tag{4.3.36}$$

In addition to the lepton-pair invariant-mass squared $q^2 = (p_\tau + p_{\bar{\nu}})^2$, we use as kinematic variables the three angles ϕ, θ_τ and θ_D, which are defined as follows. Taking as positive z- axis the direction of the D^* momentum in the B rest frame, θ_τ and θ_D are the polar angles of the τ and the final D meson in the $\tau\nu$ and $D\pi$ rest frames, respectively. The azimuth ϕ is the angle between the decay planes formed by $\tau\nu$ and $D\pi$. See Fig. 4.1 for a visual representation of these kinematical variables.

Measuring this four-dimensional distribution is obviously a major experimental challenge, since the subsequent τ decay involves one ($\tau \to \nu_\tau$+hadrons) or two ($\tau \to \nu_\tau\,\ell\,\bar{\nu}_\ell$) additional neutrinos, making difficult to reconstruct the τ direction. Some information can be recovered by measuring the distribution of the secondary τ decay [84–86], but we refrain to enter here into this type of technical (but important) details.

The angular coefficients I_i's are functions of q^2 that encode both short- and long-distance physics contributions. They can be written in terms of the hadronic FFs given

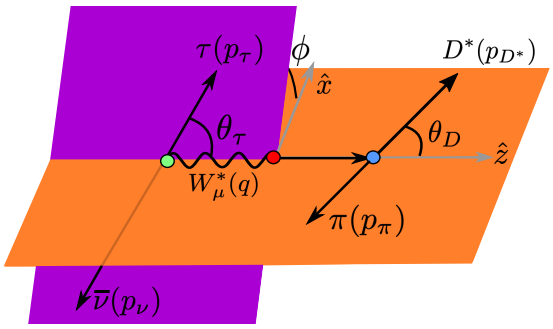

Figure 4.1: Schematic representation of the kinematical variables for the $B \to D^*(\to D\,\pi)\tau\bar{\nu}$ process.

in Appendix A. Using the global normalization

$$N_F = \frac{G_F^2\,|V_{cb}|^2}{2^7\,3\pi^3 m_B^3}\,q^2\,\lambda_{D^*}^{1/2}(q^2)\left(1-\frac{m_\tau^2}{q^2}\right)^2\,\mathcal{B}(D^*\to D\pi)\,, \tag{4.3.37}$$

where $\mathcal{B}(D^* \to D\,\pi)$ is the branching fraction of the D^* decay into $D\,\pi$ states described in Appendix C. The expressions for the angular coefficients are:

$$\begin{aligned}
I_1^c &= N_F\left[2\left(1+\frac{m_\tau^2}{q^2}\right)\left(|\mathcal{A}_0^L|^2+4\,|\mathcal{A}_{T\,0}^L|^2\right)-\frac{16m_\tau}{\sqrt{q^2}}\,\mathcal{R}\mathrm{e}[\mathcal{A}_0^L\mathcal{A}_{T\,0}^{L\,*}]+\frac{4m_\tau^2}{q^2}\,|A_{tP}^L|^2+(L\to R)\right],\\
I_1^s &= N_F\left[\frac{1}{2}\left(3+\frac{m_\tau^2}{q^2}\right)\left(|\mathcal{A}_\perp^L|^2+|\mathcal{A}_\parallel^L|^2\right)+2\left(1+\frac{3m_\tau^2}{q^2}\right)\left(|\mathcal{A}_{T\,\perp}^L|^2+|\mathcal{A}_{T\,\parallel}^L|^2\right)\right.\\
&\qquad\left.-\,8\,\frac{m_\tau}{\sqrt{q^2}}\,\mathcal{R}\mathrm{e}[\mathcal{A}_\perp^L\mathcal{A}_{T\,\perp}^{L\,*}+\mathcal{A}_\parallel^L\mathcal{A}_{T\,\parallel}^{L\,*}]+(L\to R)\right],\\
I_2^c &= -2\,N_F\left(1-\frac{m_\tau^2}{q^2}\right)\left(|\mathcal{A}_0^L|^2-4\,|\mathcal{A}_{T\,0}^L|^2+(L\to R)\right),\\
I_2^s &= \frac{1}{2}\,N_F\left(1-\frac{m_\tau^2}{q^2}\right)\left(|\mathcal{A}_\perp^L|^2+|\mathcal{A}_\parallel^L|^2-4\,(|\mathcal{A}_{T\,\perp}^L|^2+|\mathcal{A}_{T\,\parallel}^L|^2)+(L\to R)\right),\\
I_3 &= N_F\left(1-\frac{m_\tau^2}{q^2}\right)\left(|\mathcal{A}_\perp^L|^2-|\mathcal{A}_\parallel^L|^2-4\,(|\mathcal{A}_{T\,\perp}^L|^2-|\mathcal{A}_{T\,\parallel}^L|^2)+(L\to R)\right),\\
I_4 &= \sqrt{2}\,N_F\left(1-\frac{m_\tau^2}{q^2}\right)\mathcal{R}\mathrm{e}[\mathcal{A}_0^L\mathcal{A}_\parallel^{L\,*}-4\,\mathcal{A}_{T\,0}^L\mathcal{A}_{T\,\parallel}^{L\,*}+(L\to R)]\,,
\end{aligned}$$

$$
\begin{aligned}
I_5 &= 2\sqrt{2}\, N_F \Big[\mathcal{R}\mathrm{e}[(\mathcal{A}_0^L - 2\,\frac{m_\tau}{\sqrt{q^2}}\,\mathcal{A}_{T\,0}^L)\,(\mathcal{A}_\perp^{L\,*} - 2\,\frac{m_\tau}{\sqrt{q^2}}\,\mathcal{A}_{T\,\perp}^{L*}) - (L\to R)] \\
&\qquad - \frac{m_\tau^2}{q^2}\,\mathcal{R}\mathrm{e}[A_{tP}^{L*}\,(\mathcal{A}_\parallel^L - 2\,\frac{\sqrt{q^2}}{m_\tau}\mathcal{A}_{T\,\parallel}^L) + (L\to R)]\Big]\,, \\
I_6^c &= N_F\,\frac{8m_\tau^2}{q^2}\,\mathcal{R}\mathrm{e}[A_{tP}^{L*}\,(\mathcal{A}_0^L - 2\,\frac{\sqrt{q^2}}{m_\tau}\,\mathcal{A}_{T\,0}^L) + (L\to R)]\,, \\
I_6^s &= 4\,N_F\,\mathcal{R}\mathrm{e}[(\mathcal{A}_\parallel^L - 2\,\frac{m_\tau}{\sqrt{q^2}}\,\mathcal{A}_{T\,\parallel}^L)(\mathcal{A}_\perp^{L\,*} - 2\frac{m_\tau}{\sqrt{q^2}}\mathcal{A}_{T\,\perp}^{L*}) - (L\to R)]\,, \\
I_7 &= -2\sqrt{2}\, N_F \Big[\mathcal{I}\mathrm{m}[(\mathcal{A}_0^L - 2\,\frac{m_\tau}{\sqrt{q^2}}\,\mathcal{A}_{T\,0}^L)\,(\mathcal{A}_\parallel^{L\,*} - 2\,\frac{m_\tau}{\sqrt{q^2}}\,\mathcal{A}_{T\,\parallel}^{L*}) - (L\to R)] \\
&\qquad + \frac{m_\tau^2}{q^2}\,\mathcal{I}\mathrm{m}[A_{tP}^{L*}\,(\mathcal{A}_\perp^L - 2\,\frac{\sqrt{q^2}}{m_\tau}\,\mathcal{A}_{T\,\perp}^L) + (L\to R)]\Big]\,, \\
I_8 &= \sqrt{2}\, N_F \left(1 - \frac{m_\tau^2}{q^2}\right)\mathcal{I}\mathrm{m}[\mathcal{A}_0^{L\,*}\mathcal{A}_\perp^L - 4\,\mathcal{A}_{T\,0}^{L*}\mathcal{A}_{T\,\perp}^L + (L\to R)]\,, \\
I_9 &= 2\,N_F \left(1 - \frac{m_\tau^2}{q^2}\right)\mathcal{I}\mathrm{m}[\mathcal{A}_\parallel^L\,\mathcal{A}_\perp^{L\,*} - 4\,\mathcal{A}_{T\,\parallel}^L\mathcal{A}_{T\,\perp}^{L*} + (L\to R)]\,.
\end{aligned}
\tag{4.3.38}
$$

In the above expressions, the $\mathcal{A}_\lambda^{L,R}$ denote the transversity amplitudes, which are the projections of the total decay amplitude into the explicit polarization basis. The contribution of the RHN transitions to the angular coefficients is equivalent to the LHN ones, *i.e.* $(L \to R)$, up to a sign that depends on the relation between right-handed and left-handed leptonic transversity amplitudes. In the SM, the decay $B \to D^*\tau\bar{\nu}$ can be described by a total of four transversity amplitudes that correspond to one longitudinal ($\mathcal{A}_0$) and two transverse ($\mathcal{A}_{\perp,\parallel}$) directions, and a time-like component ($\mathcal{A}_t$) for the virtual vector boson decaying into the $\tau\bar{\nu}$ pair. However, with the inclusion of RHNs, we must distinguish the left and right chiralities of the leptonic current; thus, we get in total eight amplitudes: $\mathcal{A}_{0,\perp,\parallel,t}^{L,R}$. Now, in presence of the NP operators given in Eq. (4.0.2), the (axial)vector contributions can be incorporated in the above mentioned eight amplitudes, modified by the presence of the new Wilson coefficients. Nevertheless, the (pseudo)scalar and tensor operators induce eight further amplitudes (four for each neutrino chirality): two (pseudo)scalar amplitudes $\mathcal{A}_P^{L,R}$ and six tensor transversities $\mathcal{A}_{T\,0,T\,\perp,T\,\parallel}^{L,R}$. Thus, with the most general dimension-six Hamiltonian in Eq. (4.0.1), the decay $B \to D^*(\to D\,\pi)\tau\bar{\nu}$ can be described by a total of sixteen tranversity amplitudes. Their explicit dependence on the hadronic

helicity amplitudes, compiled in Eq. (4.2.23), and the Wilson coefficients is listed below,

$$\begin{aligned}
\mathcal{A}_0^L &= H_{V,0}\ (1 + C_{LL}^V - C_{RL}^V), & \mathcal{A}_0^R &= H_{V,0}\ (C_{LR}^V - C_{RR}^V),\\
\mathcal{A}_\parallel^L &= \frac{1}{\sqrt{2}}\,(H_{V,+} + H_{V,-})\ (1 + C_{LL}^V - C_{RL}^V), & \mathcal{A}_\parallel^R &= \frac{1}{\sqrt{2}}\,(H_{V,+} + H_{V,-})\ (C_{LR}^V - C_{RR}^V),\\
\mathcal{A}_\perp^L &= \frac{1}{\sqrt{2}}\,(H_{V,+} - H_{V,-})\ (1 + C_{LL}^V + C_{RL}^V), & \mathcal{A}_\perp^R &= \frac{1}{\sqrt{2}}\,(H_{V,+} - H_{V,-})\ (C_{LR}^V + C_{RR}^V),\\
\mathcal{A}_t^L &= H_{V,t}\ (1 + C_{LL}^V - C_{RL}^V), & \mathcal{A}_t^R &= H_{V,t}\ (C_{LR}^V - C_{RR}^V),\\
\mathcal{A}_P^L &= H_S\ (C_{RL}^S - C_{LL}^S), & \mathcal{A}_P^R &= H_S\ (C_{RR}^S - C_{LR}^S),\\
\mathcal{A}_{T0}^L &= 2H_{T,0}\ C_{LL}^T, & \mathcal{A}_{T0}^R &= -2H_{T,0}\ C_{RR}^T,\\
\mathcal{A}_{T\parallel}^L &= \sqrt{2}\,(H_{T,+} - H_{T,-})\ C_{LL}^T, & \mathcal{A}_{T\parallel}^R &= -\sqrt{2}\,(H_{T,+} - H_{T,-})\ C_{RR}^T,\\
\mathcal{A}_{T\perp}^{L,R} &= \sqrt{2}\,(H_{T,+} + H_{T,-})\ C_{LL}^{T,R}\,, & & & (4.3.39)
\end{aligned}$$

where the t and the P amplitudes arise in the $B \to D^*$ observables combined as

$$\mathcal{A}_{tP}^{L,R} \;=\; \left(\mathcal{A}_t^{L,R} + \frac{\sqrt{q^2}}{m_\tau}\,\mathcal{A}_P^{L,R}\right). \tag{4.3.40}$$

With these definitions, the left-handed contributions to the angular coefficients in Eq. (4.3.38) are in agreement with Ref. [79].

Twelve helicity amplitudes (six for each neutrino chirality) can be written in terms of these amplitudes (see Eq. (4.2.13)). For LHNs they take the form:

$$\begin{aligned}
\mathcal{M}_L^{+1,+\frac{1}{2}} &= -\sqrt{q^2}\,\beta_\tau\ \sin\theta_\tau\,\mathrm{e}^{-2i\phi}\left\{\frac{m_\tau}{\sqrt{q^2}}\left(\mathcal{A}_\parallel^L + \mathcal{A}_\perp^L\right) - 2\,(\mathcal{A}_{T\parallel}^L + \mathcal{A}_{T\perp}^L)\right\},\\
\mathcal{M}_L^{+1,-\frac{1}{2}} &= -\sqrt{q^2}\,\beta_\tau\,(1 + \cos\theta_\tau)\,\mathrm{e}^{-i\phi}\left\{\mathcal{A}_\parallel^L + \mathcal{A}_\perp^L - \frac{2m_\tau}{\sqrt{q^2}}\,(\mathcal{A}_{T\parallel}^L + \mathcal{A}_{T\perp}^L)\right\},\\
\mathcal{M}_L^{0,+\frac{1}{2}} &= -2\,m_\tau\,\beta_\tau\,\mathrm{e}^{-i\phi}\left\{\mathcal{A}_{tP}^L + \cos\theta_\tau\left[\mathcal{A}_0^L - \frac{2\sqrt{q^2}}{m_\tau}\,\mathcal{A}_{T\,0}^L\right]\right\},\\
\mathcal{M}_L^{0,-\frac{1}{2}} &= 2\sqrt{q^2}\,\beta_\tau\ \sin\theta_\tau\left[\mathcal{A}_0^L - \frac{2m_\tau}{\sqrt{q^2}}\,\mathcal{A}_{T\,0}^L\right],\\
\mathcal{M}_L^{-1,+\frac{1}{2}} &= \sqrt{q^2}\,\beta_\tau\ \sin\theta_\tau\left\{\frac{m_\tau}{\sqrt{q^2}}\,(\mathcal{A}_\parallel^L - \mathcal{A}_\perp^L) - 2\,(\mathcal{A}_{T\parallel}^L - \mathcal{A}_{T\perp}^L)\right\},\\
\mathcal{M}_L^{-1,-\frac{1}{2}} &= -\sqrt{q^2}\,\beta_\tau\,(1 - \cos\theta_\tau)\,\mathrm{e}^{i\phi}\left\{\mathcal{A}_\parallel^L - \mathcal{A}_\perp^L - 2\,\frac{m_\tau}{\sqrt{q^2}}\,(\mathcal{A}_{T\parallel}^L - \mathcal{A}_{T\perp}^L)\right\}, \qquad (4.3.41)
\end{aligned}$$

while the corresponding amplitudes for RHNs are given by:

$$\begin{aligned}
\mathcal{M}_R^{+1,+\frac{1}{2}} &= -\sqrt{q^2}\,\beta_\tau\,(1-\cos\theta_\tau)\,\mathrm{e}^{-i\phi}\left\{\mathcal{A}_\parallel^R + \mathcal{A}_\perp^R - 2\,\frac{m_\tau}{\sqrt{q^2}}\,(\mathcal{A}_{T\parallel}^R + \mathcal{A}_{T\perp}^R)\right\},\\
\mathcal{M}_R^{+1,-\frac{1}{2}} &= -\sqrt{q^2}\,\beta_\tau\,\sin\theta_\tau\left\{\frac{m_\tau}{\sqrt{q^2}}\,(\mathcal{A}_\parallel^R + \mathcal{A}_\perp^R) - 2\,(\mathcal{A}_{T\parallel}^R + \mathcal{A}_{T\perp}^R)\right\},\\
\mathcal{M}_R^{0,+\frac{1}{2}} &= -2\sqrt{q^2}\,\beta_\tau\,\sin\theta_\tau\left[\mathcal{A}_0^R - \frac{2m_\tau}{\sqrt{q^2}}\,\mathcal{A}_{T0}^R\right],\\
\mathcal{M}_R^{0,-\frac{1}{2}} &= -2\,m_\tau\,\beta_\tau\,\mathrm{e}^{i\phi}\left\{\mathcal{A}_{tP}^R + \cos\theta_\tau\left[\mathcal{A}_0^R - \frac{2\sqrt{q^2}}{m_\tau}\,\mathcal{A}_{T0}^R\right]\right\},\\
\mathcal{M}_R^{-1,+\frac{1}{2}} &= -\sqrt{q^2}\,\beta_\tau\,(1+\cos\theta_\tau)\,\mathrm{e}^{i\phi}\left\{\mathcal{A}_\parallel^R - \mathcal{A}_\perp^R - 2\,\frac{m_\tau}{\sqrt{q^2}}\,(\mathcal{A}_{T\parallel}^R - \mathcal{A}_{T\perp}^R)\right\},\\
\mathcal{M}_R^{-1,-\frac{1}{2}} &= \sqrt{q^2}\,\beta_\tau\,\sin\theta_\tau\,\mathrm{e}^{2i\phi}\left\{\frac{m_\tau}{\sqrt{q^2}}\left(\mathcal{A}_\parallel^R - \mathcal{A}_\perp^R\right) - 2\,(\mathcal{A}_{T\parallel}^R - \mathcal{A}_{T\perp}^R)\right\}. \qquad (4.3.42)
\end{aligned}$$

Performing the angular integrations in Eq. (4.3.36), one easily obtains the differential distribution with respect to q^2, given by

$$\frac{d\Gamma}{dq^2} \equiv \Gamma_f = \frac{1}{4}\,(3I_1^c + 6I_1^s - I_2^c - 2I_2^s)\,, \qquad (4.3.43)$$

which written explicitly in terms of the different Wilson coefficients takes the following form:

$$\begin{aligned}
\frac{d\Gamma(\bar{B}\to D^*\tau\bar{\nu})}{dq^2} &= \frac{G_F^2\,|V_{cb}|^2}{192\,\pi^3 m_B^3}\,q^2\,\lambda_{D^*}^{1/2}(q^2)\left(1-\frac{m_\tau^2}{q^2}\right)^2\mathcal{B}(D^*\to D\pi)\\
&\times\Bigg\{\left(\left|1+C_{LL}^V\right|^2+\left|C_{RL}^V\right|^2+\left|C_{LR}^V\right|^2+\left|C_{RR}^V\right|^2\right)\left(1+\frac{m_\tau^2}{2q^2}\right)\left(H_{V,+}^2+H_{V,-}^2\right)\\
&+\left(\left|1+C_{LL}^V-C_{RL}^V\right|^2+\left|C_{LR}^V-C_{RR}^V\right|^2\right)\left[\left(1+\frac{m_\tau^2}{2q^2}\right)H_{V,0}^2+\frac{3}{2}\frac{m_\tau^2}{q^2}H_{V,t}^2\right]\\
&-4\,\mathcal{R}\mathrm{e}\left[\left(1+C_{LL}^V\right)C_{RL}^{V*}+C_{LR}^V\,C_{RR}^{V*}\right]\left(1+\frac{m_\tau^2}{2q^2}\right)H_{V,+}H_{V,-}\\
&+\frac{3}{2}\left(\left|C_{RL}^S-C_{LL}^S\right|^2+\left|C_{RR}^S-C_{LR}^S\right|^2\right)H_S^2\\
&+8\left(\left|C_{LL}^T\right|^2+\left|C_{RR}^T\right|^2\right)\left(1+\frac{2m_\tau^2}{q^2}\right)\left(H_{T,+}^2+H_{T,-}^2+H_{T,0}^2\right)\\
&+3\,\mathcal{R}\mathrm{e}\left[\left(1+C_{LL}^V-C_{LR}^V\right)\left(C_{RL}^S-C_{LL}^S\right)^*+\left(C_{LR}^V-C_{RR}^V\right)\left(C_{RR}^S-C_{LR}^S\right)^*\right]\frac{m_\tau}{\sqrt{q^2}}H_S H_{V,t}\\
&-12\,\mathcal{R}\mathrm{e}\left[\left(1+C_{LL}^V\right)C_{LL}^{T*}+C_{RR}^V\,C_{RR}^{T*}\right]\frac{m_\tau}{\sqrt{q^2}}\left(H_{T,0}H_{V,0}+H_{T,+}H_{V,+}-H_{T,-}H_{V,-}\right)\\
&+12\,\mathcal{R}\mathrm{e}\left[C_{RL}^V\,C_{LL}^{T*}+C_{LR}^V\,C_{RR}^{T*}\right]\frac{m_\tau}{\sqrt{q^2}}\left(H_{T,0}H_{V,0}+H_{T,+}H_{V,-}-H_{T,-}H_{V,+}\right)\,. \qquad (4.3.44)
\end{aligned}$$

Differential distributions with respect to a single angle, which can be obtained by integrating two angles at a time, are also of special interest. These are

$$\frac{d^2\Gamma}{dq^2\,d\cos\theta_\tau} = \frac{3}{8}\left[\,(I_1^c+2I_1^s-I_2^c-2I_2^s)+(I_6^c+2I_6^s)\cos\theta_\tau+(2I_2^c+4I_2^s)\cos^2\theta_\tau\right], \qquad (4.3.45)$$

$$\begin{aligned}
\frac{d^2\Gamma}{dq^2\,d\cos\theta_D} &= \frac{3}{8}\left[\,(3I_1^s-I_2^s)+(3I_1^c-I_2^c-3I_1^s+I_2^s)\cos^2\theta_D\right]\\
&= \frac{3}{4}\,\Gamma_f\left[F_T^{D^*}\sin^2\theta_D+2\,F_L^{D^*}\cos^2\theta_D\right], \qquad (4.3.46)\\
\frac{d^2\Gamma}{dq^2\,d\phi} &= \frac{1}{8\pi}\left[\,(3I_1^c+6I_1^s-I_2^c-2I_2^s)+4I_3\cos 2\phi+4I_9\sin 2\phi\right]\\
&= \frac{1}{2\pi}\,\Gamma_f\left[1+A_3\cos 2\phi+A_9\sin 2\phi\right]. \qquad (4.3.47)
\end{aligned}$$

In the following we define several observables constructed from the coefficients of various angular dependences. The distribution with respect to $\cos\theta_D$ in Eq. (4.3.46) provides the

longitudinal and transverse polarization fractions for the D^* meson, defined as [79]

$$F_L^{D^*} = \frac{3I_1^c - I_2^c}{3I_1^c + 6I_1^s - I_2^c - 2I_2^s}, \qquad \text{and} \qquad F_T^{D^*} = \frac{2(3I_1^s - I_2^s)}{3I_1^c + 6I_1^s - I_2^c - 2I_2^s}, \tag{4.3.48}$$

which satisfy that $F_L^{D^*} + F_T^{D^*} = 1$. Notice that these quantities are functions of q^2. We define the q^2-integrated observables as follows,

$$\bar{\mathcal{O}} \equiv \frac{1}{\Gamma} \int_{q^2_{\rm min}}^{q^2_{\rm max}} dq^2 \, \mathcal{O}[q^2] \, \Gamma_f[q^2], \tag{4.3.49}$$

where Γ is the total decay width and the q^2 dependence of the observables has been written explicitly. The angular coefficients I_3 and I_9 can simply be extracted by measuring the terms proportional to $\cos 2\phi$ and $\sin 2\phi$ in Eq. (4.3.47),

$$A_3 = \frac{I_3}{\Gamma_f}, \qquad \text{and} \qquad A_9 = \frac{I_9}{\Gamma_f}, \tag{4.3.50}$$

respectively. Furthermore, we define several asymmetries starting with the well-known forward-backward asymmetry, defined as

$$\mathcal{A}_{FB}^{D^*} = \frac{1}{\Gamma_f} \Big[\int_0^1 - \int_{-1}^0 \Big] d\cos\theta_\tau \, \frac{d^2\Gamma}{dq^2 d\cos\theta_\tau}. \tag{4.3.51}$$

The coefficients I_4 and I_5 in Eq. (4.3.36) can be extracted with the two angular asymmetries:

$$\begin{aligned} A_4 =& \frac{1}{\Gamma_f} \Big[\int_{-\pi/2}^{\pi/2} - \int_{\pi/2}^{3\pi/2} \Big] d\phi \Big[\int_0^1 - \int_{-1}^0 \Big] d\cos\theta_D \Big[\int_0^1 - \int_{-1}^0 \Big] d\cos\theta_\tau \, \frac{d^4\Gamma}{dq^2 d\cos\theta_\tau d\cos\theta_D d\phi}, \\ A_5 =& \frac{1}{\Gamma_f} \Big[\int_{-\pi/2}^{\pi/2} - \int_{\pi/2}^{3\pi/2} \Big] d\phi \Big[\int_0^1 - \int_{-1}^0 \Big] d\cos\theta_D \int_{-1}^1 d\cos\theta_\tau \, \frac{d^4\Gamma}{dq^2 d\cos\theta_\tau d\cos\theta_D d\phi}. \end{aligned} \tag{4.3.52}$$

One can further define the following two observables,

$$\begin{aligned} A_7 =& \frac{1}{\Gamma_f} \Big[\int_0^{\pi} - \int_{\pi}^{2\pi} \Big] d\phi \Big[\int_0^1 - \int_{-1}^0 \Big] d\cos\theta_D \int_{-1}^1 d\cos\theta_\tau \, \frac{d^4\Gamma}{dq^2 d\cos\theta_\tau d\cos\theta_D d\phi}, \\ A_8 =& \frac{1}{\Gamma_f} \Big[\int_0^{\pi} - \int_{\pi}^{2\pi} \Big] d\phi \Big[\int_0^1 - \int_{-1}^0 \Big] d\cos\theta_D \Big[\int_0^1 - \int_{-1}^0 \Big] d\cos\theta_\tau \, \frac{d^4\Gamma}{dq^2 d\cos\theta_\tau d\cos\theta_D d\phi}, \end{aligned} \tag{4.3.53}$$

which are non-vanishing only if NP induces a complex contribution to the amplitude. This holds true for the coefficient A_9 as well. These asymmetries are simply related to the angular coefficients in (4.3.36):

$$A_4 = \frac{2}{\pi}\frac{I_4}{\Gamma_f}\,, \qquad A_5 = \frac{3}{4}\frac{I_5}{\Gamma_f}\,, \qquad \mathcal{A}_{FB}^{D^*} = \frac{3}{8}\frac{I_6^c + 2I_6^s}{\Gamma_f}\,, \qquad A_7 = \frac{3}{4}\frac{I_7}{\Gamma_f}\,, \qquad A_8 = \frac{2}{\pi}\frac{I_8}{\Gamma_f}\,. \tag{4.3.54}$$

Finally, the total branching ratio can be decomposed in terms of the τ polarization, giving rise to another observable: the lepton polarization asymmetry, defined as

$$\mathcal{P}_\tau^{D^*} = \frac{d\Gamma_{\lambda_\tau=1/2}/dq^2 - d\Gamma_{\lambda_\tau=-1/2}/dq^2}{\Gamma_f}. \tag{4.3.55}$$

Chapter 5

HEPfit

The search of NP beyond the SM is one of the most promising paths to follow in order to obtain a deeper understanding of nature. In the last years, particle colliders have provided us with a large amount of experimental information. At the same time, theoretical calculations are improving, giving precise predictions for several observables. Combining experimental results with theoretical calculations to obtain information in the most efficient way has become an important challenge that makes necessary the development of sophisticated analysis tools.

To obtain relevant information using all these data, one can think about performing a parameter scan, *i.e.*, one generates random points, evaluates the different observables at these points and then takes the points that best reproduce the experimental results. However, this method is quite inefficient and one may lose some solutions as well as the statistical meaning of the procedure. A more sophisticated way to perform these analyses are random scans with a χ^2 determination. This method is still inefficient, and the global mode can also be missed, so it results inconvenient. In the last years several *fitters* have been developed to combine the data in a more efficient way. We call fitters to statistical frameworks that fit the model parameters to the experimentally measured observables by maximising the likelihood. These fitters are more efficient than the previously mentioned procedures and have a clear statistical meaning. There are many fitters in the market,

which can be divided into two main categories: *frequentist* and *Bayesian*. Frequentist fitters determine the probability of the data for a given set of parameters and then calculate the p-value. Bayesian fitters use the Bayes' theorem and the posterior probability. This will be explained in detail in Section 5.1.

Several fitters available in the market present features that make them inconvenient for our purpose: some of them are not open-source codes, they depend on external libraries or are focused to work on small subsets of observables. The code presented in this chapter, `HEPfit`, pretends to be a general purpose code that avoids all these issues.

`HEPfit` is a general tool designed to combine direct and indirect constraints in EFTs or particular SM extensions. These extensions are NP models that can be added or modified by the user. It also offers the possibility of sampling the parameter space using a Markov Chain Monte Carlo (MCMC) implemented using the `BAT` library [88–90]. It is written in `C++` and parallelized with Message Passing Interface (`MPI`) [91]. `HEPfit` is released under the GNU General Public License, so that contributions from users are possible and welcome. The observables included can be classified into theoretical observables, EWPO, flavour and Higgs observables (direct searches and signal strengths). They are calculated in several models, such as the SM, the 2HDM or the Minimal Supersymmetric Standard Model (MSSM).

The developers' version can be downloaded at [92] and full documentation of the code, describing the models and observables included can be found in Ref. [93].

The rest of the chapter is organized as follows: in Section 5.1 the statistical framework used in `HEPfit` is briefly described. In Section 5.2 three different models implements in `HEPfit` are presented: the SM, the A2HDM and the basis operators needed to perform a fit to top and bottom EW operators. A summary is given in Section 5.3.

5.1 The `HEPfit` code, statistical framework and usage

`HEPfit` can be used both as a library to compute observables with fixed values of the parameters or as a Bayesian analysis framework. For the former, the code is based on

Bayesian statistics and makes use of the Bayes' theorem. The MCMC implemented in BAT is used and the code is parallelized with MPI.

5.1.1 Bayesian statistics

In a Bayesian framework, probability expresses a *degree of belief*. Let's consider the model parameters $\vec{x}$ and the data D. The *posterior probability* is defined according to the Bayes' theorem [94] as,

$$P(\vec{x}|D) = \frac{P(D|\vec{x})P_0(\vec{x})}{\int P(D|\vec{x})P_0(\vec{x})\,d\vec{x}}\,, \tag{5.1.1}$$

where $P_0(\vec{x})$ is the *prior probability* of the parameters and represents the prior knowledge about them. This prior knowledge may come from theoretical assumptions, previous experimental analysis or can just follow a flat distribution where all points are equally probable. The denominator is called the *evidence* and can be used to compare different models defining the Bayes factor [95]. $P(D|\vec{x})$ is the likelihood function, which is interpreted as the probability of measuring the data D given $\vec{x}$. Finally, $P(\vec{x}|D)$ is the posterior probability, *i.e.* the probability of measuring D after taking into account the evidence or information about $\vec{x}$. This posterior distribution depends on several parameters and can be marginalized using sample methods to obtain the individual 1D probability of x_i, from which credibility regions can be computed,

$$P(x_i|D) = \int P(\vec{x}|D) \prod_{j\neq i} dx_j\,. \tag{5.1.2}$$

Here, all the variables but the one we want to calculate the distribution of are integrated over.

5.1.2 Markov Chain Monte Carlo

Determining the 1D probability of Eq. (5.1.2) is not simple, specially when the number of parameters is large. Using a naive Monte Carlo sampling algorithm is really inefficient when sampling the parameter space and can lead to an unnaceptable execution time. The

method implemented in `HEPfit` is the MCMC procedure, which overcomes this obstacle and provides an algorithm to make use of Bayes' theorem and then calculate these probabilities. The implementation of MCMC in `BAT` uses a Metropolis-Hastings algorithm to sample the parameter space from the posterior distribution. The steps are the following (see [93]):

1. Start at a random point in the parameter space $\vec{x}$
2. Generate a proposal point $\vec{y}$ according to a symmetric probability distribution $g(\vec{x}, \vec{y})$
3. Compare the value of the function f at the proposal point $\vec{y}$ with the value at the current point $\vec{x}$. The proposal point is accepted if:
   - $f(\vec{y}) \geq f(\vec{x})$
   - otherwise, generate a random number r from a uniform distribution in the range [0, 1] and accept the proposal if $f(\vec{y})/f(\vec{x}) > r$

   If neither conditions are satisfied the proposal is rejected.
4. Continue from step 1

The function $f(\vec{y})$ corresponds to the denominator of Eq. (5.1.1).

The MCMC implementation contains two parts. First of all, there is a *pre-run* in which each chain starts from an arbitrary random point in the parameter space. Then, the tuning of the proposal function continues until the chains reach a stationary state. This is reached once the targeted efficiency of the proposal and the R-value are close to one. The targeted efficiency is a measure of the qualitiy of the proposal point and the R-value of a parameter is defined as the distance of its mean value in the various chains in units of the standard deviation of the parameter in each chain [96, 97].

The second part is the *run*. In the run, samples of parameters are collected to obtain the marginalized probability and the posterior distribution of all the observables defined. More details about the implementation of the MCMC framework can be found at [88–90].

5.1.3 BAT

The MCMC framework implemented in BAT is integrated in HEPfit using the library provided by BAT on compilation. The MonteCarloEngine class inherits from the BCModel class in BAT and overloads the LogLikelihood function. This generates a numerical likelihood for one point in the parameter space with the values of the observables computed by HEPfit and the theoretical and experimental constraints provided to it. The parameters and their distributions are passed by HEPfit to BAT through the MonteCarloEngine class. Then, HEPfit rotates the correlated parameters to increase the efficiency. BAT is only used while running in MCMC mode, and it is not necessary if HEPfit is being used as an event generation.

5.1.4 Parallelization with MPI

One of the main advantages of HEPfit with respect to other codes is that it allows both for the usage of single CPUs and for clusters with its parallelized version. This is done parallelizing BAT with OpenMPI and it is very useful because one can run one chain per core. It is done at the level of the likelihood and of the computation of the observables, so it is implemented both in the run and in the pre-run. The computation of efficiencies and the convergence among the chains requires information of the different chains, and therefore it is not parallelized.

5.1.5 Usage

To use HEPfit one needs a text configuration file (or a set of files). The *model configuration file* should include the name of the model, the model parameters (ModelParameter) and their Gaussian or/and flat errors. These parameters can be correlated with the option CorrelatedGaussianParameters. The observables (Observable) are computed specifying the name defined in HEPfit, the flag (no)MCMCM that indicates whether the observable should be included in the likelihood used for the MCMC sampling or not, and the (no)weight option to specify if the observable weight will be computed or not. If

the `weight` option is set, at least a Gaussian or a flat error need to be specified. One can also use a `BinnedObservable`, containing two extra arguments, the upper and lower limit of the bin. Correlations between several observables can also be specified with `CorrelatedGaussianObservables`. One or several flags (`ModelFlag`), controlling specific options, can also be added. Additional configuration files can be added to the model configuration file with the `IncludeFile` directive.

To use `HEPfit` in Monte Carlo mode, an additional configuration file, the *Monte Carlo configuration file* is needed. There are several available parameters and options. The most relevant are `Nchains` (the number of chains in the Monte Carlo run), `PrerunMaxIter` (the maximum number of iterations that the pre-run will go through) and `Iterations` (the number of iterations per chain).

For more details about the configuration files see Section 7 of Ref. [93].

5.2 Models implemented in `HEPfit`

The building blocks of `HEPfit` are the `Model` and `Observable` classes. Models extend the base classes sequentially. For instance `QCD` ← `StandardModel` ← `GeneralTHDM`. This allows to add extensions or models in a very efficient way, since only the new ingredients with respect to the SM or a previous model need to be added.

The class `Observable` contains the relevant experimental information of a given physical observable. It is passed to the class `ThObservables`, responsible for computing this observable in a given model.

In the following sections some models implemented in `HEPfit` will be briefly described. We start with the `StandardModel`, which acts as a parent model for several extensions. Then, we focus in the `GeneralTHDM`, which contains the A2HDM and can be distinguished from the `THDM` where a $\mathcal{Z}_2$ symmetry is imposed. Finally we refer to a model class contained in the class `NewPhysics` (`NPSMEFT6dtopquark`) that allows to constrain electroweak dimension-six operators related to the top and bottom quarks.

5.2.1 The Standard Model

The `StandardModel` class allows to calculate and fit observables in the SM. It is extended from the `QCD` class containing $\alpha_s(M)$ and the quark masses $\bar{m}_q$ at the scale M in the $\overline{\text{MS}}$ scheme (except for the top quark, where the pole mass is used). This information allows to initialize several objects as `Particle` or `Meson`. Additional information (lifetimes, decay widths) are added to `HEPfit` as model parameters.

The `QCD` class is extended to the `StandardModel` class by adding the parameters G_F, the fine structure constant α, the Z and the Higgs masses (M_Z and m_h) and the elements of the CKM mixing matrix. It also fixes the scale M introduced in `QCD` to be M_Z. It contains `Particle` objects for leptons and additional model parameters that describe the hadronic vacuum polarization contribution to the running of α and uncertainties related to the EWPO. Moreover, the running of α_s is extended to include electromagnetic corrections. The `StandardModelMatching` model class provides the matching conditions for the weak effective Hamiltonian and the class `Flavour` provides the low-energy Hamiltonians for $\Delta F = 1, 2$ transitions.

As previously mentioned, the `StandardModel` and `QCD` classes act as base classes for many NP models.

5.2.2 The General A2HDM

The NHDM and the particular case of $N = 2$ doublets, *i.e.* the 2HDM were studied in detail in Chapter 2. There are many types of 2HDM models. CP-conserving models with natural flavour conservation, achieved though a softly broken $\mathcal{Z}_2$ symmetry, are implemented in `HEPfit` in the `THDM` class. The four independent choices of the $\mathcal{Z}_2$ symmetric types (type I, type II, type X and type Y) can be obtained setting the flag `modelTypeflag` in the configuration file to `type1`, `type2`, `typeX` or `typeY`.

The A2HDM is also implemented in `HEPfit` in the `GeneralTHDM` class. This class is intended to contain a general 2HDM, allowing for off-Yukawa diagonal terms and CP-violation. However, at this stage only the CP-conserving A2HDM is implemented for the

observables described in the following. This is selected with the `true` value of boolean flags `ATHDMflag` and `CPconserving`.

In the A2HDM, the observed Higgs, predicted by the SM, can be either the lightest or the heaviest CP-even scalar of the model. [1] The boolean flag `SMHiggs` allows us to select if the 125 GeV Higgs is the lightest (flag set to `true`) or heaviest (flag set to `false`).

Two additional flags are implemented in the `GeneralTHDM`. The `RGEorder` determines the order in perturbation theory of the RGE. At this stage only `LO` is implemented. The `use_sq_masses` allows to use square (`true`) or linear (`false`) priors for the scalar masses. The dependence on the mass priors will be interesting for the interpretation of the fits, as we will see in Chapter 7. A summary of the flags of the `GeneralTHDM` is displayed in Table 5.1.

Flag	Possible values	Description
`ATHDMflag`	`true/false`	Sets if the model is flavour aligned
`CPconservation`	`true/false`	Sets if the model is CP-conserving
`RGEorder`	`LO`	Sets the order of the RGEs
`SMHiggs`	`true/false`	Sets if the 125 GeV Higgs is light or heavy
`use_sq_masses`	`true/false`	Sets if square or mass priors are used for the masses

Table 5.1: Different flags implemented in the `GeneralTHDM` class.

The scalar potential of the model (see Eq. (2.1.39)) can be rewritten in terms of 9 independent parameters (6 in the CP-conserving limit): the vev (fixed to be $v = 246.22$ GeV), the four scalar masses (with the SM Higgs mass fixed to be $M_h = 125.10$ GeV) and the complex parameters $\lambda_{5,6,7}$. Therefore, the parameters of the model in the CP-conserving limit are:

- The masses of the three scalars (squared or non-squared, depending on the `use_sq_masses` flag), $M_{H^\pm}, M_H, M_A$: `mHp2, mH2sq, mH3sq` or `mHp1, mH21, mH31`

[1] The option that the 125 GeV Higgs is CP-odd is not considered here.

- Three parameters of the potential, $\lambda_5^R, \lambda_6^R, \lambda_7^R$: `Relambda5, Relambda6, Relambda7`
- The mixing angle between the two CP-even scalars, $\tilde{\alpha}$: `alpha1`
- The up, down and lepton Yukawa couplings, $\varsigma_u, \varsigma_d, \varsigma_\ell$: `Nu_11r, Nd_11r, Nl_11r`

Two additional mixing angles (`alpha2, alpha3`), describing a model in which the CP-even and CP-odd scalars mix, three imaginary potential parameters (`Imlambda5, Imlambda6, Imlambda7`) and 51 additional Yukawa couplings, describing complex non-diagonal terms can be added to the configuration files, but several observables are not implemented for these cases yet.

The implemented observables can be classified into,

- Theoretical constraints: Vacuum stability, perturbativity and unitarity of the S-matrix
- Electroweak precision observables: The oblique parameters STU and the ratio R_b
- Flavour observables: $B_s \to \mu^+\mu^-, B \to X_s\gamma, \Delta M_B$ and $(g-2)_\mu$
- Higgs observables: Direct searches and Higgs signal strengths

Detailed results on a fit to all of these observables, both in the case in which the SM Higgs is the heavy or the light Higgs can be seen in Chapter 7.

5.2.3 NPSMEFT6dtopquark

Effective dimension-six operators, relevant for the study of top and bottom EW couplings are implemented in the model class `NPSMEFT6dtopquark` in the class `NewPhyics`. This model class contains a total of seventeen parameters, each one corresponding to a dimension-six operator relevant in observables of the LHC, LEP/SLC as well as in future

colliders. These parameters are summarized in Table 5.2. The effective Lagrangian takes the form,

$$\mathcal{L}_{\text{eff}} = \mathcal{L}_{\text{SM}} + \left(\sum_i \mathcal{O}_i \frac{C_i}{\Lambda^2} + \text{h.c.} \right) , \tag{5.2.3}$$

where Λ is the NP scale. A detailed description of the effective Lagrangian and the operator basis is given in Chapter 9. The implemented observables are of the form,

$$\text{obs} = \text{obs}_{\text{SM}} + \sum_i C_i \, \text{obs}_i + \sum_j \sum_k C_j C_k \, \text{obs}_{jk} \, . \tag{5.2.4}$$

The first term, obs_{SM}, is the SM prediction for a given observable. obs_i and obs_{jk} arise from one and two insertions of dimension-six operators (plus interferences with the SM contributions). In this description, the first, second and third terms are suppressed by Λ^0, Λ^{-2} and Λ^{-4} respectively. The Λ^{-4} terms come from two insertions of Λ^{-2} and not from dimension-eight operators. As it will be seen in Chapter 9 this could endanger the validity of the EFT and thus it is interesting to see the effect of adding the terms obs_{jk}. This can be done through the flag `QuadraticFlag`. When `QuadraticFlag` is set to `true`, both obs_i and obs_{jk} terms enter in a given observable. If `QuadraticFlag` is `false` only obs_i are considered.

Name	Parameter	Name	Parameter	Name	Parameter	Name	Parameter
`C_phit`	$C_{\varphi t}$	`C_tphi`	$C_{t\varphi}$	`C_phitb`	$C_{\varphi tb}$	`C_lqP`	C_{lq}^{+}
`C_phiQ3`	$C_{\varphi Q}^{3}$	`C_phib`	$C_{\varphi b}$	`C_ed`	C_{ed}	`C_eu`	C_{eu}
`C_phiQ1`	$C_{\varphi Q}^{1}$	`C_bW`	C_{bW}	`C_eq`	C_{eq}	`C_lu`	C_{lu}
`C_tW`	C_{tW}	`C_bB`	C_{bB}	`C_ld`	C_{ld}	`C_lqM`	C_{lq}^{-}
`C_tB`	C_{tB}						

Table 5.2: Model Parameters in the `NPSMEFT6dtopquark`. "Name" refers to the name of the parameter in `HEPfit` that can be used in the configuration file. "Parameter" correspond to the Wilson coefficients defined in Section 9.1 of Chapter 9.

Results using this class can be seen in Chapter 9.

5.3 Summary

In this chapter the basic features of `HEPfit` have been presented. `HEPfit` is a Bayesian fitter that allows us to combine direct and indirect constraints in the SM and several NP models. Being a flexible, open-source code makes it a useful tool to implement additional models, perform fits and obtain constraints for the parameters of these models. In this chapter, a basic description of the statistical framework has been presented, *i.e.* the Bayesian framework, the Markov Chain Monte Carlo, the integration with `BAT` and the parallelization of the code using `MPI`. Several relevant technical details are omitted and can be found in Ref. [93]. In this thesis, the `HEPfit` package has been used for two different projects. They were presented in Section 5.2. First of all, the `GeneralTHDM` class, describing a CP-conserving A2HDM was briefly described in Section 5.2.2. A global fit of this model using `HEPfit` can be found in Chapter 7. Then, we presented the `NPSMEFT6dtopquark`, a model of the class `NewPhysics` containing top and bottom electroweak operators. This class is used in Chapter 9 to perform a global fit to the SM+ LEP/SLC data and find prospects for future colliders.

Chapter 6

Flavour alignment in multi-Higgs doublet models

Scalar multiplets transforming as doublets or singlets under the $SU(2)_L$ gauge group are the favoured candidates for building extended models of perturbative EWSB, beyond the SM framework [20]. Assigning a zero hypercharge to the singlets and $Y = Q - T_3 = \frac{1}{2}$ to the doublet scalars, these models automatically reproduce the SM electroweak ρ parameter defined as $\rho = M_W^2/M_Z^2 \cos^2\theta_W$.

The observable signals of the singlet scalar fields are quite restricted because they do not have Yukawa interactions with the SM fermions, nor they couple to the gauge bosons. Therefore, they can only communicate with those SM particles through their mixing with other neutral scalars in non-singlet multiplets.

Doublet fields present deeper implications and a richer phenomenology. As it was described in Chapter 2, by adding N scalar doublets the scalar spectrum is enlarged: the $N-1$ charged fields $H^\pm$ and the $2N-1$ neutral scalars, give rise to a rich variety of possible interactions. In general, these include non-diagonal Yukawa couplings of the neutral scalars, implying dangerous FCNC transitions, which are tightly constrained experimentally [98].

To avoid the presence of unwanted FCNC phenomena, one must impose ad-hoc dynamical restrictions, suppressing these effects below the empirically forbidden level. The models most frequently considered in the literature [99–101] assume that only one single scalar doublet can couple to a given type of right-handed fermion f_R. This guarantees identical flavour structures for the Yukawa interactions and the fermion mass matrices, so that FCNC vertices are absent as in the SM. While this assumption is quite strong, it can be easily implemented in the models, enforcing appropriately defined discrete $\mathcal{Z}_2$ symmetries which forbid the Yukawa couplings of all other scalar doublets to f_R [27–31,102–106] and keep the resulting flavour structure stable under quantum corrections (natural flavour conservation) [107,108]. One can also relax this assumption using a continuous symmetry instead of a discrete one [109].

Flavour alignment [24, 25] is a much more general possibility, based on the weaker assumption that the couplings of all scalar doublets to a given right-handed fermion have the same flavour structure [24, 25, 110]. All Yukawas can then be diagonalized simultaneously, eliminating the FCNC vertices from the tree-level Lagrangian. FCNCs effects reappear at higher perturbative orders because quantum corrections misalign the different Yukawas [111–113]. However, the build-in flavour symmetries strongly constrain the possible FCNC operators that can be generated at the quantum level [24,25], implying an effective theory with minimal flavour violation [114,115].

The induced one-loop FCNC Yukawas have been explicitly analysed within the A2HDM [24,25,112,116–120], and their effects have been found to be small and well below all known experimental constraints, giving further support to the successful phenomenology of this particular new-physics scenario [112, 118–144]. However, some recent flavour anomalies observed in $B \to D^{(*)}\tau\nu$ data [63–66, 68, 69, 145–147] have triggered the consideration of flavour non-universal aligned-like structures [148–155], which have not been explored at the quantum level.

In the following, we present a detailed study of the stability of flavour alignment under quantum corrections. We analyse the FCNC operators generated at one loop for a generic scalar sector with N doublets, both for the flavour-aligned model and for its generalization

with non-universal aligned-like structures. We want to understand the quantum structure of these models and their phenomenological viability. The general Yukawa Lagrangian for the N-Higgs-doublet model has been discussed in Section 2.1.3 and the usual models with natural flavour conservation were briefly described in Section 2.1.4 of Chapter 2. The alignment assumption is implemented in Section 2.1.5, where its possible generalizations are discussed. The one-loop RGEs of the model are used in Section 6.1 to pin down the induced FCNC operators in the most general case. The result is then particularized to the different situations we are interested in, and the usual scenarios with $\mathcal{Z}_2$ symmetries are easily recovered. Section 6.2 analyses the underlying symmetries governing the specific flavour structures obtained through the RGEs. The phenomenological implications are discussed in Sections 6.3, 6.4 and 6.5, and a brief summary is given in Section 6.6. Some technical details are summarized in Appendix D. This chapter is based in [156] with an update of the experimental input when needed.

6.1 Renormalization group equations of the NHDM

The renormalization flow of the Yukawa couplings in a generic two-Higgs-doublet model was studied in Refs. [157, 158]. The extension to a multi-Higgs-doublet model was first analysed in the lepton sector, neglecting all quark contributions ($\Gamma_a = \Delta_a = 0$) [159], and later extended to the most general case in Ref. [111]. At the one-loop level, the Yukawa

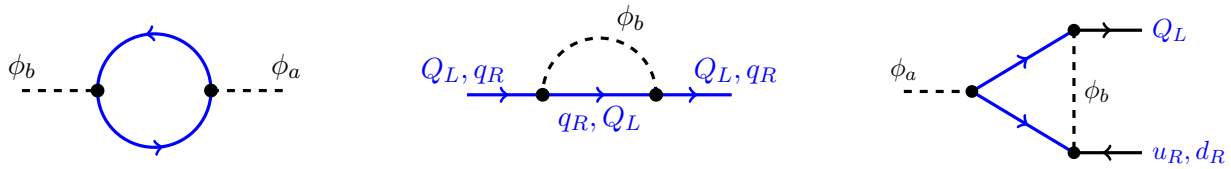

(a) (b) (c)

Figure 6.1: One-loop topologies generating the flavour structures in Eqs. (6.1.1), (6.1.2) and (6.1.3): scalar self-energies (a), Q_L and q_R self energies (b), and vertex corrections (c).

structures in Eq. (2.1.20) satisfy the RGEs [111, 117]:

$$\begin{aligned}
\mathcal{D}\Gamma_a &= a_\Gamma\,\Gamma_a + \sum_{b=1}^{N}\left[N_C\,\mathrm{Tr}\left(\Gamma_a\Gamma_b^\dagger + \Delta_a^\dagger\Delta_b\right) + \mathrm{Tr}\left(\Pi_a\Pi_b^\dagger\right)\right]\Gamma_b \\
&+ \sum_{b=1}^{N}\left(-2\,\Delta_b\Delta_a^\dagger\Gamma_b + \Gamma_a\Gamma_b^\dagger\Gamma_b + \frac{1}{2}\,\Delta_b\Delta_b^\dagger\Gamma_a + \frac{1}{2}\,\Gamma_b\Gamma_b^\dagger\Gamma_a\right), \qquad (6.1.1)\\
\mathcal{D}\Delta_a &= a_\Delta\,\Delta_a + \sum_{b=1}^{N}\left[N_C\,\mathrm{Tr}\left(\Delta_a\Delta_b^\dagger + \Gamma_a^\dagger\Gamma_b\right) + \mathrm{Tr}\left(\Pi_a^\dagger\Pi_b\right)\right]\Delta_b \\
&+ \sum_{b=1}^{N}\left(-2\,\Gamma_b\Gamma_a^\dagger\Delta_b + \Delta_a\Delta_b^\dagger\Delta_b + \frac{1}{2}\,\Gamma_b\Gamma_b^\dagger\Delta_a + \frac{1}{2}\,\Delta_b\Delta_b^\dagger\Delta_a\right), \qquad (6.1.2)\\
\mathcal{D}\Pi_a &= a_\Pi\,\Pi_a + \sum_{b=1}^{N}\left[N_C\,\mathrm{Tr}\left(\Gamma_a\Gamma_b^\dagger + \Delta_a^\dagger\Delta_b\right) + \mathrm{Tr}\left(\Pi_a\Pi_b^\dagger\right)\right]\Pi_b \\
&+ \sum_{b=1}^{N}\left(\Pi_a\Pi_b^\dagger\Pi_b + \frac{1}{2}\,\Pi_b\Pi_b^\dagger\Pi_a\right), \qquad (6.1.3)
\end{aligned}$$

where $\mathcal{D} \equiv 16\pi^2\mu\,(d/d\mu)$, being μ the renormalization scale, and $N_C = 3$ is the number of quark colours.

The gauge-boson corrections are incorporated through the factors

$$a_\Gamma = -8\,g_s^2 - \frac{9}{4}\,g^2 - \frac{5}{12}\,g'^2\,, \qquad a_\Delta = a_\Gamma - g'^2\,, \qquad a_\Pi = -\frac{9}{4}\,g^2 - \frac{15}{4}\,g'^2\,, \quad (6.1.4)$$

where g_s, g and g' are the $SU(3)_C$, $SU(2)_L$ and $U(1)_Y$ couplings, respectively. These contributions do not change the flavour structure and only amount to a multiplicative global factor.

One-loop diagrams involving scalar propagators introduce two additional Yukawa matrices. The terms where these two matrices are traced (first lines in the right-hand sides of Eqs. (6.1.1), (6.1.2) and (6.1.3)) originate in the scalar self-energies (Fig. 6.1a). They correct each Yukawa vertex Γ_b, Δ_b, Π_b with a different multiplicative factor, leaving untouched its own flavour configuration, and mix the different 'b' structures. The additional flavour-dependent quantum corrections in the second lines arise from fermion self-energies and vertex contributions. The Q_L self-energy (Fig. 6.1b) generates the $(\Gamma_b\Gamma_b^\dagger + \Delta_b\Delta_b^\dagger)$ terms multiplying the left-hand sides of Γ_a in (6.1.1) and Δ_a in (6.1.2), while the d_R and u_R self-energies (Fig. 6.1b) give rise to the $\Gamma_a\Gamma_b^\dagger\Gamma_b$ and $\Delta_a\Delta_b^\dagger\Delta_b$ contributions, respectively. The vertex topology (Fig. 6.1c) introduces the remaining structures $\Delta_b\Delta_a^\dagger\Gamma_b$ and $\Gamma_b\Gamma_a^\dagger\Delta_b$, with '$b$' indices in both sides of the primary 'a' Yukawa. The corresponding terms in $\mathcal{D}\Pi_a$ are easily obtained with the changes $\Gamma_a \to \Pi_a$, $\Delta_a \to 0$. We have recalculated all these topologies, finding complete agreement with Refs. [111, 117].

Let us now consider a tree-level Yukawa structure having the generalized aligned-like form of Eq. (2.1.34) with $\varsigma_f^{(a)}$ diagonal matrices. Focusing for the moment on the Γ_a couplings, one can rewrite Eq. (6.1.1) as

$$\mathcal{D}\Gamma_a \,=\, \mathrm{e}^{-i\tilde{\theta}_a}\,\left\{\xi_d^{(a)}\,\mathcal{D}\Gamma_1 + \left[\delta\xi_d^{(a)} + \Theta_{d,FC}^{(a)} + \Theta_{d,FV}^{(a)}\right]\,\Gamma_1\right\}\,. \tag{6.1.5}$$

The parameters $\delta\xi_d^{(a)}$ contain those terms in the first line of Eq. (6.1.1) which do not fit in $\xi_d^{(a)}\mathcal{D}\Gamma_1$. Since they are constants without flavour structure, these contributions can be reabsorbed into a quantum redefinition of the alignment factors, $\mathrm{e}^{-i\tilde{\theta}_a}\,\delta\xi_d^{(a)} = \mathcal{D}\left(\mathrm{e}^{-i\tilde{\theta}_a}\,\xi_d^{(a)}\right)$, promoting them to μ-dependent quantities. The contributions from the second line of Eq. (6.1.1) have been split in two parts: $\Theta_{d,FC}^{(a)}$ incorporates the flavour-conserving terms with Γ_b structures, while $\Theta_{d,FV}^{(a)}$ contains the flavour-violating pieces with Δ_b matrices.

A similar decomposition can be performed for $\mathcal{D}\Delta_a$ and $\mathcal{D}\Pi_a$. Obviously, one does not generate any FCNC couplings through $\mathcal{D}\Pi_a$ because there is only one flavour structure in the second line of (6.1.3) (in aligned-like models), *i.e.*, $\Theta_{\ell,FV}^{(a)} = 0$.

Since we are only interested in the flavour-violating structures, we can neglect the quantum corrections to the vacuum expectation values and work directly in the Higgs basis where all expressions simplify considerably. Dropping all flavour-conserving contributions, the integration of the RGEs is quite straightforward. At leading order, one gets the following local FCNC interactions (in the neutral scalar mass eigenstates basis):

$$\begin{aligned}\mathcal{L}_{\text{FCNC}} &= \frac{1}{4\pi^2 v^3}\sum_{k=1}^{2N-1}\varphi_k^0\sum_{a=1}^{N-1}\Big\{\mathcal{C}_d^{(a+1)}\,(\mathcal{R}_{k,2a}+i\,\mathcal{R}_{k,2a+1})\;\bar{d}_L\widetilde{\Theta}_d^{(a+1)}M_d d_R \\ &+ \mathcal{C}_u^{(a+1)}\,(\mathcal{R}_{k,2a}-i\,\mathcal{R}_{k,2a+1})\;\bar{u}_L\widetilde{\Theta}_u^{(a+1)}M_u u_R\Big\}+\text{ h.c.}\,, \end{aligned} \tag{6.1.6}$$

where each quark vertex is proportional to the corresponding mass. The structures

$$\widetilde{\Theta}_d^{(a)} = -V_{\text{CKM}}^\dagger\sum_{b=1}^{N}\varsigma_u^{(b)\dagger}M_u M_u^\dagger\varsigma_u^{(a)}V_{\text{CKM}}\varsigma_d^{(b)}+\varsigma_d^{(a)}V_{\text{CKM}}^\dagger\sum_{b=1}^{N}\varsigma_u^{(b)\dagger}M_u M_u^\dagger V_{\text{CKM}}\varsigma_d^{(b)}+\Delta\widetilde{\Theta}_d^{(a)}\,, \tag{6.1.7}$$

$$\widetilde{\Theta}_u^{(a)} = -V_{\text{CKM}}\sum_{b=1}^{N}\varsigma_d^{(b)}M_d M_d^\dagger\varsigma_d^{(a)\dagger}V_{\text{CKM}}^\dagger\varsigma_u^{(b)\dagger}+\varsigma_u^{(a)\dagger}V_{\text{CKM}}\sum_{b=1}^{N}\varsigma_d^{(b)}M_d M_d^\dagger V_{\text{CKM}}^\dagger\varsigma_u^{(b)\dagger}+\Delta\widetilde{\Theta}_u^{(a)}\,,$$

involve two additional quark mass matrices, two CKM mixing matrices and three alignment factors. Thus, the generated FCNC operators have dimension seven and are strongly suppressed by CKM mixings. The last terms in (6.1.7),

$$\Delta\widetilde{\Theta}_d^{(a)} = \frac{1}{4}\left[V_{\text{CKM}}^\dagger\left(\sum_{b=1}^{N}\varsigma_u^{(b)\dagger}M_u M_u^\dagger\varsigma_u^{(b)}\right)V_{\text{CKM}}\,,\,\varsigma_d^{(a)}\right] = \frac{N}{4}\left[V_{\text{CKM}}^\dagger M_u M_u^\dagger V_{\text{CKM}}\,,\,\varsigma_d^{(a)}\right], \tag{6.1.8}$$

$$\Delta\widetilde{\Theta}_u^{(a)} = \frac{1}{4}\left[V_{\text{CKM}}\left(\sum_{b=1}^{N}\varsigma_d^{(b)}M_d M_d^\dagger\varsigma_d^{(b)\dagger}\right)V_{\text{CKM}}^\dagger\,,\,\varsigma_u^{(a)\dagger}\right] = \frac{N}{4}\left[V_{\text{CKM}}M_d M_d^\dagger V_{\text{CKM}}\,,\,\varsigma_d^{(a)}\right],$$

are only present in the most general aligned-like scenario with diagonal matrices $\varsigma_f^{(a)}$, otherwise the commutators would vanish identically.

In the simpler case of normal alignment (see Section 2.1.5), where the factors $\varsigma_f^{(a)}$ are just family-universal parameters, these expressions adopt the much simpler forms:

$$\widetilde{\Theta}_d^{(a)} = \left(\varsigma_d^{(a)} - \varsigma_u^{(a)}\right) \left(\sum_{b=1}^{N} \varsigma_u^{(b)\dagger} \varsigma_d^{(b)}\right) V_{\rm CKM}^\dagger M_u M_u^\dagger V_{\rm CKM}\,, \tag{6.1.9}$$

$$\widetilde{\Theta}_u^{(a)} = \left(\varsigma_u^{(a)\dagger} - \varsigma_d^{(a)\dagger}\right) \left(\sum_{b=1}^{N} \varsigma_u^{(b)\dagger} \varsigma_d^{(b)}\right) V_{\rm CKM} M_d M_d^\dagger V_{\rm CKM}^\dagger\,. \tag{6.1.10}$$

For $N = 2$, these results agree with the previously known one-loop misalignment of the A2HDM [111–113, 116–120].

The RGEs determine the μ dependence of the Wilson coefficients $\mathcal{C}_{d,u}^{(a)}(\mu)$. At leading order, one finds ($f = d, u$)

$$\mathcal{C}_f^{(a)}(\mu) \,=\, \mathcal{C}_f^{(a)}(\mu_0) - \log\left(\mu/\mu_0\right). \tag{6.1.11}$$

One can easily check that $\mathcal{L}_{\rm FCNC}$ vanishes identically for all models with natural flavour conservation, discussed in Section 2.1.4. Each of these models is characterized by three numbers $\{a_d, a_u, a_\ell\}$, specifying the choice of three scalar fields coupling to the different types of right-handed fermions, and real alignment parameters $\varsigma_f^{(a)} = \Omega_{aa_f}/\Omega_{1a_f}$. Therefore,

$$\left(\varsigma_d^{(a)} - \varsigma_u^{(a)}\right) \sum_{b=1}^{N} \varsigma_u^{(b)} \varsigma_d^{(b)} \,=\, \left(\Omega_{aa_d} - \Omega_{aa_u}\right) \frac{\sum_{b=1}^{N} \Omega_{ba_u}\Omega_{ba_d}}{\left(\Omega_{1a_u}\Omega_{1a_d}\right)^2} \,=\, \left(\Omega_{aa_d} - \Omega_{aa_u}\right) \frac{\delta_{a_u a_d}}{\left(\Omega_{1a_u}\Omega_{1a_d}\right)^2} \,=\, 0\,, \tag{6.1.12}$$

which implies $\widetilde{\Theta}_d^{(a)} = \widetilde{\Theta}_u^{(a)} = 0$.

The one-loop FCNC local interactions also disappear if the Yukawa matrices satisfy the relations

$$\begin{aligned} &\sum_{b=1}^{N} \Delta_b \Delta_a^\dagger \Gamma_b \,=\, \lambda_\Gamma\, \Gamma_a\,, && \sum_{b=1}^{N} \Delta_b \Delta_b^\dagger \Gamma_a \,=\, \lambda'_\Gamma\, \Gamma_a\,, \\ &\sum_{b=1}^{N} \Gamma_b \Gamma_a^\dagger \Delta_b \,=\, \lambda_\Delta\, \Delta_a\,, && \sum_{b=1}^{N} \Gamma_b \Gamma_b^\dagger \Delta_a \,=\, \lambda'_\Delta\, \Delta_a\,, \end{aligned} \tag{6.1.13}$$

with λ_Γ, λ'_Γ, λ_Δ, λ'_Δ arbitrary complex parameters. In this very particular case, $\mathcal{L}_{\rm FCNC}$ becomes flavour conserving. The conditions (6.1.13) have been analysed in Ref. [113], within the A2HDM, finding a phenomenologically viable solution with all Yukawa matrices

proportional to the "democratic" matrix $\mathcal{Y}_{ij} = 1\,, \forall i,j$. This stable aligned solution is protected by a $\mathcal{Z}_3 \otimes \mathcal{Z}_3'$ symmetry and corresponds to the limit where only one generation of quarks (top and bottom) acquires mass, while $V_{\rm CKM}$ is the identity matrix.

6.2 Flavour symmetries

The flavour structure of $\mathcal{L}_{\rm FCNC}$ can be easily understood with symmetry considerations [24]. In the absence of Yukawa couplings, the Lagrangian of the N-Higgs-doublet model has a huge $SU(3)^5$ flavour symmetry, corresponding to independent transformations of the Q_L, L_L, d_R, u_R and ℓ_R fermion fields in the 3-generation flavour space: $f_X \to S_{f_X}\, f_X\,,\ S_{f_X} \in SU(3)_{f_X}$. One can formally extend this symmetry to the Yukawa sector, assigning appropriate transformation properties to the flavour matrices Γ_a, Δ_a and Π_a, which are then treated as spurion fields [114, 115]:

$$\Gamma_a \;\to\; S_{Q_L}\,\Gamma_a\,S_{d_R}^\dagger\,, \qquad \Delta_a \;\to\; S_{Q_L}\,\Delta_a\,S_{u_R}^\dagger\,, \qquad \Pi_a \;\to\; S_{L_L}\,\Pi_a\,S_{\ell_R}^\dagger\,. \tag{6.2.14}$$

These auxiliary fictitious fields allow for an easy bookkeeping of operators invariant under the enlarged symmetry, and encode the explicit symmetry breakings introduced by the Yukawa interactions. Obviously, the renormalization group equations (6.1.1), (6.1.2) and (6.1.3) transform homogeneously under (6.2.14) because quantum corrections respect the Lagrangian symmetries (modulo anomalies). Only those structures which are invariant under this formal flavour symmetry can be generated at higher orders.

Once the symmetry breakings are explicitly included, the Yukawa Lagrangian (2.1.26) remains still invariant under flavour-dependent phase transformations of the fermion mass eigenstates, provided one performs appropriate rephasings of all flavour structures (masses, Yukawa couplings and quark-mixing factors) [24, 25, 112]:

$$\begin{aligned} f_X^i \;&\to\; \mathrm{e}^{i\alpha_i^{f,X}}\, f_X^i\,, & Y_f^{(a),ij} \;&\to\; \mathrm{e}^{i\alpha_i^{f,L}}\, Y_f^{(a),ij}\, \mathrm{e}^{-i\alpha_j^{f,R}}\,, \\ M_f^{ij} \;&\to\; \mathrm{e}^{i\alpha_i^{f,L}}\, M_f^{ij}\, \mathrm{e}^{-i\alpha_j^{f,R}}\,, & V_{\rm CKM}^{ij} \;&\to\; \mathrm{e}^{i\alpha_i^{u,L}}\, V_{\rm CKM}^{ij}\, \mathrm{e}^{-i\alpha_j^{d,L}}\,. \end{aligned} \tag{6.2.15}$$

Here, $f = d, u, \ell$, $X = L, R$ and i, j refer to the three different fermion families. The generalized alignment condition (2.1.36) implies then

$$\varsigma_f^{(a),ij} \;\to\; \mathrm{e}^{i\alpha_i^{f,L}}\, \varsigma_f^{(a),ij}\, \mathrm{e}^{-i\alpha_j^{f,L}}\,. \tag{6.2.16}$$

Since quantum corrections preserve these flavour symmetries, they can only give rise to FCNC operators of the form

$$\mathcal{O}_d^{n,m} = \bar{d}_L(\varsigma_d)^{p_1} V_{\rm CKM}^\dagger (\varsigma_u^\dagger)^{p_n} (M_u M_u^\dagger)^n (\varsigma_u)^{p'_n} V_{\rm CKM} (\varsigma_d)^{p_m} (M_d M_d^\dagger)^m (\varsigma_d^\dagger)^{p'_m} (\varsigma_d)^{p'_1} M_d d_R\,,$$
$$\mathcal{O}_u^{n,m} = \bar{u}_L(\varsigma_u)^{p_1} V_{\rm CKM} (\varsigma_d)^{p_n} (M_d M_d^\dagger)^n (\varsigma_d^\dagger)^{p'_n} V_{\rm CKM}^\dagger (\varsigma_u^\dagger)^{p_m} (M_u M_u^\dagger)^m (\varsigma_u)^{p'_m} (\varsigma_u^\dagger)^{p'_1} M_u u_R\,, \tag{6.2.17}$$

or similar structures with additional factors of $V_{\rm CKM}$, $V_{\rm CKM}^\dagger$, $(M_f M_f^\dagger)$ and alignment matrices. To generate a FCNC operator one needs at least two insertions of the CKM mixing matrix, and the unitarity of $V_{\rm CKM}$ requires the presence of quark mass matrices between these two insertions, *i.e.*, a product $(M_f M_f^\dagger)^n$ with $n \geq 1$. An additional (single) mass factor is needed at the end of the chain to preserve chirality. Thus, the lowest-order operators must contain two quark-mixing matrices and three mass matrices, as explicitly shown in Eq. (6.1.6).

The alignment factors originate in the Yukawa matrices $Y_f^{(a)} = \varsigma_f^{(a)} M_f$. Since $\varsigma_f^{(1)} = 1$, the terms $(\varsigma_f)^{p_k,p'_k}$ and $(\varsigma_f^\dagger)^{p_k,p'_k}$ in (6.2.17) refer to the possible presence of $p_k, p_{k'} \leq k$ non-trivial alignment parameters with possibly different values of the superindex (a). To simplify notation, we have loosely skipped this superindex and have made use of the commutation property of the diagonal matrices M_f and $\varsigma_f^{(a)}$ (in the fermion-mass eigenstate basis) to collect together alignment factors of a given type. Thus, the operators $\widetilde{\Theta}_d^{(a)}$ and $\widetilde{\Theta}_u^{(a)}$ in Eq. (6.1.7) contain up to three alignment factors. Notice that alignment structures with $b \neq a$ can only appear pairwise, $\varsigma_f^{(b)} \varsigma_{f'}^{(b)\dagger}$, since they are generated through the exchange of a scalar propagator between two 'b' Yukawa vertices.

The first possible alignment factor in the r.h.s of Eqs. (6.2.17), just before the first CKM matrix, has a more subtle origin. It compensates the $\varsigma_d^{(a)} \mathcal{D}\Gamma_1$ terms in Eq. (6.1.5) which are not present in $\mathcal{D}\Gamma_2$, and the $\varsigma_u^{(a)\dagger} \mathcal{D}\Delta_1$ terms not present in $\mathcal{D}\Delta_2$. Therefore, in

this position there is at most a single alignment factor which must be either $\varsigma_d^{(a)}$ or $\varsigma_u^{(a)\dagger}$, for $\mathcal{O}_d^{n,m}$ and $\mathcal{O}_u^{n,m}$, respectively, as explicitly shown in Eqs. (6.1.7).

6.3 Phenomenological constraints

In the absence of protecting $\mathcal{Z}_2$ symmetries, the alignment hypothesis can only be exactly fulfilled at a single value of the renormalization scale $\mu = \Lambda_A$. Quantum corrections unavoidably misalign the Yukawa matrices at $\mu \neq \Lambda_A$, generating FCNC vertices that contribute to processes which are very suppressed in the SM. However, the flavour symmetries embodied in the tree-level aligned Lagrangian restrict very efficiently the possible structures that can be generated at higher perturbative orders. At the one-loop level, the resulting FCNC local interaction in Eq. (6.1.6) only contains two operators, one for each quark sector, up or down. Both operators contain two insertions of the CKM matrix and three Yukawa matrices, which entails a strong phenomenological suppression of FCNC effects. Nevertheless, it is worth to investigate whether any interesting contributions could still show up at a level relevant for present or forthcoming experiments.

For simplicity, from now on we will restrict the analysis to the usual A2HDM framework, *i.e.*, a two-Higgs-doublet Lagrangian with aligned Yukawa structures, parametrized with three alignment constants $\varsigma_{d,u,\ell}$ as it is described in Section 2.1.6. The one-loop FCNC effective Lagrangian (6.1.6) reduces in this case to [112]

$$\begin{aligned}\mathcal{L}_{\rm FCNC} &= \frac{1}{4\pi^2 v^3}\,(1+\varsigma_u^*\varsigma_d)\sum_{k=1}^{3}\varphi_k^0\,\Big\{\mathcal{C}_d(\mu)\,(\mathcal{R}_{k2}+i\,\mathcal{R}_{k3})\,(\varsigma_d-\varsigma_u)\,\bar{d}_L V_{\rm CKM}^\dagger M_u M_u^\dagger V_{\rm CKM} M_d d_R \\ &- \mathcal{C}_u(\mu)\,(\mathcal{R}_{k2}-i\,\mathcal{R}_{k3})\,(\varsigma_d^*-\varsigma_u^*)\,\bar{u}_L V_{\rm CKM} M_d M_d^\dagger V_{\rm CKM}^\dagger M_u u_R\Big\} + \text{h.c.}\end{aligned} \tag{6.3.18}$$

with $\mathcal{C}_{d,u}(\mu)$ encoding the renormalization-scale dependence, which at leading order takes the simple form: $\mathcal{C}_{d,u}(\mu) = \mathcal{C}_{d,u}(\mu_0) - \log(\mu/\mu_0)$.

The sum runs over the three neutral scalars of the model. Assuming that CP is a symmetry of the scalar potential (and vacuum), there are two CP-even neutral scalars ($\varphi_1^0 = h$, $\varphi_2^0 = H$) which mix through a two-dimensional rotation matrix, while the third

neutral scalar $\varphi_3^0 = A$ is CP-odd and does not mix with the others. Therefore:

$$\mathcal{R}_{11} = \mathcal{R}_{22} = \cos\tilde{\alpha}\,, \quad \mathcal{R}_{12} = -\mathcal{R}_{21} = \sin\tilde{\alpha}\,, \quad \mathcal{R}_{33} = 1\,, \quad \mathcal{R}_{13} = \mathcal{R}_{23} = \mathcal{R}_{31} = \mathcal{R}_{32} = 0\,. \tag{6.3.19}$$

We adopt the convention $0 \leq \tilde{\alpha} \leq \pi$, so that $\sin\tilde{\alpha}$ is always positive, and will identify the CP-even neutral state h with the Higgs particle found at LHC, *i.e.*, $M_h = (125.09 \pm 0.24)$ GeV [160]. The data shows that h behaves like the SM Higgs boson, within the current experimental uncertainties, which constrains the mixing angle to satisfy $|\cos\tilde{\alpha}| > 0.90$ (68% CL) [123, 124].

One could speculate that flavour alignment originates in some underlying new-physics dynamics at a high-energy scale Λ_A, where alignment is exact due to a flavour symmetry of the new-physics Lagrangian, *i.e.*, $\mathcal{C}_f(\Lambda_A) = 0$. Several models with this property have been discussed in the literature [142, 143, 161–163]. In that case, the RGEs determine $\mathcal{C}_f(\mu) = \log(\Lambda_A/\mu)$ at an arbitrary renormalization scale μ. Taking $\Lambda_A \leq M_{\text{Planck}} \sim 10^{19}$ GeV, one gets $\mathcal{C}_f(M_W) \leq 40$, which puts an upper bound on the size of any possible FCNC effects. Tree-level implications of $\mathcal{L}_{\text{FCNC}}$ have been already analysed in Refs. [116, 120], with the extreme choice $\Lambda_A = M_{\text{Planck}}$, while different values of the high-energy scale Λ_A were investigated in Ref. [117].

While being illustrative of the possible phenomenological relevance of the Yukawa misalignment, the simplified tree-level analyses completely neglect the non-local FCNC loop contributions generated by the A2HDM Lagrangian [112, 118, 119, 121, 122, 129–132, 138], which are usually dominant. The most important FCNC processes originate in one-loop diagrams (penguins and boxes) involving charged-current flavour-changing vertices, through the exchange of $W^\pm$ gauge bosons and the unique charged scalar ($\varphi_1^\pm = H^\pm$) present in the model. Most of these loop contributions generate finite amplitudes (also at higher orders) because symmetry considerations forbid the presence of the relevant FCNC counterterms in the Lagrangian. This is no-longer true for the effective FCNC interactions of the neutral scalars; the loop contributions generate in this case ultraviolet (UV) divergences that get exactly cancelled through the renormalization of the $\mathcal{C}_f$ couplings in

Figure 6.2: Feynman diagrams contributing to $\bar{B}^0 \to \mu^+\mu^-$ (left) and B^0–$\bar{B}^0$ mixing (right). The crossed vertex represents the one-loop effective FCNC neutral interaction in Eq. (6.1.6).

Eq. (6.3.18) (and similar counterterms at higher orders). The renormalization-scale dependence of the loop contributions cancels also the μ dependence of the $\mathcal{C}_f(\mu)$ misalignment parameters. Complete one-loop calculations, including the proper renormalization of the misalignment Lagrangian $\mathcal{L}_{\rm FCNC}$ have been already published for the FCNC transitions $B^0_{d,s} \to \ell^+\ell^-$ [118] and $t \to \varphi^0_k c$ [119].

Owing to the quark-mass and CKM suppressions of $\mathcal{L}_{\rm FCNC}$ the potentially largest misalignment effects should appear in the $\varphi^0_k \bar{s}_L b_R$ effective vertex, with a top contribution proportional to $V^*_{ts}V_{tb}m_t^2 m_b/(4\pi^2 v^3)$. In the absence of any direct evidence of FCNC Higgs decays, this singles out $B^0_s \to \mu^+\mu^-$ and B^0_s–$\bar{B}^0_s$ mixing as prime candidates to test the local FCNC interaction. As shown in Fig. 6.2, both processes get tree-level contributions from $\mathcal{L}_{\rm FCNC}$, through φ^0_k exchange. There is, however, an important difference between the two transitions. The leptonic $B^0_s \to \mu^+\mu^-$ decay occurs with a single insertion of the effective $\varphi^0_k \bar{s}_L b_R$ vertex which, therefore, renormalizes the corresponding one-loop scalar-penguin contribution [118]. On the other side, to generate a B^0_s–$\bar{B}^0_s$ mixing transition through neutral scalar exchange, one needs to insert two FCNC effective vertices. This contribution is then of a higher-perturbative order and should be considered together with the relevant two-loop contributions to the meson-mixing amplitude, since it renormalizes the UV divergence from diagrams with two (one-loop) scalar-penguin triangles. The one-loop diagrammatic calculation of the meson-antimeson transition is in fact UV convergent [112].

6.3.1 Inputs and numerical treatment

We are interested in a scalar sector testable at the LHC, with the masses of the additional scalars not too far from the electroweak scale. A lower bound $M_{H^\pm} \geq 78.6$ GeV (95% CL) is imposed by LEP searches [164], with the only assumption that the charged scalar decays into fermions. In addition, the precise measurements of the Z and $W^\pm$ self-energies, usually encoded through the so-called oblique parameters S, T and U [165], impose strong constraints on the scalar mass splittings. Together with the requirement of perturbativity and perturbative unitary bounds on the scalar potential couplings [166], this implies that the additional neutral scalars H and A should have masses below the TeV, if $M_{H^\pm} < 500$ GeV [124].

In order to illustrate the possible phenomenological scenarios, we will adopt the following benchmark configurations for the unknown scalar masses:

$$\begin{aligned}
&\text{A}: \quad M_{H^\pm} = 100\ \text{GeV}\,, \quad M_H = 50\ \text{GeV}\,, \quad M_A = 50\ \text{GeV}\,,\\
&\text{B}: \quad M_{H^\pm} = 100\ \text{GeV}\,, \quad M_H = 200\ \text{GeV}\,, \quad M_A = 200\ \text{GeV}\,,\\
&\text{C}: \quad M_{H^\pm} = 500\ \text{GeV}\,, \quad M_H = 500\ \text{GeV}\,, \quad M_A = 200\ \text{GeV}\,,\\
&\text{D}: \quad M_{H^\pm} = 500\ \text{GeV}\,, \quad M_H = 200\ \text{GeV}\,, \quad M_A = 500\ \text{GeV}\,,\\
&\text{E}: \quad M_{H^\pm} = 1000\ \text{GeV}\,, \quad M_H = 500\ \text{GeV}\,, \quad M_A = 1000\ \text{GeV}\,,\\
&\text{F}: \quad M_{H^\pm} = 1000\ \text{GeV}\,, \quad M_H = 1000\ \text{GeV}\,, \quad M_A = 1000\ \text{GeV}\,.
\end{aligned} \tag{6.3.20}$$

These mass configurations satisfy the present experimental constraints on the oblique parameters [124,167]. The first four choices are representative of a plausible nearby scalar spectrum, while the last two approach the decoupling regime.

The up-type alignment parameter is strongly constrained by the measured $Z \to b\bar{b}$ decay width, which leads to an upper bound that scales linearly with the charged scalar mass [112]:

$$|\varsigma_u| \ < \ 0.72 \ + \ 0.0024\ M_{H^\pm}/\text{GeV} \qquad (95\%\ \text{CL})\,. \tag{6.3.21}$$

With $M_{H^\pm} \leq 500$ GeV, this gives $|\varsigma_u| < 1.9$ at 95% CL. For the other two alignment parameters we require the Yukawa couplings to remain in the perturbative regime, *i.e.*, $\frac{\sqrt{2}}{v}\varsigma_f m_f < 1$. This implies the absolute upper bounds $|\varsigma_d| < 50$ and $|\varsigma_\ell| < 100$. Our

numerical analysis will be performed in the CP-conserving limit to reduce the number of free parameters.

The choice of CKM parameters is subtle because global CKM fits assume the SM. We have performed a specific fit to obtain the CKM elements needed for our analysis, taking as entries determinations which are not sensitive to new physics. First of all V_{ud} is extracted from the $(0^+ \to 0^+)$ nuclear β decays [168] and CKM unitarity is used to determine $V_{us} \equiv \lambda$. The values of V_{ub} and V_{cb} are obtained combining the exclusive and inclusive averages from $b \to u\ell\bar{\nu}_\ell$ and $b \to c\ell\bar{\nu}_\ell$ decays, performed by HFLAV [48], and increasing the error with the usual PDG scale factor to account for their present discrepancy [75]. Then, combining V_{cb} with the previous value of λ, the Wolfenstein A parameter is obtained. The apex $(\bar{\rho}, \bar{\eta})$ of the 'bd' unitarity triangle is determined from $V_{ub}/V_{cb}, \lambda$ and the ratio $\Delta m_{B_s^0}/\Delta m_{B_d^0}$, which fixes V_{td}/V_{ts} [48], by performing a χ^2 minimization. These ratios are related to $\bar{\rho}$ and $\bar{\eta}$ through:

$$\left|\frac{V_{ub}}{V_{cb}}\right| = \frac{\lambda}{1-\frac{\lambda^2}{2}}\ |\bar{\rho} - i\bar{\eta}|\ , \qquad \left|\frac{V_{td}}{V_{ts}}\right| = \frac{\lambda}{1-\frac{\lambda^2}{2}}\ \left|1 - \frac{\lambda^2}{2} - \bar{\rho} - i\bar{\eta}\right|\ . \tag{6.3.22}$$

With that we find $|V_{ts}^* V_{tb}| = 0.0422 \pm 0.0009$. The rest of inputs used in the analysis are given in Table 6.1.

Parameter	Value	Comment
$f_{B_d^0}$	(192.0 ± 4.3) MeV	[49]
$f_{B_s^0}$	(228.4 ± 3.7) MeV	[49]
f_K	(155.7 ± 0.3) MeV	[49]
$\tau_{B_d^0}$	(1.519 ± 0.004) ps	[48]
τ_{B_s}	(1.510 ± 0.004) ps	[48]
$\frac{1}{\Gamma_H^s}$	(1.619 ± 0.009) ps	[48]
$\frac{1}{\Gamma_L^s}$	(1.414 ± 0.006) ps	[48]
$\Delta\Gamma_s$	(0.090 ± 0.005) ps^{-1}	[48]
$\Delta m_{B_d^0}$	(0.5065 ± 0.0019) ps^{-1}	[48]
$\Delta m_{B_s^0}$	(17.757 ± 0.021) ps^{-1}	[48]
$m_t(m_t)$	(165.9 ± 2.1) GeV	[169, 170]
$\lvert V_{ud}\rvert$	0.97417 ± 0.00021	[168]
λ	0.2258 ± 0.0009	$(1 - \lvert V_{ud}\rvert^2)^{1/2}$
$\lvert V_{ub}\rvert$	$(3.99 \pm 0.16) \cdot 10^{-3}$	[75]
$\lvert V_{cb}\rvert$	$(39.6^{+1.1}_{-1.0}) \cdot 10^{-3}$	[75]
A	0.828 ± 0.017	From V_{cb} and λ
$\bar{\rho}$	$0.168^{+0.020}_{-0.019}$	Our fit
$\bar{\eta}$	$0.37^{+0.03}_{-0.04}$	Our fit
$\mathrm{Br}(B_s^0 \to \mu^+\mu^-)$	$(3.0 \pm 0.6^{+0.3}_{-0.2}) \cdot 10^{-9}$	[171]
$\mathrm{Br}(B_d^0 \to \mu^+\mu^-)$	$(1.4^{+1.6}_{-1.4}) \cdot 10^{-10}$	[75]

Table 6.1: Inputs used in our analysis. Other masses and constants are taken from Ref. [75].

6.4 $B_s^0 \to \mu^+\mu^-$

A complete one-loop calculation of the $B_{d,s}^0 \to \ell^+\ell^-$ decay amplitudes within the A2HDM was performed in Ref. [118],[1] including the effective one-loop FCNC local interaction of Eq. (6.3.18), which is needed to properly reabsorb the UV divergences. The phenomenological study needs to be updated in view of the more precise LHCb measurement [171] of the time-integrated $B_s^0 \to \mu^+\mu^-$ branching ratio. Moreover, in Ref. [118] $\mathcal{C}_d(\mu)$ was taken to be zero at $\mu = M_W$, in order to simplify the numerical analysis, while we are now interested in finding out how large this parameter could be. The decay $B_d^0 \to \mu^+\mu^-$ is also sensitive to the A2HDM contributions, but it leads to much weaker constraints at present, so we will concentrate in the B_s^0 decay mode.

At the B_q^0 meson mass scale, the decay $B_q^0 \to \ell^+\ell^-$ can be described with the effective low-energy Hamiltonian

$$\mathcal{H}_{\text{eff}} \;=\; -\frac{G_F\alpha}{\sqrt{2}\pi\sin^2\theta_W}\, V_{tb}V_{tq}^*\, \left\{C_{10}\, O_{10} + C_S\, O_S + C_P\, O_P\right\}\,, \tag{6.4.23}$$

where

$$O_{10} \;=\; (\bar{q}\gamma_\mu\mathcal{P}_L b)(\bar{\ell}\gamma^\mu\gamma_5\ell)\,, \qquad O_S \;=\; \frac{m_b m_\ell}{M_W^2}\,(\bar{q}\mathcal{P}_R b)(\bar{\ell}\ell)\,, \qquad O_P \;=\; \frac{m_b m_\ell}{M_W^2}\,(\bar{q}\mathcal{P}_R b)(\bar{\ell}\gamma_5\ell)\,, \tag{6.4.24}$$

with $m_b = m_b(\mu)$ the running b-quark mass and $\mathcal{P}_{L/R} = (1\mp\gamma_5)/2$ the chirality projectors. Operators with the opposite quark chiralities are neglected because their contributions are very suppressed in the SM and many extensions as the NDHM, being proportional to the light-quark mass m_q.

In the SM the scalar and pseudo-scalar Wilson coefficients are mass-suppressed, so their contribution is tiny, and only the operator O_{10} is numerically relevant. However C_S and C_P can be much more sizeable in models with extended scalar sectors. Neglecting any

[1] The one-loop computation has been recently checked within (softly-broken) $\mathcal{Z}_2$ models [172]. The two calculations are in good agreement, except for a small difference in the Z-penguin contribution to C_P which is numerically insignificant and originates in a different matching prescription.

additional sources of CP violation beyond the CKM phase, the time-integrated branching ratio can be written as

$$\overline{\mathcal{B}}(B_q^0 \to \ell^+\ell^-) \;=\; \overline{\mathcal{B}}(B_q^0 \to \ell^+\ell^-)_{\rm SM}\,\left\{|P|^2 + \left(1 - \frac{\Delta\Gamma_q}{\Gamma_L^q}\right)\,|S|^2\right\}\,, \tag{6.4.25}$$

where

$$P \equiv \frac{C_{10}}{C_{10}^{\rm SM}} + \frac{M_{B_q}^2}{2M_W^2}\left(\frac{m_b}{m_b+m_q}\right)\,\frac{C_P - C_P^{\rm SM}}{C_{10}^{\rm SM}}\,, \tag{6.4.26}$$

$$S \equiv \sqrt{1-\frac{4m_\ell^2}{M_{B_q}^2}}\,\frac{M_{B_q}^2}{2M_W^2}\left(\frac{m_b}{m_b+m_q}\right)\,\frac{C_S - C_S^{\rm SM}}{C_{10}^{\rm SM}}\,. \tag{6.4.27}$$

Complete analytical expressions for C_{10}, C_P and C_S are given in Ref. [118]. In the CP-conserving limit, they depend on ten A2HDM parameters: 3 Yukawa alignment factors $(\varsigma_u, \varsigma_d, \varsigma_\ell)$, 3 scalar masses $(M_H, M_A, M_{H^\pm})$, 2 scalar potential couplings (λ_3, λ_7), the mixing angle $\tilde{\alpha}$ and the misalignment coefficient $\mathcal{C}_d(M_W)$.

The only new-physics contribution to C_{10} comes from Z-penguin diagrams (Z exchange between the leptonic current and an effective $\bar{q}bZ$ vertex generated through one-loop diagrams with internal $H^\pm$ propagators):

$$\Delta C_{10}^{\rm A2HDM} \;=\; |\varsigma_u|^2\,\frac{x_t^2}{8}\,\left[\frac{1}{x_{H^+}-x_t} + \frac{x_{H^+}}{(x_{H^+}-x_t)^2}\,(\ln x_t - \ln x_{H^+})\right]\,. \tag{6.4.28}$$

It only depends on $|\varsigma_u|^2$ and the mass ratios $x_t \equiv m_t^2/M_W^2$ and $x_{H^+} \equiv M_{H^\pm}^2/M_W^2$.

The neutral scalar exchanges contribute to the scalar and pseudo-scalar Wilson coefficients. In the CP-conserving limit:

$$\begin{aligned}
\Delta C_S^{\varphi_i^0,\,\rm A2HDM} \;=\;& \frac{x_t}{2x_h}\,(c_{\tilde{\alpha}} + s_{\tilde{\alpha}}\,\varsigma_\ell)\,\left\{s_{\tilde{\alpha}}\,(\varsigma_u-\varsigma_d)\,(1+\varsigma_u\,\varsigma_d)\,\mathcal{C}_d(M_W)\right. \\
&\left. + (c_{\tilde{\alpha}}\,\lambda_3 + s_{\tilde{\alpha}}\,\lambda_7)\,\frac{2v^2}{M_W^2}\,g_0 \,+ c_{\tilde{\alpha}}\,g_1^{(a)} + s_{\tilde{\alpha}}\,g_2^{(a)}\right\} \\
+\;& \frac{x_t}{2x_H}\,(c_{\tilde{\alpha}}\,\varsigma_\ell - s_{\tilde{\alpha}})\,\left\{c_{\tilde{\alpha}}\,(\varsigma_u-\varsigma_d)\,(1+\varsigma_u\,\varsigma_d)\,\mathcal{C}_d(M_W)\right. \\
&\left. - (s_{\tilde{\alpha}}\,\lambda_3 - c_{\tilde{\alpha}}\,\lambda_7)\,\frac{2v^2}{M_W^2}\,g_0 \,- s_{\tilde{\alpha}}\,g_1^{(a)} + c_{\tilde{\alpha}}\,g_2^{(a)}\right\},
\end{aligned} \tag{6.4.29}$$

$$\Delta C_P^{\varphi_i^0,\,\rm A2HDM} \;=\; -\varsigma_\ell\,\frac{x_t}{2x_A}\,\left[(\varsigma_u-\varsigma_d)\,(1+\varsigma_u\,\varsigma_d)\,\mathcal{C}_d(M_W) + g_3^{(a)}\right]\,, \tag{6.4.30}$$

where $c_{\tilde{\alpha}} = \cos\tilde{\alpha}$ and $s_{\tilde{\alpha}} = \sin\tilde{\alpha}$ are the scalar mixing factors, and $x_{\varphi_i^0} \equiv M^2_{\varphi_i^0}/M_W^2$ with $\varphi_i^0 = h, H, A$. The functions $g_0(x_t, x_{H^+}, \varsigma_u, \varsigma_d)$ and $g_i^{(a)}(x_t, x_{H^+}, \varsigma_u, \varsigma_d)$ $(i = 1, 2, 3)$ can be found in the Appendix of Ref. [118]. We do not reproduce them here to avoid reiterating lengthy formulae. There are, in addition, box-diagram contributions to $C_{S,P}$ and Z-penguin contributions to C_P, which only depend on the three alignment parameters ς_f and the mass ratios x_t and x_{H^+}; their explicit expressions are also given in Ref. [118].[2] The SM Higgs-exchange contribution can be easily recovered from Eq. (6.4.29) by taking the appropriate limit: $\varsigma_f, s_{\tilde{\alpha}}, \lambda_{3,7} \to 0$, $x_{H,H^+} \to \infty$.

Once constrained in the range $\cos\tilde{\alpha} \in [0.9, 1]$, the mixing angle has a very marginal impact on the predictions. Therefore, we will choose $\cos\tilde{\alpha} = 0.95$ to simplify the numerical analysis. Since the results are not very sensitive either to the scalar potential parameters, we will also set $\lambda_3 = \lambda_7 = 1$.[3] The current (95% CL) experimental constraints on $\mathcal{C}_d(M_W)$ are displayed in Figs. 6.3, 6.4 and 6.5, for different choices of the remaining free parameters. The left and right panels on these three figures correspond to $\varsigma_\ell = 0$ and $\varsigma_\ell = 30$, respectively. Fig. 6.3 exhibits the correlated constraints on the plane $\mathcal{C}_d(M_W)$, ς_d, taking $\varsigma_u = 0$. Fig. 6.4 shows the constraints on $\mathcal{C}_d(M_W)$ and ς_u, taking $\varsigma_d = 0$, while a large value $\varsigma_d = 50$ is adopted in Fig. 6.5. Different assumptions on the scalar mass spectrum are analysed in all these figures.

The plots take also into account the constraints enforced by the weak radiative decay $\bar{B} \to X_s\gamma$ [112, 121, 122, 173–176], which drastically reduce the allowed parameter space, specially for large values of $\varsigma_u^*\varsigma_d$. The Wilson coefficients that are relevant for this process take the form $C_i^{\rm eff} = C_{i,\rm SM} + |\varsigma_u|^2 C_{i,uu} - (\varsigma_u^*\varsigma_d) C_{i,ud}$, where $C_{i,uu}$ and $C_{i,ud}$ contain the dominant A2HDM contributions from virtual top and $H^\pm$ propagators [112]. The combined result is very sensitive to the ratio ς_d/ς_u, implying a correlated constraint on ς_d, ς_u and $M_{H^\pm}$ that becomes very strong for real values of the alignment parameters. This

[2] All gauge-dependent terms have been removed from (6.4.29) and (6.4.30) since they must be combined with boxes and Z-penguin diagrams to get gauge-independent results. See Ref. [118] for details.

[3] By varying $\lambda_{3,7}$ in the perturbative allowed region the ratio $\frac{\mathrm{Br}(B_s^0 \to \mu^+\mu^-)}{\mathrm{Br}(B_s^0 \to \mu^+\mu^-)_{\rm SM}}$ varies in less than a 1%.

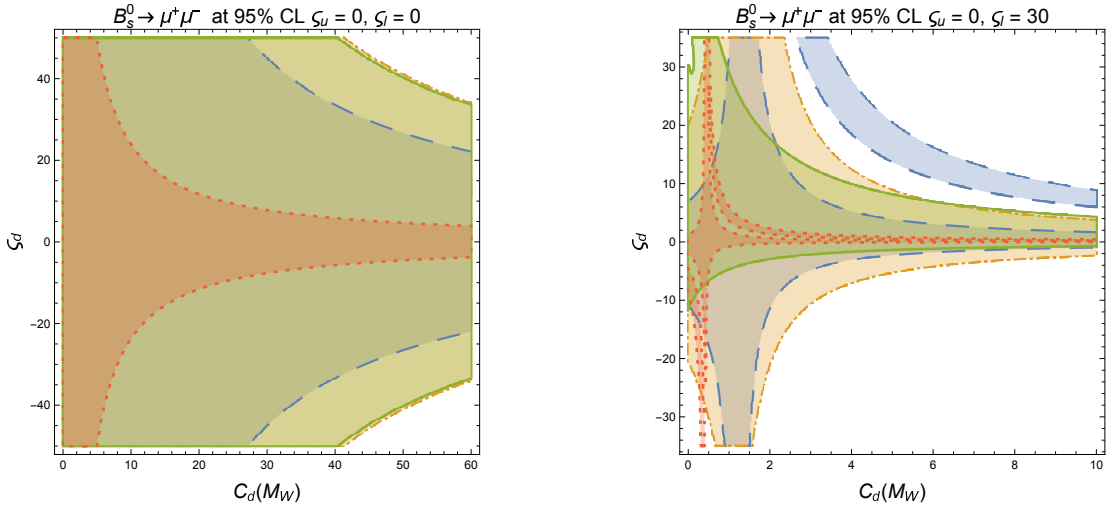

Figure 6.3: $B_s^0 \to \mu^+\mu^-$ constraints on $\mathcal{C}_d(M_W)$ and ς_d, in the CP-conserving limit, for $\lambda_3 = \lambda_7 = 1$, $c_{\tilde{\alpha}} = 0.95$ and $\varsigma_u = 0$, with $\varsigma_l = 0$ (left) and $\varsigma_l = 30$ (right). The coloured areas show the allowed regions (95% CL) for different mass configurations defined in Eq. (6.3.20): A (red, dotted), B (green, solid line), C (blue, dashed) and D (orange, dot-dashed).

constraint may be relaxed by including a (CP-violating) relative phase between ς_d and ς_u [112, 121, 122].

The following generic conclusions can be extracted:

- Since the misalignment contribution is proportional to $(\varsigma_u - \varsigma_d)(1 + \varsigma_u\varsigma_d)$, there are no constraints on $C_d(M_W)$ at $\varsigma_u = \varsigma_d$ or $\varsigma_u = -1/\varsigma_d$. These specific values of the alignment parameters correspond to models with natural flavour conservation, where $\mathcal{L}_{\text{FCNC}} = 0$.

- The comparison of the left and right panels shows the importance of the terms proportional to ς_ℓ. At $\varsigma_\ell = 0$ many A2HDM contributions are eliminated: all box corrections with $H^\pm$ exchanges vanish in this limit and all diagrams mediated through non-SM scalars are removed, up to small mixing effects proportional to $s_{\tilde{\alpha}}$; only the Z-penguin and the SM Higgs-exchange diagrams survive. $\Delta C_P^{\varphi_i^0,\,\text{A2HDM}}$ vanishes

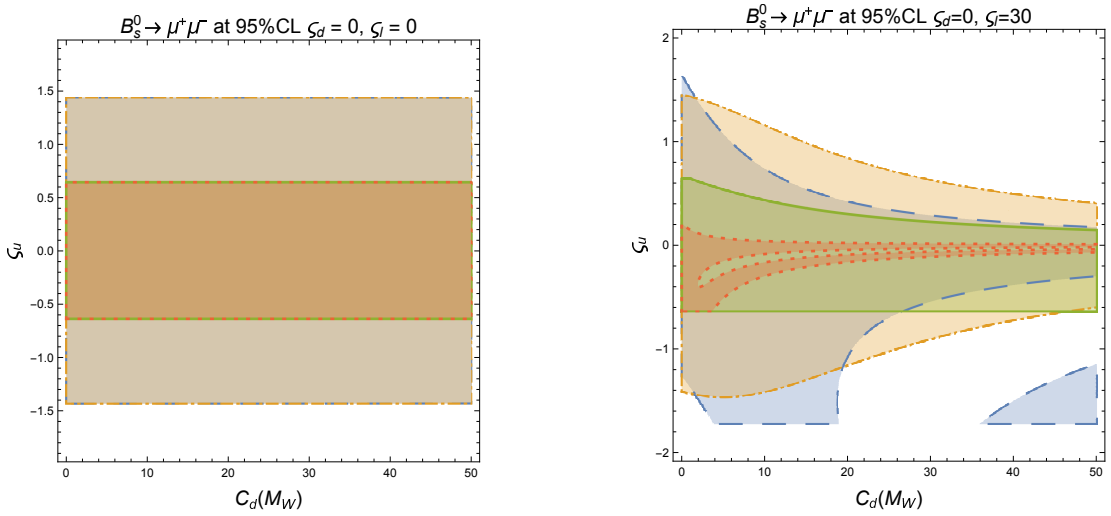

Figure 6.4: $B_s^0 \to \mu^+\mu^-$ constraints (95% CL) on $\mathcal{C}_d(M_W)$ and ς_u, in the CP-conserving limit, for $\lambda_3 = \lambda_7 = 1$, $c_{\tilde{\alpha}} = 0.95$ and $\varsigma_d = 0$, with $\varsigma_l = 0$ (left) and $\varsigma_l = 30$ (right). Same colour coding than Fig. 6.3.

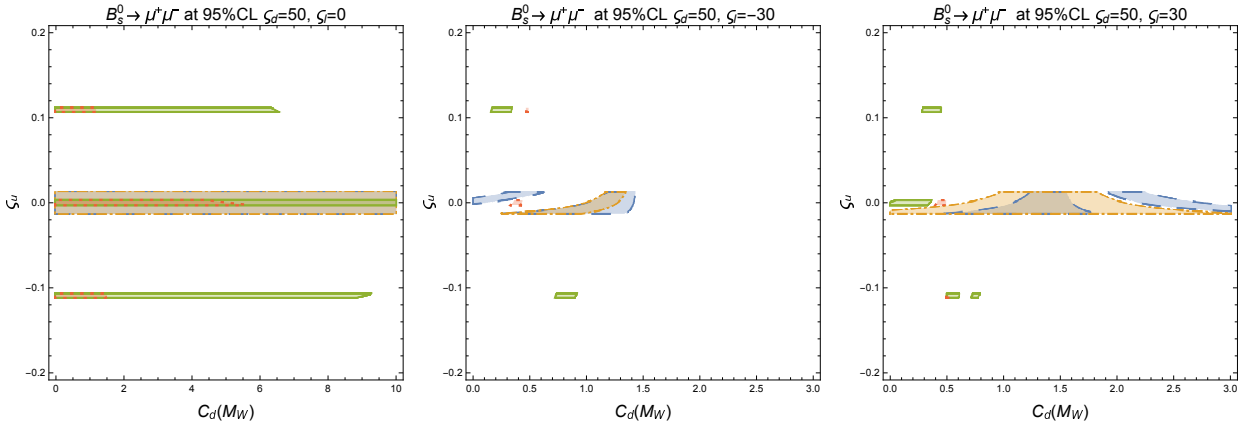

Figure 6.5: $B_s^0 \to \mu^+\mu^-$ constraints (95% CL) on $\mathcal{C}_d(M_W)$ and ς_u, in the CP-conserving limit, for $\lambda_3 = \lambda_7 = 1$, $c_{\tilde{\alpha}} = 0.95$ and $\varsigma_d = 50$, with $\varsigma_l = 0$ (left), $\varsigma_l = -30$ (middle) and $\varsigma_l = +30$ (right) . Same colour coding than Fig. 6.3.

identically at $\varsigma_\ell = 0$, while the misalignment contribution to C_S is proportional to $c_{\tilde{\alpha}} s_{\tilde{\alpha}}(x_H - x_h)$, disappearing when the mixing angle or the neutral mass splitting

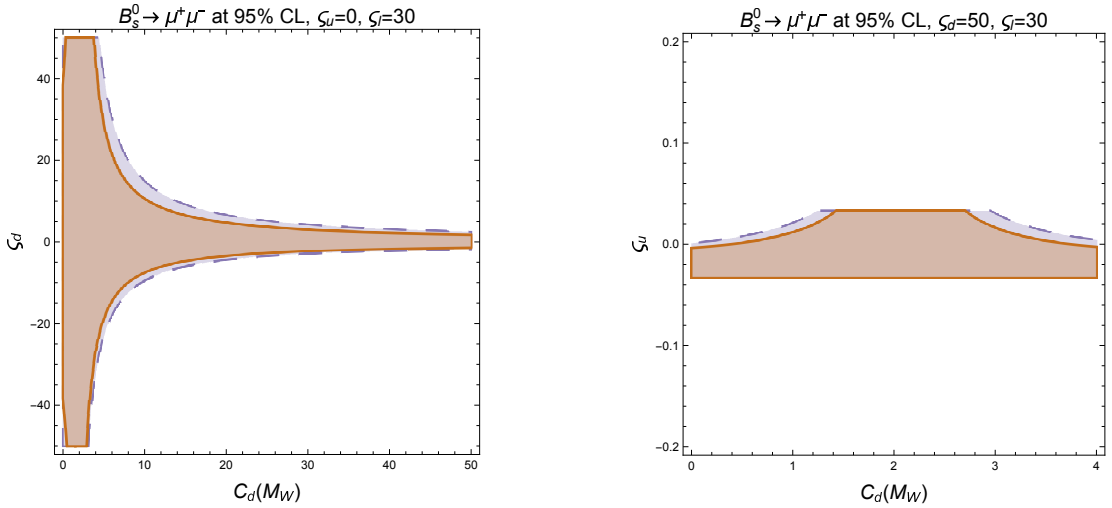

Figure 6.6: The left (right) panels show the $B_s^0 \to \mu^+\mu^-$ constraints (95% CL) on $\mathcal{C}_d(M_W)$ and ς_d (ς_u), in the CP-conserving limit, for $\lambda_3 = \lambda_7 = 1$, $c_{\tilde{\alpha}} = 0.95$ and $\varsigma_l = 30$, with $\varsigma_u = 0$ ($\varsigma_d = 50$) and the two heavy-mass configurations in Eq. (6.3.20): E (orange, solid line) and F (violet, dashed).

approach zero. Therefore, if $\varsigma_\ell = 0$, no constraints on $\mathcal{C}_d(M_W)$ can be set at $c_{\tilde{\alpha}} = 1$ or when $M_H = M_h$.

- When $\varsigma_u = 0$, there are no charged-scalar contributions to $\bar{B} \to X_s\gamma$. Therefore the constraints displayed in Fig. 6.3 and the left panel of Fig. 6.6 fully originate from the decay $B_s^0 \to \mu^+\mu^-$. Moreover, $\Delta C_{10}^{\text{A2HDM}} \propto |\varsigma_u|^2 = 0$, and the Z-penguin A2HDM correction to C_P is also zero. The misalignment contributions to $C_{S,P}$ are proportional in this case to $\varsigma_d\, C_d(M_W)$, which explains the $C_d(M_W) \lesssim 1/\varsigma_d$ scaling exhibited in Figs. 6.3 and 6.6 (left). If additionally $\varsigma_\ell = \varsigma_u = 0$, the only non-zero scalar contributions are $\Delta C_S^{h,\text{A2HDM}}$ and $\Delta C_S^{H,\text{A2HDM}}$, which are obviously independent of M_A and generate the strong dependence on M_H, roughly scaling as $1/M_H^2$, displayed on Fig. 6.3 (left). The right panel in Fig. 6.3 shows that much stronger constraints are obtained with $\varsigma_\ell \neq 0$. The allowed regions obviously expand with increasing scalar masses. Notice, however, how the configurations A (red) and

C (blue), with $M_A < M_{H^\pm}$, generate additional allowed bands, not present for B (green) and D (orange), which originate in the interference of $\Delta C_P^{A,\mathrm{A2HDM}}$ with box-diagram contributions to C_P proportional to the product $\varsigma_\ell \varsigma_d$.

- For small values of $|\varsigma_{d,\ell}| \leq |\varsigma_u|$, the one-loop contributions to $C_{S,P}$ are negligible compared to $\Delta C_{10}^{\mathrm{A2HDM}} \propto |\varsigma_u|^2$. The measured rate $\overline{\mathcal{B}}(B_q^0 \to \mu^+\mu^-)$ provides then an upper bound on $|\varsigma_u|$ that is stronger than the one extracted from $Z \to b\bar{b}$ and only depends on $M_{H^\pm}$ [118]. As shown in the left panel of Fig. 6.4, this limit (identical for configurations A and B, and also for C and D) is independent on $\mathcal{C}_d(M_W)$. For very large values of $\mathcal{C}_d(M_W)$, such that the misalignment contribution $\sim \varsigma_u\, \mathcal{C}_d(M_W)$ could be sizeable, the upper bound on $|\varsigma_u|$ would obviously become stronger.

- At large values of ς_ℓ, the misalignment contribution to $C_{S,P}$ increases proportionally to ς_ℓ. This needs to be compensated with smaller values of both ς_u and ς_d, in order to satisfy the $\overline{\mathcal{B}}(B_q^0 \to \mu^+\mu^-)$ constraint. Thus, sizeable values of $\mathcal{C}_d(M_W)$ imply very small quark alignment parameters. The figures show, however, that this can be avoided at very specific values of $\mathcal{C}_d(M_W)$ where the misalignment and loop contributions cancel.

- The restrictions imposed by $\bar{B} \to X_s\gamma$ can completely dominate over constraints coming from $B_s^0 \to \mu^+\mu^-$ at large values of ς_d. This is reflected in the horizontal bands in the left panel of Fig. 6.5. The $B_s^0 \to \mu^+\mu^-$ data puts nevertheless a limit on $|C_d(M_W)|$ for non-zero values of ς_u. Allowing also for large values of $|\varsigma_\ell|$, the combined constraints from $\bar{B} \to X_s\gamma$ and $B_s^0 \to \mu^+\mu^-$ become very stringent, as shown in the middle and right panels of Fig. 6.5, which also illustrate the impact of the $\varsigma_d\varsigma_\ell$ sign.

- When the scalar masses are increased, the new-physics contributions gradually decouple and the allowed regions become larger. This is shown in Fig. 6.6, taking $\varsigma_\ell = 30$ and two different mass configurations: E ($M_{H^\pm} = M_A = 10^3$ GeV, $M_H = 500$ GeV; orange) and F ($M_{H^\pm} = M_H = M_A = 10^3$ GeV; violet). Taking

$M_{H^\pm} = M_H = 10^3$ GeV and $M_A = 500$ GeV gives results similar to the E configuration. The left (right) panel show the constraints on $C_d(M_W)$ and ς_d (ς_u), for $\varsigma_u = 0$ ($\varsigma_d = 50$). They should be compared with the analogous plots for lighter mass configurations in the right panels of Figs. 6.3 and 6.5.

6.5 Meson mixing

As already commented before, two insertions of $\mathcal{L}_{\rm FCNC}$ are needed in order to generate a misalignment contribution to meson-antimeson mixing. This is a two-loop correction and, therefore, it is expected to be quite small. Nevertheless, previous tree-level analyses of $\mathcal{L}_{\rm FCNC}$ have focused on the $\Delta B = 2$ transition, owing to the high sensitivity of B_q^0–$\bar{B}_q^0$ mixing to new-physics effects,

The one-loop scalar contribution to the neutral meson mixing has been analysed, within the A2HDM, in Refs. [112, 129, 132]. It proceeds through box diagrams with internal $H^\pm$ propagators and provides stringent constraints on $|\varsigma_u|$, which depend on $M_{H^\pm}$. Actually, the B_s^0–$\bar{B}_s^0$ mass difference and the CP-violating ε_K parameter, both provide bounds on $|\varsigma_u|$ which are quite similar to the ones extracted from $Z \to b\bar{b}$ [112]. So far, we did not use this information because we would like to get constraints on $\mathcal{C}_d$, which was not taken into account in those one-loop analyses.

While being a second-order effect, the neutral scalar exchange between two $\mathcal{L}_{\rm FCNC}$ vertices could be of a similar size, or even larger, than the one-loop charged scalar contribution, due to a large $\mathcal{C}_d$ coupling or a very light neutral scalar. However, the fact that the analyses of $\Delta M_{B_q^0}$ and ε_K, without any misalignment contribution, give similar constraints than $Z \to b\bar{b}$ does not seem to favour this possibility. This is also confirmed by our previous study of $B_s^0 \to \mu^+\mu^-$, although the constraints on $\mathcal{C}_d$ obtained there could be avoided for some specific choices of A2HDM parameters (for instance, $\varsigma_\ell = s_{\tilde{\alpha}} = 0$).

The (one-loop) charged-current and (tree-level) misalignment contributions to B_q^0–$\bar{B}_q^0$ mixing are roughly proportional to the factors

$$\omega_{\rm CC} \,=\, \frac{1}{16\pi^2}\,\frac{m_t^4}{M_{H^\pm}^2 v^4}\,\left(V_{tq}^* V_{tb}\right)^2\,, \qquad\qquad \omega_{\rm NC} \,=\, \frac{|\mathcal{C}_d(\mu)|^2}{16\pi^4}\,\frac{m_b^2 m_t^4}{M_{\varphi_k^0}^2 v^6}\,\left(V_{tq}^* V_{tb}\right)^2\,. \tag{6.5.31}$$

Their relative size scales approximately as $\omega_{\rm NC}/\omega_{\rm CC} = |\mathcal{C}_d(\mu)|^2 m_b^2 M_{H^\pm}^2/(M_{\varphi_k^0}^2 v^2\pi^2)$. In order to have a ratio $\omega_{\rm NC}/\omega_{\rm CC}\sim\mathcal{O}(1)$, one needs $|\mathcal{C}_d(\mu)|M_{H^\pm}/M_{\varphi_k^0}\sim\mathcal{O}(10^2)$. A proper calculation of the misalignment effects would require in any case the inclusion of two-loop diagrams in order to cancel the renormalization-scale dependence of $\mathcal{C}_d(\mu)$.[4]

To estimate the possible size of the misalignment correction, we will consider the tree-level scalar exchange in Fig. 6.2 (right), taking $\mu = M_W$ to normalize the coupling $\mathcal{C}_d$. It contributes to the effective low-energy Hamiltonian,

$$\mathcal{H}_{\rm eff} \,\supset\, \sum_{i,j=d,s,b} \left\{ C_{1,ij}^{SRR}\,\mathcal{O}_{1,ij}^{SRR} + C_{1,ij}^{SLL}\,\mathcal{O}_{1,ij}^{SLL} + C_{2,ij}^{LR}\,\mathcal{O}_{2,ij}^{LR} \right\}\,, \tag{6.5.32}$$

generating $\Delta S = 2$ and $\Delta B = 2$ transitions through the four-quark operators

$$\mathcal{O}_{1,ij}^{SRR} \,=\, (\bar{d}_{iL} d_{jR})(\bar{d}_{iL} d_{jR})\,, \quad \mathcal{O}_{1,ij}^{SLL} \,=\, (\bar{d}_{iR} d_{jL})(\bar{d}_{iR} d_{jL})\,, \quad \mathcal{O}_{2,ij}^{LR} \,=\, (\bar{d}_{iR} d_{jL})(\bar{d}_{iL} d_{jR})\,, \tag{6.5.33}$$

with

$$C_{1,ij}^{SRR} \,=\, \frac{g_{ij}^2}{16\pi^4 v^6}\,\sum_{k=1}^3 E_k^2\,, \qquad C_{1,ij}^{SLL} \,=\, \frac{g_{ji}^{*2}}{16\pi^4 v^6}\,\sum_{k=1}^3 E_k^{*2}\,, \qquad C_{2,ij}^{LR} \,=\, \frac{g_{ij} g_{ji}^*}{8\pi^4 v^6}\,\sum_{k=1}^3 |E_k|^2\,. \tag{6.5.34}$$

To simplify the numerical analysis, we have split the Wilson coefficients into a global constant that reabsorbs all A2HDM parameters,

$$E_k \,\equiv\, \mathcal{C}_d(M_W)(\varsigma_d - \varsigma_u)(1+\varsigma_d\varsigma_u^*)\,\frac{1}{M_{\varphi_k^0}}\,\left(\mathcal{R}_{k2} + i\,\mathcal{R}_{k3}\right)\,, \tag{6.5.35}$$

[4] In the absence of a complete two-loop computation, one could extract effective μ-independent $\varphi_k^0\bar{q}b$ vertices from the $B_q^0\to\ell^+\ell^-$ computation presented in Ref. [118]. However, they would still contain small gauge dependences.

and a flavour structure which is fully determined by the quark masses and mixings,

$$g_{ij} \equiv \left(V_{\rm CKM}^\dagger M_u M_u^\dagger V_{\rm CKM} M_d\right)_{ij} . \tag{6.5.36}$$

Neglecting any additional source of CP violation beyond the CKM phase, E_1 and E_2 are real, while E_3 is imaginary; this implies different relative signs for the CP-even and CP-odd scalar contributions to $C_{1,ij}^{SRR}$ and $C_{1,ij}^{SLL}$, while they enter with the same sign in $C_{2,ij}^{LR}$.

In our phenomenological analysis we have also included the full one-loop charged-current contribution [112,129,132], which is obviously μ-independent. The hadronic matrix elements of the $\Delta F = 2$ four-quark operators (6.5.33) are detailed in appendix D. The most restrictive limits are obtained from B_s^0–$\bar{B}_s^0$ mixing (slightly weaker bounds result from B_d^0–$\bar{B}_d^0$ mixing and ε_K), taking always into account the correlated restrictions from $\bar{B} \to X_s\gamma$. The measured mass difference in the B_s^0–$\bar{B}_s^0$ system imposes stringent constraints on ς_u, ς_d and $M_{H^\pm}$, originating in the one-loop contributions, but the sensitivity to the misalignment parameter is quite small, except at very large values of $|\varsigma_d|$. This is illustrated in Fig. 6.7 which shows two different parametric configurations, $\varsigma_d = 50$ (left) and $\varsigma_u = 0.5$ (right). In both cases one observes horizontal lines, exhibiting the low sensitivity to $C_d(M_W)$. Nevertheless, a bound on $C_d(M_W)$ finally emerges when $\varsigma_d\, C_d(M_W)$ is large enough to generate a sizeable misalignment effect. The panels display the same mass configurations analysed in the previous section (C and D give here equivalent results). Obviously, the sensitivity to $C_d(M_W)$ is larger for low scalar masses (configurations A and B).

The $\Delta B = 2$ amplitudes are independent of the leptonic alignment parameter ς_ℓ. Therefore, the constraints extracted from the B_s^0–$\bar{B}_s^0$ mixing may become relevant at small values of ς_ℓ where the $B_s^0 \to \ell^+\ell^-$ limits are somewhat weaker. In Fig. 6.8, we display the B_s^0–$\bar{B}_s^0$ mixing constraints obtained for $\varsigma_u = 0$ (left) and $\varsigma_d = 0$ (right), to be compared with Figs. 6.3 and 6.4, respectively. The left panel shows indeed that at $\varsigma_u = \varsigma_\ell = 0$ (the one-loop charged contributions to the mixing are proportional to ς_u and are thus zero) the mixing constraints on $C_d(M_W)$ are stronger than the limits from $B_s^0 \to \ell^+\ell^-$. This may be related to the much better experimental relative error on $\Delta m_{B_s^0}$ (0.1%), compared with

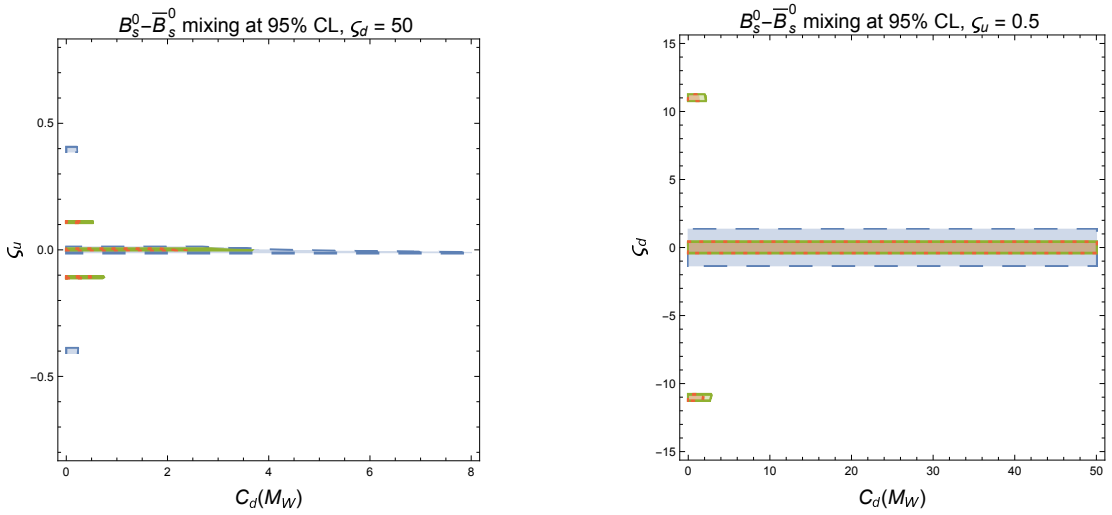

Figure 6.7: The left (right) panels show the B_s^0–$\bar{B}_s^0$ mixing constraints on $C_d(M_W)$ and ς_u (ς_d) for a fixed value of $\varsigma_d = 50$ ($\varsigma_u = 0.5$), in the CP-conserving limit and with different mass configurations: A (red, dotted), B (green, solid line) and C/D (blue, dashed).

the present 21.7% of the measured $B_s^0 \to \mu^+\mu^-$ branching fraction. At $\varsigma_d = 0$, however, the previous constraints on Fig. 6.4 are stronger. The dominant one-loop contribution to $B_s^0 \to \mu^+\mu^-$ originates then in $\Delta C_{10}^{\text{A2HDM}} \propto |\varsigma_u|^2$ that puts a quite stringent limit on $|\varsigma_u|$. With $\varsigma_d = 0$ and ς_u small, the B_s^0–$\bar{B}_s^0$ mixing amplitude becomes insensitive to $C_d(M_W)$, while $B_s^0 \to \mu^+\mu^-$ can still constrain this parameter at large values of ς_ℓ.

6.6 Summary

The simplicity and versatility of multi-Higgs-doublet models make them favourable candidates for building alternative scenarios of EWSB with extended scalar sectors. The physical spectrum of these models contains a rich variety of bosonic states, with $N-1$ charged and $2N-1$ neutral scalars. The neutral scalar fields can, in general, couple to fermions through non-diagonal flavour interactions, generating unwanted FCNC transitions at tree level that need to be strongly suppressed in order to satisfy the stringent experimental constraints.

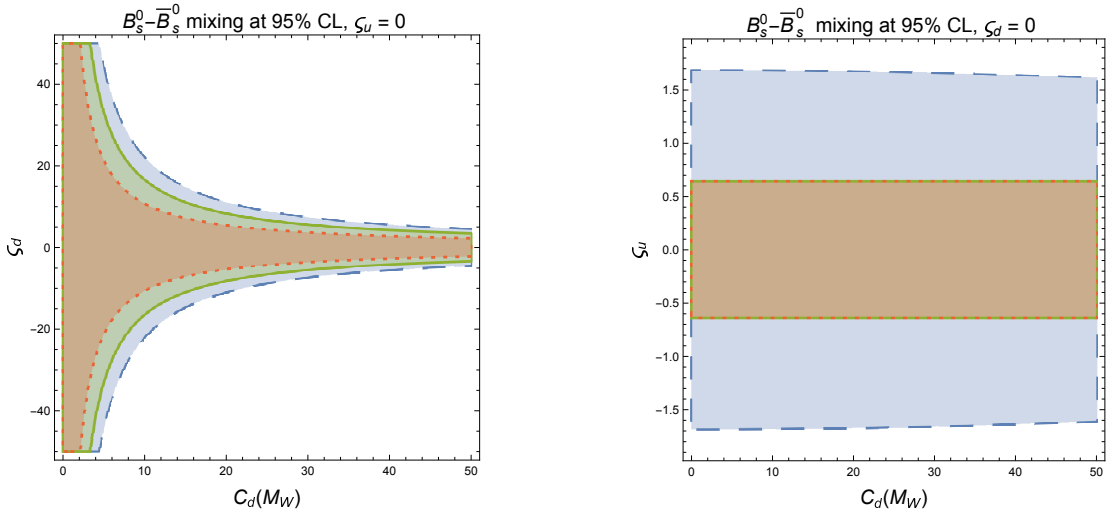

Figure 6.8: The left (right) panels show the B_s^0–$\bar{B}_s^0$ mixing constraints on $C_d(M_W)$ and ς_d (ς_u) for a fixed value of $\varsigma_u = 0$ ($\varsigma_d = 0$), in the CP-conserving limit and with different mass configurations: A (red, dotted), B (green, solid line) and C/D (blue, dashed).

One could force these FCNC effects to be unobservable through very small Yukawa couplings or very large scalar masses, making these models irrelevant for present experiments. A more interesting possibility, allowing for new scalar particles not too far from the electroweak scale, is a highly non-generic set of Yukawa couplings. The huge $SU(3)^5$ flavour symmetry of the electroweak Lagrangian is only broken by the Yukawa interactions, but the data clearly indicate that this symmetry breaking only occurs along very specific directions in the flavour space [114, 115].

As we saw in Chapter 2 the simplest way to avoid tree-level FCNCs is minimizing drastically the number of flavour couplings, imposing most of them to be zero. Usually, only one scalar doublet is allowed to have Yukawa interactions with a given type of right-handed fermion, fixing in this way a unique flavour-breaking structure associated with each f'_R field. Since this requirement can be always imposed through discrete $\mathcal{Z}_2^d \otimes \mathcal{Z}_2^u \otimes \mathcal{Z}_2^\ell$ symmetries, the resulting flavour configuration is stable under quantum corrections, leading to the so-called models with natural flavour conservation [107, 108]. With $N > 3$

Higgs doublets, this type of models necessarily involves a minimum of $N-3$ scalar doublets that are decoupled from the fermion sector.

The more general assumption of flavour alignment [24,25] is based on the simultaneous diagonalization of all the Yukawa matrices in the fermion-mass eigenstate basis. This implies the appearance of $3(N-1)$ alignment factors, which in the most general case are 3×3 complex diagonal matrices. In the absence of a specific symmetry protection, the resulting flavour structure is unstable under quantum corrections, which misalign the different Yukawa matrices. Nevertheless, the induced misalignment is a quite small effect, thanks to the residual flavour symmetries of the aligned multi-Higgs Lagrangian, which tightly constrain the type of FCNC operators that can be generated at higher orders.

In this chapter, we have studied the misalignment local structure $\mathcal{L}_{\rm FCNC}$ induced at one loop, for the most generic aligned multi-Higgs Lagrangian, using the known RGEs of these models. We have particularized the result to different scenarios of phenomenological relevance and have discussed in detail the role of the underlying flavour-dependent phase symmetries. While the misalignment is a very small effect, being suppressed by at least two insertions of the CKM matrix, three Yukawa couplings and the one-loop $1/(4\pi)^2$ factor, it could still lead to interesting phenomenological effects through $V_{tb}V_{ts}^* m_t^2 m_b$ contributions to effective $\varphi_k^0 \bar{s}_L b_R$ vertices.

We have investigated the current constraints on the misalignment parameter $C_d(M_W)$, emerging from the measured $B_s^0\to\ell^+\ell^-$ branching fraction and B_s^0–$\bar{B}_s^0$ mixing, taking into account the strong correlated limits on ς_u, ς_d and $M_{H^\pm}$ from $\bar{B}\to X_s\gamma$. These FCNC transitions receive non-local one-loop contributions with internal top and $H^\pm$ propagators [112, 118] that dominate in large regions of the parameter space and were neglected in previous phenomenological studies of the flavour misalignment [116, 117, 120]. The local misalignment Lagrangian $\mathcal{L}_{\rm FCNC}$ contributes to these processes through tree-level neutral scalar exchange. For $B_s^0\to\ell^+\ell^-$, where only one insertion of $\mathcal{L}_{\rm FCNC}$ is needed, this contribution is actually needed to renormalize the effective $\varphi_k^0\bar{s}_L b_R$ vertex and, therefore, appears at the one-loop level. The contribution to B_s^0–$\bar{B}_s^0$ mixing involves, however, two insertions of $\mathcal{L}_{\rm FCNC}$; it is a two-loop effect that should be considered together with two-loop

diagrams involving two one-loop effective $\varphi_k^0 \bar{s}_L b_R$ vertices. We have nevertheless analysed whether the neutral-scalar-exchange amplitude could lead to relevant phenomenological signals through very large values of $C_d(M_W)$.

The present phenomenological constraints on $C_d(M_W)$ are shown in Figs. 6.3 to 6.8, with different choices of $\varsigma_{u,d,\ell}$ and several benchmark configurations for the scalar mass spectrum. To simplify the analysis we have assumed the absence of any CP-violation effects beyond the usual CKM phase. While stringent bounds emerge on the alignment parameters $\varsigma_{u,d,\ell}$, the sensitivity to $C_d(M_W)$ is very small, as expected, exhibiting the strong phenomenological suppression of the misalignment. The local $\mathcal{L}_{\text{FCNC}}$ contribution is proportional to the product $(\varsigma_u - \varsigma_d)(1 + \varsigma_u\varsigma_d)C_d(M_W)$, which explains the pattern displayed by the obtained constraints. Only at large values of ς_d and/or ς_ℓ ($|\varsigma_u|$ is bounded to be small) one obtains a somewhat enhanced misalignment contribution that can result in useful limits on $C_d(M_W)$.

The hypothesis of flavour alignment at a very high scale $\mu = \Lambda_A$, *i.e.*, $C_{d,u}(\Lambda_A) = 0$, survives the phenomenological limits in all cases. With $\Lambda_A \leq M_{\text{Planck}} \sim 10^{19}$ GeV, it implies $\mathcal{C}_{d,u}(M_W) = \log \frac{\Lambda_A}{M_W} \leq 40$, which can easily satisfy all present constraints. This simple relation between $\mathcal{C}_{d,u}(M_W)$ and Λ_A has been obtained at the lowest perturbative order. For very large values of the Yukawa couplings and $\Lambda_A \gg M_W$, the long running between the scales Λ_A and M_W makes necessary to perform a resummation of large logarithmic corrections, through a numerical solution of the RGEs [116, 117, 120] that can modify the high-scale relation by a factor of $\mathcal{O}(1)$. While this slightly changes the scale Λ_A associated with a given value of $C_{d,u}(M_W)$, it does not modify our conclusion that high-scale alignment is compatible with all known experimental constraints.

Our phenomenological analyses have been restricted to the simplest case of the A2HDM. Since this is the most constrained scenario of multi-Higgs flavour alignment (the one with the smallest number of free parameters), our conclusion is obviously also valid for more generic situations with $N > 2$ Higgs doublets and/or generalized alignment structures.

Chapter 7

Global fits in the Aligned Two-Higgs-doublet model

The NHDM and the particular case of the A2HDM were introduced in Chapter 2.

Constraints on the 2HDM parameters have been widely studied, taking into account recent LHC data [123,124,140,177–195], together with other requirements from flavour and LEP physics, and theoretical considerations. However these analyses normally considered specific 2HDM models with $\mathcal{Z}_2$ symmetries [182, 190, 194, 196–201]. In this work we have performed a global fit to the relevant experimental and theoretical constraints in the most general CP-conserving model which preserves tree-level flavour alignment, the A2HDM [24, 25]. The fits have been performed using the `HEPfit` code described in Chapter 5.

This chapter is organized as follows. In Section 7.1 the fit set up and the constraints considered are explained. Results of assuming the observed 125 GeV Higgs is the lightest (heaviest) CP-even scalar of the model are presented in Section 7.2 (Section 7.3). These two possibilities will be referred as the *light scenario* and *heavy scenario*. We present a summary of the work in Section 7.4.

7.1 Fit constraints

For our analysis we assume the CP-conserving limit, so both the parameters of the potential of Eq. (2.1.39) and the alignment parameters of Eq. (2.1.36) are real. The parameter space of the A2HDM is then characterized by twelve real quantities: the three alignment parameters and nine degrees of freedom in the scalar potential which we choose to be v, the four scalar masses, the CP-even mixing angle $\tilde{\alpha}$ and the quartic couplings $\lambda_{5,6,7}$. Two inputs are already empirically determined: the vacuum expectation value and the Higgs mass $m_h = 125.10 \pm 0.14$ GeV [75].[1]

We assume the following priors for the fit parameters in our main Bayesian fit:

$$|\lambda_{5,6,7}| < 10\,, \qquad \tilde{\alpha} \in \left[-\frac{\pi}{2}, \frac{\pi}{2}\right], \qquad M^2_{A,H^\pm} \in [10^2, 1500^2]\,\text{GeV}^2\,.$$

$$\varsigma_u \in [-1.5, 1.5]\,, \qquad \varsigma_d \in [-50, 50]\,, \qquad \varsigma_\ell \in [-100, 100]\,. \tag{7.1.1}$$

The priors of the remaining CP-even scalar mass depend on the scenario studied. *Light (heavy) scenario* refer to the case in which the observed Higgs with a mass around 125 GeV (h) is the lightest (heaviest) CP-even scalar of the model. For the *light scenario*, selected with the boolean flag `SMHiggs` set to `true` the mass priors are of the non-SM Higgs (H),

$$M^2_H \in [125^2, 1500^2]\,\text{GeV}^2\,, \tag{7.1.2}$$

while for the *heavy scenario*, selected with the boolean flag `SMHiggs` set to `false`,

$$M^2_H \in [10^2, 125^2]\,\text{GeV}^2\,. \tag{7.1.3}$$

The scalar masses are chosen in a range such that they are relevant for the future LHC searches. The parameters of the potential λ_i are taken in a conservative range, since larger values are excluded by theoretical constraints. The mixing angle $\tilde{\alpha}$ is varied in its

[1] From now on we denote by h the already discovered Higgs-like boson, and use H for the second CP-even boson, irrespective of their mass ordering.

full range, and the alignment parameters $\varsigma_f\,(f = u, d, \ell)$ are varied in their perturbative range, *i.e.*, $\frac{\sqrt{2}}{v}\varsigma_f m_f \leq 1$.

Bayesian statistics do not provide an unambiguous way to determine the prior distributions. A rule of thumb would be considering as flat priors the ones appearing linearly in our observables. However, for the mass parameters this does not give a unique choice: while direct searches depend linearly on the heavy scalar masses, loop-induced processes appearing in flavour observables and in Higgs signal strengths depend on the masses squared. To avoid a possible bias in the choice of these priors, we have performed fits with two different mass parametrizations. These two choices of mass priors are selected with the boolean flag `use_sq_mass`. If it is set to `true` (`false`) square (linear) mass priors are used. The effect of the choice of mass priors will be commented in the cases of interest. When the choice of the mass priors is irrelevant, square mass priors will be used.

7.1.1 Theoretical constraints

To assure that the scalar potential is bounded from below, one must impose the following positivity constraints on the quartic couplings λ_i [31, 202]:

$$\begin{aligned}&\lambda_1 \geq 0\,, \qquad \lambda_2 \geq 0\,, \qquad \sqrt{\lambda_1\lambda_2} + \lambda_3 \geq 0\,, \qquad \sqrt{\lambda_1\lambda_2} + \lambda_3 + \lambda_4 - |\lambda_5| \geq 0\,,\\ &\frac{1}{2}\left(\lambda_1 + \lambda_2\right) + \lambda_3 + \lambda_4 + \lambda_5 - 2\,|\lambda_6 + \lambda_7| \geq 0\,.\end{aligned} \tag{7.1.4}$$

These necessary conditions restrict the allowed pattern of scalar masses.

By imposing perturbative unitarity of the S-matrix we avoid that a given combination of parameters results in a too large scattering amplitude that violates the unitarity limit at a given perturbative order. Thus, we are actually requiring that the perturbative series does not break down. Here, unitarity is enforced for two-to-two scattering of scalar particles at leading order (LO), [203] using

$$\left(a_j^{(0)}\right)^2 \leq \frac{1}{4}\,, \tag{7.1.5}$$

where $a_j^{(0)}$ are the tree-level contributions to the j partial wave amplitude. For the high-energy scattering of scalars, only the S-wave amplitude ($j = 0$) is relevant at LO. The

corresponding matrix of partial wave amplitudes is given by

$$(\mathbf{a_0})_{i,f} \;=\; \frac{1}{16\pi s}\int_{-s}^{0} dt\; \mathcal{M}_{i\to f}(s,t)\,, \tag{7.1.6}$$

and the a_0 are the eigenvalues of $\mathbf{a_0}$. Again, these conditions are relevant to constrain the scalar potential parameters λ_i.

7.1.2 Electroweak constraints

EWPOs measured at LEP and SLC are used in the analysis. We use best-fit fixed values for the SM inputs M_Z, m_t, α_s and $\Delta\alpha^{(5)}(M_Z)$. The study of the oblique parameters S, T and U [165, 204, 205], which are very sensitive to the scalar mass splittings, is not enough to disentangle the A2HDM contributions because of the presence of additional Z-vertex corrections [206, 207]. The most relevant ones are the quantum corrections to $\Gamma(Z \to b\bar{b})$, which are enhanced by the large top-quark mass [208–210]. We take this into account through a combined fit of EWPOs, excluding the ratio $R_b \equiv \Gamma(Z \to b\bar{b})/\Gamma(Z \to \text{hadrons})$ [210, 211], which updates the analysis of Ref. [212]. The updated results can be seen in Table 7.1.

	Result	**Correlation Matrix**		
S	0.093 ± 0.101	1.00	0.86	-0.54
T	0.111 ± 0.116	0.86	1.00	-0.83
U	-0.016 ± 0.088	-0.54	-0.83	1.00

Table 7.1: Results for the fit of the oblique parameters S, T and U without R_b.

7.1.3 Higgs constraints

The Higgs signal strengths are defined as the ratio of the production cross section σ_i times the branching ratio $\mathcal{B}_f$, over the SM prediction, for a given production channel ($i =$ ggF, VBF, VH, ttH) and decay mode ($f = \bar{b}b$, $\gamma\gamma$, $\mu^+\mu^-$, $\tau^+\tau^-$, WW, $Z\gamma$, ZZ),

$$\mu_i^f = \frac{(\sigma_i \cdot \mathcal{B}_f)_{\text{A2HDM}}}{(\sigma_i \cdot \mathcal{B}_f)_{\text{SM}}} = \frac{r_i \cdot r_f}{\sum_{f'} r_{f'} \cdot \mathcal{B}_{SM}(h \to f')}\,, \tag{7.1.7}$$

where $r_{i,f}$ are the ratios of the production cross section σ_i and decay width Γ_f, respectively, with respect to their SM predictions.

The signal strengths are calculated in the narrow-width approximation and depend on the alignment parameters, the mixing angle $\tilde{\alpha}$ and the scalar potential parameters. The input used contains LHC data (Run I and II) from the ATLAS and CMS collaborations, and data collected by D0 and CDF at the Tevatron. The data entering our fit are detailed in Appendix F (Table F.1).

Information about heavy Higgs searches of ATLAS and CMS, both at Run I and II, is summarized in Tables F.2, F.3, F.4 and F.5, also in Appendix F. The analyses provided are quoted as 95% upper limits, for different production and decay channels, on either $\sigma \cdot \mathcal{B}$ or $(\sigma \cdot \mathcal{B}) \,/\, (\sigma \cdot \mathcal{B})_{\text{SM}}$, as functions of the resonance mass in the narrow width approximation.

7.1.4 Flavour constraints

Since most of the standard CKM fits assume the SM and this would not be consistent with the study of NP, the choice of the CKM parameters is subtle. To avoid inconsistencies, a fit to the CKM entries is performed. V_{ud} is extracted from superallowed ($0^+ \to 0^+$) nuclear β decays [168]. Given the very small value of V_{ub}, this fixes $V_{us} \approx \lambda$ through CKM unitarity. $|V_{ub}|$ and $V_{cb} \approx A\lambda^2$ are obtained by combining exclusive and inclusive measurements of $b \to u\bar{\nu}_\ell\ell$ and $b \to c\bar{\nu}_\ell\ell$ transitions [48]. Finally, the apex $(\bar{\rho}, \bar{\eta})$ of the unitarity triangle is determined with the additional information of the ratio $|V_{td}/V_{ts}|$, extracted from $\Delta M_{B_s}/\Delta M_{B_d}$ [48] that is not sensitive to charged scalar contributions [112].

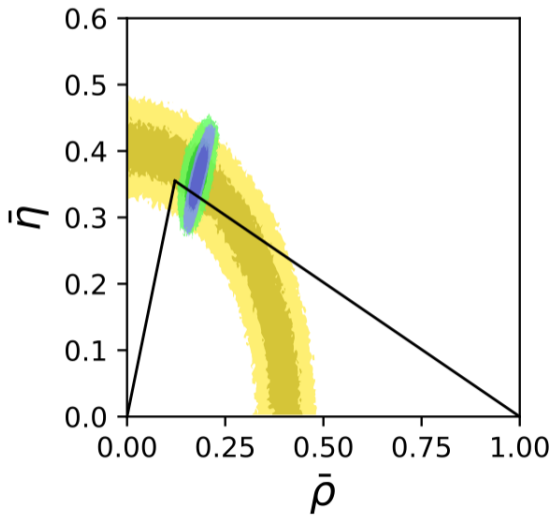

Input	Value
λ	0.2256 ± 0.0009
A	0.829 ± 0.017
$\bar{\rho}$	0.182 ± 0.016
$\rho_{\lambda,A}$	-0.39
$\rho_{\bar{\rho},\bar{\eta}}$	0.82

Figure 7.1 & Table 7.2: Results of the CKM fit. Fitting only tree-level observables, gives the allowed regions in yellow. The green regions include ΔM_{B_d} and ΔM_{B_s}, and the blue regions the ratio V_{td}/V_{ts} from HFLAV [48]. Darker and light colours correspond to 68% and 95.5% probability, respectively. The black triangle is the best fit point from the SM CKM fit to all observables [75].

The CKM inputs obtained in this way and later used in our global fits are summarized in Fig. 7.1 and Table 7.2.

Charged-scalar exchanges contribute to neutral meson mixing through one-loop box diagrams [112, 129, 132]. The corrections induced by virtual top quarks are quite sizeable, specially for $\Delta M_{B_{s,d}}$ and ε_K, and provide strong constraints on $|\varsigma_u|$ (also R_b) as function of $M_{H^\pm}$. The weak radiative decay $B \to X_s\gamma$ [112, 121, 122, 173–176] gives also important correlated constraints on ς_u and ς_d, specially for large values of $|\varsigma_u\varsigma_d|$. The region $\varsigma_u\varsigma_d < 0$ is actually excluded, except for very small values of the alignment parameters [112]. NNLO corrections [213] are quite relevant for this observable and should be taken into account.

A complete one-loop calculation within the A2HDM of the decay $B_s \to \mu^+\mu^-$ was performed in [118, 172]. This observable depends on the $b \to s\mu^+\mu^-$ Wilson coefficients $\mathcal{O}_{10}$, $\mathcal{O}_S$ and $\mathcal{O}_P$. The decay amplitude involves both charged and neutral scalar contribu-

tions, and provides complementary information on the alignment parameters $\varsigma_{u,d,\ell}$ and the scalar masses. It also includes small contributions from higher-order FCNC interactions, needed to reabsorb UV divergences, which are assumed to be negligible here. A study of these effects can be found at [156].

Finally, the muon anomalous magnetic moment, calculated within the A2HDM in Refs. [127, 214], is of interest because it shows a deviation with respect to the SM and strongly constrains the leptonic coupling. Its effects will be commented in Section 7.2.

7.2 Results: *light scenario*

In this section, results of fits in the *light scenario*, assuming the observed SM Higgs is the CP-even lightest scalar of the model, are summarized. The complementary possibility (the observed scalar is the heaviest) will be studied in Section 7.3.

7.2.1 Theoretical constraints

Perturbative unitarity and positivity of the potential set strong limits on the scalar masses and in the quartic parameters of the potential. The mass differences among H, A and $H^{\pm}$ are strongly constrained, as shown in Fig. 7.2,

$$|M_i - M_j| \leq 600 \text{ GeV}, \qquad i,j = H, A, H^{\pm}, \qquad \text{(square mass priors)}. \tag{7.2.8}$$

From these figures, several conclusions can be obtained. First of all, there is a clear correlation between the masses of any two scalar particles: large masses of one scalar will imply that the other scalar is also restricted to be large. This effect is stronger for higher values of the scalar masses. The effect of the mass priors has also been studied, and has a minor effect. While the shape for the mass planes are the same, regions with square priors are slightly larger (see Fig. 7.3).

Theoretical constraints also restrict the allowed ranges of the scalar quartic couplings. Two-dimensional plots of $(\lambda_5, \lambda_6, \lambda_7)$ are shown in the right panel of Fig. 7.2, which displays

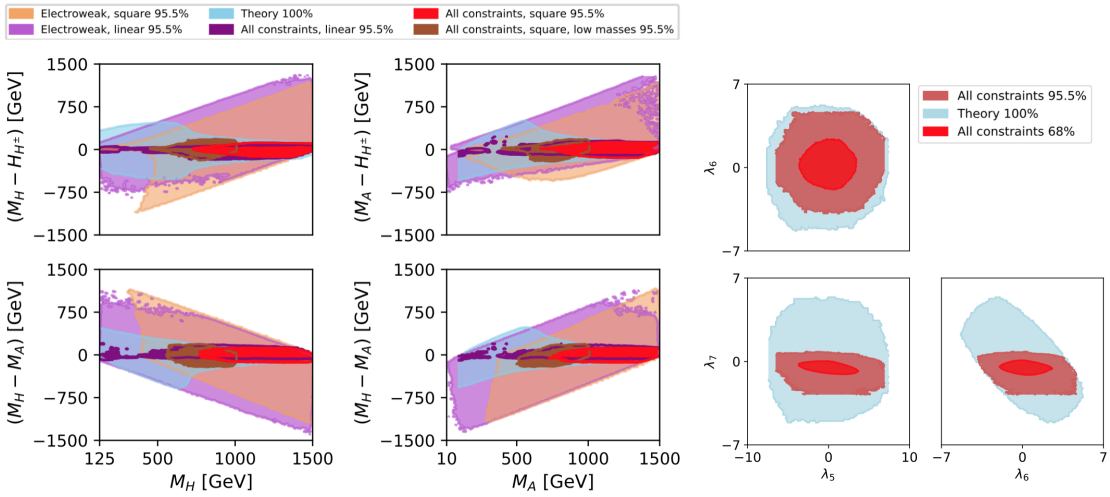

Figure 7.2: **Left panel:** Allowed regions for the scalar mass splittings coming from theoretical constraints at 100% probability (blue), from EWPO at 95.5% probability (in orange, square mass priors and in light purple, linear priors), and combining all constraints at 95.5% probability (linear mass priors in purple, square mass priors in red and square mass priors and lower masses in brown). The "All constraints" contains only the right-sign branch discussed in Section 7.2.5. **Right panel:** Two-dimensional bounds on the λ_5, λ_6 and λ_7 parameters of the potential resulting from imposing theoretical constraints with (blue, 100% probability), and considering all constraints (in brown 95.5% probability, in red 68% probability).

the correlations among the different couplings of the scalar potential. The blue regions in the figure satisfy the bounds derived in previous works [99].

7.2.2 Electroweak constraints

Electroweak precision observables restrict the individual masses of the scalar particles in the low-mass range, and are very useful to constrain their mass splittings. The oblique parameters are very sensitive to the scalar mass differences, which results in strong upper limits for the masses. This can be clearly observed in Figs. 7.4 and 7.7. The EWPOs information complements in a very useful way the theoretical constraints discussed before.

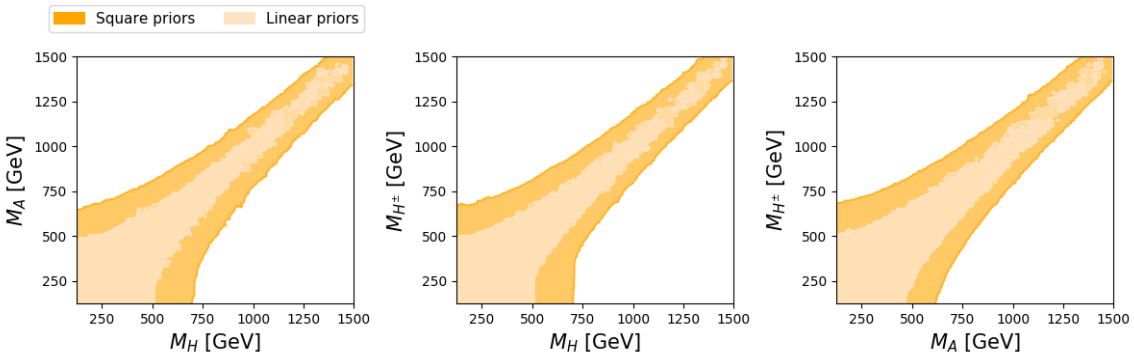

Figure 7.3: Theoretical constraints at a 100% probability obtained with square mass priors (dark orange) and linear mass priors (light orange).

Constraints obtained from EWPO present a strong dependence on the mass priors. Several choices for the mass priors are summarized in Fig. 7.4. Independently of the priors, large values for the masses and small splitting are favoured. Light and dark blue regions show the strong dependence in the mass ranges for square priors. If masses are varied until 1500 GeV, masses below approximately 750 GeV are not allowed at a 68% probability and if they are reduced to be less than 1000 GeV, masses of 500 GeV are allowed at the same probability. The same tendency is observed if lower mass regions are chosen. If the fit is repeated with linear mass priors (purple regions), masses as low as 10 GeV are allowed at a 68% probability. In this case, the dependence in the mass ranges is also weaker. Masses up to 1500 GeV (1000 GeV) are denoted as dark (light) purple regions.

7.2.3 Higgs constraints

Since the measured Higgs signal strengths are consistent with the SM, within the current uncertainties, the Yukawa couplings of the SM-like Higgs boson should be close to the SM limit. Actually, most Higgs observables are not sensitive to the signs of the Yukawa couplings and, therefore, the LHC data imply that the modulus of $|y_f^h| - 1$ cannot be larger than about 0.1-0.2. This gives two different types of solutions for the Yukawa couplings:

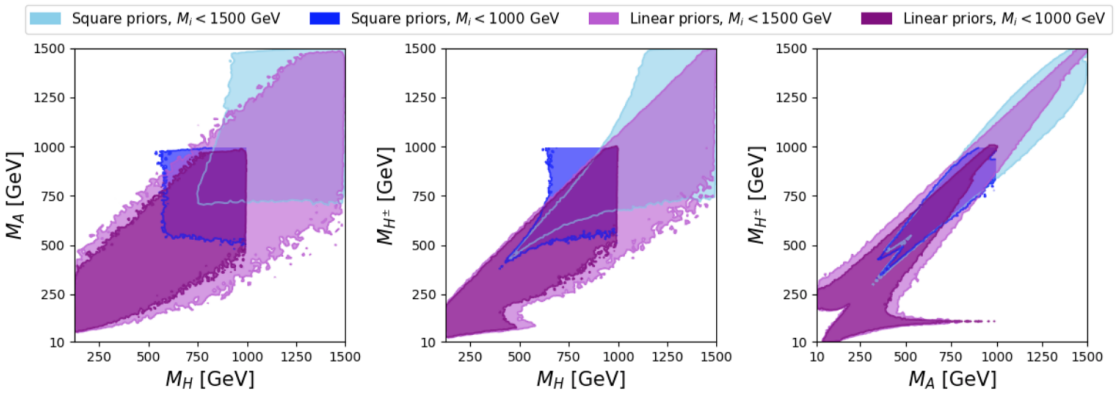

Figure 7.4: Allowed mass ranges from EWPO at a 68% probability. Light and dark blue (purple) correspond to square (linear) mass priors with $M_{H^\pm,A} \in [10, 1500]$ GeV and $M_H \in [125, 1500]$ GeV (lighter regions) and with $M_{H^\pm,A} \in [10, 1000]$ GeV and $M_H \in [125, 1000]$ GeV (darker regions).

there will be a broad range of allowed values of ς_f with $\tilde{\alpha} \approx 0$, corresponding to $y_f^h \approx 1$, and another region with larger values of the coupling angle corresponding to $y_f^h \approx -1$.

For small values of $\tilde{\alpha}$, Eq. (2.1.47) gives $y_f^h = 1 + \tilde{\alpha}\,\varsigma_f + \mathcal{O}(\tilde{\alpha}^2)$ (assuming h to be the lightest CP-even neutral scalar), so that the Yukawa coupling is close to -1 for $\tilde{\alpha}\,\varsigma_f \approx -2$. This effect can be observed in the allowed $(\tilde{\alpha}, \varsigma_f)$ regions of Fig. 7.5, for the down and leptonic alignment parameters.

The up Yukawa sign ambiguity gets broken by the two-photon decay amplitude of the Higgs that involves one-loop contributions from virtual $W^\pm$, t and $H^\pm$. Assuming that the charged-scalar correction is small, the measured $H \to \gamma\gamma$ signal strength determines the relative sign between y_u^h and g_{hWW} to be positive.

In the following we will distinguish among the two different possibilities: the "right-sign" solution, corresponding to $y_{d,\ell}^h \approx 1$ and the "wrong-sign" corresponding to $y_{d,\ell}^h \approx -1$. The former was previously analyzed in the A2HDM [124] and, more recently, in the particular case of $\mathcal{Z}_2$ symmetric models [197].

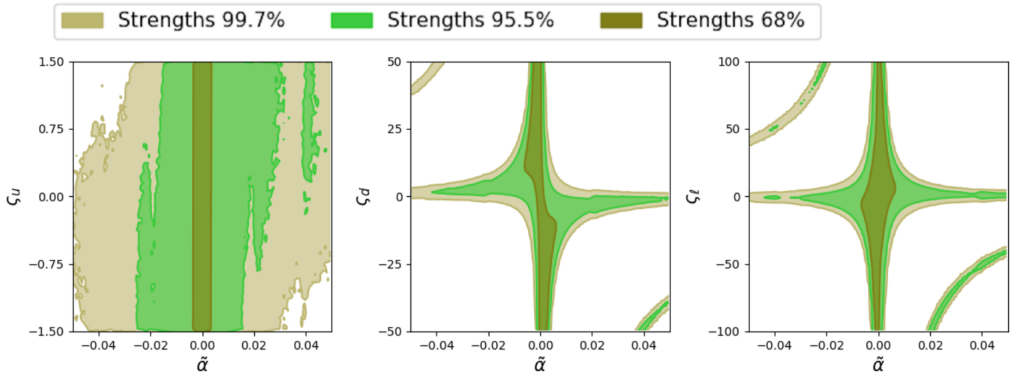

Figure 7.5: Constraints on the planes $\varsigma_f - \tilde{\alpha}$ from the Higgs signal strengths at a 68% (dark green), 95.5% (light green) and 99.7% (olive green) probability.

For the "right-sign" we find that the value of $\tilde{\alpha}$ is strongly constrained,

$$\begin{aligned} |\tilde{\alpha}| &\leq 0.003 \qquad 68\% \text{ probability}, \\ |\tilde{\alpha}| &\leq 0.023 \qquad 95.5\% \text{ probability}. \end{aligned} \tag{7.2.9}$$

The effect of direct searches restrict the masses of the scalar particles. In order to access to the information that these observables provide, we first calculate the theoretical production cross section times branching ratio $\sigma \cdot \mathcal{B}$ in the A2HDM. Then, to compare a specific $\sigma \cdot \mathcal{B}$ with the experimental upper limit, we define a ratio for the theoretical value and the observed limit ($R \equiv \frac{(\sigma \cdot \mathcal{B})^{\text{theo}}}{(\sigma \cdot \mathcal{B})^{\text{obs}}}$), to which we assign a Gaussian likelihood with zero central value, which is in agreement with the null results in the searches of heavy scalars so far. The corresponding standard deviation of the likelihood is adjusted in a way that the value $R = 1$ can be excluded with a probability of the 95%.

In general, direct searches prefer larger values of the scalar masses, but the fact that there are less searches for a low-mass range of the masses gives less restrictive constraints for masses below 100 GeV.

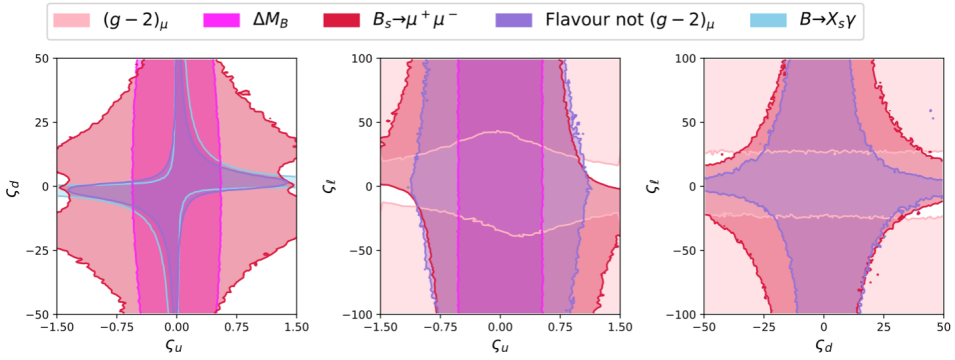

Figure 7.6: Constraints at the 95.5% probability on the alignment parameters from $(g-2)_\mu$ (light pink), $B_s \to \mu^+\mu^-$ (magenta), meson mixing (pink), $B \to X_s\gamma$ and all the flavour observables but $(g-2)_\mu$ (purple). For clarity observables that do not give relevant constraints in a given plane are omitted in the plot.

7.2.4 Flavour constraints

Flavour observables are useful to constrain the alignment parameters ς_f. As previous works showed, Fig. 7.6 illustrates that the anomaly in $(g-2)_\mu$ cannot be accommodated with small deviations from the SM. Therefore, a confirmation of the anomaly would require non-zero values for ς_ℓ [214, 215]. In the global fit we will use only observables whose deviation from the SM is smaller than 2σ, so this anomaly will be excluded. For clarity the observables that do not give relevant constraints in a given plane are omitted in the plot.

From Fig. 7.6 it can be seen that the remaining flavour observables prefer values for the alignment parameters, ς_f close to zero. This figure also illustrates the strong correlation between these couplings. $B_s \to \mu^+\mu^-$ is the only observable that constrains the leptonic couplings, excluding large values for $|\varsigma_{u,d}\varsigma_\ell|$ as it can be seen in Fig. 7.6. The same effect can be seen for the $\varsigma_u - \varsigma_d$ plane.

In meson mixing, box diagrams are dominated by top quarks and therefore ς_u couplings, enhanced by the top mass get strongly constrained, allowing to obtain an upper limit for

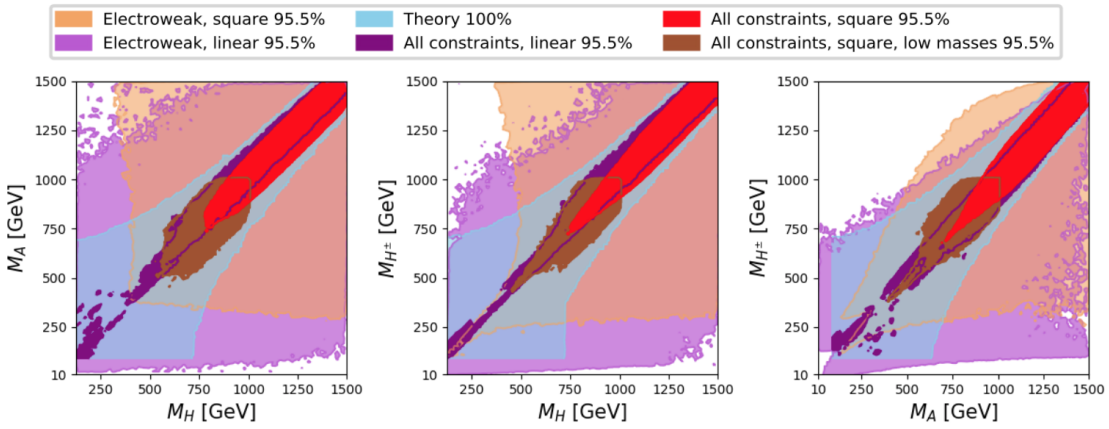

Figure 7.7: Allowed regions on the planes M_H–M_A (left), M_H–$M_{H^\pm}$ (middle) and M_A–$M_{H^\pm}$ (right) from theoretical constraints at 100% probability (blue), from EWPO at 95.5% probability (in orange, square mass priors and in light purple, linear priors), and combining all constraints at 95.5% probability (linear mass priors in purple, square mass priors in red and square mass priors and lower masses in brown). The "All constraints" contains only the right-sign branch discussed in Section 7.2.5.

$|\varsigma_u|$. A similar and stronger effect can be seen in the radiative decay $b \to s\gamma$. This decay constrains the $\varsigma_u - \varsigma_d$ plane.

7.2.5 Global fit

After discussing the separate effect of each type of observables, let us analyze the limits emerging from the global fit to all experimental and theoretical inputs.

The combined constraints on the scalar masses and mass differences are shown in the left panel of Fig. 7.2 and in Fig. 7.7. From these plots, it can be seen that theoretical and EWPOs constraints are complementary and by combining them with the remaining observables, light values for the masses are excluded. As for the electroweak constraints, there is a clear dependence on the mass priors. Fits with square mass priors with $M_i^2 \leq 1500^2$ GeV^2 and $M_i^2 \leq 1000^2$ GeV^2 are displayed in the figures as red and brown regions, respectively. Results show that if the mass regions are reduced, lower values of the masses

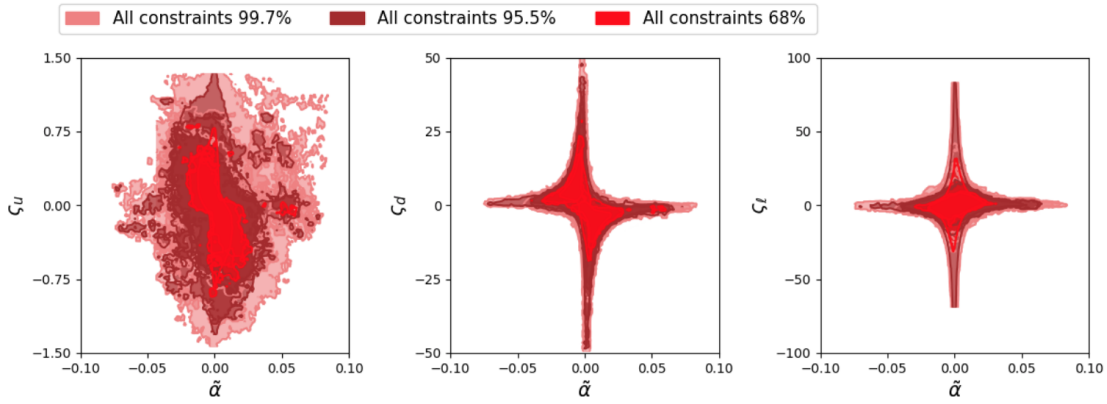

Figure 7.8: Constraints on the planes $\varsigma_f - \tilde{\alpha}$ from the global fit at a 68% (dark red), 95.5% (brown) and 99.7% (light red) probability.

are allowed at the same probability. Linear priors are displayed in purple, for $M_i \leq 1500$ GeV, showing that lighter masses are allowed than with square mass priors. A similar, but weaker effect is observed for mass splittings. From square mass priors one can set bounds on the difference

$$|M_i - M_j| \leq 150 \text{ GeV}, \qquad i, j = H, A, H^{\pm}, \qquad \text{(square mass priors)}. \tag{7.2.10}$$

This strong dependence on the mass priors indicates that the results on the mass constraints should be taken carefully.

The effect of imposing all constraints in the λ_i parameters can be observed in the right panel of Fig. 7.2. The addition of the Higgs signal strengths and the direct searches restrict the parameter space obtained before from theoretical observables. This effect is specially strong for λ_7.

Adding the rest of observables to the Higgs signal strengths is subtle because of the two different branches commented on Section 7.1.3. Convergence is difficult to reach once the set of observables that do not depend on the Yukawa couplings y_f^h, but on the alignment parameters ς_f, are combined with the Higgs signal strengths, which contained fine-tuned "wrong-sign" branches. To solve that, we have performed the fits shown in this section with the condition $y_{d,\ell}^h \approx 1$. The negative branch solution will be discussed in Section 7.2.6.

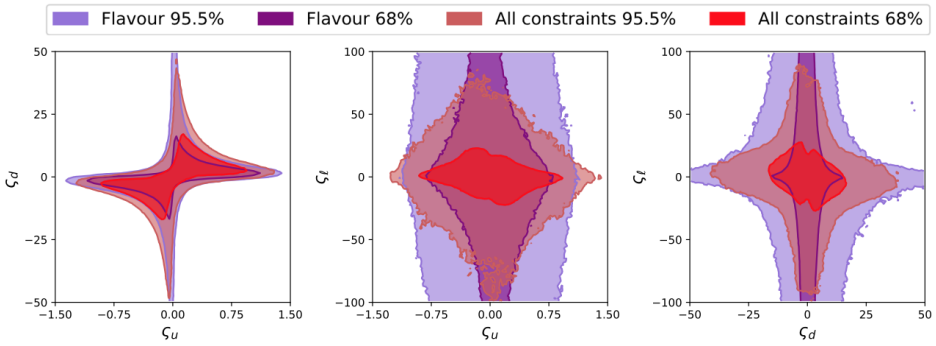

Figure 7.9: Constraints at the 95.5% probability on the alignment parameters from a fit with only flavour observables (purple) and the global fit (brown).

For the positive branch, once we add the rest of observables to the Higgs signal strengths the constraints of Fig. 7.5 get modified into the ones of Fig. 7.8. The fact of having a wider range allowed for $\tilde{\alpha}$ is explained from the fact that other observables do not constrict this parameter in such a strong way, so the combined effect results in weaker limits for $\tilde{\alpha}$. In particular we find,

$$\begin{aligned} -0.015 \quad &\leq \tilde{\alpha} \leq \quad 0.013 \qquad 68\% \text{ probability}, \\ -0.04 \quad &\leq \tilde{\alpha} \leq \quad 0.04 \qquad 95.5\% \text{ probability}. \end{aligned} \tag{7.2.11}$$

As commented before, the experimental value of $(g-2)_\mu$, shows large deviations with respect to the SM prediction. Its effect was commented in Section 7.2.4, but this observable is removed from the global fit. The effect of a global fit in the $\varsigma_f - \varsigma'_f$ planes is displayed in Fig. 7.9. The allowed parameter space for the down and leptonic coupling gets reduced once all constraints are considered. This comes from the combined effect of the Higgs and flavour observables. Again, a strong correlation between up and down alignment parameters can be observed: larger values of the up coupling will require smaller values of the down coupling and vice versa. A similar but weaker effect can be observed in the $\varsigma_u - \varsigma_d$ and $\varsigma_d - \varsigma_\ell$ planes.

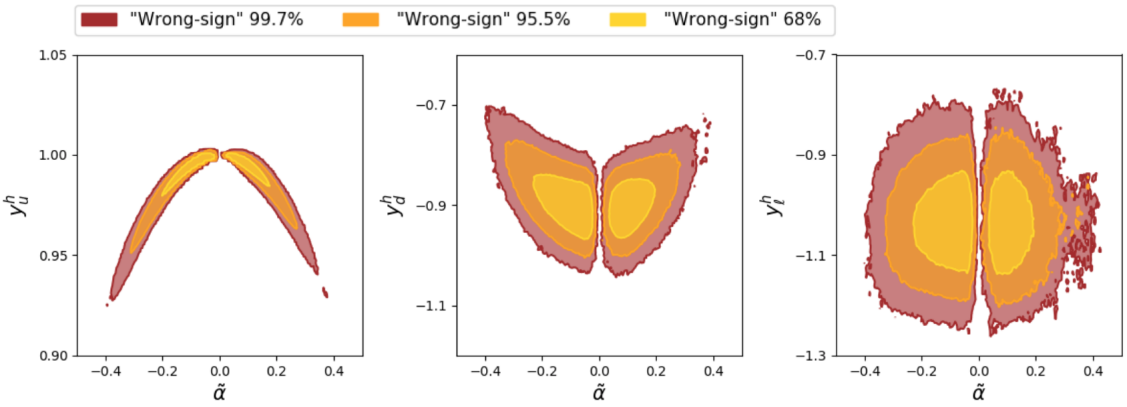

Figure 7.10: Constraints on the mixing angle $\tilde{\alpha}$ and Yukawa coupling planes at 99.7% (brown), 95.5% (orange) and 68% (yellow) probability. The fits correspond to theoretical constraints, EWPO, flavour observables and Higgs signal strengths for the "wrong-sign" solution.

7.2.6 "Wrong-sign" solution

It is complicated to reach convergence in a global fit with the "wrong-sign" solution. In Fig. 7.10 results of a fit including theoretical constraints, EWPO, flavour observables and Higgs signal strengths is presented. The region $\tilde{\alpha} = 0$ is forbidden, since it implies $y_f^h = 1$, independently of the value of the alignment parameter ς_f, and therefore corresponds to the other solution of the fit. As expected,the fitted solutions correspond to $\left|y_f^h\right| \approx 1$.

7.3 Results: *heavy scenario*

In the previous section we have described the situation in which the observed Higgs corresponds to the lightest CP-even scalar of the model. In this section we will analyze the complementary situation, *i.e.* the heaviest CP-even scalar is the SM Higgs and there is an additional neutral scalar with mass below 125 GeV.

Theoretical constraints show the same tendency as for the *light scenario*. Since the mass of the CP-even scalar is now bounded to be light, the remaining two scalar masses

cannot be heavier than 700 GeV. This can be seen in Fig. 7.11 for square mass priors. Linear mass priors give very similar constraints, so they are omitted in the plot.

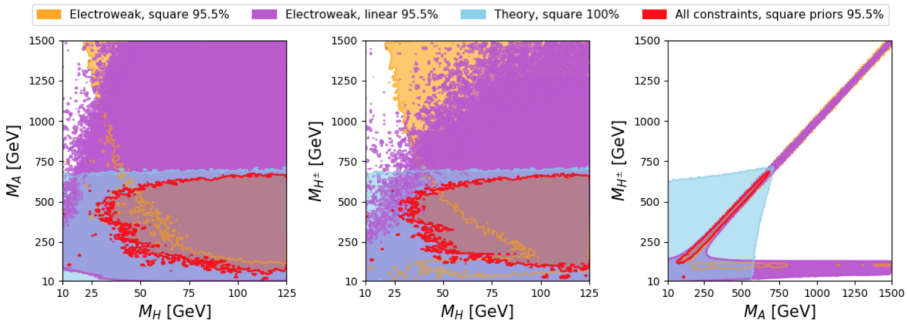

Figure 7.11: Constraints on the mass planes in the *heavy* scenario from theoretical constraints (blue, square priors, 100%), from a global fit (red, square priors, 95.5%) and from EWPO (orange, square priors, 95.5%).

Results from electroweak constraints are similar than the ones of the *light scenario*. Lower masses and large mass splittings are excluded. Now M_H is bounded to be smaller than 125 GeV, so regions become narrower. The difference between linear and squared mass priors is also similar as in the *light scenario*. Square priors present stronger constraints for light masses. These constraints can be seen at Fig. 7.11. For the plane $M_A - M_H^\pm$ the two regions overlap, so it not easy to distinguish them.

Higgs signal strengths give similar results as for the *light scenario*, shifting the angle $\tilde{\alpha} \to \tilde{\alpha} - \pi/2$. The "right-branch" now corresponds to the region with $\tilde{\alpha} \approx -\frac{\pi}{2}$ plus a region with $\tilde{\alpha}\,\varsigma_f \approx -2$. The "wrong-branch" is now the region with $\tilde{\alpha} \approx \frac{\pi}{2}$ plus the region with $\tilde{\alpha}\,\varsigma_f \approx 2$. As for the *light scenario*, the up Yukawa has de same sign as g_{hVV} and therefore only $y_u^h \approx 1$ is possible. This can be seen in Fig. 7.12. The sharp cut close to $\tilde{\alpha} = -\frac{\pi}{2}$ in the negative branch is a consequence of the correlation between $\tilde{\alpha}$ and the down coupling ς_d. Lower values of the angle will require $\varsigma_d < -50$, not allowed from our priors. A similar region is found for $\tilde{\alpha} \approx \frac{\pi}{2}$.

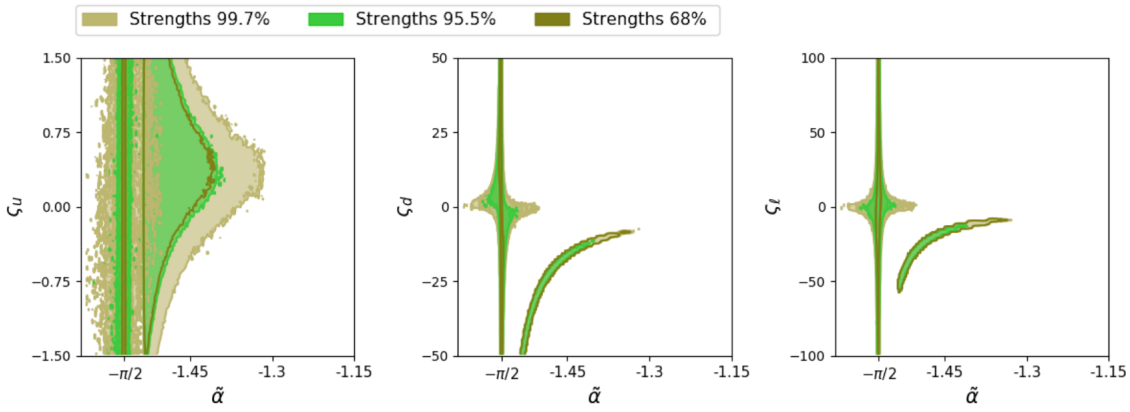

Figure 7.12: Constraints from Higgs signal strengths at the *heavy scenario* for $\tilde{\alpha} = -\frac{\pi}{2}$. A similar region is found for $\tilde{\alpha} = \frac{\pi}{2}$. Green regions represent the positive branch and purple regions the negative branch.

Finally, flavour constraints are independent of the neutral scalar masses, so they are identical in the *light* and *heavy* scenario. Therefore, constraints from Fig. 7.6 can be applied to both scenarios.

Global fit results are displayed for mass planes in Fig. 7.11. Larger masses for the CP-odd and the charged scalar are not allowed at a 95.5% probability. Since one of the scalars is forced to have a small mass, electroweak constraints restrict the mass spitting between the two other masses to be small. This can be seen in the $M_A - M_{H^\pm}$ plane of Fig. 7.11.

Global fit results for the $\tilde{\alpha} - \varsigma_f$ planes in the positive branch are equivalent to the ones in the *light* scenario (see Fig. 7.8) shifting the mixing angle $\tilde{\alpha} \to \tilde{\alpha} - \frac{\pi}{2}$.

7.4 Summary

In this chapter we have performed several Bayesian fits to the CP-conserving A2HDM using the `HEPfit` tool. First of all, we have worked in the *light scenario*, in which the observed Higgs is the lightest CP-even scalar of the model. Theoretical constraints and EWPO give important limits on the masses of the scalar particles. These observables present

a strong dependence on the mass priors, specially EWPO. Consequently, unambiguous bounds cannot be set on these parameters, but it can be concluded that large values of the masses and small splittings are preferred. Higgs signal strengths help us to constrain the mixing angle $\tilde{\alpha}$ and the couplings ς_f. Since these observables depend on the squared Yukawa couplings $(y_f^h)^2$, two different branches will satisfy the constraints: a "positive-branch" with $y_{d,\ell}^h \approx 1$ and a "negative branch" with $y_{d,\ell}^h \approx -1$. Flavour observables also restrict the values of the couplings, and the correlations among them.

In addition, the *heavy scenario* has been studied. In this scenario the new CP-even scalar is assumed to be lighter than the SM one, *i.e.* $M_H \leq 125$ GeV. This restricts the values of the remaining scalar masses to be smaller than approximately 700 GeV at a 95.5% probability. The effect in the mass priors is maintained, and similar results are obtained for the angle $\tilde{\alpha}$ (shifting $\tilde{\alpha} \to \tilde{\alpha} - \frac{\pi}{2}$) and for the couplings ς_f.

These results represent the most general global A2HDM fits up to date. While previous fits focused on $\mathcal{Z}_2$ models or used only small subsets of observables, we have worked with a minimal set of assumptions (aligned, CP-conserved model). In the future this could be generalized to include non-aligned and CP-violating structures.

Chapter 8

Fits to $b \to c\tau\bar{\nu}$ transitions

The success of the SM has reached its climax with the discovery of the Brout-Englert-Higgs boson [12–14], which seems to suggest the simplest scenario where the electroweak spontaneous symmetry breaking is linearly realized. In spite of its success as a low-energy EFT, there are both experimental signals and conceptual issues that cannot be accommodated in the SM framework and, therefore, motivate the search of NP beyond the SM. In this context, the series of anomalies in semi-leptonic B-meson decays, recently reported by several experiments, have caught a great attention in the scientific community. The unexpected deviations seem to appear in both $b \to c$ and $b \to s$ semi-leptonic decay transitions when different generations of leptons are involved, see Ref. [216–218] for recent reviews.

The $b \to c$ transitions are of particular interest, because the necessary NP effect would be comparable with the tree-level contribution of the SM, which in turn would require NP to be either rather light or strongly coupled to the SM particles.

Deviations from the SM predictions in those modes were first observed by the BaBar collaboration in 2012 [63], with discrepancies around the 25% for $B \to D^{(*)}$ decays. Later, these deviations or anomalies, as they were called, were confirmed by different measurements at BaBar [64] and by Belle [65,145] in the $\mathcal{R}_{D^{(*)}}$ ratios defined in Eq. (4.3.24). Also LHCb found a deviation in $\mathcal{R}_{D^*}$ of $\sim 2\sigma$ [68]. Combining all these data the word averages

of $\mathcal{R}_{D^{(*)}}$ at 2016 were,

$$\mathcal{R}_D^{\text{avg, 2016}} = 0.403 \pm 0.040 \pm 0.024 \qquad \text{and} \qquad \mathcal{R}_{D^*}^{\text{avg, 2016}} = 0.310 \pm 0.015 \pm 0.008\,, \tag{8.0.1}$$

with a correlation of -0.23. At that time it represented a deviation of 3.9σ with respect to the SM predictions. This is summarized in Table 8.1 and the left panel of Fig. 8.1.

Experiment	$\mathcal{R}_{D^*}$	$\mathcal{R}_D$	ρ	2016 WA	2019 WA
BaBar [63, 64]	$0.332 \pm 0.024 \pm 0.018$	$0.440 \pm 0.058 \pm 0.042$	-0.27	✓	✓
Belle [65]	$0.293 \pm 0.038 \pm 0.015$	$0.375 \pm 0.064 \pm 0.026$	-0.48	✓	✓
LHCb [68]	$0.336 \pm 0.027 \pm 0.030$			✓	✓
Belle [145]	$0.302 \pm 0.030 \pm 0.011$			✓	✗
Belle [66]	$0.270 \pm 0.035^{+0.028}_{-0.025}$			✓	✓
LHCb [69, 147]	$0.280 \pm 0.018 \pm 0.029$			✗	✓
Belle [67]	$0.283 \pm 0.018 \pm 0.014$	$0.307 \pm 0.037 \pm 0.016$	-0.51	✗	✓
2016 WA [219]	$\mathbf{0.310 \pm 0.015 \pm 0.008}$	$\mathbf{0.403 \pm 0.040 \pm 0.024}$	$\mathbf{-0.23}$		
2019 WA [48]	$\mathbf{0.295 \pm 0.011 \pm 0.008}$	$\mathbf{0.340 \pm 0.027 \pm 0.013}$	$\mathbf{-0.38}$		
SM 2016 [63, 64, 220]	0.252 ± 0.003	0.300 ± 0.008			
SM 2019 [59, 60, 62]	0.258 ± 0.005	0.299 ± 0.003			

Table 8.1: Mesurements of $\mathcal{R}_D$ and $\mathcal{R}_{D^*}$ of different collaborations. The first uncertainty corresponds to the statistical error and the second one to the systematic. The world averages are performed by the HFLAV collaboration [48, 219]. The SM predictions correspond to the ones used by Refs. [48, 219] in the year the analysis was made.

Later LHCb performed another measurement of $\mathcal{R}_{D^*}$ [69, 147] and Belle measured both $\mathcal{R}_D$ and $\mathcal{R}_{D^*}$ with a negative correlation of -0.51 [67]. The experimental situation of 2019 is summarized in the right panel of Fig. 8.1 and in Table 8.1. Combining these results the new word averages were,

$$\mathcal{R}_D^{\text{avg, 2019}} = 0.340 \pm 0.027 \pm 0.013 \qquad \text{and} \qquad \mathcal{R}_{D^*}^{\text{avg, 2019}} = 0.295 \pm 0.011 \pm 0.008\,, \tag{8.0.2}$$

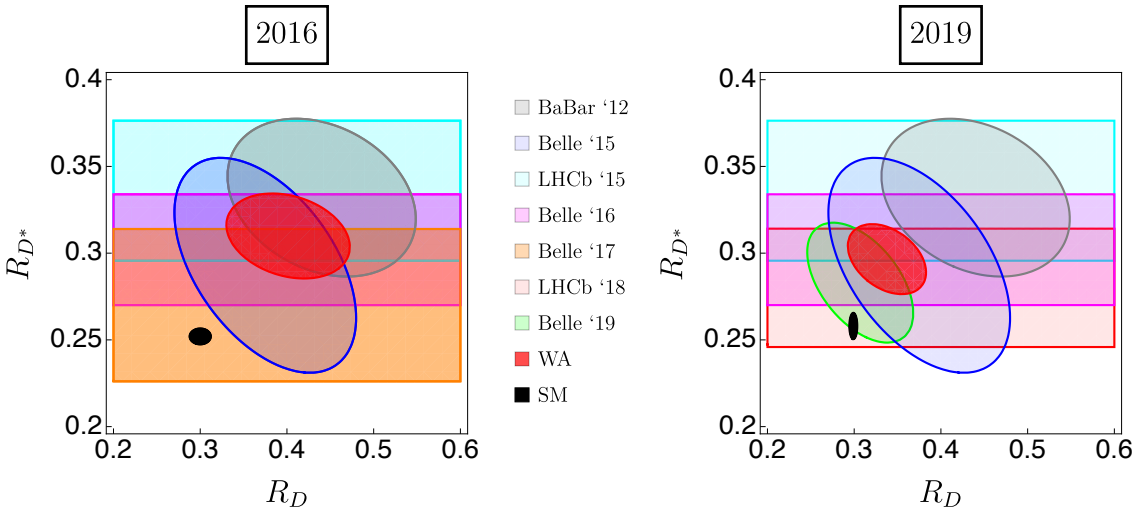

Figure 8.1: Different experimental measurements of $\mathcal{R}_D$ and $\mathcal{R}_{D^*}$. The ellipses and the bands correspond to the 1σ uncertainty ($\Delta\chi^2 = 2.3$ for the ellipses and $\Delta\chi^2 = 1$ for the bands). The word averages and the SM predictions are denoted as red and black ellipses respectively.

with a correlation of -0.38. Although experimental results were closer to the numerical values of the SM predictions, the improvement in the precision in the calculation of $\mathcal{R}_D$ and $\mathcal{R}_{D^*}$, related to a best control of the FFs resulted in smaller uncertainties for the ratios, only reducing the tension slightly to 3.08σ.

Apart from the above observables, also the recent LHCb measurement [72] of the $B_c \to J/\Psi$ ratio defined in Eq. (4.3.27),

$$\mathcal{R}_{J/\psi} \equiv \frac{\mathcal{B}(B_c \to J/\psi\tau\bar{\nu}_\tau)}{\mathcal{B}(B_c \to J/\psi\mu\bar{\nu}_\mu)} = 0.71 \pm 0.17 \pm 0.18\,, \tag{8.0.3}$$

deviates from the SM predictions $\mathcal{R}^{SM}_{J/\psi} \approx 0.25$–$0.28$ [221–232]. This points naively into the same direction, although the central value is in fact so large that it cannot be accommodated with NP contributions either.

These deviations could be interpreted as hints at lepton flavour universality violation (LFUV), which cannot be accommodated in the SM and therefore suggest the existence of NP. The lack of evidence of similar discrepancies in K and π semi-leptonic and purely

leptonic decays, or in electroweak precision observables, favours a scenario in which the potential NP contribution responsible for LFUV is only coupled to the third generation of leptons. The fact that in universality ratios large parts of the hadronic uncertainties cancel, renders underestimated theory uncertainties as an explanation extremely unlikely. This remains true considering recent discussions of radiative corrections [233,234], see also, *e.g.*, Refs. [235, 236] for earlier discussions. The correct inclusion of radiative corrections is, however, very important for the forthcoming precision analyses.

However, recent measurements of $\mathcal{R}_{D^*}$ by LHCb [69] and Belle [66], which identify the final τ through its hadronic decays, result in values more compatible with the SM and yield a downward shift in the average that might suggest that the anomaly is smaller than indicated by the above numbers. [1]

In addition to the ratios defined in Eq. (4.3.24) and summarized in Eqs. (8.0.1) and (8.0.2), we consider the normalized experimental distributions of $\Gamma(B \to D^{(*)}\tau\bar{\nu}_\tau)$ measured by BaBar [64] and Belle [65]. Although this shape information was shown to provide quite stringent constraints in Ref. [64, 74, 150, 237, 238], it has been so far ignored in most phenomenological analyses. We also analyze the effect of including the value for the integrated longitudinal polarization $\bar{F}_L^{D^*}$ (see Eq. (4.3.48)) by the Belle collaboration [71],

$$\bar{F}_L^{D^*} = 0.60 \pm 0.08 \text{ (stat)} \pm 0.04 \text{ (syst)}, \tag{8.0.4}$$

which differs from its SM prediction by 1.6σ, and discuss its consequences in detail. Other related observables, such as $\bar{\mathcal{P}}_\tau^{D^*}$ [66] and $\mathcal{R}_{J/\psi}$ [72], present large experimental uncertainties, being less relevant for studying $b \to c$ transitions.

Our analyses started in the early 2019. At that time numerous discussions could be found in the literature [51, 60, 70, 74, 82, 149, 150, 238–264], where the $b \to c\tau\bar{\nu}_\tau$ transitions were studied from a model-independent point of view. However, most of these works restricted their analyses to either effects from a single NP operator or a single heavy particle mediating the interaction. The natural step for us was adopting the most general

[1] The average of these measurements, only, agrees with the SM at the level of 1-1.5σ.

possible scenario under a set of well-motivated assumptions instead. Working with these ideas our first project consisted in a global fit in which EWSB is linearly realized, the CP-conserving limit is taken and there are not light right-handed neutrinos. This project corresponds to [52]. As previously mentioned, in the middle of 2019 more experimental data involving $b \to c$ transitions was available. This, combined with the idea of exploring scenarios beyond our theoretical assumptions yielded into a work containing the relevant operators to include right-handed neutrinos [265].

In this chapter we start by describing the FFs in Section 8.1.1 and the χ^2 that will be used in our fits in Section 8.1.2. The rest of the chapter is divided into two parts. The first one is based in Ref. [52] and corresponds to a global fit without light right-handed neutrinos. The second part of this chapter corresponds to an analysis including right-handed neutrinos and corresponds to Ref. [265]. Many technical details, such as hadronic matrix elements, FFs, and the full set of relevant helicity amplitudes common for the two parts, are compiled in several appendices.

8.1 Generalities

In this section we describe several ingredients used in the two analyses: the FFs and the general structure of the χ^2 that will be used to perform the different fits.

8.1.1 Form Factors

The relevance of hadronic uncertainties in the determination of $|V_{cb}|$ has opened an intense debate about the most adequate way to parametrise the relevant hadronic form factors [59–62, 266–269]. It has been suggested that the accuracy of the usually adopted Caprini-Lellouch-Neubert (CLN) parametrisation [270] has been probably overestimated and the current experimental precision requires to use more generic functional forms such as the one advocated by Boyd, Grinstein and Lebed (BGL) [271–273]. However, we note that the observables considered here are mostly ratios, reducing the overall form-factor sensitivity. We consider a heavy quark effective theory (HQET) [274, 275] parametrization, including

corrections of order α_s, $\Lambda_{\rm QCD}/m_{b,c}$ and partly $\Lambda^2_{\rm QCD}/m_c^2$, mostly following [60, 253]. In the heavy-quark limit all form factors either vanish or reduce to a common functional form, the Isgur-Wise function $\xi(q^2)$ [276]. Thus, it is convenient to factor out $\xi(q^2)$ by defining [60]

$$\hat{h}(q^2) \,=\, h(q^2)/\xi(q^2)\,. \tag{8.1.5}$$

The leading Isgur-Wise function can be more conveniently expressed in terms of the kinematical parameters

$$\omega(q^2) \,=\, \frac{m_B^2 + m_{D^{(*)}}^2 - q^2}{2 m_B m_{D^{(*)}}} \qquad \text{and} \qquad z(q^2) \,=\, \frac{\sqrt{\omega(q^2)+1}-\sqrt{2}}{\sqrt{\omega(q^2)+1}+\sqrt{2}}\,. \tag{8.1.6}$$

The variable $\omega(q^2)$ is the inner product of the B and $D^{(*)}$ velocities, so that $\omega = 1$ corresponds to the zero-recoil point, $q^2_{\rm max} = (m_B - m_{D^{(*)}})^2$, where $\xi(q^2_{\rm max}) = 1$. The conformal mapping $z(q^2)$ encodes in a very efficient way the analyticity properties of the form factors, transforming the cut q^2 plane into the circle $|z| < 1$ [277], so that a perturbative expansion in powers of $z(q^2)$ has an optimized convergence. Up to $\mathcal{O}(z^4)$ corrections, $\xi(q^2)$ can be written as[2]

$$\begin{aligned} \xi(q^2) \;&=\; 1 - \rho^2\,[\omega(q^2)-1] + c\,[\omega(q^2)-1]^2 + d\,[\omega(q^2)-1]^3 + \mathcal{O}([\omega-1]^4) \\ &=\; 1 - 8\rho^2 z(q^2) + (64c - 16\rho^2)\,z^2(q^2) + (256c - 24\rho^2 + 512d)\,z^3(q^2) + \mathcal{O}(z^4)\,, \end{aligned} \tag{8.1.7}$$

and it is characterized through the parameters ρ^2, c and d.

The functions $\hat{h}(q^2)$ introduce corrections of order $\Lambda_{\rm QCD}/m_{b,c}$ and $\Lambda^2_{\rm QCD}/m_c^2$ via the subleading Isgur-Wise functions $\chi_{2,3}(\omega), \eta(\omega)$ at order $1/m_{c,b}$ and $l_{1,2}(\omega)$ at order $1/m_c^2$, parametrized by the parameters $\{\chi_2(1), \chi_2'(1), \chi_3'(1), \eta(1), \eta'(1)\}$ and $\{l_1(1), l_2(1)\}$, respectively. They also include the corrections of order α_s. The detailed parametrization of the different form factors can be found in Ref. [60, 253]. The main difference to the latter

[2] The phenomenological necessity to include orders higher than z^2 in this expansion has first been found in [278].

article is the introduction of the z^3 term in the leading Isgur-Wise function, that renders the fit compatible with the extrapolation of the recent lattice data [266,279] to large recoil.

The corresponding fit to the inputs from LQCD [266, 279–281], light-cone sum rules [282] and QCD sum rules [283–285] has been updated (see [253] for details); note that this fit does not make use of experimental data, thereby rendering the form factors independent of the NP scenario considered. The results obtained for the 10 form-factor parameters are given in Table 8.2, while the corresponding correlation matrix can be found in Table A.1 of Appendix A.

Parameter	Value
ρ^2	1.32 ± 0.06
c	1.20 ± 0.12
d	-0.84 ± 0.17
$\chi_2(1)$	-0.058 ± 0.020
$\chi_2'(1)$	0.001 ± 0.020
$\chi_3'(1)$	0.036 ± 0.020
$\eta(1)$	0.355 ± 0.040
$\eta'(1)$	-0.03 ± 0.11
$l_1(1)$	0.14 ± 0.23
$l_2(1)$	-2.00 ± 0.30

Table 8.2: Inputs used to determine the form factors in the HQET parametrization as in [60]. The first three parameters determine the leading Isgur-Wise function, while the last seven enter in the $1/m_{c,b}$ and $1/m_c^2$ corrections. The correlations between these parameters can be found in Table A.1 of Appendix A

.

8.1.2 χ^2 of the fit

In order to extract the information on the NP parameters C_{AB}^X, we will perform several standard χ^2 fits. The χ^2 function can be splitted in two parts,

$$\chi^2 = \chi^2_{\text{exp}} + \chi^2_{\text{FF}}\,, \tag{8.1.8}$$

where χ^2_{exp} contains the experimental information that will be discussed below (Sections 8.2.1 and 8.3.3) and χ^2_{FF} the information on the form factors discussed in Section 8.1.1 in the form of pseudoobservables with the "experimental" information presented in Table 8.2. Each individual χ^2 is defined as:

$$\chi^2(y_i) = F^T(y_i)\, V^{-1}\, F(y_i)\,, \qquad F(y_i) = f_{\text{th}}(y_i) - f_{\text{exp}}\,, \qquad V_{ij} = \rho_{ij}\sigma_i\sigma_j\,, \tag{8.1.9}$$

with y_i denoting the input parameters of the fit, *i.e.*, $y_i = \{C_{AB}^X,\ \rho^2,\ c,\ d,\ \chi_2(1),\ \chi_2'(1),\ \chi_3'(1),\ \eta(1),\ \eta'(1),\ l_1(1),\ l_2(1)\}$, ρ_{ij} the correlation between the observables i and j, and σ_i the uncertainty of the observable i. In the above equation, f_{th} represents the theoretical expression for a certain observable and f_{exp} its experimental value. The χ^2 also contains information about the $B_c \to \tau\bar{\nu}_\tau$ branching ratio. Instead of being an additional observable it is an upper limit that should be fulfilled. More details about this limit will be given in Section 8.2.1. It is implemented in the χ^2 function as a Heavyside Theta function, its contribution being zero for parameter combinations where the limit is obeyed and infinity for those where it is not. The uncertainty of a parameter y_i is determined as the shift Δy_i in that parameter, where the minimization of $\chi^2|_{y_i = y_i^{\min} + \Delta y_i}$ varying all remaining parameters in the vicinity of the minimum leads to an increase of $\Delta\chi^2 = 1$.

8.2 Global fit without right-handed neutrinos

Our work aims at a better understanding of the nature of $b \to c$ anomalies, assuming in the following that they are indeed due to NP contributions and not due to underestimated systematic uncertainties or statistical fluctuations. Instead of considering any specific NP model, we follow a bottom-up approach, in which the available experimental input

is used to constrain any possible higher-scale effect and in this way infer information on NP without prejudice. Besides the ratios $\mathcal{R}_{D^{(*)}}$ we consider the normalized experimental distributions $\Gamma\left(B \to D^{(*)}\tau\bar{\nu}\right)$ measured by Belle [65] and BaBar [63]. These measurements were previously considered in Refs. [64, 74, 150, 237, 238] but have been ignored in most of the recent works. The last observable considered is the Belle measurement of the integrated longitudinal D^* polarization, $\bar{F}_L^{D^*}$ [71], which has an strong impact in our fits. The effect of this observable and the consequences of its deviation with respect to the SM are studied in detail.

The rest of the section is organized as follows: in Section 8.2.1, the theoretical framework used in this work is presented, and the physical observables and experimental inputs are defined. In Section 8.2.2, we discuss our global χ^2 fit and detail the resulting values of the fitted parameters. The interpretation of these results and their relation to NP are given in Section 8.2.3, where we complete our discussion with several additional fits, relaxing some of the assumptions. A set of predictions for relevant observables, for which measurements will be published or improved soon, is presented in Section 8.2.4. Finally, we draw conclusions of the fits without right-handed neutrinos in Section 8.2.6.

8.2.1 Theoretical framework and observables of our fit

Here we perform a global fit to $b \to c\tau\bar{\nu}$ without right-handed neutrinos. Such transitions are described by the Hamiltonian of Eq. (4.0.1) with $\mathcal{O}_{AL}^X$ and $A = L, R$, $X = V, S, T$. This effective Hamiltonian forms the basis of our analysis, restricted only by a minimal set of well-motivated assumptions:

- **Possible NP contributions are assumed to be present only in the third generation of leptons:** This is motivated by the absence of experimental evidence of deviations from the SM in tree-level transitions involving light leptons; specifically, precision measurements like the ratio $\mathcal{B}(\tau \to \mu\nu_\tau\bar{\nu}_\mu)/\mathcal{B}(\tau \to e\nu_\tau\bar{\nu}_e) = 0.9762 \pm 0.0028$ [75] and the analysis of $b \to c(e,\mu)\bar{\nu}_{(e,\mu)}$ transitions in Ref. [253] constrain potential effects to be negligible in the present context.

- **The coefficient C_{RL}^V is assumed to be lepton-flavour universal in our main fit:** This statement can be derived [286–288] in the context of the Standard Model Effective Field Theory (SMEFT) [289,290], which is the appropriate effective theory in the presence of a sizeable energy gap above the electroweak scale if the electroweak symmetry breaking is linearly realized. The experimental facts that no new states beyond the SM have been found so far up to an energy scale of approximately 1 TeV and that measurements of the Higgs couplings are all consistent with the SM expectations support this scenario. In this case, C_{RL}^V is strongly constrained from $b \to c(e,\mu)\bar{\nu}_{(e,\mu)}$ data [253], and we set it to zero for convenience. If the assumption of linearity is relaxed, a non-universal C_{RL}^V coefficient can be generated [288]; we will consider this case separately.

- **The CP-conserving limit is taken, so all Wilson coefficients C_{AL}^X are assumed to be real:** This is mostly done for convenience; however, none of the measurements related to the B anomalies refers to a CP-violating observable. Possible CP-violating contributions have been analyzed before in, *e.g.*, Ref. [150,259,260, 291,292]. Note that in the presence of such couplings other observables can become relevant, like electric dipole moments, see, *e.g.*, [126,293]. This assumption will be briefly commented in Section 8.2.2.

The experimental observables included in the fit are the following,

- **The ratios $\mathcal{R}_{D^{(*)}}$:** These ratios are defined in Eq. (4.3.24) and as it has been mentioned at the beginning of the chapter have been measured by Belle, BaBar and LHCb. This work has been performed with the averages of Eq. (8.0.1). The more recent measurements of (8.0.2) will also be analyzed in Section 8.2.5.

- **Differential distributions of the decay rates $\Gamma(B \to D^{(*)}\tau\bar{\nu}_\tau)$:** Belle and BaBar have also provided data on the measured q^2 distributions for $B \to D^{(*)}\tau\bar{\nu}_\tau$ [63, 65]. The reported binned values can be found in Table 9 of Ref. [52]. Since the global normalizations of these distributions are effectively already included via the values

for $\mathcal{R}_{D^{(*)}}$ in these analyses, they are not independent degrees of freedom. This can be taken into account either by introducing a free normalization factor for the distributions as in Ref. [150] or by normalizing the differential binned distributions in the following way:

$$\tilde{\Gamma}(B \to D^{(*)}\tau\bar{\nu}_\tau)_{\text{bin}} \equiv \frac{\Gamma(B \to D^{(*)}\tau\bar{\nu}_\tau)_{\text{bin}}}{\sum\limits_{\text{all bins}} \Gamma(B \to D^{(*)}\tau\bar{\nu}_\tau)_{\text{bin}}}\,, \tag{8.2.10}$$

which keeps the information about the shape of the distribution, independently of the global normalization. The treatment of systematic uncertainties and correlations follows Ref. [150].

- **The leptonic decay rate $B_c \to \tau\bar{\nu}_\tau$:** This observable is described in Eq. (4.1.8) of Chapter 4. The upper bound for the leptonic decay rate $\mathcal{B}(B_c \to \tau\bar{\nu})$ is taken to be either 30% or 10%. The first limit is derived from the B_c lifetime [70, 150, 294], while a stronger bound of 10% is obtained from the LEP data at the Z peak [295].[3] The bounds are used in a way that only points in the parameter space that fulfil this constraint will be considered.

- **The longitudinal polarization fraction $\bar{F}_L^{D^*}$**: This observable defined in Eq. (4.3.48) was announced by the Belle collaboration in early 2019 [71]. Being normalized to the total rate, this observable also enjoys the advantages of the other ratios. To study the implications of this measurement, we perform fits both considering and not considering this observable.

[3]Note, however, that the 10% bound assumes the probability of a b quark hadronizing into a B_c meson to be the same in LEP, Tevatron and LHCb, which exhibit very different transverse momenta. This has been proved to be an inaccurate approximation for b-baryons [48]. Since the dominant contribution to the B_c decay width comes from the decay of the c quark, the 30% limit could also be relaxed to about 60% [259] by lowering the charm mass used in the lifetime analysis [294].

8.2.2 Fit and results

8.2.2.1 Standard Model

We start by discussing the situation in the SM, corresponding to $C_{AL}^X \equiv 0$. The global fit to the data discussed above does actually appear to be reasonable: we obtain $\chi^2_{\text{min}} = 65.5$ for, naively, 57 d.o.f., corresponding to a naive confidence level (CL) of $\sim 20\%$. However, these numbers are misleading for the following reason: the systematic uncertainties added to the $d\Gamma/dq^2$ distributions have been chosen to be maximally conservative. Therefore, it can be expected that the corresponding χ^2 contribution is reduced; this is indeed seen since the contribution from these distributions is $\chi^2_{\text{min,d}\Gamma} \sim 43$ for, again naively, 54 d.o.f.. Considering instead the contribution from $\mathcal{R}_{D^{(*)}}$ we find a 4.4σ with our SM predictions[4] (see also [59–62, 219, 220, 296]),

$$\mathcal{R}_D^{\text{SM}} = 0.300^{+0.005}_{-0.004} \qquad \text{and} \qquad \mathcal{R}_{D^*}^{\text{SM}} = 0.251^{+0.004}_{-0.003}\,, \tag{8.2.11}$$

and we do of course reproduce the well-known puzzle, *i.e.*, we obtain $\chi^2 = 22.6$ for 2 d.o.f., corresponding to a 4.4σ tension. The fact of obtaining a larger discrepancy with respect to the SM corresponds to a lower uncertainty in our SM predictions. Note also that the limit from the B_c lifetime is irrelevant in the SM fit.

These observations imply that also NP scenarios should not be judged simply by χ^2 vs. d.o.f., but by the improvement they yield when compared to the SM.

8.2.2.2 New Physics

Since the Wilson coefficients enter each observable bilinearly (the coefficient of the left-handed vector operator being $(1 + C_{LL}^V)$), there is a degeneracy between a set of Wilson coefficients and a mirror minimum with

$$C_{LL}^{V'} = -2 - C_{LL}^V \qquad \text{and} \qquad C_{AL}^{X'} = -C_{AL}^X \qquad \text{for} \qquad {}^X_{AL} = {}^S_{RL},\ {}^S_{LL},\ {}^T_{LL}\,. \tag{8.2.12}$$

[4] Note that this prediction does not rely on experimental inputs, but includes only part of the $1/m_q^2$ corrections in heavy quark effective theory.

The two sets of Wilson coefficients give identical predictions for all observables and consequently have the same χ^2 value.[5] In the following, we will always discuss the closest minimum to the SM scenario, *i.e.*, with smaller $|C_{LL}^V|$, and will omit the sign-flipped solution; this corresponds to considering only values $C_{LL}^V \geq -1$.

The global fit to the data described in Section 8.2.1 without including the longitudinal polarization yields a unique global minimum (for $C_{LL}^V > -1$) with $\chi^2_{\text{Min 1}} = 34.1$ for 53 d.o.f.; in addition, we find two local minima, with $\chi^2_{\text{Min 2}} = 37.5$ and $\chi^2_{\text{Min 3}} = 58.6$, the latter of which is, however, highly disfavoured by the differential distributions. We summarize the results for the NP parameters in Table 8.3. Including the longitudinal polarization in the global fit, we find that the overall structure for the lower two minima (referred in the following as *Min 1b* and *Min 2b*) remains the same; however, this observable reduces slightly the available parameter space for the NP parameters. The central values of the scalar NP parameters are smaller for the global minimum, while the 1σ-ranges remain almost constant. The most striking effect is that the already less favoured local minimum disappears. The results for the NP parameters in this context can be found in Table 8.4. In both cases the form factor parameters reproduce their input distributions up to very small shifts. For illustration we show graphically in Fig. 8.2 the NP parameters for the different minima obtained in the two scenarios. There are important correlations between the NP parameters obtained from the fit. We illustrate them in the two-dimensional plots in Fig. 8.3 for the different scenarios. The contours shown there are relative to the global minimum.

We note that the distributions for, especially, the scalar parameters are highly non-gaussian. Reasons are the way the upper limit on $\mathcal{B}(B_c \to \tau\bar{\nu}_\tau)$ is included and the fact that the first two minima overlap to some extent. The former is also the reason for the strong asymmetry in the uncertainties for $C_{LL,RL}^S$. Since only their sum and difference enter $B \to D$ and $B \to D^*$ decays, respectively, these parameters are furthermore highly correlated.

[5] This discrete degeneracy is what is left of the continuous rephasing invariance when considering complex contributions, *i.e.*, the invariance under shifting all coefficients by the same complex phase.

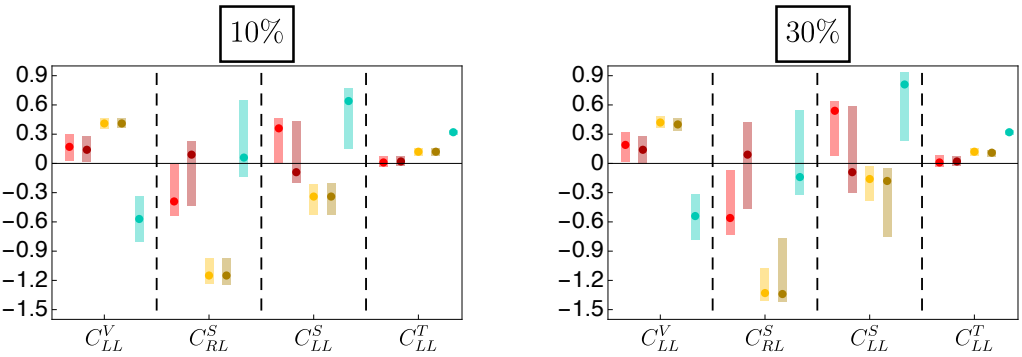

Figure 8.2: Wilson coefficients for the minima obtained in the global fit with and without including the $\bar{F}_L^{D^*}$ polarization. On the left (right) panel, $\mathcal{B}(B_c \to \tau\bar{\nu}_\tau) < 10\%$ (30%). See Tables 8.3 and 8.4 for the explicit values.

The local minima are not very deep, resulting in complications in the determination of the uncertainties for the Wilson coefficients at these points.

The fit results for the $\mathcal{R}_D$ and $\mathcal{R}_{D^*}$ ratios at the different minima are presented in Fig. 8.4. As expected, the predictions obtained from the fit are compatible at the 1σ level with the experimental data, in the case of *Min 1* and *Min 1b* essentially reproducing them. From the fit results without including $\bar{F}_L^{D^*}$, the following information can be extracted:

- The reduction of the global χ^2 by 31.4 (31.7) for 4 NP parameters implies a strong preference of NP compared to the SM, taking the present data set at face value and $\mathcal{B}(B_c \to \tau\bar{\nu}_\tau) \leq 10\%$ (30%).

- There is no absolute preference of a single Wilson coefficient in the sense that for the global minimum each individual Wilson coefficient is compatible with zero within at most 1.1σ.

- On the other hand, considering scenarios with only a single Wilson coefficient present, there *is* a clear preference for C_{LL}^V: removing the other three Wilson coefficients increases χ^2 only by 1.4, corresponding to 0.14σ. Hence, *Min 1* is well compatible with a global modification of the SM, that is, C_{LL}^V being the only non-zero coefficient.

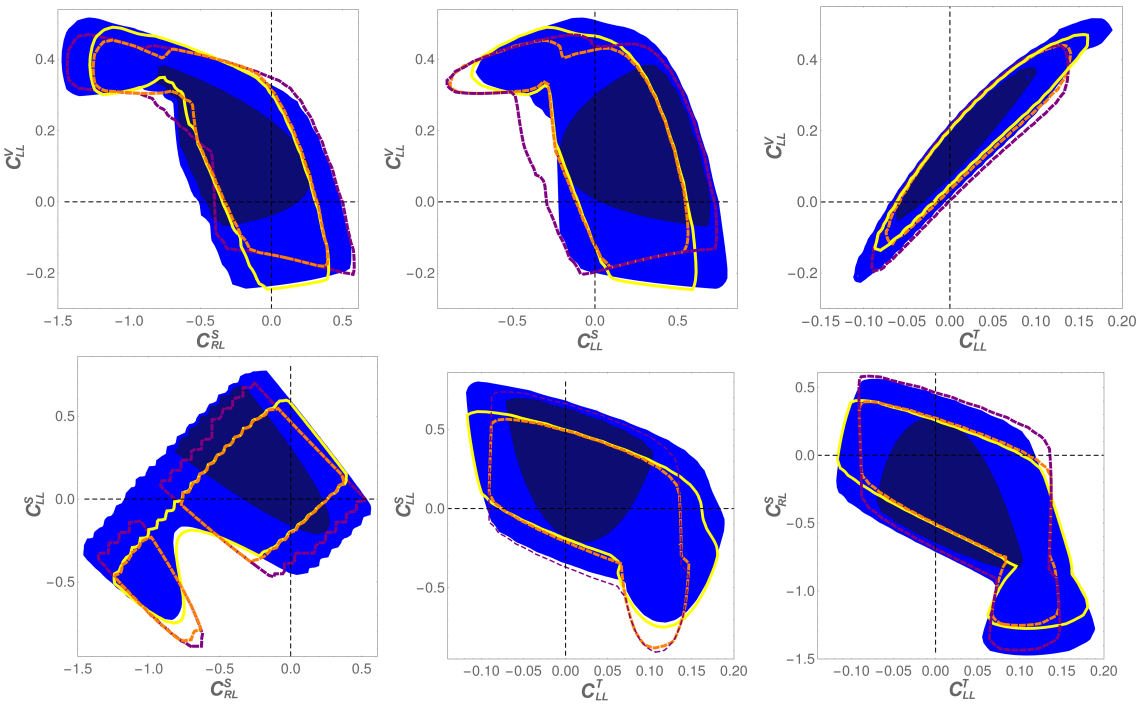

Figure 8.3: Allowed regions for all possible combinations of two Wilson coefficients for different scenarios: Blue areas (lighter 95% and darker 68% CL) show the minima without $\bar{F}_L^{D^*}$ and with $\mathcal{B}(B_c \to \tau\bar{\nu}_\tau) \leq 30\%$. The yellow lines display how the 95% CL bounds change when $\mathcal{B}(B_c \to \tau\bar{\nu}_\tau) \leq 10\%$. The dashed lines show the effect of adding the observable $\bar{F}_L^{D^*}$ for both $\mathcal{B}(B_c \to \tau\bar{\nu}_\tau) \leq 30\%$ (purple) and for $\mathcal{B}(B_c \to \tau\bar{\nu}_\tau) \leq 10\%$ (orange).

- The other two minima are numerically further away from the SM; instead of a single dominant contribution, there are several sizeable Wilson coefficients whose contributions partly cancel each other in some observables. These minima also imply different values for the fitted observables: *Min 2* corresponds to a slightly worse fit for both, $\mathcal{R}_{D^{(*)}}$ and their q^2 distributions, while *Min 3* fits $\mathcal{R}_{D^{(*)}}$ perfectly, but is essentially already excluded by the (rather coarse) measurements of the distributions available.

	Min 1	*Min 2*	*Min 3*	*Min 1*	*Min 2*	*Min 3*
$\mathcal{B}(B_c \to \tau\nu)$	10%			30%		
χ^2_{min}/d.o.f.	34.1/53	37.5/53	58.6/53	33.8/53	36.6/53	58.4/53
C_{LL}^V	$0.17^{+0.13}_{-0.14}$	$0.41^{+0.05}_{-0.06}$	$-0.57^{+0.23}_{-0.24}$	$0.19^{+0.13}_{-0.17}$	$0.42^{+0.06}_{-0.06}$	$-0.54^{+0.23}_{-0.24}$
C_{RL}^S	$-0.39^{+0.38}_{-0.15}$	$-1.15^{+0.18}_{-0.08}$	$0.06^{+0.59}_{-0.19}$	$-0.56^{+0.49}_{-0.17}$	$-1.33^{+0.25}_{-0.08}$	$-0.14^{+0.69}_{-0.18}$
C_{LL}^S	$0.36^{+0.11}_{-0.35}$	$-0.34^{+0.12}_{-0.19}$	$0.64^{+0.13}_{-0.49}$	$0.54^{+0.10}_{-0.46}$	$-0.16^{+0.13}_{-0.22}$	$0.81^{+0.12}_{-0.58}$
C_{LL}^T	$0.01^{+0.06}_{-0.05}$	$0.12^{+0.04}_{-0.04}$	$0.32^{+0.02}_{-0.03}$	$0.01^{+0.07}_{-0.05}$	$0.12^{+0.04}_{-0.04}$	$0.32^{+0.02}_{-0.03}$

Table 8.3: NP parameters for the minima obtained from the χ^2 minimization and 1σ uncertainties. There are, in addition, three corresponding sign-flipped minima, as indicated in Eq. (8.2.12). In the first three columns, the constraint $\mathcal{B}(B_c \to \tau\bar{\nu}_\tau) \leq 10\%$ has been applied, whereas in the last three columns, this requirement has been relaxed to $\mathcal{B}(B_c \to \tau\bar{\nu}_\tau) \leq 30\%$.

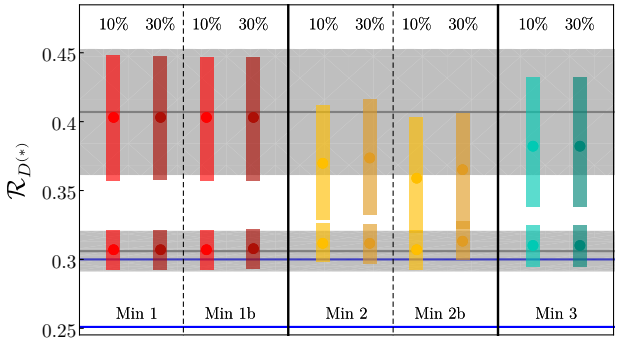

Figure 8.4: Predictions for $\mathcal{R}_D$ (higher numerical values) and $\mathcal{R}_{D^*}$ (lower numerical values) for the minima obtained in the fit, both with and without including $\bar{F}_L^{D^*}$, with $\mathcal{B}(B_c \to \tau\bar{\nu}_\tau) \leq 10\%$ and $\mathcal{B}(B_c \to \tau\bar{\nu}_\tau) \leq 30\%$. The experimental values are represented by the horizontal black lines, with their corresponding uncertainties (grey bands). The blue lines show the SM predictions, $\mathcal{R}_D = 0.300^{+0.005}_{-0.004}$ (upper blue line) and $\mathcal{R}_{D^*} = 0.251^{+0.004}_{-0.003}$ (lower blue line).

	Min 1b	*Min 2b*	*Min 1b*	*Min 2b*
$\mathcal{B}(B_c \to \tau\nu)$	10%		30%	
χ^2_{min}/d.o.f.	37.6/54	42.1/54	37.6 /54	42.0/54
C_{LL}^V	$0.14^{+0.14}_{-0.12}$	$0.41^{+0.05}_{-0.05}$	$0.14^{+0.14}_{-0.14}$	$0.40^{+0.06}_{-0.07}$
C_{RL}^S	$0.09^{+0.14}_{-0.52}$	$-1.15^{+0.18}_{-0.09}$	$0.09^{+0.33}_{-0.56}$	$-1.34^{+0.57}_{-0.08}$
C_{LL}^S	$-0.09^{+0.52}_{-0.11}$	$-0.34^{+0.13}_{-0.19}$	$-0.09^{+0.68}_{-0.21}$	$-0.18^{+0.13}_{-0.57}$
C_{LL}^T	$0.02^{+0.05}_{-0.05}$	$0.12^{+0.04}_{-0.04}$	$0.02^{+0.05}_{-0.05}$	$0.11^{+0.03}_{-0.04}$

Table 8.4: NP parameters for the minima obtained from the χ^2 minimization including $\bar{F}_L^{D^*}$ and their 1σ uncertainties. There are, in addition, the corresponding sign-flipped minima, as indicated in Eq. (8.2.12).

- All minima saturate the constraint $\mathcal{B}(B_c \to \tau\bar{\nu}_\tau) \leq 10\%$ (30%). Relaxing the upper bound allows for a larger splitting between the two scalar Wilson coefficients, and the contribution of the scalar operators gets enlarged. This constraint is consequently the main argument at low energies disfavouring a solution with only scalar coefficients. Any such solution would require a lower value for $\mathcal{R}_{D^*}$ by about 2σ.

- Having solutions with relevant contributions from all Wilson coefficients illustrates the importance of taking into account scalar and tensor operators in the fit.

- The fit results for the form factor parameters reproduce their input values displayed in Table 8.2 up to tiny shifts. This implies that the uncertainties of the experimental data with tauonic final states are large compared to the hadronic uncertainties. Differently stated, while the ranges obtained for the NP parameters are obtained in fits varying all form factor parameters simultaneously with the NP ones, they are essentially determined by the experimental uncertainties at the moment.

- Generalizing the fit to complex Wilson coefficients does not improve the minimal χ^2 value, but opens up a continuum of solutions. Hence complex Wilson coefficients can explain the anomalies as well as real ones, but they do not offer any clear advan-

tages regarding the fit quality, so they have not been considered here for simplicity. It should be mentioned, however, that in specific models the option of complex Wilson coefficients can open up qualitatively new solutions, as for example the model proposed in Ref. [291], where only the coefficients $C_{LL}^{S,T}$ ($C_{LL}^{S} \sim C_{LL}^{T}$) are present, *requiring* a non-vanishing imaginary part in order to accommodate the experimental data. This fact implies correlations with new observables like electric dipole moments, which can then be used to differentiate this model from solutions allowing for real coefficients [293].

- As discussed above, for each minimum given in Table 8.3 there is a degenerate solution, see Eq. (8.2.12).

Including the recent measurement of the longitudinal polarization $\bar{F}_L^{D^*}$ in the global fit, the above statements hold up to the following differences:

- Still there is no clear preference for a single Wilson coefficient. The central values for the scalar coefficients are smaller for the global minimum, such that the bound from the B_c lifetime is not saturated even in the 10% case. As a consequence, the minimum does not change when allowing for larger values of $\mathcal{B}(B_c \to \tau\bar{\nu}_\tau)$, only the allowed parameter ranges increase.

- The second local minimum (previously referred to as *Min 3*) disappears.

It is not straightforward to compare our fit with the results from other analyses in the literature, because we are including the information from the q^2 distributions that has been ignored in previous fits with the exception of Ref. [74, 150, 237, 238]. Besides that, some works include additional observables such as $\mathcal{R}_{J/\psi}$ or slightly different bounds on $\mathcal{B}(B_c \to \tau\bar{\nu}_\tau)$. Nevertheless, comparing the findings of previous fits with our results is quite enlightening since it illustrates the relevance of the additional observables we are considering.

Generic fits to the $\mathcal{R}_{D^{(*)}}$ world averages in Eq. (8.0.1), with the effective Hamiltonian of Eq. (4.0.1) [51, 60, 70, 74, 82, 149, 150, 238–257, 259, 260], have shown the existence of

many possible solutions, some of them involving only one or two Wilson coefficients. Including the $\mathcal{B}(B_c \to \tau\bar{\nu}_\tau)$ upper bound reduces the number of allowed possibilities, but several different scenarios remain still consistent with the data. Dropping the binned q^2 distributions from our fit, we can easily reproduce all those solutions. However, most of them lead to differential distributions in clear conflict with the BaBar and Belle measurements. While a sizeable new-physics contribution to some Wilson coefficient can easily generate the needed enhancement of the $B \to D^{(*)}\tau\bar{\nu}_\tau$ rates, it tends to distort the shape of the differential distributions in a way than can no-longer accommodate the data, similarly to what happens for *Min 3*. Once the full experimental information on $\mathcal{R}_{D^{(*)}}$ (rates and binned distributions) is taken into account, the χ^2 minimization only gives the three solutions shown in Table 8.3, and when including $\bar{F}_L^{D^*}$ in the fit, the number of solutions is further reduced to two.

8.2.3 Interpretation of results

In Section. 8.2.2 we have described the global fit to the available data on $b \to c\tau\bar{\nu}_\tau$ transitions in terms of the Wilson coefficients of an EFT framework defined at the b-quark mass scale. The EFT in this range is conventionally called Weak Effective Theory (WET) and is composed of the five lightest quarks and the three generations of leptons, and ruled by the $SU(3)_C \otimes U(1)_Q$ gauge symmetry. This is a valid approach assuming – as strongly suggested by all available collider data – that no new degree of freedom exists coupling to this channel with a mass around or lower than the b quark. However, ultimately the goal is to gain insight into the high-energy structure of the theory. To that aim, renormalization-group techniques are used to relate the coefficients extracted in our analysis to those relevant at the scale of the potential new high-energy degree(s) of freedom. This process involves several scales and thresholds, see Fig. 8.5.

The relation to the coefficients at the electroweak scale is determined by QCD and are known [297–300]. Above the electroweak (EW) scale, the Lagrangian has not undergone spontaneous symmetry breaking and, therefore, the fermionic fields should be expressed

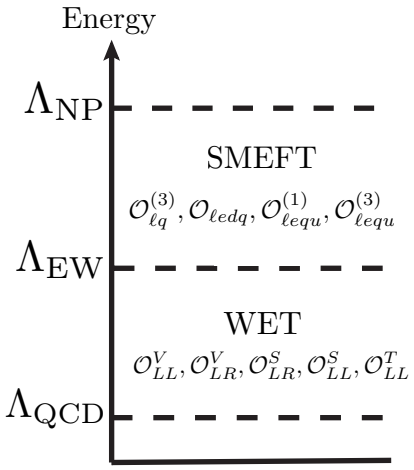

Figure 8.5: Relevant scales for the study of the B anomalies. The dashed lines indicate the thresholds between different EFTs.

in terms of weak eigenstates rather than mass eigenstates. Moreover, the top quark, the electroweak gauge bosons and the Higgs boson have to be considered as new degrees of freedom in the theory. The relevant framework at this scale is the full SM, with the addition of the effects of NP. For relatively low NP scales $\lesssim 1$ TeV, the relevant new degrees of freedom can be included explicitly. However, the suggested absence of new degrees of freedom below ~ 1 TeV allows us to parametrize any NP contribution in the framework of another effective theory. This can be the so-called SMEFT under the conditions specified in Section 8.2.1, or a more general framework with a non-linear representation for the Higgs, see, *e.g.*, Ref. [301, 302].

In SMEFT, the effective Lagrangian can be expanded in inverse powers of the NP scale, $\Lambda_{\rm NP}$, *i.e.*,

$$\mathcal{L}_{\rm NP} = \sum_{d=6} \frac{1}{\Lambda_{\rm NP}^{d-4}} \sum_i C_i^{(d)} \mathcal{O}_i^{(d)} \,, \tag{8.2.13}$$

built from a series of higher-dimensional operators in terms of the SM fields and invariant under the SM gauge group $SU(3)_C \otimes SU(2)_L \otimes U(1)_Y$ [289]. A convenient complete and non-redundant basis of dimension-six operators is the Warsaw basis [290]. In order to

relate both EFTs, the matching between the WET theory and the SMEFT has to be performed at the EW scale [286, 287, 299, 300, 303, 304]. The matching onto the basis in the non-linear case [305, 306] is given in Ref. [288].

Finally, one has to consider the running from $\Lambda_{\rm EW}$ to $\Lambda_{\rm NP}$ [256, 307–310]. The corresponding equations can be solved numerically, but also analytically to very good approximation [311].

As an illustration of the effect of the running, we show the relation between the WET Wilson coefficients at $\mu_b \approx 5$ GeV and the SMEFT Wilson coefficients at an hypothetical NP scale of $\Lambda = 1$ TeV, calculated in Ref. [256, 310], which can be trivially inverted:

$$\begin{aligned} C^V_{LL}(\mu_b) &= -1.503\, \tilde{C}^V_{LL}(\Lambda)\,, \\ C^S_{LL}(\mu_b) &= -1.257\, \tilde{C}^S_{LL}(\Lambda) + 0.2076\, \tilde{C}^T_{LL}(\Lambda)\,, \\ C^S_{RL}(\mu_b) &= -1.254\, \tilde{C}^S_{RL}(\Lambda)\,, \\ C^T_{LL}(\mu_b) &= 0.002725\, \tilde{C}^S_{LL}(\Lambda) - 0.6059\, \tilde{C}^T_{LL}(\Lambda)\,. \end{aligned} \tag{8.2.14}$$

For a discussion of the notation used for the SMEFT Wilson coefficients in the Warsaw basis see Appendix E.

With the coefficients at the potential NP scale at hand, one can try to go beyond the EFT framework and get an idea about which class of NP might be responsible for the observed pattern: at the scale Λ, the coefficients C^X_{AL} should result from integrating out the new heavy degrees of freedom. In Table 8.5, the quantum numbers of all possible candidates able to participate in the $b \to c$ transitions are listed and their nature is identified (see also [74]). We note that, in some cases, a given NP mediator may contribute to more than one Wilson coefficient, thus resulting in correlations among them. In Appendix E, we list the effective Lagrangians obtained after integrating out each of the possible heavy degrees of freedom. We show in the last two columns of Table 8.5 the set of Wilson coefficients to which the new degrees of freedom contribute, both in the SMEFT and in the WET. The RGE running changes the relative size of these coefficients, as seen above, and causes mixing among the operators $\mathcal{O}^S_{LL}$ and $\mathcal{O}^T_{LL}$. When considering such specific classes of models, generally other constraints apply. Specifically, searches for the corresponding

Spin	Q.N.	Nature	Allowed couplings	SMEFT	WET
0	$S_1 \sim (\bar{3}, 1, 1/3)$	LQ	$\overline{q_L^c}\ell_L$, $\overline{d_R}u_R^c$, $\overline{u_R^c}e_R$	$\tilde{C}_{LL}^V, \tilde{C}_{LL}^S, \tilde{C}_{LL}^T$	$C_{LL}^V, C_{LL}^S, C_{LL}^T$
0	$S_3 \sim (\bar{3}, 3, 1/3)$	LQ	$\overline{q_L^c}\ell_L$	$\tilde{C}_{LL}^V$	C_{LL}^V
0	$R_2 \sim (3, 2, 7/6)$	LQ	$\overline{u_R}\ell_L$, $\overline{q_L}e_R$	$\tilde{C}_{LL}^S, \tilde{C}_{LL}^T$	C_{LL}^S, C_{LL}^T
0	$H_2 \sim (1, 2, 1/2)$	SB	$\overline{q_L}d_R$, $\overline{\ell_L}e_R$, $\overline{u_R}q_L$	$\tilde{C}_{S_R}, \tilde{C}_{LL}^S$	$C_{RL}^S, C_{LL}^S, C_{LL}^T$
1	$V_2 \sim (\bar{3}, 2, 5/6)$	LQ	$\overline{d_R^c}\gamma_\mu\ell_L$, $\overline{e_R^c}\gamma_\mu q_L$	$\tilde{C}_{RL}^S$	C_{RL}^S
1	$U_1 \sim (3, 1, 2/3)$	LQ	$\overline{q_L}\gamma_\mu\ell_L$, $\overline{d_R}\gamma_\mu e_R$	$\tilde{C}_{LL}^V, \tilde{C}_{RL}^S$	C_{LL}^V, C_{RL}^S
1	$U_3 \sim (3, 3, 2/3)$	LQ	$\overline{q_L}\gamma_\mu\ell_L$	$\tilde{C}_{LL}^V$	C_{LL}^V
1	$W'_\mu \sim (1, 3, 0)$	VB	$\overline{\ell_L}\gamma_\mu\ell_L$, $\overline{q_L}\gamma_\mu q_L$	$\tilde{C}_{LL}^V$	C_{LL}^V

Table 8.5: Spin, $SU(3)_C \otimes SU(2)_L \otimes U(1)_Y$ quantum numbers, nature (LQ = leptoquarks, SB = scalar boson and VB = vector boson) and allowed interactions of the possible candidates to mediate $b \to c$ transitions. In our notation, $\Psi_L^c \equiv (\Psi_L)^c$.

mediators can exclude a large part of the parameter space, or even the whole scenario (like the W') [312–314]. In the following we will not discuss these constraints, but simply give examples for how the required coefficients could be generated, irrespective of their actual viability.

We are now in a position to interpret the different solutions obtained in the fit shown in Table 8.3 and Table 8.4. Let us focus first on the scenarios where $\bar{F}_L^{D^*}$ is not included. The minimum with highest χ^2, *Min 3*, presents relevant contributions from the operators $\mathcal{O}_{LL}^S$ and $\mathcal{O}_{LL}^T$. The origin of these Wilson coefficients could be explained, for instance, with the presence of the scalar leptoquarks $R_2 \sim (3, 2, 7/6)$ or $S_1 \sim (\bar{3}, 1, 1/3)$, whose contributions to the Lagrangian at the NP scale are given in Appendix E. An additional mediator would be necessary to generate the sizeable contribution to C_{LL}^V, however, in

the former case. *Min 2*, which exhibits non-zero values for all Wilson coefficients, could be explained by combinations of several candidates, for instance S_1 and H_2. Also for *Min 1* there are different possibilities, since the fit does not single out a specific coefficient. However, the simplest option remains the scenario where the only relevant contribution is proportional to the SM one, *i.e.*, all Wilson coefficients but C_{LL}^V are compatible with zero at 1.1σ. This possibility could be generated, for instance, by the effect of a $W^{'}$ boson,

$$\mathcal{L}_{\text{eff}} \supset -\frac{\tilde{g}_{\ell\nu_\ell}\tilde{g}_{du}^\dagger}{M_{W'}^2}\,(\bar{\ell}_L\gamma_\mu\nu_{\ell L})(\bar{u}_L\gamma^\mu d_L)\,, \tag{8.2.15}$$

with $M_{W'}/(\tilde{g}_{\ell\nu_\ell}\tilde{g}_{du}^\dagger)^{1/2} \sim 2$ TeV. For a sequential W' with SM couplings, one would need $M_{W'} \sim 0.2$ TeV, which is already ruled out by direct searches [315]. More exotically, but more realistically given the aforementioned high-energy constraints, one could explain the modification on the $\mathcal{O}_{LL}^V$ operator by introducing leptoquarks (LQs), such as the vector $U_3 \sim (3,3,2/3)$ or the scalar $S_1 \sim (\bar{3},1,1/3)$ LQs. However, extra symmetries in the UV regime would have to be assumed in order to guarantee that other flavour transitions compatible with the SM are respected.

In Fig. 8.6 we show the dependence of selected observables on individual Wilson coefficients. The left-top panel in Fig. 8.6 shows that it is straightforward to achieve consistency with the experimental measurements for $\mathcal{R}_{D^{(*)}}$ by shifting only the Wilson coefficient C_{LL}^V, *i.e.*, modifying the SM coefficient. The polarization observables show a good potential to differentiate between different contributions. Particularly interesting is the longitudinal polarization fraction in $B \to D^*\tau\bar{\nu}_\tau$, shown in the bottom-right panel, for which the Belle collaboration recently announced a first measurement [71]. As this sub-figure shows, it is difficult to accommodate it at 1σ for any of the individual Wilson coefficients [316]. The only contributions allowing for a significantly larger value of this observable than in the SM are those from scalar operators; however, values accommodating $\bar{F}_L^{D^*}$ are in conflict with the bound from $\mathcal{B}(B_c \to \tau\bar{\nu}_\tau) < 10\%$ (dashed lines), and extending this bound to 30% still does not allow to accommodate its central value. This figure therefore indicates why none of the fit scenarios yields values for $\bar{F}_L^{D^*}$ in the 1σ range; we take this as a motivation to investigate the consistency of the different measurements in more detail.

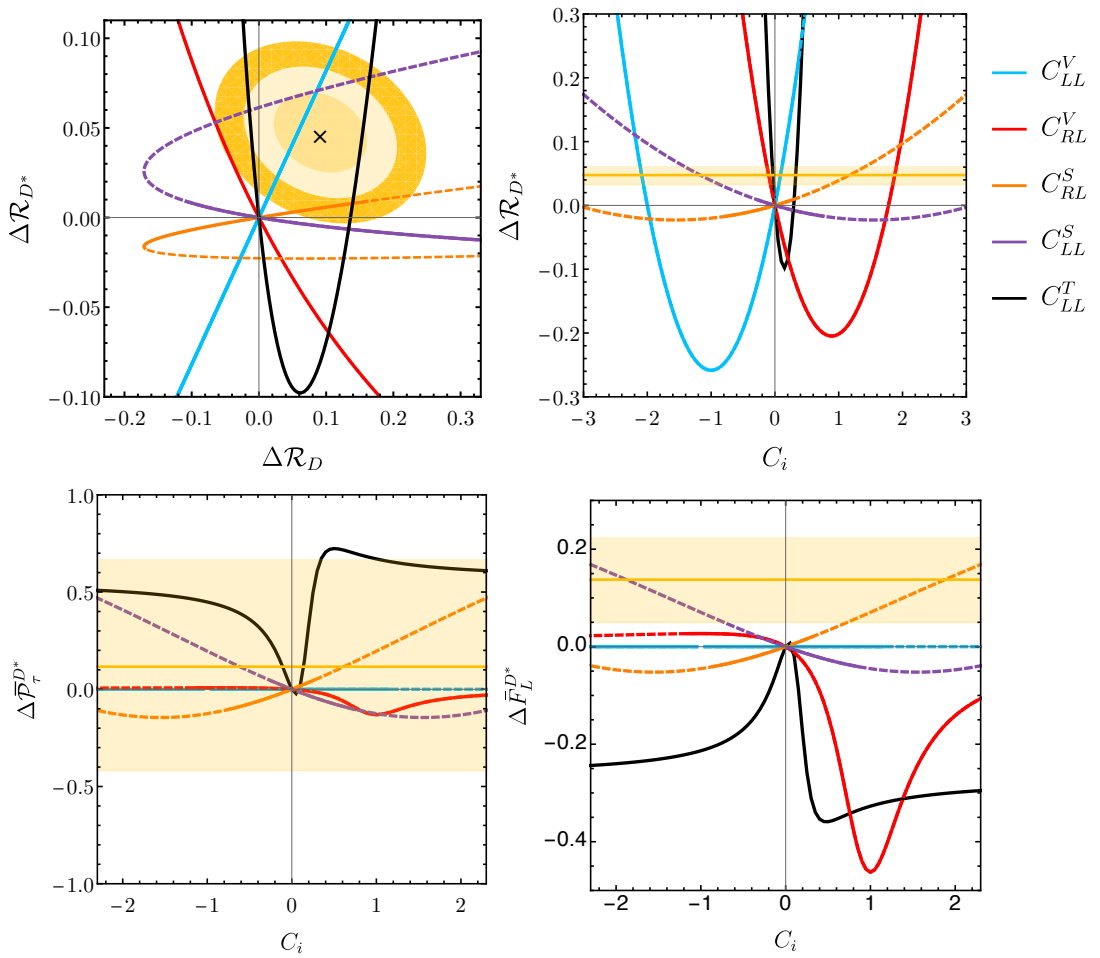

Figure 8.6: Individual contributions of the Wilson coefficients of the WET Hamiltonian in different observables ($\Delta X \equiv X - X_{\rm SM}$): correlation between $\Delta\mathcal{R}_D$ and $\Delta\mathcal{R}_{D^*}$, and $\Delta\mathcal{R}_{D^*}$, $\Delta\bar{\mathcal{P}}_\tau^{D^*}$ and $\Delta\bar{F}_L^{D^*}$ as a function of the Wilson coefficients. Left-top panel: the experimental central value is denoted by a black cross and the $1\sigma, 2\sigma$ and 3σ uncertainties by yellow rings. Right-top and bottom panels: experimental central values are displayed by a solid yellow line and their 1σ uncertainty by a yellow band. Dashed lines indicate regions excluded by the constraint $\mathcal{B}(B_c \to \tau\bar{\nu}_\tau) < 10\%$.

In order to do so, we use the fact that only three combinations of the four Wilson coefficients enter $B \to D^*\tau\bar{\nu}_\tau$ observables as well as the leptonic B_c decay: C_{LL}^V, C_{LL}^T

and the pseudo-scalar coefficient $C_P \equiv C_{LR}^S - C_{LL}^S$. Every observable therefore results in a non-trivial constraint in the $C_P - C_{LL}^V$ plane if C_{LL}^T is fixed to some value. We show the preferred parameter ranges obtained for the individual observables in Fig. 8.7, for a representative set of C_{LL}^T values. The combination of $\mathcal{R}_{D^*}$ and the bound on $\mathcal{B}(B_c \to \tau\bar{\nu}_\tau)$ determines a narrow strip in this parameter plane, dominated by the former for the bound on C_{LL}^V and the latter for the bound on C_P. The overlap of the other observables varies with the value for C_{LL}^T; however, there is no value of C_{LL}^T for which all 1σ bands overlap. In fact, the 1σ range for $\bar{F}_L^{D^*}$ cannot be reached by any NP parameter combination in this setup, when only imposing the $\mathcal{B}(B_c \to \tau\bar{\nu}_\tau)$ constraint of 10% or even 30% and at the same time requiring a positive shift in $\mathcal{R}_{D^*}$. Agreement can presently be achieved at the 2σ level; nevertheless, a confirmation of the present central values with higher precision could indicate the inconsistency between the data and any NP with flavour-universal C_{LR}^V.

This potential incompatibility would suggest one of several possibilities:

1) One of our theoretical assumptions is incorrect and the SMEFT cannot be applied at the electroweak scale. This could happen if one or several of the following cases apply: (a) There is an insufficient gap between the electroweak and the NP scale, *i.e.*, there are new degrees of freedom close enough to the EW scale to invalidate an EFT approach. (b) The electroweak symmetry breaking is non-linear, changing also the character of the observed Higgs-like particle. In that case C_{RL}^V could contribute to the fitted observables, because it would no-longer be necessarily flavour universal. (c) There are additional light degrees of freedom like right-handed neutrinos [317–319], yielding additional operators.

   Note that we also assumed the semi-leptonic decays with light leptons to be free from NP. However, the corresponding constraints are so strong that even relaxing this assumption would not significantly change our analysis [253].

2) An unidentified or underestimated systematic uncertainty in one or several of the experimental measurements.

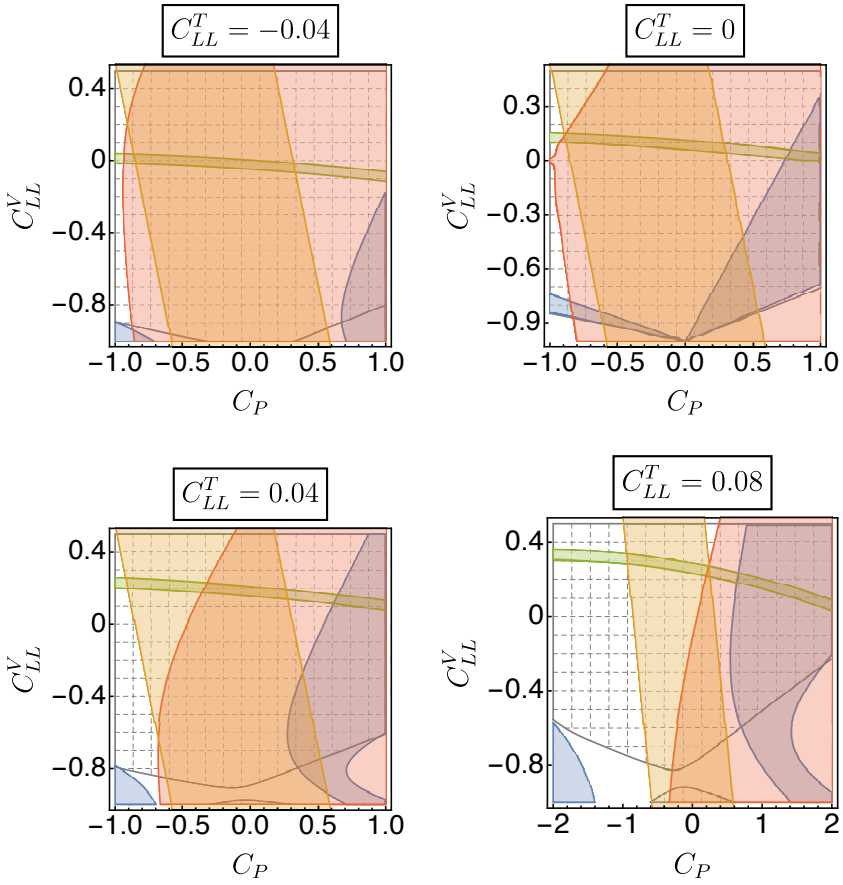

Figure 8.7: Allowed regions at 1σ from $\bar{F}_L^{D^*}$ (blue), $\mathcal{R}_{D^*}$ (green), $\bar{\mathcal{P}}_\tau^{D^*}$ (gray grid) and the q^2 distribution of $\Gamma(B \to D^*\tau\bar{\nu}_\tau)$ (red), together with the region satisfying the bound $\mathcal{B}(B_c \to \tau\bar{\nu}_\tau) < 10\%$ (orange).

In any case, the upcoming experimental studies of not only the LHCb collaboration, but also the Belle II experiment which started to take data will hopefully resolve this question soon.

For completeness of our discussion, we have consequently performed the fit relaxing the condition of flavour universality on C_{RL}^V. As a consequence of adding C_{RL}^V as an extra d.o.f. to fit, the number of solutions is enlarged. As shown in Fig. 8.8, one finds now four different solutions (plus their sign-flipped counterparts), given numerically in Table 8.6.

	Min 4	*Min 5*	*Min 6*	*Min 7*
χ^2_{min}/d.o.f.	32.5/53	33.3/53	37.6/53	38.9/53
C_{LL}^V	$-0.91^{+0.10}_{-0.09}$	$-0.85^{+0.20}_{-0.10}$	$0.14^{+0.14}_{-0.12}$	$0.35^{+0.08}_{-0.08}$
C_{RL}^V	$1.89^{+0.19}_{-0.22}$	$-1.58^{+0.23}_{-0.22}$	$0.02^{+0.21}_{-0.24}$	$0.34^{+0.18}_{-0.18}$
C_{RL}^S	$-0.44^{+0.12}_{-0.45}$	$-0.33^{+0.52}_{-0.16}$	$0.10^{+0.15}_{-0.59}$	$-0.68^{+0.54}_{-0.14}$
C_{LL}^S	$-1.34^{+0.49}_{-0.12}$	$0.56^{+0.23}_{-0.54}$	$-0.12^{+0.65}_{-0.15}$	$-0.92^{+0.58}_{-0.11}$
C_{LL}^T	$-0.22^{+0.10}_{-0.11}$	$0.19^{+0.10}_{-0.10}$	$0.01^{+0.09}_{-0.07}$	$-0.02^{+0.08}_{-0.07}$

Table 8.6: Minima with their 1σ uncertainties obtained from the global χ^2 minimization, including $\bar{F}_L^{D^*}$ and $\mathcal{B}(B_c \to \tau\bar{\nu}_\tau) < 10\%$ in the fit while allowing for $C_{RL}^V \neq 0$. There are, in addition, the corresponding sign-flipped minima, as indicated in Eq. (8.2.12).

The doubling of minima can be understood qualitatively in the following way: $B \to D$ is dominated by the combination of Wilson coefficients corresponding to the vector coupling $C_V = 1 + C_{LL}^V + C_{RL}^V$, while $B \to D^*$ is dominated by the axial-vector coupling $C_A = C_{RL}^V - (1 + C_{LL}^V)$. Their rates are correspondingly roughly given by $|C_{V,A}|^2$. For $C_{RL}^V \equiv 0$ we have $C_V = -C_A$, and the only remaining discrete symmetry is that discussed in Section 8.2.2.2, the second solution being eliminated by our choice $C_{LL}^V > -1$. With a finite coefficient C_{RL}^V, these two solutions become four ($\{C_A = \pm|C_A|, C_V = \pm|C_V|\}$), since now $|C_A| \neq |C_V|$; two of those are again eliminated by our choice for C_{LL}^V, leaving two solutions per minimum with $C_{RL}^V \equiv 0$. This degeneracy is broken by interference terms, notably $\text{Re}(C_A C_V^*)$ in $B \to D^*$, but also the interference with scalar and tensor operators. Nevertheless, this approximate degeneracy explains the doubling of solutions for finite C_{RL}^V.

As can be seen from the comparison of Table 8.6 with Table 8.4, the previous global minimum, *Min 1b*, remains a solution of this more general fit, now called *Min 6*. *Min 7* is

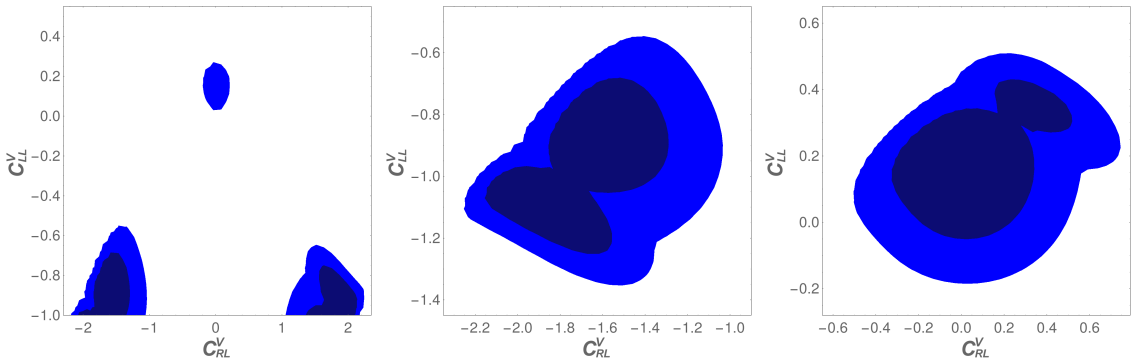

Figure 8.8: Allowed regions in the $C_{RL}^V - C_{LL}^V$ plane, for the global fit including $\bar{F}_L^{D^*}$, restricting $\mathcal{B}(B_c \to \tau\nu) \leq 10\%$. Lighter and darker blue areas show regions with 95% and 68% CL, respectively. Left: All four minima shown in the chosen parameter convention with $C_{LL}^V > -1$, relative to the global minimum. Center: the two minima with $C_{LL}^V \sim -1$, without restricting $C_{LL}^V > -1$, see text. Right: the two minima with $|C_{V_{R,L}}| < 1$, relative to *Min 6*.

again relatively close to *Min 6*, however with a significant contribution from C_{RL}^V and hence qualitatively different from *Min 2* in the previous fits. The new global minimum *Min 4* and the close-lying *Min 5* improve the agreement of the fit with the data significantly. However, in these scenarios the SM coefficient is almost completely cancelled and its effect replaced by several NP contributions. These are hence fine-tuned scenarios, and should be taken with a grain of salt.

We have also analyzed the individual observables in $B \to D^*$ and the bound on $\mathcal{B}(B_c \to \tau\bar{\nu}_\tau)$ for this case. This is illustrated in Fig. 8.9, for different benchmark values of C_{LL}^V and C_{LL}^T, in the plane $C_{RL}^V - C_P$. The figure shows again the allowed regions at 1σ for the different observables. In accordance with the above reduction for χ^2_{min}, we observe that in this case it is possible to have an overlap of all the bands. However, it is still not possible to reach the central value for the longitudinal polarization fraction, and as mentioned above, this scenario corresponds to a highly fine-tuned combination of parameters.

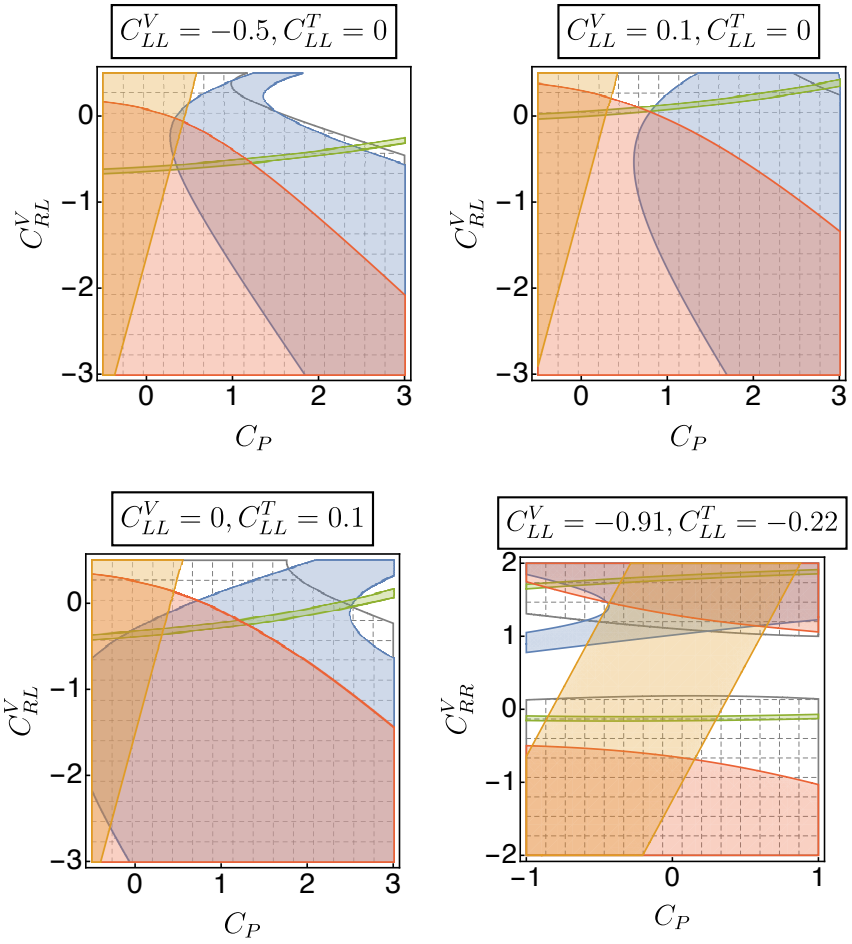

Figure 8.9: Allowed regions at 1σ from $\bar{F}_L^{D^*}$ (blue), $\mathcal{R}_{D^*}$ (green), $\bar{\mathcal{P}}_\tau^{\mathcal{D}^*}$ (gray grid) and the q^2 distribution of $\Gamma(B \to D^* \tau \bar{\nu}_\tau)$ (red), together with the region satisfying the bound $\mathcal{B}(B_c \to \tau \bar{\nu}_\tau) < 10\%$ (orange), with $C_{RL}^V \neq 0$.

8.2.4 Predictions

We use our global fits from Section 8.2.2 to predict selected observables that are either not measured yet, but expected to be measured soon, or presently measured with uncertainties that are larger than those from the fits. These additional measurements serve two purposes: firstly, they provide additional information that is theoretically related, but experimentally independent (to varying extent) from existing measurements, thereby help-

ing to establish NP and excluding underestimated systematic uncertainties as the source for the anomaly. Secondly, they can provide experimental information on combinations of Wilson coefficients that are not or only weakly constrained so far, thereby allowing to distinguish different NP scenarios.

We will first present the predictions for observables of the key modes $B \to D^{(*)}\tau\bar{\nu}_\tau$, before focusing on other semi-leptonic decays, specifically $\Lambda_b \to \Lambda_c\,\tau\bar{\nu}_\tau$ and $B_c \to J/\psi\,\tau\bar{\nu}_\tau$.

We start by analyzing the q^2 distributions of several angular observables. While these distributions can be very effective in distinguishing different NP scenarios, they are difficult to measure, due to the missing information on the neutrinos. The angular dependence of the differential decay width $B \to D^{(*)}\ell\nu$ can be parametrized by three independent angular coefficients,

$$\frac{d^2\Gamma^{D^{(*)}}}{dq^2\, d\cos\theta_\ell} = a_\ell^{(*)}(q^2) - b_\ell^{(*)}(q^2)\cos\theta_\ell + c_\ell^{(*)}(q^2)\cos^2\theta_\ell\,, \tag{8.2.16}$$

which are in principle experimentally accessible. Here, θ_ℓ is the angle between the $D^{(*)}$ and charged-lepton three-momenta in the ℓ–ν center-of-mass frame. An angular observable commonly defined in the literature is the forward-backward asymmetry, which is determined by the $b_\ell^{(*)}(q^2)$ coefficient according to Eqs. (4.3.34) and (4.3.51) of Chapter 4 or in terms of $b_\ell^{(*)}(q^2)$,

$$\mathcal{A}_{\rm FB}^{D^{(*)}}(q^2) \equiv b_\ell^{(*)}(q^2) \Big/ \frac{d\Gamma^{D^{(*)}}}{dq^2}\,. \tag{8.2.17}$$

This observable yields complementary information, since it does not contribute for quantities integrated over the full range of $\cos\theta_\ell$. One can also decompose the differential branching ratio according to the two possible polarizations of the charged (τ) lepton, giving rise to another observable named τ polarization asymmetry of Eqs. (4.3.35) and (4.3.55).

Analogously, one can extract from the angular distribution in the secondary $D^* \to D\pi$ decay the fraction of longitudinally polarised D^* mesons by constructing the observable $F_L^{D^*}(q^2)$ of Eq. (4.3.48). In Fig. 8.10, we show the q^2 dependence of the $B \to D^{(*)}\tau\bar{\nu}$

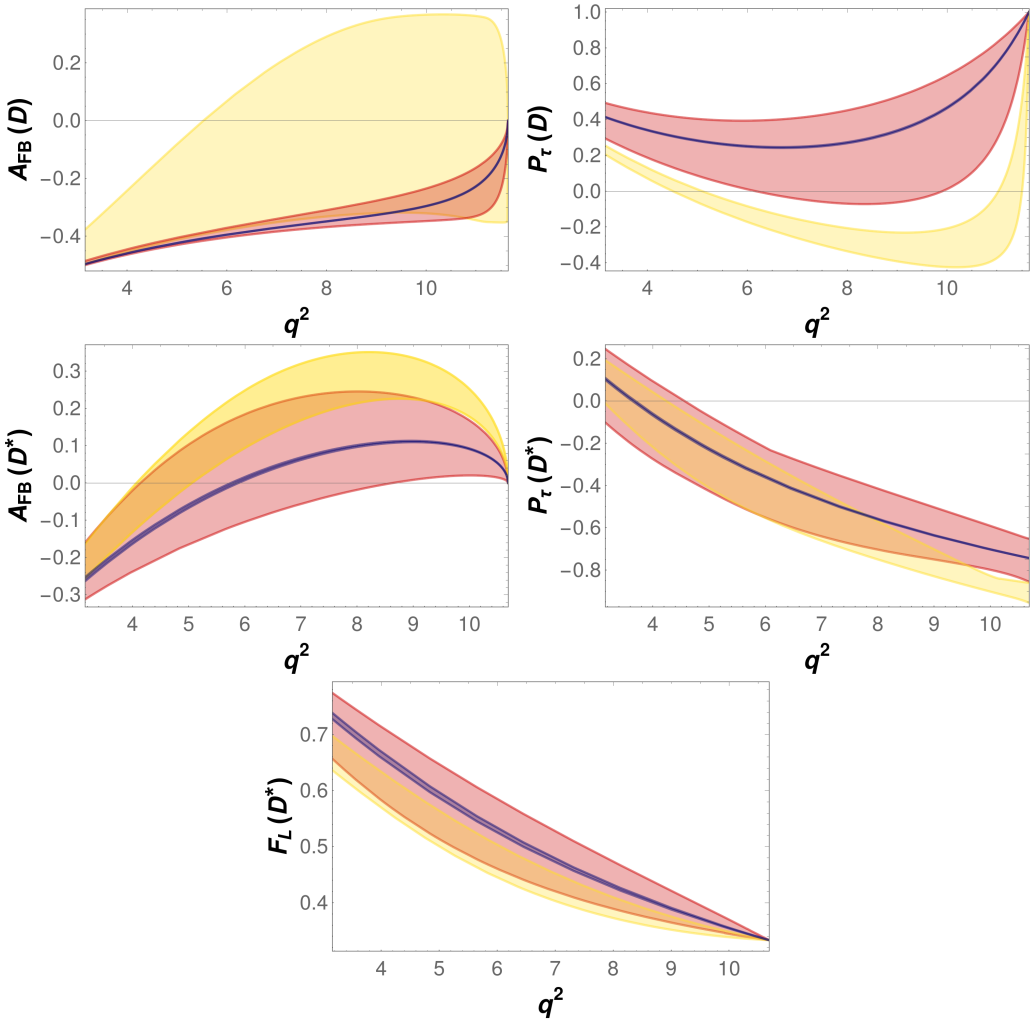

Figure 8.10: Predictions and 1σ uncertainty on the q^2 dependence of the $B \to D^{(*)}\tau\bar{\nu}_\tau$ observables, for the solutions of the fit including the Moriond result and $F_L^{D^*}$. An upper bound of $\mathcal{B}(B_c \to \tau\bar{\nu}_\tau) \leq 30\%$ has been adopted. The predictions of *Min 1b*, *Min 2b* and the SM are represented by a red, yellow and blue band, respectively.

observables defined above, for the two solutions obtained in the global fit including $\bar{F}_L^{D^*}$, *Min 1b* and *Min 2b*, together with their SM prediction.

Using these observables, *Min 2b* could rather clearly be differentiated from both the SM and *Min 1b*. The same is not true for *Min 1b* and the SM, for the simple reason that

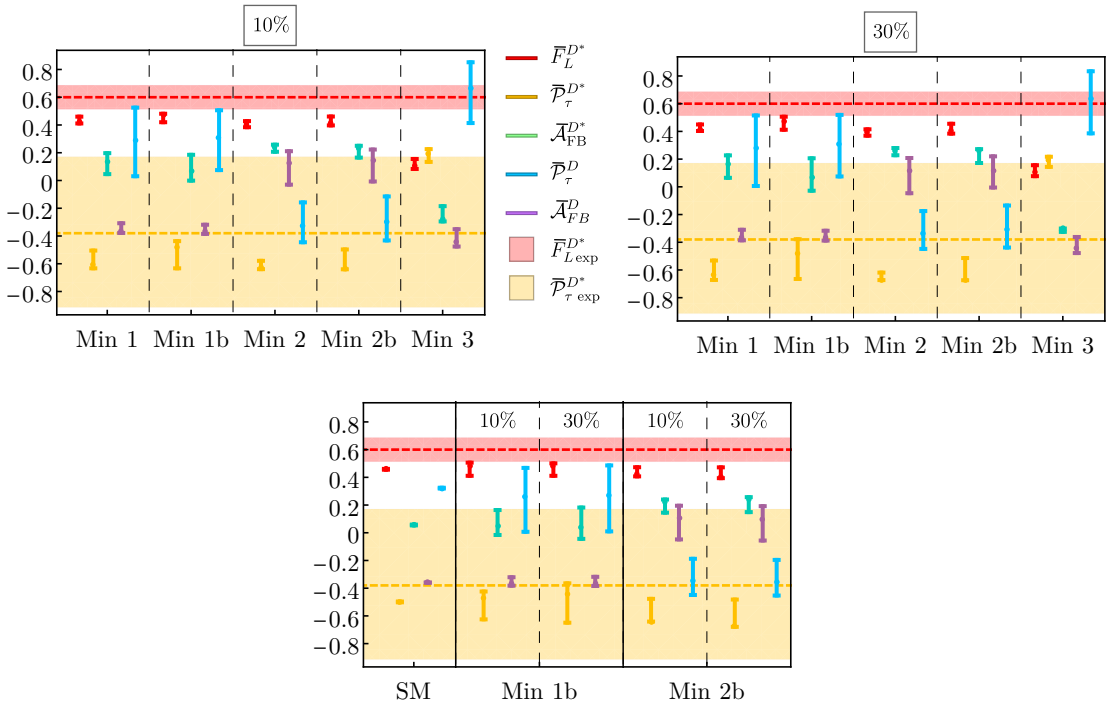

Figure 8.11: The upper panels show the predictions of selected observables for the different minima without (*Min 1*, *Min 2* and *Min 3*) and with (*Min 1b*, *Min 2b*) the inclusion of $\bar{F}_L^{D^*}$ in the fit. The shaded areas show the experimental results at 1σ where applicable. On the left (right) panel, a bound of $\mathcal{B}(B_c \to \tau\bar{\nu}_\tau) \leq 10\%$ (30%) has been applied. The lower panel shows the predictions of the same observables for the two minima obtained in the fit including $\bar{F}_L^{D^*}$ and the preliminary Belle result, with a bound of $\mathcal{B}(B_c \to \tau\bar{\nu}_\tau) \leq 10\%$ and 30%, and for the SM (first column).

this minimum is compatible with only shifting the SM coefficient at 1σ. In that case the SM predictions are unchanged, which means that the width of the red bands is due to the possible presence of additional NP operators. Precise measurements of these distributions could hence show the existence of operators other than $\mathcal{O}_{LL}^V$.

Given the aforementioned difficulty with measuring q^2 distributions, defined as $\bar{\mathcal{O}}$ (see Eq. (4.3.49)). The Belle collaboration has in fact released results for two integrated quantities, the τ polarisation asymmetry $\bar{\mathcal{P}}_\tau^{D^*} = -0.38 \pm 0.51\,(\text{stat})\,^{+0.21}_{-0.16}\,(\text{syst})$ [146],

and the recently announced longitudinal polarisation of the D^* meson, $F_L^{D^*} = 0.60 \pm 0.08\ (\text{stat}) \pm 0.04\ (\text{syst})$ [71,320]. In Fig. 8.11, we show the predictions for the integrated observables of $B \to D^{(*)}\tau\bar{\nu}_\tau$, together with their experimental values where available. Clearly already the integrated observables provide a possibility to distinguish the different NP scenarios. The fitted values for $\bar{F}_L^{D^*}$ are closer to the experimental results for the fits including this observable, which is to be expected. However, they fail to reproduce the measurement within 1σ, as discussed above, which renders a more precise measurement of this quantity an exciting prospect.

Another observable that could shed light on the $\mathcal{R}_D^{(*)}$ puzzle is the $\Lambda_b \to \Lambda_c\tau\bar{\nu}_\tau$ decay, in particular the universality ratio

$$\mathcal{R}_{\Lambda_c} = \frac{\mathcal{B}(\Lambda_b \to \Lambda_c\tau\bar{\nu}_\tau)}{\mathcal{B}(\Lambda_b \to \Lambda_c\ell\bar{\nu}_\ell)}\,. \tag{8.2.18}$$

This decay mode has not been observed yet, but LHCb has the potential to perform this measurement in the near future.

On the theoretical side, the differential decay rate $\Lambda_b \to \Lambda_c\ell\bar{\nu}_\ell$ has been calculated in terms of the helicity amplitudes [321,322]:

$$\begin{aligned}\frac{d\Gamma(\Lambda_b \to \Lambda_c\ell\nu)}{dq^2} &= \frac{G_F^2\,|V_{cb}|^2}{348\pi^3}\,\frac{q^2\sqrt{Q_+Q_-}}{m_{\Lambda_b}^3}\left(1-\frac{m_\ell^2}{q^2}\right)^2\left[A_1^{VA} + \frac{m_\ell^2}{2q^2}\,A_2^{VA} + \frac{3}{2}\,A_3^{SP}\right.\\ &+ \left. 2\left(1+\frac{2m_\ell^2}{q^2}\right)A_4^T + \frac{3m_\ell}{\sqrt{q^2}}\,A_5^{VA-SP} + \frac{6m_\ell}{\sqrt{q^2}}\,A_6^{VA-T}\right],\end{aligned} \tag{8.2.19}$$

where $Q_\pm = (m_{\Lambda_b} \pm m_{\Lambda_c})^2 - q^2$. The superindices VA indicate vector and axial-vector contributions ($C_{RL}^V \pm C_{LL}^V$), SP scalar and pseudoscalar ($C_{RL}^S \pm C_{LL}^S$), and T tensor contributions (C_{LL}^T). Being a baryonic decay, this mode is sensitive to different combinations of Wilson coefficients than $B \to D^{(*)}\tau\bar{\nu}_\tau$. We use the parametrization of the QCD form factors from Ref. [321,322], which take the simple form:

$$f(q^2) = \frac{1}{1 - q^2/(m_{\text{pole}}^f)^2}\left[a_0^f + a_1^f(z^f(q^2))^2\right], \qquad z^f(q^2) = \frac{\sqrt{t_+^f - q^2} - \sqrt{t_+^f - t_0}}{\sqrt{t_+^f - q^2} + \sqrt{t_+^f - t_0}}\,. \tag{8.2.20}$$

The numerical values of the corresponding form-factor parameters, extracted from lattice data [321,322], are displayed in Table 8.7.

$a_0^{f_+}$	0.8146 ± 0.0167	$a_0^{h_+}$	0.9752 ± 0.0303	$m_{\text{pole}}^{f_+,\perp}$	6.332 GeV
$a_1^{f_+}$	-4.8990 ± 0.5425	$a_1^{h_+}$	-5.5000 ± 1.2361	$m_{\text{pole}}^{f_0}$	6.725 GeV
$a_0^{f_0}$	0.7439 ± 0.0125	$a_0^{h_\perp}$	0.7054 ± 0.0137	$m_{\text{pole}}^{g_+,\perp}$	6.768 GeV
$a_1^{f_0}$	-4.6480 ± 0.6084	$a_1^{h_\perp}$	-4.3578 ± 0.5114	$m_{\text{pole}}^{g_0}$	6.276 GeV
$a_0^{f_\perp}$	1.0780 ± 0.0256	$a_0^{\tilde{h}_{\perp},+}$	0.6728 ± 0.0088	$m_{\text{pole}}^{h_+,\perp}$	6.332 GeV
$a_1^{f_\perp}$	-6.4170 ± 0.8480	$a_1^{\tilde{h}_+}$	-4.4322 ± 0.3882	$m_{\text{pole}}^{\tilde{h}_+,\perp}$	6.768 GeV
$a_0^{g_\perp,+}$	0.6847 ± 0.0086	$a_1^{\tilde{h}_\perp}$	-4.4928 ± 0.3584		
$a_1^{g_+}$	-4.4310 ± 0.3572				
$a_0^{g_0}$	0.7396 ± 0.0143				
$a_1^{g_0}$	-4.3660 ± 0.3314				
$a_1^{g_\perp}$	-4.4630 ± 0.3613				

Table 8.7: Central values and uncertainties of the nominal form-factor parameters for $\Lambda_b \to \Lambda_c \ell \nu_\ell$ [321, 322].

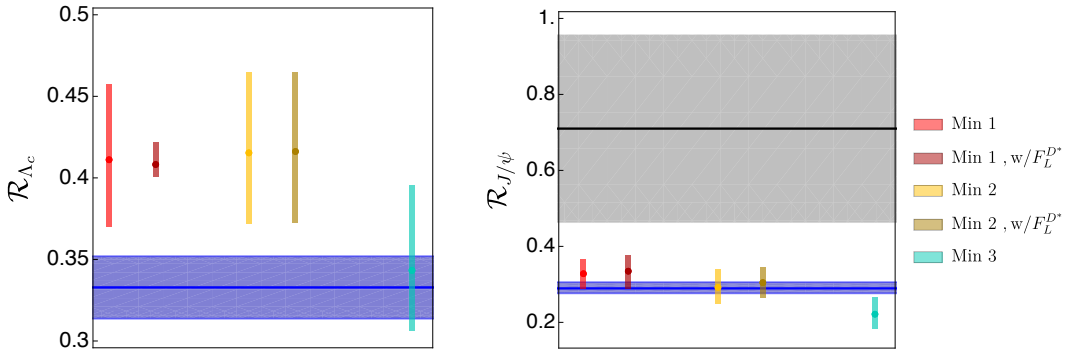

Figure 8.12: Predictions for $\mathcal{R}_{\Lambda_c}$ (left) and $\mathcal{R}_{J/\psi}$ (right) for the minima of Table 8.3 and Table 8.4, with an upper bound $\mathcal{B}(B_c \to \tau\nu) \leq 10\%$. The SM prediction is shown as a blue band. The experimental value of $\mathcal{R}_{J/\psi}$ is given by the gray band.

Fig. 8.12 shows the predicted ratio $\mathcal{R}_{\Lambda_c}$ and its uncertainty for the three minima of Table 8.3 (*Min 1*, *Min 2* and *Min 3*) and the two minima including $\bar{F}_L^{D^*}$ of Table 8.4 (*Min 1b* and *Min 2b*), with the upper limit $\mathcal{B}(B_c \to \tau\nu) \leq 10\%$, and the SM prediction. The errors considered here just take into account the variation of the Wilson coefficients and the parametric error for the lattice input. Other systematic errors are not shown. In all cases the predicted value of $\mathcal{R}_{\Lambda_c}$ is above the SM expectation. This agrees with the observation made in Ref. [259] that the measured enhancement of the ratios $\mathcal{R}_D^{(*)}$ implies an enhancement of $\mathcal{R}_{\Lambda_c}$ for any model of new physics described by the effective Hamiltonian (4.0.1). The prediction closest to the SM is obtained with the unstable minimum *Min 3*, which disappears when $\bar{F}_L^{D^*}$ is included, because it involves a larger value of C_{LL}^T.

The ratio

$$\mathcal{R}_{J/\psi} = \frac{\mathcal{B}(B_c \to J/\psi\tau\bar{\nu}_\tau)}{\mathcal{B}(B_c \to J/\psi\mu\bar{\nu}_\mu)} = 0.71 \pm 0.17 \pm 0.18\,, \tag{8.2.21}$$

has been recently measured by LHCb with the run-1 dataset (3fb^{-1}) [72]. We have not included this observable in our fit because the hadronic uncertainties are not at the same level as for the observables related to $B \to D^{(*)}$ transitions and the experimental error

is large. [6] Instead, the predictions for this observable are computed and compared with the current data. The experimental uncertainties are expected to be significantly reduced with the larger statistics already accumulated at LHCb.

The differential decay rate for this transition can be expressed in a similar way than the $\bar{B} \to D^*$ distribution in Eq. (4.3.44) [325]:

$$\begin{aligned}
\frac{d\Gamma(B_c \to J/\psi \ell \bar{\nu})}{dq^2} &= \frac{G_F^2 \left|V_{cb}\right|^2}{192\pi^3 m_{B_c}} q^2 \sqrt{\lambda_{J/\psi}(q^2)} \left(1 - \frac{m_\ell^2}{q^2}\right) \times \\
&\left\{ (\left|1 + C_{LL}^V\right|^2 + \left|C_{RL}^V\right|^2) \left[\left(1 + \frac{m_\ell^2}{2q^2}\right) \left(H_{V,+}^2 + H_{V,-}^2 + H_{V,0}^2\right) + \frac{3}{2} \frac{m_\ell^2}{q^2} H_{V,t}^2 \right] \right. \\
&- 2\,\mathcal{R}\mathrm{e}\left[(1 + C_{LL}^V) C_{RL}^{V*}\right] \left[\left(1 + \frac{m_\ell^2}{2q^2}\right) \left(H_{V,0}^2 + 2H_{V,+} \cdot H_{V,-}\right) + \frac{3}{2} \frac{m_\ell^2}{q^2} H_{V,t}^2 \right] \\
&+ \frac{3}{2} \left|C_{LL}^S - C_{RL}^S\right|^2 H_S^2 + 8 \left|C_{LL}^T\right|^2 \left(1 + \frac{2m_\ell^2}{q^2}\right) \left(H_{T,+}^2 + H_{T,-}^2 + H_{T,0}^2\right) \\
&+ 3\,\mathcal{R}\mathrm{e}\left[\left(1 + C_{LL}^V - C_{RL}^V\right) \left(C_{LL}^{S*} - C_{RL}^{S*}\right)\right] \frac{m_\ell}{\sqrt{q^2}} H_S \cdot H_{V,t} \qquad (8.2.22) \\
&- 12\,\mathcal{R}\mathrm{e}\left[\left(1 + C_{LL}^V\right) C_{LL}^{T*}\right] \frac{m_\ell}{\sqrt{q^2}} \left(H_{T,0} \cdot H_{V,0} + H_{T,+} \cdot H_{V,+} - H_{T,-} \cdot H_{V,-}\right) \\
&+ \left. 12\,\mathcal{R}\mathrm{e}\left[C_{RL}^V C_{LL}^{T*}\right] \frac{m_\ell}{\sqrt{q^2}} \left(H_{T,0} \cdot H_{V,0} + H_{T,+} \cdot H_{V,-} - H_{T,-} \cdot H_{V,+}\right) \right\},
\end{aligned}$$

where $\lambda_{J/\psi}(q^2) = \left[(m_{B_c} - m_{J/\psi})^2 - q^2\right] \left[(m_{B_c} + m_{J/\psi})^2 - q^2\right]$ is the usual Källén function and H_i are the hadronic helicity amplitudes.

The predicted values of $R_{J/\psi}$ for the minima of Tables 8.3 and 8.4 as well as for the SM, are given in the right panel of Fig. 8.12. Again the errors considered here just take into account the variation of the Wilson coefficients and the parametric error for the lattice input. For this observable, there are additional theoretical uncertainties associated with the parametrization of the form factors, which are difficult to quantify. Given the large errors, the predictions from all minima are in agreement with the experimental measurement. We note that the prediction from the global minimum is the one that approaches closest to the experimental measurement, albeit only slightly.

[6] After the submission of this thesis the first lattice QCD determination of $B_c \to J/\psi$ vector and axial-vector FFs was presented [323]. This gives a value of $\mathcal{R}_{J/\psi} = 0.2601(36)$ [324].

8.2.5 Results after Moriond 2019

In summer 2019, after Moriond results the HFLAV collaboration released a new world average of the $\mathcal{R}_D$ and $\mathcal{R}_{D^*}$ ratios [219]: [7]

$$\mathcal{R}_D^{\text{avg,new}} = 0.340 \pm 0.027 \pm 0.013 \qquad \text{and} \qquad \mathcal{R}_{D^*}^{\text{avg,new}} = 0.295 \pm 0.011 \pm 0.008\,, \tag{8.2.23}$$

with a correlation of -0.38. These averages give a 3.7σ discrepancy with respect to our SM prediction instead of the 3.1σ calculated by HFLAV. The slightly larger significance with respect to the value quoted by HFLAV is due to our different SM prediction and has three aspects: slightly smaller central value and uncertainty for $\mathcal{R}_{D^{(*)}}$, as well as the inclusion of the correlation between the SM predictions for $\mathcal{R}_D$ and $\mathcal{R}_{D^*}$. Regarding the central value, note also the $\sim 1\sigma$ lower central value of the SM prediction for $\mathcal{R}_{D^*}$ in [44] compared to [61] after taking into account new data for $B \to D^* \ell\nu$.

In Table 8.8 we update the results of our baseline fit with the new HFLAV averages (assuming a lepton universal C_{RL}^V and including the longitudinal D^* polarisation, $\bar{F}_L^{D^*}$). Comparing it with Table 8.4 one can note that the results vary slightly with central values for the Wilson coefficients, in general closer to the SM. The conclusion of our work do not change significantly with this new measurements.

8.2.6 Conclusions

In this first work we have analysed the new-physics parameter space able to explain the current anomalies in $b \to c\tau\nu$ data, taking the available experimental information at face value, *i.e.*, disregarding the possibility that these anomalies could originate in underestimated systematic uncertainties or statistical fluctuations. We have performed a global fit

[7] The additional shift with respect to our preliminary average given in Eq. (7) is due to a different treatment for $\mathcal{B}(B \to D^{(*)}\ell\nu)$: in the new HFLAV average a measurement by the BaBar collaboration [326] is omitted, because it does not allow for a separation of the different isospin modes.

	Min 1b	*Min 2b*
χ^2_{min}/d.o.f.	37.4/54	40.4/54
C_{LL}^V	$0.09^{+0.13}_{-0.12}$	$0.34^{+0.05}_{-0.07}$
C_{RL}^S	$0.086^{+0.12}_{-0.61}$	$-1.10^{+0.48}_{-0.07}$
C_{LL}^S	$-0.14^{+0.52}_{-0.07}$	$-0.30^{+0.11}_{-0.50}$
C_{LL}^T	$0.008^{+0.046}_{-0.044}$	$0.093^{+0.029}_{-0.030}$

Table 8.8: Minima and 1σ uncertainties obtained from the global χ^2 minimization, including the new HFLAV world average on the ratios $\mathcal{R}_D$ and $\mathcal{R}_{D^*}$ [219] and the $F_L^{D^*}$ polarization, using $\mathcal{B}(B_c \to \tau\bar{\nu}_\tau) < 10\%$. There are, in addition, the corresponding sign-flipped minima, as indicated in Eq. (8.2.12).

to the available data in $b \to c\tau\bar{\nu}_\tau$ transitions, adopting an EFT approach with a minimal set of assumptions: 1) NP only enters in the third generation of fermions. 2) There is a sizeable energy gap between NP and the electroweak scale, the EFT operators are $SU(2)_L \otimes U(1)_Y$ invariant and the electroweak symmetry breaking is linearly realized. 3) All Wilson coefficients are real (CP is conserved). We have tested the impact of the latter assumption, but did not find an improved description of the data. In contrast to previous works, we considered the q^2 distributions measured by BaBar and Belle. Moreover, we study the effect of including the $\bar{F}_L^{D^*}$ measurement by the Belle collaboration in the fit. A comparison with earlier analyses, either not including the q^2 distributions, the $\bar{F}_L^{D^*}$ measurement, or considering smaller sets of operators, precisely illustrates the benefits of our fit: as described in Section 8.2.2, most of the NP solutions found in previous fits are disfavoured once all the information considered in this work is added.

We performed the global fit in different scenarios. As a baseline, we considered the full dataset before the announcement of the $\bar{F}_L^{D^*}$ measurement with the subset of opera-

tors implied by our assumptions, *i.e.* with a flavour-universal coefficient C_{RL}^V. We then performed extensive comparisons to datasets including the recent $\bar{F}_L^{D^*}$ measurement, the preliminary Belle measurement of $\mathcal{R}_{D^{(*)}}$, and different bounds on $\mathcal{B}(B_c \to \tau\bar{\nu}_\tau)$, as well as a second parameter set, allowing for a non-universal C_{RL}^V.

In the baseline fit, three minima have been obtained, given in Table 8.3. The global minimum, referred to in the text as *Min 1*, has an excellent χ^2; while none of the fitted Wilson coefficients are required to be non-zero for this minimum, the simplest interpretation of this solution is a global modification of the SM: setting all Wilson coefficients but C_{LL}^V to zero increases the χ^2 only by $\Delta\chi^2 = 1.4$, implying an even better fit. The other two solutions are local minima which numerically exhibit stronger deviations from the SM, with larger contributions of the tensor and scalar operators. While the global minimum is compatible with a SM-like scenario, *Min 2* and *Min 3* require additional operators. For instance, they could involve scalar LQs with quantum numbers $R_2 \sim (3, 2, 7/6)$ or $S_1 \sim (\bar{3}, 1, 1/3)$.

The measurement of the D^* longitudinal polarization fraction $\bar{F}_L^{D^*}$ has quite a strong impact on our EFT analysis. It removes *Min 3* as a solution for the fit, which was, however, already strongly disfavoured by the differential distributions. Fig. 8.7 illustrates the tension between the present measurement of $\bar{F}_L^{D^*}$, the bound on $\mathcal{B}(B_c \to \tau\bar{\nu}_\tau)$, and the observation $\Delta\mathcal{R}_{D^*} > 0$: the set of operators considered within our assumptions cannot accommodate all three observations at 1σ for any combination of Wilson coefficients. Indeed, including the $\bar{F}_L^{D^*}$ measurement in the fit increases the minimal χ^2 significantly also for the two lower-lying minima (*Min 1b* and *Min 2b*), see Table 8.4.

We find that most of the minima saturate the upper bound $\mathcal{B}(B_c \to \tau\bar{\nu}_\tau) \leq 10\%$, and it is interesting to study the effect of changing this constraint on the fit. As shown in Tables 8.3 and 8.4, adopting a more conservative upper bound of $\mathcal{B}(B_c \to \tau\bar{\nu}_\tau) \leq 30\%$ we find the same number of minima; they are qualitatively similar to the previous ones, but with larger central values and ranges of the scalar Wilson coefficients, specifically their pseudoscalar combination. While even this larger upper bound is saturated in most of our fits, the overall decrease in χ^2 is small.

The fact that $\bar{F}_L^{D^*}$ cannot be accommodated within 1σ for $C_{RL}^V = 0$ could have important consequences, should the present value be confirmed with higher precision. This led us to investigate the scenario with non-zero C_{RL}^V as a possible resolution of this tension on the theory side. We find that its inclusion helps to reduce the tension among the experimental $B \to D^*$ data, and it is now possible to satisfy all constraints at 1σ, as illustrated in Fig. 8.9. The global fit including C_{RL}^V leads to four different minima, as Fig. 8.8 shows. Two of these minima have a significantly lower χ^2 than the previous fits, however, they correspond to fine-tuned solutions where the SM coefficient becomes very small and its effect is substituted by several sizeable NP contributions, especially C_{RL}^V. This scenario seems therefore not to be a satisfactory resolution of the tension. The new experimental results, summarized in Section 8.2.5 do not yield to significant different results.

We have also presented predictions for selected $b \to c\tau\bar{\nu}_\tau$ observables, such as $\mathcal{R}_{\Lambda_c}$, $\mathcal{R}_{J/\psi}$ or the forward-backward asymmetries and τ polarization in $B \to D^{(*)}\tau\bar{\nu}_\tau$, which have not been included in the fits because either they have not been measured yet or their current experimental values have too large uncertainties. We have studied these observables for the different solutions emerging from our fits, finding that they provide complementary information to the existing data. This is displayed in Figs. 8.10, 8.11 and 8.12. The future measurement of these observables could both establish NP in these modes and allow for a discrimination among the currently favoured scenarios.

We conclude that the anomaly in $b \to c\tau\bar{\nu}_\tau$ transitions remains and can be addressed by NP contributions. Apart from $\mathcal{R}_{D^{(*)}}$, also the differential q^2 distributions, $F_L^{D^*}$ and $\mathcal{B}(B_c \to \tau\bar{\nu}_\tau)$ are important to constrain NP, leaving only two viable minima in the global fit. Our general EFT approach does not allow to identify uniquely the potential mediator, since the global minimum can be generated by several combinations of parameters. The generality of our analysis on the other hand allows to use the obtained parameter ranges in more general SMEFT analyses. An improved measurement of $\bar{F}_L^{D^*}$ close to its present central value holds the exciting potential to invalidate this general approach, which would have major implications, like a Higgs sector different from the SM one, the existence of

NP particles relatively close to the electroweak scale, or new light degrees of freedom. As we have shown, additional measurements will be able to clarify these questions.

8.3 Global fit with right-handed neutrinos

Light RHNs have been suggested [80, 85, 317–319, 327–332] as a possibility to evade the current phenomenological constraints on the EFT operators containing LHN fields. Sterile neutrinos are singlets under the SM gauge group and, therefore, their properties are not linked to any charged electroweak partners. Moreover, the existing limits from the neutrino sector do not constrain significantly the scale of ν_R operators beyond what is probed in $b \to c\tau\bar{\nu}$ transitions. In order not to disrupt the measured $B \to D^{(*)}\tau\bar{\nu}$ invariant-mass distributions [64, 65], one just needs to assume the ν_R fields to be light, $m_{\nu_R} \lesssim O(100)$ MeV, which also helps to avoid other cosmological and astrophysical limits. Neglecting neutrino masses, there is no interference between the two neutrino chiralities, and the decay probability becomes an incoherent sum of ν_L and ν_R contributions: $\mathcal{B}(b \to c\tau\bar{\nu}) = \mathcal{B}(b \to c\tau\bar{\nu}_L) + \mathcal{B}(b \to c\tau\bar{\nu}_R)$. Therefore, it is not difficult to increase the predicted rates towards the experimentally favoured range. However, a large ν_R contribution requires the corresponding Wilson coefficients to be large, of the order of the SM ν_L interaction, because the rates are quadratic in the ν_R transition amplitude.

Previous works considering RHNs in $B \to D^{(*)}\tau\bar{\nu}$ decays [80,85,317–319,327–332] have focused on reproducing the integrated rates, most of them within particular scenarios of NP. All phenomenological analyses need to rely on the underlying assumption that the differential decay distributions, and hence the experimental acceptances, are not significantly modified by the NP contributions. While this assumption is unavoidable, in the absence of direct access to the data, none of the previous studies have included the measured q^2 distributions in their fits. This shape information has been shown to play an important role, discarding many proposed solutions with ν_L fields [52, 74, 150, 237, 238], and could be expected to be even more relevant for those solutions based on RHNs, since they induce distortions in the rates that are quadratic in NP contributions.

We aim to improve the situation in this section, by extending the EFT analysis of the previous Section (see also Ref. [52]) to a basis of dimension-six operators that includes light RHNs. In our fit procedure, we consider all observables measured for $B \to D^{(*)}\tau\bar{\nu}$ decays until date; including the data for binned differential distributions with respect to the lepton-neutrino invariant-mass squared, the D^* longitudinal polarization fraction $\bar{F}_L^{D^*}$, the lepton polarization asymmetry $\bar{\mathcal{P}}_\tau^{D^*}$ and the experimental results for $\mathcal{R}_{D^{(*)}}$. The last ratios have been recently altered, reducing the tension with the SM and making a fresh re-analysis necessary. We also study the differential three-body $B \to D\tau\bar{\nu}$ decay distribution and derive the four-body angular distribution of the $B \to D^*(\to D\pi)\tau\bar{\nu}$ decay for the most general dimension-six Hamiltonian. By identifying the possible high-scale NP mediators which can generate the operators involving RHNs, we predict several angular observables that can be tested at the experiment.

The rest of the section is organized as follows. In Section 8.3.1 the experimental status of the $b \to c$ transitions is interpreted from an EFT approach, by looking at the effect that individual Wilson coefficients may produce in the relevant observables. In addition, all possible NP mediators that can effectively generate a $b \to c\tau\bar{\nu}_R$ transition, and the corresponding Wilson coefficients that will arise at low energies after their integration, are listed. In Section 8.3.2 the results of our fits are presented and discussed. We consider different scenarios, originated by the integration of the relevant NP mediators, and compare their fitted results with the SM case. Section 8.3.4 contains the predicted angular coefficients of the $B \to D\tau\bar{\nu}$ and $B \to D^*(\to D\pi)\tau\bar{\nu}$ distributions for the best fit scenarios, including the forward-backward asymmetries $\mathcal{A}_{FB}^{D^{(*)}}$, the τ polarization asymmetries $\mathcal{P}_\tau^{D^{(*)}}$, and the longitudinal polarization fraction $F_L^{D^*}$. Finally, conclusions are exposed in Section 8.3.5.

8.3.1 Interpreting the anomalies with RHN

This section is devoted to study the origin of the observed experimental deviations from the SM predictions. We show from a theoretical perspective the implications of new physics

in the observables involving $b \to c$ transitions and discuss the possible ultraviolet (UV) scenarios that could give rise to such anomalies in the context of $b \to c$ processes involving both left- and right-handed neutrinos.

8.3.1.1 Fit-independent results

The Wilson coefficients introduced in Eq. (4.0.1) encode all NP contributions that can enter in $b \to c$ transitions at dimension-six operator level, also in the presence of sterile light RHNs. Therefore, the landscape of possibilities generating the anomalies can be classified by the impact of these ten parameters on the measurable observables. To get a general idea about the sensitivity to the different Wilson coefficients, we quote the numerical expressions of several observables that have already been measured. These expressions have been obtained setting the FFs at their central values and, therefore, ignoring the uncertainties and correlations among the different numerical factors. The complete analytical expressions, with a proper account of hadronic uncertainties, will be used instead in the data fits that we will present in Section 8.3.2. The observables $\mathcal{R}_D$ and $\mathcal{R}_{D^*}$ are normalized to their SM predictions:

$$\begin{aligned}
\mathcal{R}_D/\mathcal{R}_D^{\rm SM} \;\approx\; & \left(|1+C_{LL}^V+C_{RL}^V|^2+|C_{LR}^V+C_{RR}^V|^2\right)+1.037\left(|C_{LL}^S+C_{RL}^S|^2+|C_{LR}^S+C_{RR}^S|^2\right)\\
+\;& 0.939\left(|C_{LL}^T|^2+|C_{RR}^T|^2\right)+1.171\,\mathcal{R}{\rm e}\left[(1+C_{LL}^V+C_{RL}^V)\,C_{LL}^{T*}+(C_{LR}^V+C_{RR}^V)\,C_{RR}^{T*}\right]\\
+\;& 1.504\,\mathcal{R}{\rm e}\left[(1+C_{LL}^V+C_{RL}^V)(C_{LL}^{S*}+C_{RL}^{S*})+(C_{LR}^V+C_{RR}^V)(C_{LR}^{S*}+C_{RR}^{S*})\right],
\end{aligned}$$

and

$$\begin{aligned}
\mathcal{R}_{D^*}/\mathcal{R}_{D^*}^{\rm SM} \;\approx\; & \left(|1+C_{LL}^V|^2+|C_{RL}^V|^2+|C_{LR}^V|^2+|C_{RR}^V|^2\right)+0.037\left(|C_{RL}^S-C_{LL}^S|^2+|C_{RR}^S-C_{LR}^S|^2\right)\\
+\;& 17.378\left(|C_{LL}^T|^2+|C_{RR}^T|^2\right)-1.781\,\mathcal{R}{\rm e}\left[(1+C_{LL}^V)\,C_{RL}^{V*}+C_{LR}^V\,C_{RR}^{V*}\right]\\
+\;& 5.748\,\mathcal{R}{\rm e}\left[C_{RL}^V C_{LL}^{T*}+C_{LR}^V C_{RR}^{T*}\right]-5.130\,\mathcal{R}{\rm e}\left[(1+C_{LL}^V)\,C_{LL}^{T*}+C_{RR}^V\,C_{RR}^{T*}\right]\\
+\;& 0.114\,\mathcal{R}{\rm e}\left[(1+C_{LL}^V-C_{RL}^V)\,(C_{RL}^{S*}-C_{LL}^{S*})+(C_{RR}^V-C_{LR}^V)\,(C_{LR}^{S*}-C_{RR}^{S*})\right]. \qquad (8.3.24)
\end{aligned}$$

For the q^2-integrated polarization observables $\bar{\mathcal{P}}_\tau^{D^*}$ and $\bar{F}_L^{D^*}$, we show their numerical values multiplied by $\mathcal{R}_{D^*}$:

$$\begin{aligned}
\bar{\mathcal{P}}_\tau^{D^*} \times \mathcal{R}_{D^*} \;\approx\; & -0.128 \left(|1 + C_{LL}^V|^2 + |C_{RL}^V|^2 - |C_{RR}^V|^2 - |C_{LR}^V|^2\right) + 0.282 \left(|C_{LL}^T|^2 - |C_{RR}^T|^2\right) \\
+ \; & 0.010 \left(|C_{RL}^S - C_{LL}^S|^2 - |C_{RR}^S - C_{LR}^S|^2\right) + 0.221\, \mathcal{R}\mathrm{e}\left[(1 + C_{LL}^V)\, C_{RL}^{V*} - C_{RR}^{V*}\, C_{LR}^V\right] \\
+ \; & 0.442\, \mathcal{R}\mathrm{e}\left[(1 + C_{LL}^V)\, C_{LL}^{T*} - C_{RR}^{V*}\, C_{RR}^T\right] - 0.592\, \mathcal{R}\mathrm{e}\left[C_{RL}^V\, C_{LL}^{T*} - C_{LR}^{V*}\, C_{RR}^T\right] \\
+ \; & 0.030\, \mathcal{R}\mathrm{e}\left[(1 + C_{LL}^V - C_{RL}^V)\, (C_{RL}^{S*} - C_{LL}^{S*}) + (C_{RR}^{V*} - C_{LR}^{V*})\, (C_{RR}^S - C_{LR}^S)\right] \qquad (8.3.25)
\end{aligned}$$

and

$$\begin{aligned}
\bar{F}_L^{D^*} \times \mathcal{R}_{D^*} \;\approx\; & 0.120 \left(|1 + C_{LL}^V - C_{RL}^V|^2 + |C_{RR}^V - C_{LR}^V|^2\right) \\
+ \; & 0.010 \left(|C_{RL}^S - C_{LL}^S|^2 + |C_{RR}^S - C_{LR}^S|^2\right) + 0.869 \left(|C_{LL}^T|^2 + |C_{RR}^T|^2\right) \\
+ \; & 0.030\, \mathcal{R}\mathrm{e}\left[(1 + C_{LL}^V - C_{RL}^V)\, (C_{RL}^{S*} - C_{LL}^{S*}) - (C_{RR}^V - C_{LR}^V)\, (C_{RR}^{S*} - C_{LR}^{S*})\right] \\
- \; & 0.525\, \mathcal{R}\mathrm{e}\left[(1 + C_{LL}^V - C_{RL}^V)\, C_{LL}^{T*} + (C_{RR}^V - C_{LR}^V)\, C_{RR}^{T*}\right]. \qquad (8.3.26)
\end{aligned}$$

With the above expressions of the four observables, namely $\mathcal{R}_D$, $\mathcal{R}_{D^*}$, $\bar{\mathcal{P}}_\tau^{D^*}$ and $\bar{F}_L^{D^*}$, we analyse the modifications induced by each individual Wilson coefficient on the SM predictions. The corresponding shifts are shown in Fig. 8.13, both for the ν_L (upper panels) and ν_R (lower panels) EFT operators. The experimental central values of the observables are displayed as yellow lines whereas bands of the same colour are used for their 1σ uncertainties. For $\bar{F}_L^{D^*}$ we also indicate the 2σ uncertainty with brown bands. The solid (dashed) lines show the parameter space allowed by the constraint $\mathcal{B}(B_c \to \tau\bar{\nu}) < 10\%\,(30\%)$. The fainted lines show the ranges for each Wilson coefficient without imposing the constraint from the leptonic branching ratio $\mathcal{B}(B_c \to \tau\bar{\nu})$.

Different Wilson coefficients could help to reproduce the measured values of $\mathcal{R}_D$ and $\mathcal{R}_{D^*}$. However, the scalar coefficients would need to take values that are already excluded by $\mathcal{B}(B_c \to \tau\bar{\nu})$, leaving vector and axial-vector contributions as the preferred options to fit the experimental results. The large uncertainties in the $\bar{\mathcal{P}}_\tau^{D^*}$ measurement make almost any shift in the Wilson coefficients to be in agreement with the experimental value, being

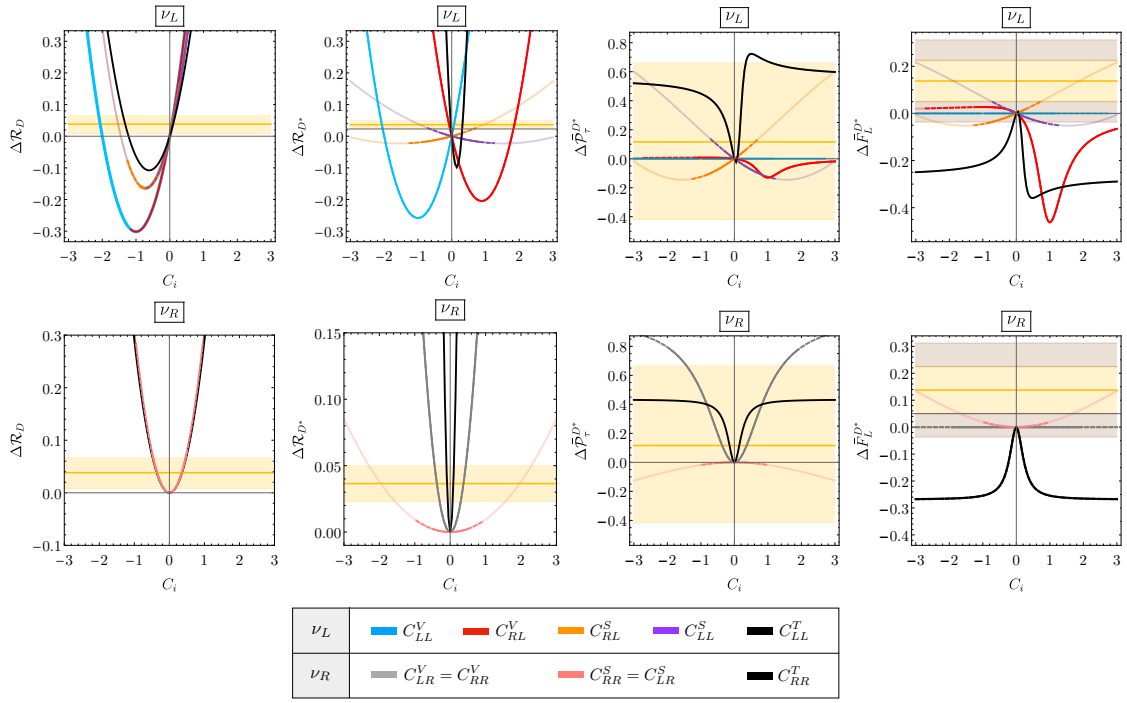

Figure 8.13: Individual contributions of the Wilson coefficients involving LHNs (upper panels) and RHNs (lower panels). The solid (dashed) lines show the parameter space allowed by the constraint $\mathcal{B}(B_c \to \tau\,\bar{\nu}) < 10\%\,(30\%)$, whereas the fainted lines show the predictions without taking into account this constraint.

the only exceptions large shifts in the vector Wilson coefficients $C_{LR,RR}^V$ and a positive increment of C_{LL}^T.

Looking at the dependence of these observables on the RHN contributions, one observes that all of them are symmetric under the exchanges $C_{LR}^V \leftrightarrow C_{RR}^V$ and $C_{LR}^S \leftrightarrow C_{RR}^S$. In particular, $\bar{F}_L^{D^*}$ is insensitive to any single right-handed operator because their contribution exactly cancels, since it is defined as a ratio as Eq. (4.3.48) shows. This does not hold true for C_{RL}^V, since there is an interference between this NP operator and the SM contribution.

It is particularly challenging to reproduce the experimental value of $\bar{F}_L^{D^*}$, regardless of the type of NP contribution; the $\pm 1\sigma$ band cannot be reached varying any of the Wilson

coefficients individually. Negative non-zero values of C_{RL}^{V} can only slightly increase the predicted longitudinal D^* polarization, while the changes induced by the tensor Wilson coefficients go in the opposite direction of the experimental value, decreasing the SM predictions. The only contributions that would help are the scalar ones, but for values of their Wilson coefficients that are already excluded by the constraint $\mathcal{B}(B_c \to \tau\bar{\nu}) < 30\%$.

8.3.1.2 UV Physics

Once the impact of individual Wilson coefficients in $B \to D^{(*)}\tau\bar{\nu}$ observables is understood, the following step is to extend the analysis to the combined effect of several coefficients that are present in these transitions simultaneously. The most general EFT Hamiltonian in Eq. (4.0.1) includes 10 Wilson coefficients, which in general can be complex. Even assuming them to be real, a 10-parameter fit would become unstable. Moreover, its interpretation in terms of NP mediators and UV completions might be unrealistic. Instead, we consider particular cases, described in Section 8.3.3.1. Most of them are motivated from the "simplified model" scenarios. In this context, "simplified" refers to a single new mediator particle that can be integrated out to contribute to one or more of the effective operators entering into the $b \to c\tau\bar{\nu}$ transitions. As the main purpose of this work is to explore the effect of light RHNs, we single out those mediators that can contribute to the $b \to c$ transitions and involve a gauge-singlet RHN.

These NP fields can be classified into scalars, vector bosons and leptoquarks, as listed in Table 8.5. Since in most cases both right- and left-handed neutrino operators are generated simultaneously after a given mediator is integrated out, we will explore both the effect of considering only the right-handed contributions as well as the scenarios in which the full set of operators is generated. Unlike in previous references discussing the role of RHNs in $b \to c$ anomalies [80, 319], we also include a fit to the Wilson coefficients that will appear if NP is mediated through the leptoquark $\tilde{V}_2 \sim (\bar{3}, 2, -1/6)$.

Spin	Q.N.	Nature	ν_L-WET	ν_R-WET
0	$S_1 \sim (\bar{3}, 1, 1/3)$	LQ	C_{LL}^V, C_{LL}^S, C_{LL}^T	C_{RR}^V, C_{RR}^S, C_{RR}^T
0	$\Phi \sim (1, 2, 1/2)$	SB	C_{LL}^S, C_{RL}^S	C_{LR}^S, C_{RR}^S
0	$\tilde{R}_2 \sim (3, 2, 1/6)$	LQ	–	C_{RR}^S, C_{RR}^T
1	$U_1^\mu \sim (3, 1, 2/3)$	LQ	C_{LL}^V, C_{RL}^S	C_{RR}^V, C_{LR}^S
1	$\tilde{V}_2^\mu \sim (\bar{3}, 2, -1/6)$	LQ	–	C_{LR}^S
1	$V^\mu \sim (1, 1, -1)$	VB	–	C_{RR}^V

Table 8.9: Spin, $SU(3)_C \otimes SU(2)_L \otimes U(1)_Y$ quantum numbers and nature (LQ = leptoquark, SB = scalar boson, VB = vector boson) of the possible candidates to mediate $b \to c$ transitions involving $\nu_R \sim (1, 1, 0)$. The fourth and fifth columns list the operators with left-handed and right-handed neutrinos, respectively, generated by the integration of the correspondent mediator.

8.3.2 Fit Results

Under the assumption that NP enters only in the third generation of leptons and that Wilson coefficients are real, we have performed fits in different scenarios of the most general dimension-six Hamiltonian, taking into account all experimental data available nowadays. We start by listing the inputs used in the fit, and then we describe the motivated scenarios, based on the previous section, that we are considering. Finally, the results obtained by performing global fits in each of the scenarios are interpreted.

8.3.3 Numerical input of the fits

As it has been previously mentioned we will use the full set of dimension six of Eq. (4.0.1). For the numerical imput of our fits we will use the most recent world-average values of $\mathcal{R}_D$ and $\mathcal{R}_{D^*}$ from Ref. [48] (see Eq. (8.0.2)), including a correlation of -0.38 between them. The longitudinal D^* polarization, $\bar{F}_L^{D^*}$, measured by BaBar [71] and the value of

the q^2-integrated τ polarization, $\bar{\mathcal{P}}_\tau^{D^*}$, measured recently by Belle [66] are also taken into account. The former was not included in the fit without RHNs but its effects can be relevant in these fits in which the set of Wilson operators is extended. Finally we consider the q^2 distributions of the D and D^* meson [64, 65], summarized in Table 9 of Ref. [52]. The different experimental inputs used in the fits are collected in Table 8.10.

Observable	Experimental Value	Reference	Comments
$\mathcal{R}_D$	$0.340 \pm 0.027 \pm 0.013$	[48]	$\mathcal{R}_D$ and $\mathcal{R}_{D^*}$ correlation of -0.38
$\mathcal{R}_{D^*}$	$0.295 \pm 0.011 \pm 0.008$	[48]	
$\bar{\mathcal{P}}_\tau^{D^*}$	$-0.38 \pm 0.51^{+0.21}_{-0.16}$	[66]	
$\bar{F}_L^{D^*}$	$0.60 \pm 0.08 \pm 0.035$	[71]	
D differential q^2 dist.		[64, 65]	
D^* differential q^2 dist.		[64, 65]	
$\mathcal{B}(B_c \to \tau\bar{\nu})$	$\leq 10\%$, 30%	[70, 150, 294, 295]	

Table 8.10: Experimental inputs used in our fits.

As we did in Section 8.2.1 the upper bound for the leptonic decay rate $\mathcal{B}(B_c \to \tau\bar{\nu})$ is taken to be either 30% or 10%. In our analyses the stronger 10% limit is first assumed in the fit and, in those cases where the 10% bound is saturated the fit is repeated by relaxing it to 30%. As Eq. (4.1.8) shows, the $B_c \to \tau\bar{\nu}$ limit constrains the splitting between the $C^V_{LL(RR)}$ and $C^V_{RL(LR)}$ and, specially, between the $C^S_{RL(LR)}$ and $C^S_{LL(RR)}$ Wilson coefficients. For the FFs, we follow the same approach as in Section 8.2, which was described in Section 8.1.1.

8.3.3.1 Scenarios and fit results

As previously mentioned, by adding RHN, the set of operators increases from 5 to 10. The large number of free parameters makes difficult to perform a global fit to the full basis of operators. Instead, we will work in different motivated scenarios that arise by integrating

out a single NP mediator and, therefore, contribute to small subsets of operators at the m_b scale. Possible candidates, their quantum numbers and the operators generated once the given mediator is integrated out are listed in Table 8.9. The last two columns show the operators involving left-handed and right-handed neutrinos. Following previous works, we consider scenarios that only take into account the contributions from RHN operators, labelling them with the letter "*a*" [319], while "*b*" scenarios also contain the LHN operators that are generated in the presence of the corresponding mediators. In addition, we define *Scenarios 1* and *2*, which correspond to consider only right-handed operators, with and without the SM-like contributions, respectively. The set of scenarios that we are going to analyse and the operators involved in each case are:

1) RHN + SM-like contribution: $\mathcal{O}_{LL}^{V}\,,\mathcal{O}_{LR}^{V}\,,\mathcal{O}_{RR}^{V}\,,\mathcal{O}_{LR}^{S}\,,\mathcal{O}_{RR}^{S}\,,\mathcal{O}_{RR}^{T}\,,$

2) RHN: $\mathcal{O}_{LR}^{V}\,,\mathcal{O}_{RR}^{V}\,,\mathcal{O}_{LR}^{S}\,,\mathcal{O}_{RR}^{S}\,,\mathcal{O}_{RR}^{T}\,,$

3) V^{μ}: $\mathcal{O}_{RR}^{V}\,,$

4a) Φ: $\mathcal{O}_{LR}^{S}\,,\mathcal{O}_{RR}^{S}\,,$

4b) Φ: $\mathcal{O}_{LL}^{S}\,,\mathcal{O}_{RL}^{S}$ and $\mathcal{O}_{LR}^{S}\,,\mathcal{O}_{RR}^{S}\,,$

5a) U_1^{μ}: $\mathcal{O}_{RR}^{V}\,,\mathcal{O}_{LR}^{S}\,,$

5b) U_1^{μ}: $\mathcal{O}_{LL}^{V}\,,\mathcal{O}_{RL}^{S}$ and $\mathcal{O}_{RR}^{V}\,,\mathcal{O}_{LR}^{S}\,,$

6) $\tilde{R}_2$: $\mathcal{O}_{RR}^{S}\,,\mathcal{O}_{RR}^{T}$ with $C_{RR}^{S}=4r\,C_{RR}^{T}\,,$

7a) S_1: $\mathcal{O}_{RR}^{V}\,,\mathcal{O}_{RR}^{S}\,,\mathcal{O}_{RR}^{T}$ with $C_{RR}^{S}=-4r\,C_{RR}^{T}\,,$

7b) S_1: $\mathcal{O}_{LL}^{V}\,,\mathcal{O}_{LL}^{S}\,,\mathcal{O}_{LL}^{T}$ and $\mathcal{O}_{RR}^{V}\,,\mathcal{O}_{RR}^{S}\,,\mathcal{O}_{RR}^{T}$ with $C_{LL}^{S}=-4r\,C_{LL}^{T}$ and $C_{RR}^{S}=-4r\,C_{RR}^{T}\,,$

8) $\tilde{V}_2^{\mu}$: $\mathcal{O}_{LR}^{S}\,.$

Scenarios 3, 6 and *8* do not generate any left-handed operator, making the "*a*" and "*b*" labelling unnecessary. In *Scenarios 6, 7a* and *7b*, where scalar and tensor couplings arise

at the NP scale, the renormalization-group running between $\Lambda_{\rm NP} \sim 1$ TeV and the scale m_b generates the factor $r \approx 2$. *Scenarios 3* to *7* have been also studied at Ref. [319].

Within each scenario we will perform a standard χ^2 fit to the data. There are 60 experimental degrees of freedom (d.o.f.), 4 corresponding to $\mathcal{R}_{D^{(*)}}$, $\bar{F}_L^{D^*}$ and $\bar{\mathcal{P}}_\tau^{D^*}$, and 56 to the binned q^2 distributions. Therefore, the number of d.o.f. of our fits is $60 - N_{\rm WC} - 1 = 59 - N_{\rm WC}$, where $N_{\rm WC}$ is the number of Wilson coefficients entering in the fit.

All solutions resulting from our fits will present up to three *flipped* minima with degenerate χ^2 values. The first flipped minimum is obtained by reversing the sign of the LHN Wilson coefficients while keeping the right-handed Wilson coefficients untouched:

$$C_{LL}^{V'} = -2 - C_{LL}^{V}\,, \qquad C_{iL}^{X'} = -C_{iL}^{X}\,, \qquad C_{iR}^{X'} = C_{iR}^{X}\,, \tag{8.3.27}$$

for $X = S, V, T$ and $i = L, R$, except for C_{LL}^V. The second flipped minimum is obtained reversing only the right-handed coefficients,

$$C_{iL}^{X'} = C_{iL}^{X}\,, \qquad C_{iR}^{X'} = -C_{iR}^{X}\,, \tag{8.3.28}$$

for $X = S, V, T$ and $i = L, R$, and the last one flipping both left and right Wilson coefficients,

$$C_{LL}^{V'} = -2 - C_{LL}^{V}\,, \qquad C_{iL}^{X'} = -C_{iL}^{X}\,, \qquad C_{iR}^{X'} = -C_{iR}^{X}\,, \tag{8.3.29}$$

for $X = S, V, T$ and $i = L, R$, except for C_{LL}^V. From now on, we will only discuss the minimum which is closest to the SM scenario.

In the following subsections, we will present the fitted solutions for each considered scenario. Whenever some uncertainties are marked with the symbol † (*i.e.*, $C_{RR}^V = -0.69^{+0.64\,\dagger}_{-0.44}$), this indicates that the χ^2 distribution has fallen to another minimum. In these cases, the uncertainty is defined as the range between the central value and the point in which the χ^2 falls to the other minimum. To complete the discussion, it is interesting to see the predicted values of the different observables within each fitted scenario. This information is given in Fig. 8.20 and in Table 8.12, where the numerical predictions are marked either with a green tick (✓) if they agree with the experimental value at 1σ or with

a red cross (✗) if they do not agree. All minima are in agreement with all experimental observables at the 2σ level.

SM fit

The SM fit, where all the Wilson coefficients are set to zero, *i.e.* $C_{AB}^{X} = 0$, gives us the following χ^2:

$$\chi^2_{\rm SM}/\text{d.o.f.} = 52.87/59, \tag{8.3.30}$$

corresponding to a 69.95% probability (p-value, defined below). As in the fit without RHN of Section 8.2.2 the "apparent" good quality of the fit, *i.e.* $\chi^2_{\rm SM}/\text{d.o.f.} < 1$, might be surprising since it contrasts with the approximately 3σ discrepancy claimed in the $\mathcal{R}_D$ and $\mathcal{R}_{D^*}$ measurements. This can be understood by looking at the split up contributions of the fit inputs. Considering only the contribution of the q^2 distributions we find that $\chi^2_{\rm SM}(q^2\,\text{distributions})/\text{d.o.f.} = 36.77/56$, while $\chi^2_{\rm SM}(\mathcal{R}_{D^*}, \bar{F}_L^{D^*}, \bar{\mathcal{P}}_\tau^{D^*})/\text{d.o.f.} = 16.1/4$, corresponding to a 2.98σ tension for the later. Taking into account only the χ^2 value of $\mathcal{R}_{D^{(*)}}$ we obtain 13.36 for 2 d.o.f., recovering the well-known 3.2σ tension.

The last results suggest an overestimation of the absolute χ^2 value, which is introduced while considering in the fit multiple inputs with large uncertainties as, in our case, the q^2 distributions for the B-meson semileptonic decays. The goodness of a fit is usually characterized through the p-value, defined as

$$p(\chi^2_{\rm min}, n) \equiv \int_{\chi^2_{\rm min}}^{\infty} dz\, \chi^2(z, n)\,, \tag{8.3.31}$$

where $\chi^2(z, n)$ is the χ^2 probability distribution function with n d.o.f.. Larger p-values correspond to better explanations of the experimental data than lower ones. In order to quantify the quality of our fit, it is convenient to introduce another parameter called *Pull* that compares any fitted solution with the SM results. This statistical measure is defined as the probability in units of σ corresponding to the difference $\Delta\chi^2_i \equiv \chi^2_{\rm SM} - \chi^2_i$, assuming that $\Delta\chi^2_i$ follows a χ^2 distributed function with $\Delta n_i \equiv n_{\rm SM} - n_i$ d.o.f., where the label i refers to the ith scenario. The translation from probability to sigmas is done

by associating such probability to the one corresponding to a *Pull* number of standard deviations in a normal distribution with Δn_i d.o.f.,[8] *i.e.* [248, 333]

$$\text{Pull}_{\text{SM}} \equiv \text{prob}(\Delta\chi^2_i, \Delta n_i)[\sigma] = \sqrt{2}\,\text{Erf}^{-1}[\text{CDF}(\Delta\chi^2_i, \Delta n_i)], \tag{8.3.32}$$

where $\text{CDF}(\Delta\chi^2_i, \Delta n_i) \equiv 1 - p(\Delta\chi^2_i, \Delta n_i)$ is the χ^2-cumulative distribution function evaluated at $\Delta\chi^2_i$ for Δn_i d.o.f..

In Table 8.11 we display the Pull $_{\text{SM}}$ values of the different fitted minima, together with their corresponding p-values, for all the scenarios analysed. In order to better quantify how favourable are the fitted scenarios with respect to the SM regarding the different observables entering in the fit, we also include their pull for the particular pieces of the χ^2, splitting it into three contributions: the polarization observables $\bar{\mathcal{P}}^{D^*}_\tau$ and $\bar{F}^{D^*}_L$, the ratios $\mathcal{R}_D$ and $\mathcal{R}_{D^*}$ and the q^2-distributions of the $B \to D^{(*)}\tau\bar{\nu}$ decay. In the former we ignore the FF contribution to the χ^2. As we can see in Table 8.11, all scenarios exhibit a sizeable improvement with respect to the SM p-value.

Scenario 1: ν_R + SM-like

Considering only RHN operators and the SM-like contribution, *i.e.* C^V_{LL}, and imposing an upper bound for $\mathcal{B}(B_c \to \tau\bar{\nu})$ of 10%, we find two different solutions: a global minimum and a local one with a slightly higher χ^2, *i.e.*

$$\begin{aligned}
\chi^2/\text{d.o.f.} &= 37.26/53\,, \\
C^V_{LL} &= -0.36^{+0.34}_{-0.64^\dagger}, \qquad C^V_{LR} = \;\; 1.10^{+0.46}_{-0.50}\,, \qquad C^V_{RR} = \;\; 0.031^{+0.14}_{-0.17}\,, \\
C^S_{RR} &= -0.03^{+0.18}_{-0.60}\,, \qquad C^S_{LR} = -0.29^{+0.31}_{-0.53}\,, \qquad C^T_{RR} = -0.105^{+0.066}_{-0.084}\,,
\end{aligned} \tag{8.3.33}$$

[8] A probability of (68.3%, 95.5%, 99.7%) equals to (1σ, 2σ, 3σ), respectively.

and

$$\begin{aligned}
\chi^2/\text{d.o.f.} &= 38.86/53\,, \\
C_{LL}^V &= -0.13^{+0.10}_{-0.82}\,, \qquad C_{LR}^V = -0.09^{+0.29}_{-0.27}\,, \qquad C_{RR}^V = -0.69^{+0.64\,\dagger}_{-0.44}\,, \\
C_{RR}^S &= 0.34^{+0.37}_{-0.56\,\dagger}\,, \qquad C_{LR}^S = -0.030^{+0.74}_{-0.18\,\dagger}\,, \qquad C_{RR}^T = -0.006^{+0.239\,\dagger}_{-0.082}\,.
\end{aligned} \tag{8.3.34}$$

Shifting the Wilson coefficients up to 1.2σ, the global minimum becomes compatible with a solution in which the only non-vanishing Wilson coefficients are C_{LR}^V and C_{RR}^T. As it can be seen in Fig. 8.13, both C_{LR}^V and C_{RR}^T help to reproduce the experimental value of $\mathcal{R}_D, \mathcal{R}_{D^*}$ and $\bar{\mathcal{P}}_\tau^{D^*}$. For $\bar{F}_L^{D^*}$ it is a combination of several operators that helps. In the local minimum, the dominant contribution comes from C_{RR}^V.

As it can be seen in Table 8.12, both minima saturate the $\mathcal{B}(B_c \to \tau\bar{\nu}) \leq 10\%$ constraint. Thus, relaxing it to be up to a 30%, we find

$$\begin{aligned}
\chi^2/\text{d.o.f.} &= 36.42/53\,, \\
C_{LL}^V &= -0.50^{+0.41}_{-0.49\,\dagger}\,, \qquad C_{LR}^V = 1.34^{+0.25}_{-0.60}\,, \qquad C_{RR}^V = 0.204^{+0.298}_{-0.020}\,, \\
C_{RR}^S &= -0.22^{+0.27\,\dagger}_{-0.27}\,, \qquad C_{LR}^S = -0.92^{+0.22\,\dagger}_{-0.15}\,, \qquad C_{RR}^T = -0.123^{+0.069}_{-0.077}\,,
\end{aligned} \tag{8.3.35}$$

and

$$\begin{aligned}
\chi^2/\text{d.o.f.} &= 38.54/53\,, \\
C_{LL}^V &= -0.15^{+0.21}_{-0.86}\,, \qquad C_{LR}^V = -0.15^{+0.31\,\dagger}_{-0.17\,\dagger}\,, \qquad C_{RR}^V = -0.69^{+0.70}_{-0.42}\,, \\
C_{RR}^S &= 0.59^{+0.38\,\dagger}_{-0.41}\,, \qquad C_{LR}^S = -0.24^{+0.61}_{-0.13\,\dagger}\,, \qquad C_{RR}^T = 0.007^{+0.114}_{-0.087}\,.
\end{aligned} \tag{8.3.36}$$

The value of the χ^2/d.o.f. slightly improves in this case, whereas the scalar Wilson coefficients are further away from the SM limit.

In both cases one can see that most of the Wilson coefficients have large uncertainties. This can be understood from the fact that a large set of variables to fit allow for larger

correlations among them, which in turn allows wider ranges for the Wilson coefficients considered. The global and local minima have in fact quite close values of χ^2/d.o.f., and the χ^2 distribution in the region between them is rather flat. Thus, when evaluating their 1σ variations, one minimum falls often into the other one, as indicated by the † symbols.

This scenario is the most general, in the sense that the preferred C_{LL}^V solution without considering RHNs [52] is included in the fit, together with all possible contributions generated as a consequence of having RHNs. No specific NP scenario has been assumed in here.

Scenario 2: ν_R

In this scenario we consider solely the contribution to $b \to c$ processes coming from the presence of RHNs in the theory. Again, this assumption is very general and model independent, in the sense that no specific types of NP mediators are assumed.

As in the previous scenario, with the constraint $\mathcal{B}(B_c \to \tau\bar{\nu}) \leq 10\%$, a global and a local minimum are obtained:

$$\begin{aligned}
\chi^2/\text{d.o.f.} &= 38.54/54\,, \\
C_{LR}^V &= 0.52^{+0.13}_{-0.16}\,, \qquad C_{RR}^V = \;\; 0.06^{+0.15}_{-0.22}\,, \\
C_{RR}^S &= 0.04^{+0.35}_{-0.66}\,, \qquad C_{LR}^S = -0.35^{+0.72}_{-0.16}\,, \qquad C_{RR}^T = -0.057^{+0.080}_{-0.058}\,,
\end{aligned} \tag{8.3.37}$$

and

$$\begin{aligned}
\chi^2/\text{d.o.f.} &= 39.05/54\,, \\
C_{LR}^V &= \;\; 0.07^{+0.30}_{-0.30^\dagger}\,, \qquad C_{RR}^V = 0.42^{+0.11}_{-0.21}\,, \\
C_{RR}^S &= -0.32^{+0.74}_{-0.21}\,, \qquad C_{LR}^S = 0.10^{+0.20^\dagger}_{-0.68}\,, \qquad C_{RR}^T = 0.004^{+0.080}_{-0.088}\,.
\end{aligned} \tag{8.3.38}$$

By shifting all the Wilson coefficients within their 1σ uncertainties, the global minimum is compatible with a solution in which the only non-zero coefficient is C_{LR}^V. This coincides

with the fit dealing only with the LHN operators where the global minimum was compatible with a global shift of the SM-like operator (*i.e.* $C_{LL}^V \neq 0$) [52]. In other words, C_{LR}^V plays a similar role as the ν_L Wilson coefficient modifying the SM contribution. In the local minimum, the main contributions to the observables are coming from C_{RR}^V.

Since the previous fit saturates the leptonic B_c decay bound, we list below the minima obtained after relaxing such constraint to $\mathcal{B}(B_c \to \tau\bar{\nu}) \leq 30\%$:

$$\begin{aligned}
\chi^2/\text{d.o.f.} &= 38.33/54\,, \\
C_{LR}^V &= 0.47^{+0.16}_{-0.20}\,, \qquad C_{RR}^V = \quad 0.10^{+0.21}_{-0.23}\,, \\
C_{RR}^S &= 0.28^{+0.24}_{-0.97}\,, \qquad C_{LR}^S = -0.59^{+0.80}_{-0.17}\,, \qquad C_{RR}^T = -0.054^{+0.081}_{-0.058}\,,
\end{aligned} \tag{8.3.39}$$

and

$$\begin{aligned}
\chi^2/\text{d.o.f.} &= 38.80/54\,, \\
C_{LR}^V &= \quad 0.12 \pm 0.30\,, \qquad C_{RR}^V = 0.38^{+0.13}_{-0.20}\,, \\
C_{RR}^S &= -0.57^{+0.57^\dagger}_{-0.28}\,, \qquad C_{LR}^S = 0.33^{+0.20^\dagger}_{-0.48^\dagger}\,, \qquad C_{RR}^T = -0.006^{+0.081}_{-0.091}\,.
\end{aligned} \tag{8.3.40}$$

Similarly to the previous scenario, when relaxing the leptonic decay bound, the χ^2 experiences an improvement and the scalar Wilson coefficients further depart from the SM limit.

Scenario 3: V_μ

The mediator $V^\mu \sim (1, 1, -1)$ only involves interactions with RHN regarding $b \to c$ transitions. Note that we call it V^μ instead of the usual nomenclature W'^μ in order to distinguish it from the $SU(2)$ triplet which does couple to the LHNs. Therefore, this scenario induces exclusively $b \to c\tau\bar{\nu}_R$ interactions, and particularly the V^μ only contributes to the vector Wilson coefficient C_{RR}^V.

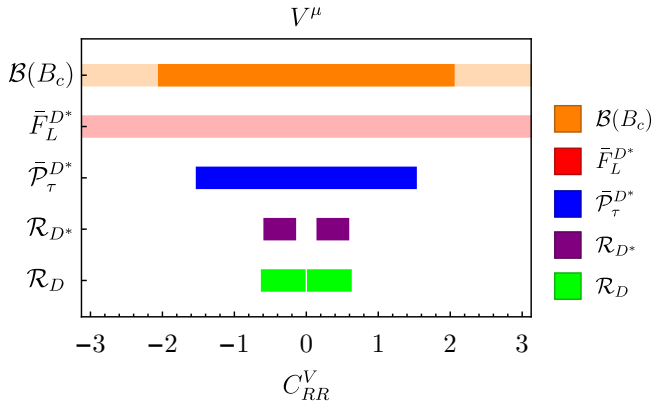

Figure 8.14: Fit-independent plot of *Scenario 3*. Dark colours indicate the allowed regions satisfying the experimental constraints at 1σ and the 10% upper limit on $\mathcal{B}(B_c \to \tau\bar{\nu})$, for a given value of C_{RR}^V. There is no allowed region for $\bar{F}_L^{D^*}$ at 1σ. The lighter orange and red shaded areas correspond to the more relaxed 30% bound on the leptonic B_c decay and the 2σ region for $\bar{F}_L^{D^*}$, respectively.

The global fit gives us the minimum value for this Wilson coefficient together with its χ^2:

$$\begin{aligned} \chi^2/\text{d.o.f.} &= 39.50/58\,, \\ C_{RR}^V &= 0.370^{+0.051}_{-0.059}\,. \end{aligned} \tag{8.3.41}$$

Given that in this case our model depends on a single Wilson coefficient, we can study the regions of the parameter space that reproduce the different experimental observables included in the global fit from a fit-independent perspective, as shown in Fig. 8.14. This figure shows that no region of common overlap can be found at 1σ. This agrees with Fig. 8.13, which showed that the shift of a single Wilson coefficient with respect to the SM scenario does not modify the $\bar{F}_L^{D^*}$ prediction. We also indicate in Fig. 8.14 the parameter space allowed when relaxing the experimental constraint on $\bar{F}_L^{D^*}$ to 2σ and taking $\mathcal{B}(B_c \to \tau\bar{\nu}) \leq 30\%$. As expected, in that context we find full agreement with the experiment.

Scenario 4a: Φ

Considering that the mediator $\Phi \sim (1, 2, 1/2)$, with the same quantum numbers as the SM Higgs, is responsible for the NP interactions, and assuming that only right-handed Wilson coefficients appear at the low-energy scale, two different minima with the same χ^2 value,

$$\begin{aligned} \chi^2/\text{d.o.f.} &= 49.93/57\,, \\ C_{RR}^S &= 0.46^{+0.05}_{-0.18}\,, \qquad C_{LR}^S = -0.06^{+0.19}_{-0.07}\,, \end{aligned} \tag{8.3.42}$$

and

$$\begin{aligned} \chi^2/\text{d.o.f.} &= 49.93/57\,, \\ C_{RR}^S &= 0.06^{+0.07}_{-0.19}\,, \qquad C_{LR}^S = -0.46^{+0.18}_{-0.05}\,, \end{aligned} \tag{8.3.43}$$

are found. As one can see, they correspond to degenerate solutions, flipping the values of C_{LR}^S and C_{RR}^S. This can be easily understood by looking at the expressions of $B \to D$ and $B \to D^*$ listed in Eqs. (4.3.33) and (4.3.44), respectively. These observables depend on the absolute values of the right-handed scalar and pseudoscalar combinations of Wilson coefficients when the vector coefficients are switched off, and therefore remain invariant under the exchange $C_{LR}^S \leftrightarrow C_{RR}^S$. The same is true for the D^* polarization observables that, as shown in Eqs. (8.3.25) and (8.3.26), are blind to a sign flip of the combination $C_{RR}^S - C_{LR}^S$. As Table 8.12 shows, these minima saturate the $\mathcal{B}(B_c \to \tau\bar{\nu}) \leq 10\%$ bound. Relaxing this constraint to $\mathcal{B}(B_c \to \tau\bar{\nu}) \leq 30\%$, the minima read

$$\begin{aligned} \chi^2/\text{d.o.f.} &= 44.49/57\,, \\ C_{RR}^S &= 0.297^{+0.074}_{-0.096}\,, \qquad C_{LR}^S = -0.673^{+0.091}_{-0.053}\,, \end{aligned} \tag{8.3.44}$$

and

$$\begin{aligned} \chi^2/\text{d.o.f.} &= 44.49/57\,, \\ C_{RR}^S &= 0.673^{+0.053}_{-0.091}\,, \qquad C_{LR}^S = -0.297^{+0.096}_{-0.074}\,, \end{aligned} \tag{8.3.45}$$

where, as expected, the pseudoscalar combination of Wilson coefficients increases its value and the χ^2 slightly improves.

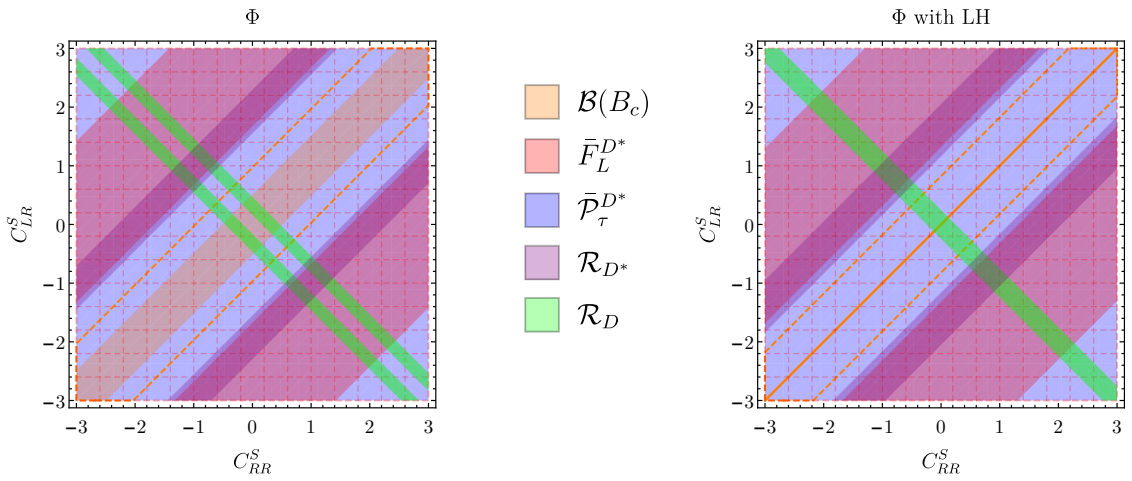

Figure 8.15: Fit-independent plot of *Scenario 4*, displaying the regions allowed at 1σ. On the left panel only the RHN Wilson coefficients shown are switched on (*Scenario 4a)*, whereas on the right panel we set the left-handed neutrino Wilson coefficients entering in *Scenario 4b* to their best-fit values. The dashed orange line shows the more relaxed bound $\mathcal{B}(B_c \to \tau\bar{\nu}) \leq 30\%$, and the red grid shows the parameter space consistent with the experimental measurement of $\bar{F}_L^{D^*}$ at 2σ.

In the left panel of Fig. 8.15 we show the two-dimensional parameter space where the different observables entering in the fit are satisfied at 1σ. As the figure shows, there is no overlap at this given probability. In this case, not even relaxing the leptonic B_c decay upper bound to 30% and the $F_L^{D^*}$ experimental measurement to 2σ, an overlap in the parameter space is achieved.

Scenario 4b: Φ

The Two Higgs Doublet Models are the simplest examples of UV physics generating this scenario. In addition to RHN operators, a second scalar doublet with the same quantum numbers as the SM one generates LHN Wilson coefficients. The preferred solution of this scenario corresponds to vanishing right-handed Wilson coefficients, which eliminates the degeneracy under $C_{LR}^S \leftrightarrow C_{RR}^S$. Owing to the interference with the SM-like contribution,

an analogous symmetry does not exist for the left-handed coefficients and, therefore, we find in this case a single solution with $\mathcal{B}(B_c \to \tau\bar{\nu}) \leq 10\%$:

$$\begin{aligned} \chi^2/\text{d.o.f.} &= 43.56/55\,, \\ C_{RL}^S &= 0.21^{+0.03}_{-0.11}\,, \qquad C_{LL}^S = -0.11^{+0.07}_{-0.08}\,, \\ C_{RR}^S &= 0.0 \pm 0.3\,, \qquad C_{LR}^S = \quad 0.0 \pm 0.3\,. \end{aligned} \tag{8.3.46}$$

With the relaxed limit $\mathcal{B}(B_c \to \tau\bar{\nu}) \leq 30\%$, the splitting between scalar operators is larger and the χ^2 slightly improves:

$$\begin{aligned} \chi^2/\text{d.o.f.} &= 40.03/55\,, \\ C_{RL}^S &= 0.407^{+0.032}_{-0.137}\,, \qquad C_{LL}^S = -0.329^{+0.146}_{-0.080}\,, \\ C_{RR}^S &= 0.00 \pm 0.45\,, \qquad C_{LR}^S = \quad 0.00 \pm 0.45\,. \end{aligned} \tag{8.3.47}$$

The right panel of Fig. 8.15 shows the two dimensional parameter space where the observables entering in the fit are satisfied at 1σ. In this figure, the LHN operators are fixed at their best-fit values. As it can be seen, there is no overlap at this given significance level. The non-existing overlap is also reflected in Table 8.12 and Fig. 8.15, where one can see that scalar solutions cannot satisfy $\mathcal{R}_{D^*}$, nor $\bar{F}_L^{D^*}$. The later is also shown in a very intuitive way in Fig. 8.13.

Scenario 5a: $U_{1\mu}$

The presence of the vector leptoquark $U_{1\mu} \sim (3, 1, 2/3)$ at the high-energy scale will contribute to both left and right-handed operators at the m_b scale. This vector leptoquark can be UV-completed in Pati-Salam based unification theories [334–339] for instance. Considering only the RHN operators, the preferred solution is compatible with a non-zero value of C_{RR}^V while $C_{LR}^S = 0$ at 0.4σ, *i.e.*

$$\begin{aligned} \chi^2/\text{d.o.f.} &= 39.39/57\,, \\ C_{RR}^V &= 0.39^{+0.07}_{-0.08}\,, \qquad C_{LR}^S = -0.1^{+0.2}_{-0.5}\,. \end{aligned} \tag{8.3.48}$$

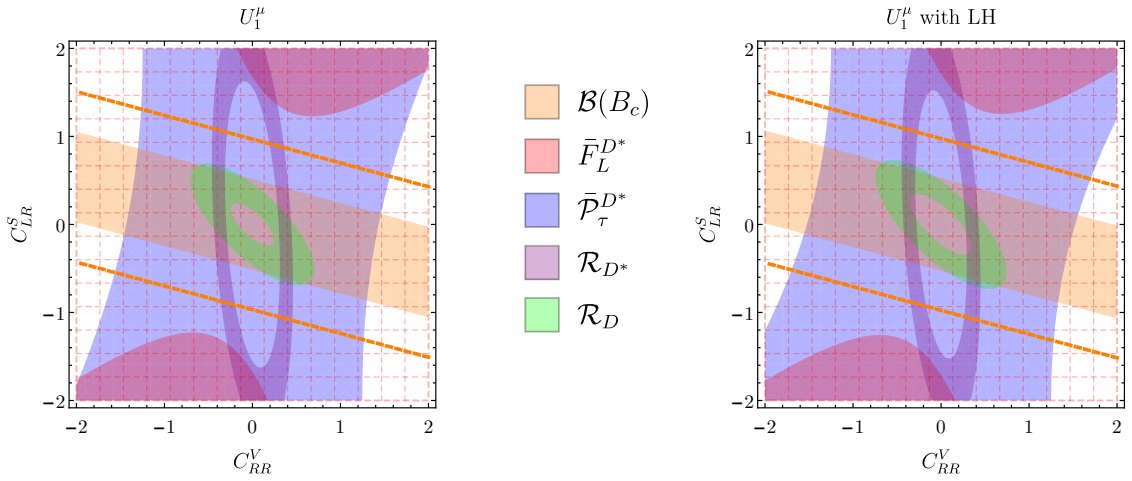

Figure 8.16: Fit-independent plot of *Scenario 5*, showing the regions allowed at 1σ. On the left panel only the right handed neutrino Wilson coefficients are switched on (*Scenario 5a*), whereas on the right panel we set the LHN Wilson coefficients entering in *Scenario 5b* to their best-fit values. The dashed orange line shows the more relaxed bound $\mathcal{B}(B_c \to \tau\bar{\nu}) \leq 30\%$, and the red grid indicates the parameter space consistent with the experimental measurement of $\bar{F}_L^{D^*}$ at 2σ.

Since the scalar coefficient is suppressed, the $\mathcal{B}(B_c \to \tau\bar{\nu})$ limit is not saturated. Furthermore, all the observables included in the fit agree at 1σ, except $\bar{F}_L^{D^*}$ which is compatible with the experimental value at 2σ, as illustrated in the left-panel of Fig. 8.16.

Scenario 5b: $U_{1\mu}$

Including the contributions to LHN operators, the value of the χ^2 remains almost constant with respect to *Scenario 5a*, $\Delta\chi^2 = -0.02$ for 2 new d.o.f., and the left-handed Wilson coefficients are compatible with zero within 1σ:

$$\begin{aligned} \chi^2/\text{d.o.f.} &= 39.37/55\,, \\ C_{LL}^V &= 0.01^{+0.10}_{-0.65}\,, \qquad C_{RL}^S = -0.03^{+0.07}_{-0.45}\,, \\ C_{RR}^V &= 0.38^{+0.60}_{-1.40}\,, \qquad C_{LR}^S = -0.01^{+0.56}_{-0.54}\,. \end{aligned} \tag{8.3.49}$$

This indicates that the best solution for a leptoquark with these quantum numbers involves only RHN operators.

The right panel in Fig. 8.16 shows the small changes on the allowed regions, in comparison with *Scenario 5a* (left panel). Again, all observables are satisfied at 1σ, except for $\bar{F}_L^{D^*}$.

Scenario 6: $\tilde{R}_2$

This scenario considers the solely presence of the scalar leptoquark $\tilde{R}_2 \sim (3, 2, 1/6)$. It is genuine from the perspective of having RHNs, since it does not mediate any interaction involving left-handed ones. The global fit gives:

$$\begin{aligned} \chi^2/\text{d.o.f.} &= 44.20/58\,, \\ C_{RR}^T &= 0.054^{+0.009}_{-0.011}\,. \end{aligned} \tag{8.3.50}$$

In this case, there is only one free parameter, since the two relevant coefficients, C_{RR}^T and C_{RR}^S, are correlated by the Fierz identities. Therefore, one can study the predictions of the fitted observables as a function of only one free parameter in a fit-independent manner, as we show in Fig 8.17. The region with larger overlap in this figure corresponds to the minimum listed in Eq. (8.3.50) and its flipped solution. As in previous scenarios, it is not possible to reproduce the experimental value of $\bar{F}_L^{D^*}$ at 1σ. However, agreement can be find when $\mathcal{B}(B_c \to \tau\bar{\nu}) \leq 30\%$ and $\bar{F}_L^{D^*}$ is considered at 2σ.

Scenario 7a: S_1

The scalar leptoquark $S_1 \sim (\bar{3}, 1, 1/3)$ is considered in this scenario. For *Scenario 7a* we obtain a solution dominated by a single Wilson coefficient, C_{RR}^V, being C_{RR}^T compatible with zero within 1σ:

$$\begin{aligned} \chi^2/\text{d.o.f.} &= 39.21/57\,, \\ C_{RR}^V &= 0.422^{+0.071}_{-0.126}\,, \qquad C_{RR}^T = 0.022^{+0.032}_{-0.037}\,. \end{aligned} \tag{8.3.51}$$

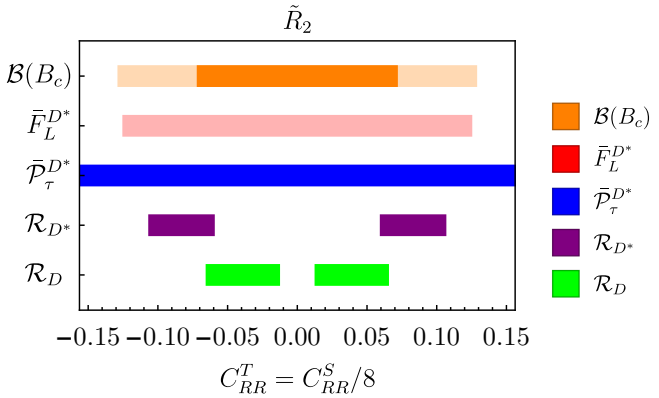

Figure 8.17: Fit-independent plot of *Scenario 6*, showing the regions allowed at 1σ (dark colours), for different values of C_{RR}^T. There is no allowed region for $\bar{F}_L^{D^*}$ at 1σ. The light orange and red shaded areas correspond to the more relaxed 30% bound on the leptonic B_c decay and the 2σ region for $\bar{F}_L^{D^*}$, respectively.

The left panel of Fig. 8.18 shows the regions in the two-dimensional parameter space where the experimental observables can be reproduced at 1σ. Again, at this level of precision, the longitudinal D^* polarization cannot be accommodated together with the other measurements, although it is possible to find overlap between all experimental data when the value of $\bar{F}_L^{D^*}$ is taken at 2σ, shown in the figure as a red grid.

Scenario 7b: S_1

Adding the left-handed operators that contribute in the presence of S_1, we find a solution compatible with vanishing left-handed Wilson coefficients ($\Delta\chi^2 = -0.15$ for 2 d.o.f.) and a slightly shifted value of C_{RR}^V:

$$\begin{aligned} \chi^2/\text{d.o.f.} &= 39.06/55\,, \\ C_{LL}^V &= 0.034^{+0.11}_{-0.70}\,, \qquad C_{LL}^T = 0.010^{+0.037}_{-0.041}\,, \\ C_{RR}^V &= 0.367^{+0.68}_{-1.41^\dagger}\,, \qquad C_{RR}^T = 0.004^{+0.048}_{-0.055^\dagger}\,. \end{aligned} \tag{8.3.52}$$

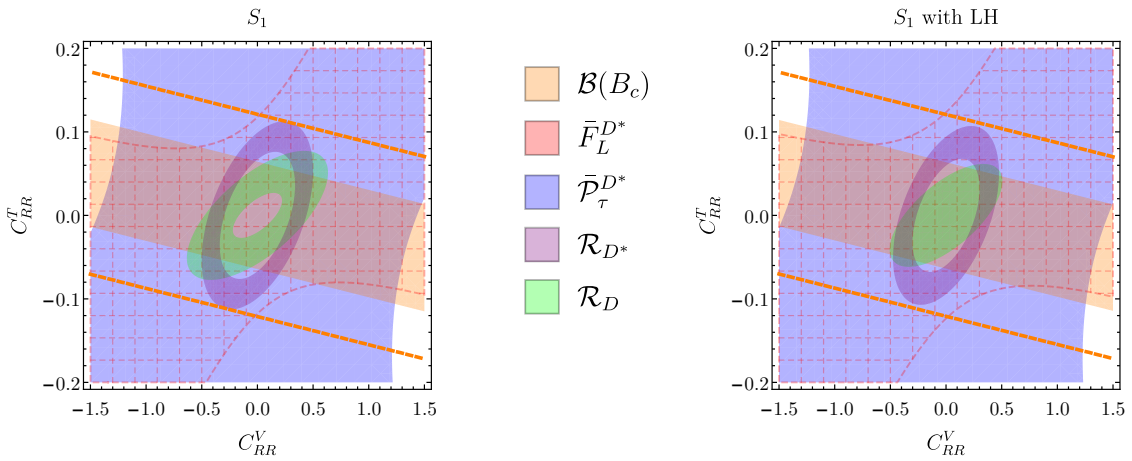

Figure 8.18: Fit-independent plot of *Scenario 7*, showing the regions allowed at 1σ. On the left panel only the RHN Wilson coefficients are considered (*Scenario 7a*), whereas on the right panel we set the LHN Wilson coefficients entering in *Scenario 7b* to their best fit values. The dashed orange line corresponds to the more relaxed bound $\mathcal{B}(B_c \to \tau\bar{\nu}) \leq 30\%$, and the red grid shows the parameter space consistent with the experimental measurement of $\bar{F}_L^{D^*}$ at 2σ.

For the RHN coefficients, C_{RR}^V and C_{RR}^T, the χ^2 distribution turns out to be very flat between the two flipped minima, which no longer can be separated. This implies a very broad negative 1σ interval for C_{RR}^V, reaching its flipped minimum $C_{RR}^{V'} = -0.367$.

As in the case of the vector leptoquark U_1^μ (*Scenarios 5a* and *5b*), the preferred solution for an S_1 leptoquark involves only RHN operators.

Scenario 8: $\tilde{V}_2^\mu$

This is another genuine scenario of RHNs, since it does not generate any $b \to c$ transition involving ν_L operators. The vector leptoquark $\tilde{V}_2^\mu \sim (\bar{3}, 2, -1/6)$ only contributes to the Wilson coefficient C_{LR}^S. This allows us to study the parameter space preferred by the experiment from a fit-independent point of view. As Fig. 8.19 shows, there is no overlap among the different experimental constraints at the 1σ level, nor even considering a more relaxed 30% bound for the leptonic decay $\mathcal{B}(B_c \to \tau\bar{\nu})$ and the experimental value of $\bar{F}_L^{D^*}$

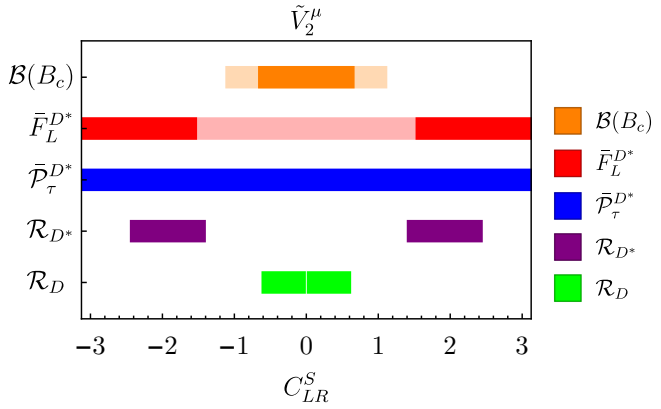

Figure 8.19: Fit-independent plot of *Scenario 8*. Dark colours correspond to the regions satisfying the experimental constraints at 1σ and a 10% upper limit on $\mathcal{B}(B_c \to \tau\bar{\nu})$, for a given value of C_{LR}^S. Lighter orange and red shaded areas correspond to the more relaxed 30% bound on the leptonic B_c decay and the 2σ region for $\bar{F}_L^{D^*}$, respectively.

at 2σ. Numerically, the fit provides the following minimum:

$$\begin{aligned} \chi^2/\text{d.o.f.} &= 47.32/57\,, \\ C_{LR}^S &= 0.418^{+0.097}_{-0.125}\,. \end{aligned} \tag{8.3.53}$$

8.3.3.2 Comments on the fit results

Table 8.11 summarizes the fit quality of the results obtained in the different scenarios analysed, quantified through the corresponding χ^2/d.o.f., the pull with respect to the SM, and the p-value. The resulting predictions in each scenario for the observables included in the fit are also given in Table 8.12, and compared with their experimental measurements in Fig 8.20. Several conclusions can be extracted from these results:

- In general, it is difficult to reproduce the experimental value of the longitudinal D^* polarization within its 1σ range. From Fig. 8.20 and Table 8.12 we can see that the only solutions reproducing all the experimental values (marked with a ✓) are

Scenario 1a with either a 10% (*Min 1*) or 30% (*Min 1* and *Min 2*) upper limit on $\mathcal{B}(B_c \to \tau\bar{\nu})$, and *Scenario 4b* with a 30%.

- All solutions exhibit pulls between 1.2 and 3.7 with respect to the SM fit, showing a clear preference for NP contributions.

- The largest pull with respect to the SM fit is obtained in *Scenario 3*, which only contributes to the C_{RR}^V coefficient. Note that C_{RR}^V plays a similar role than C_{LL}^V in the observables involving $b \to c$ transitions. Therefore, the preference of the fit for this scenario can be easily understood, since a SM-like modification was the best fit solution in absence of RHN [52].

- *Scenarios 4a, 4b, 6* and *8*, involving only scalar (and tensor) operators, have the largest χ^2 value. As Table 8.12 and Fig. 8.20 show, *Scenarios 4a, 4b* and *8* fail badly reproducing the experimental value of $\mathcal{R}_{D^*}$.

- *Scenarios 4a, 4b, 6, 8* and *Scenario 2 Min2*, are disfavoured by the q^2 differential distributions of the $B \to D^{(*)}$ decay with respect to the SM, as the corresponding Pull_{SM} in Table 8.11 shows.

- Those solutions further away from the SM (larger pulls) present higher p-values, as Table 8.11 shows.

- In scenarios with several operators, the best fits correspond to solutions where all Wilson coefficients but one are compatible with zero. The non-zero Wilson coefficient is typically C_{RR}^V (*Scenarios 5a, 5b, 7a* and *7b*).

- When scenarios with and without LHN operators ("*b*" and "*a*" variants, respectively) are compared, the fit indicates a preference for solutions with all left-handed Wilson coefficients compatible with zero within 1σ.

Comparing our results with similar fits previously done in the literature, we can quantify the impact of adding the differential q^2 distributions and considering recently measured

observables such as $\bar{F}_L^{D^*}$ or $\bar{\mathcal{P}}_\tau^{D^*}$, together with the update of some experimental measurements. Ref. [319] analysed all mediators that can contribute to the $b \to c\tau\bar{\nu}_R$ transition, except the $\tilde{V}_2^\mu$ vector leptoquark, but only included in the fit the values of $\mathcal{R}_D$ and $\mathcal{R}_{D^*}$. The global minimum obtained in Ref. [319] for an extra gauge boson V' (*Scenario 3*) agrees with ours, while the two minima obtained for our *Scenario 4a* deviate more from the SM solution than ours. The latter is due to the fact that the $B_c \to \tau\bar{\nu}$ constraint, which has a strong impact on solutions involving scalar Wilson coefficients, was not taken into account in the fit. Indeed, Fig. 2 from Ref. [319] shows that their minima are excluded by this constraint, and this is the reason why in our analysis, this χ^2 is the most unfavourable among all the scenarios considered. For our *Scenario 5a*, mediated by U_1^μ, two minima are observed in Ref. [319] where the furthest one from the SM solution is ruled out by the constraint $\mathcal{B}(B_c \to \tau\bar{\nu}) \leq 10\%$. This situation is repeated in the scenario mediated by S_1, *Scenario 7a*. Finally, in the case of the $\tilde{R}_2$ mediator (our *Scenario 6*), both minima differ slightly from ours since, again, as their Fig. 2 shows, they are excluded by the B_c leptonic decay limit; however, taking into account the minimum value of the χ^2 satisfying this constraint, our result is compatible with Ref. [319].

8.3.4 Predictions

In this section we show the predictions of different observables for the fitted scenarios considered in the previous section. As we will discuss in the following, these results can be used to discriminate between the different scenarios and, in some cases, even distinguish the contribution originated by light RHNs from the SM one.

8.3.4.1 Predictions of integrated observables

In Table 8.12 we list the predictions of the different integrated observables considered in the fit, *i.e.* $\mathcal{R}_D$, $\mathcal{R}_{D^*}$, $\bar{F}_L^{D^*}$, $\bar{P}_\tau^{D^*}$ and the leptonic branching fraction $\mathcal{B}(B_c \to \tau\bar{\nu})$, for each of the scenarios considered. Those predictions that are in agreement with the measured values at the 1σ level are marked with a ✓, while a ✗ mark indicates disagreement. Only in

Scenario	$\mathcal{B}(B_c \to \tau\bar{\nu})$	χ^2/d.o.f	Pull$_{\rm SM}$			Pull$_{\rm SM}$	p-value
			$\bar{\mathcal{P}}_\tau^{D^*}$, $F_L^{D^*}$	$\mathcal{R}_{D,D^*}$	$d\Gamma/dq^2$		
SM	2.16%	52.87/59					69.95%
Scenario 1, Min 1	$< 10\%$	37.26/53	0.007	2.08	0.0414	2.4	95.02%
Scenario 1, Min 2	$< 10\%$	38.86/53	0.001	2.08	0.0006	2.2	92.68%
Scenario 1, Min 1	$< 30\%$	36.42/53	0.022	2.08	0.0866	2.5	96.00%
Scenario 1, Min 2	$< 30\%$	38.54/53	0.011	2.08	0.000	2.2	93.21%
Scenario 2, Min 1	$< 10\%$	38.54/54	0.006	2.32	0.0113	2.5	93.20%
Scenario 2, Min 2	$< 10\%$	39.05/54	0.004	2.32	0.0003	2.4	93.73%
Scenario 2, Min 1	$< 30\%$	38.33/54	0.035	2.32	0.0023	2.5	94.73%
Scenario 2, Min 2	$< 30\%$	38.80/54	0.025	2.32	0*	2.4	94.09%
Scenario 3	$< 10\%$	39.50/58	0.150	3.65	0.0835	3.7	97.00%
Scenario 4a, Min 1	$< 10\%$	49.93/57	0.079	2.34	0*	1.2	73.52%
Scenario 4a, Min 2	$< 10\%$	49.93/57	0.079	2.34	0*	1.2	73.52%
Scenario 4a, Min 1	$< 30\%$	44.49/57	0.311	2.66	0*	2.4	88.62%
Scenario 4a, Min 2	$< 30\%$	44.49/57	0.311	2.66	0*	2.4	88.62%
Scenario 4b	$< 10\%$	43.56/55	0.054	2.07	0*	1.9	86.70%
Scenario 4b	$< 30\%$	40.03/55	0.218	2.52	0*	2.5	93.54%
Scenario 5a	$< 10\%$	39.39/57	0*	3.22	0.0981	3.2	96.36%
Scenario 5b	$< 10\%$	39.37/55	0*	3.34	0.0060	2.6	94.47%
Scenario 6	$< 10\%$	44.20/58	0*	3.34	0*	2.9	90.93%
Scenario 7a	$< 10\%$	39.21/57	0.126	3.22	0.0616	3.3	96.53%
Scenario 7b	$< 10\%$	39.06/55	0.014	2.56	0.0112	2.7	94.87%
Scenario 8	$< 10\%$	47.32/57	0.259	2.56	0*	1.9	81.60%

Table 8.11: Fit quality of the different fits: χ^2/d.o.f, pulls with respect to the SM hypothesis and p-values. The * symbol indicates that the χ^2 of a given scenario is greater than the SM one.

Scenario	$\mathcal{B}(B_c \to \tau\bar{\nu})$	$\mathcal{R}_D$	$\mathcal{R}_{D^*}$	$\bar{F}_L^{D^*}$	$\bar{\mathcal{P}}_\tau^{D^*}$
Experiment	-	$0.340 \pm 0.027 \pm 0.013$	$0.295 \pm 0.011 \pm 0.008$	$0.60 \pm 0.08 \pm 0.04$	$-0.38 \pm 0.51^{+0.21}_{-0.16}$
Scenario 1, Min 1	10%	0.339 ± 0.030 ✓	0.295 ± 0.014 ✓	$0.494^{+0.025}_{-0.045}$ ✓	$0.06^{+0.43}_{-0.45}$ ✓
Scenario 1, Min 2	10%	0.338 ± 0.030 ✓	0.296 ± 0.014 ✓	$0.472^{+0.023}_{-0.044}$ ✗	$-0.20^{+0.67}_{-0.30}$ ✓
Scenario 1, Min 1	30%	0.338 ± 0.030 ✓	0.295 ± 0.014 ✓	$0.510^{+0.014}_{-0.043}$ ✓	$0.08^{+0.32}_{-0.46}$ ✓
Scenario 1, Min 2	30%	0.338 ± 0.030 ✓	0.296 ± 0.014 ✓	$0.488^{+0.032}_{-0.050}$ ✓	$-0.24^{+0.64}_{-0.28}$ ✓
Scenario 2, Min 1	10%	$0.341^{+0.029}_{-0.028}$ ✓	0.296 ± 0.013 ✓	$0.474^{+0.010}_{-0.024}$ ✗	$-0.42^{+0.13}_{-0.07}$ ✓
Scenario 2, Min 2	10%	0.339 ± 0.030 ✓	0.296 ± 0.014 ✓	$0.471^{+0.012}_{-0.033}$ ✗	$-0.401^{+0.094}_{-0.064}$ ✓
Scenario 2, Min 1	30%	$0.341^{+0.029}_{-0.028}$ ✓	0.296 ± 0.013 ✓	$0.489^{+0.011}_{-0.048}$ ✗	$-0.47^{+0.15}_{-0.05}$ ✓
Scenario 2, Min 2	30%	0.340 ± 0.030 ✓	0.295 ± 0.014 ✓	$0.484^{+0.015}_{-0.045}$ ✗	$-0.45^{+0.13}_{-0.07}$ ✓
Scenario 3	2.5%	0.343 ± 0.012 ✓	0.294 ± 0.010 ✓	0.462 ± 0.004 ✗	$-0.377^{+0.031}_{-0.033}$ ✓
Scenario 4a, Min 1	10%	$0.353^{+0.028}_{-0.027}$ ✓	$0.2638^{+0.0034}_{-0.0049}$ ✗	$0.4662^{+0.0039}_{-0.0057}$ ✗	$-0.5028^{+0.0051}_{-0.0035}$ ✓
Scenario 4a, Min 2	10%	$0.353^{+0.028}_{-0.027}$ ✓	$0.2638^{+0.0034}_{-0.0049}$ ✗	$0.4662^{+0.0039}_{-0.0057}$ ✗	$-0.5028^{+0.0051}_{-0.0034}$ ✓
Scenario 4a, Min 1	30%	$0.348^{+0.028}_{-0.027}$ ✓	$0.2699^{+0.0032}_{-0.0058}$ ✗	$0.4792^{+0.0041}_{-0.0064}$ ✗	$-0.5144^{+0.0056}_{-0.0032}$ ✓
Scenario 4a, Min 2	30%	$0.348^{+0.028}_{-0.027}$ ✓	$0.2699^{+0.0032}_{-0.0058}$ ✗	$0.4792^{+0.0041}_{-0.0064}$ ✗	$-0.5144^{+0.0056}_{-0.0032}$ ✓
Scenario 4b	10%	0.353 ± 0.028 ✓	$0.2708^{+0.0032}_{-0.0052}$ ✗	$0.4815^{+0.0041}_{-0.0068}$ ✗	$-0.442^{+0.005}_{-0.026}$ ✓
Scenario 4b	30%	0.340 ± 0.028 ✓	$0.2866^{+0.0030}_{-0.0081}$ ✓	$0.5125^{+0.0044}_{-0.0126}$ ✓	$-0.356^{+0.006}_{-0.066}$ ✓
Scenario 5a	2.2%	$0.335^{+0.027}_{-0.017}$ ✓	$0.2966^{+0.0043}_{-0.0042}$ ✓	$0.4611^{+0.0056}_{-0.0070}$ ✗	$-0.364^{+0.048}_{-0.050}$ ✓
Scenario 5b	2.0%	0.334 ± 0.029 ✓	0.297 ± 0.013 ✓	$0.4609^{+0.0059}_{-0.0083}$ ✗	$-0.38^{+0.77}_{-0.16}$ ✓
Scenario 6	7.6%	$0.361^{+0.022}_{-0.021}$ ✓	$0.2748^{+0.0066}_{-0.0059}$ ✓	0.4522 ± 0.0050 ✗	$-0.4800^{+0.0078}_{-0.0076}$ ✓
Scenario 7a	4.6%	$0.335^{+0.021}_{-0.011}$ ✓	0.297 ± 0.011 ✓	$0.468^{+0.007}_{-0.011}$ ✗	$-0.377^{+0.033}_{-0.058}$ ✓
Scenario 7b	4.3%	$0.328^{+0.026}_{-0.025}$ ✓	0.299 ± 0.012 ✓	$0.471^{+0.014}_{-0.013}$ ✗	$-0.38^{+0.77}_{-0.12}$ ✓
Scenario 8	7.3%	$0.359^{+0.028}_{-0.027}$ ✓	0.2629 ± 0.0036 ✗	0.4644 ± 0.0043 ✗	-0.5012 ± 0.0039 ✓

Table 8.12: Predictions for the fitted observables in the different minima, and their experimental values.

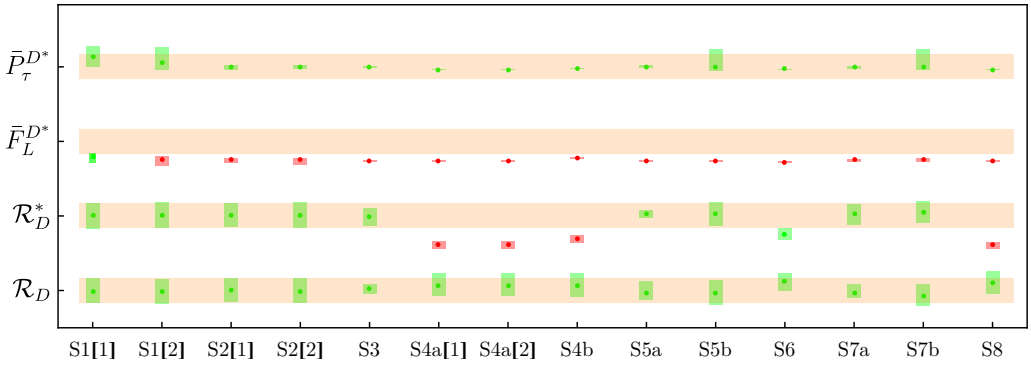

Figure 8.20: Predictions for the fitted observables, normalized to their measured values, with their 1σ experimental uncertainties shown as orange bands. For these predictions $\mathcal{B}(B_c \to \tau\bar{\nu}) \leq 10\%$ is taken. The green and red regions indicate the predictions arising from each NP scenario that are in agreement or not with the experimental value, respectively, at the 1σ level. The labels within brackets specify the minimum within a given scenario. The numerical values of these predictions are listed in Table 8.12.

Scenarios 1 and *4b* it is possible to simultaneously satisfy all experimental constraints. The second column shows that the upper bound on the B_c leptonic decay is always saturated in *Scenarios 1, 2*, and *4*, which denotes that larger pseudoscalar and axial combinations of the Wilson coefficients would still be preferred.

8.3.4.2 Predictions of angular coefficients

The three-body differential distribution in $B \to D\tau\bar{\nu}$ and the full four-body angular analysis of $B \to D^*\tau\bar{\nu} \to (D\pi)\tau\bar{\nu}$ provide a multitude of observables that could be experimentally accessible. The presence of neutrinos in the final state makes the measurement troublesome, compared to the case of well-known neutral-current transitions like $B \to K^*\mu\bar{\mu}$. Nevertheless, measuring the distribution of the secondary τ decay, some information on the angular coefficients J_i and I_i, defined in Eqs. (4.3.28) and (4.3.36), could be obtained in the near future. As it can be seen from their explicit analytic expressions in Eqs. (4.3.29) and (4.3.38), these q^2-dependent functions can be very sensitive to the NP Wilson coeffi-

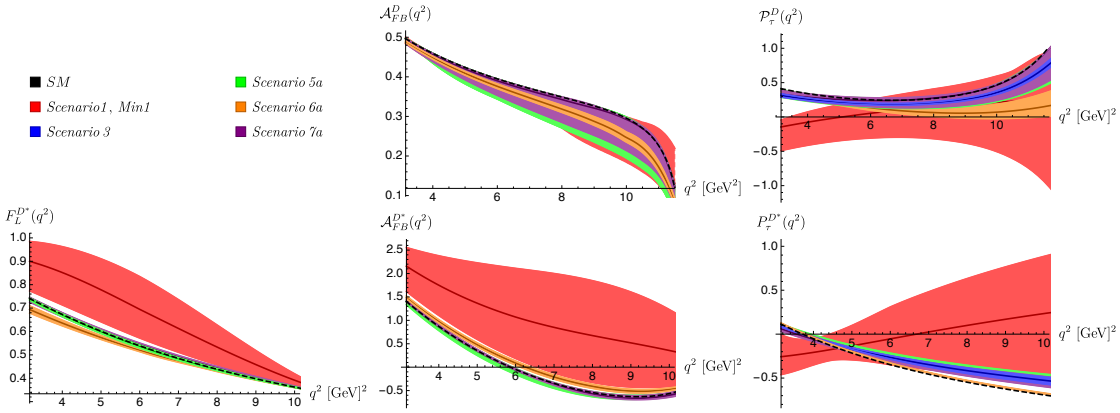

Figure 8.21: Dependence on q^2 of the forward-backward asymmetries $\mathcal{A}_{FB}^{D}$ and $\mathcal{A}_{FB}^{D^*}$, the longitudinal polarizations $\mathcal{P}_{\tau}^{D^{(*)}}$ and the longitudinal polarization fraction $F_L^{D^*}$, for the best-fit scenarios.

cients present in the theory. In this section, we provide the predictions of such observables in some relevant NP scenarios considered in this work.

Fig. 8.21 shows the predictions for the forward-backward asymmetries $\mathcal{A}_{FB}^{D^{(*)}}$ defined in Eqs. (4.3.34) and (4.3.51), the lepton polarization asymmetries of Eqs. (4.3.35) and (4.3.55) and the longitudinal D^* polarization $F_L^{D^*}$ defined in Eq. (4.3.48), as functions of q^2. For simplicity we have illustrated the four NP scenarios with largest pulls with respect to the SM. Note that *Scenario 3*, which contains the single Wilson coefficient C_{RR}^{V}, will always give the same predictions as the SM scenario for the forward-backward asymmetries, $F_L^{D^*}(q^2)$ and the angular coefficients $\bar{I}_i(q^2)$. Therefore, this scenario is only included in the τ polarization asymmetries. Error bands in these plots correspond only to the uncertainties arising from the fitted Wilson coefficients. These uncertainties have been obtained by minimizing the χ^2, imposing $O_i = O_{i,\text{min}} + \Delta O_{i,\text{min}}$, and taking the value of the observable O_i for which $\chi^2 = \chi^2_{\text{min}} + 1$. Other smaller errors such as FF parameters or additional inputs are not taken into account. Therefore the SM predictions, plotted as dotted black lines, do not present any uncertainties.

From these plots, we can see that scenarios with a larger number of Wilson coefficients also have larger uncertainties (*Scenario 1, Min 1*), as expected because of the wider allowed

range of variation of their Wilson coefficients. The forward-backward asymmetry $\mathcal{A}_{FB}^{D}$ could be useful to distinguish *Scenario 6a* from the SM, but the large uncertainties make difficult to discriminate it from other scenarios or to differentiate the SM from *Scenarios 1, 6a* and *7*. A precise measurement of $\mathcal{A}_{FB}^{D^*}$ would allow to distinguish *Scenarios 1* and *6a* from the rest of NP scenarios, which partly overlap with the SM prediction. A similar situation occurs for $F_L^{D^*}$, where clear differences manifest at low values of q^2 while the different scenarios considered tend to overlap at high q^2. The τ polarizations $\mathcal{P}_\tau^{D^{(*)}}$ are useful to distinguish *Scenario 3* from the SM, since these are the only observables that are sensitive to a single shift in C_{RR}^V. Moreover, in *Scenario 1* $\mathcal{P}_\tau^D$ and $\mathcal{P}_\tau^{D^*}$ exhibit a quite different dependence on q^2 compared to the other scenarios, which could be exploited to distinguish it at low q^2 values. In the high q^2 region, $\mathcal{P}_\tau^{D^*}$ also allows to discriminate *Scenario 1* from the other possibilities.

In Fig. 8.22 we plot the $B \to D^* \tau \bar{\nu}$ angular coefficients, as functions of q^2, normalized by the decay width:

$$\bar{I}_i(q^2) \equiv \frac{I_i(q^2)}{\Gamma_f(q^2)} \,. \tag{8.3.54}$$

The CP-odd quantities I_7, I_8 and I_9 are identically zero in our case, because we have only considered real Wilson coefficients in our fits. It is interesting to notice that despite the large uncertainties *Scenario 1, Min 1* can be easily distinguished from the SM predictions and from other minima (for instance looking at $\bar{I}_{1s}$ or $\bar{I}_5$). However, being able to distinguish other scenarios would be more complicated, unless the current errors on the Wilson coefficients are sizeable reduced. There is always an overlap between the SM predictions, *Scenario 7a* and *Scenario 5a*. *Scenario 6a* is close to *Scenarios 5a, 7a* and the SM predictions, but it is still possible to distinguish it looking at low ($\bar{I}_{1s}$, $\bar{I}_5$) or high ($\bar{I}_{2s}$, $\bar{I}_{2c}$, $\bar{I}_3$ and $\bar{I}_4$) q^2 values.

Using the symmetries of the angular distribution, Ref. [340] has proposed an alternative measurement of $F_L^{D^*}(q^2)$, which is only valid in (CP-conserving) scenarios without tensor couplings. In those scenarios, a difference between the two measurements would signal the presence of RHN contributions [340].

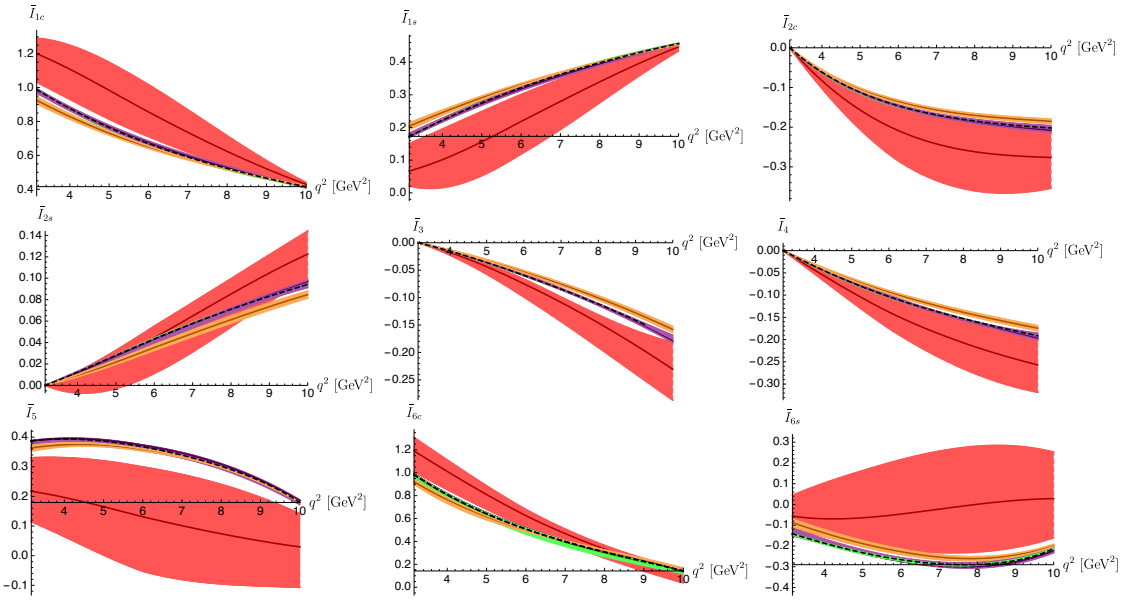

Figure 8.22: $\bar{I}_i$, defined in Eq. (8.3.54), for different scenarios. Same colour legend as in Fig. 8.21.

8.3.5 Conclusions

Using an EFT approach, we have explored the impact of various NP operators on the recently observed anomalies in $b \to c\tau\bar{\nu}$ transitions. In particular, the focus of this work has been to identify the role of NP operators which can arise due to the presence of RHN in the theory. This has been achieved through a global-fit analysis of all available $b \to c\tau\bar{\nu}$ data until date: $\mathcal{R}_{D^{(*)}}, \bar{\mathcal{P}}_\tau^{D^*}, \bar{F}_L^{D^*}$ and the q^2 differential distributions of $B \to D^{(*)}$. Previous analyses only studied the integrated rates and did not include the polarization information ($\bar{\mathcal{P}}_\tau^{D^*}, \bar{F}_L^{D^*}$) and the q^2 distributions measured by the BaBar and Belle collaborations, which play an important role in discarding many proposed NP explanations.

We have also studied the differential $B \to D\tau\bar{\nu}$ decay distribution and have derived the full four-body angular distribution of the decay $\bar{B} \to D^*(\to D\,\pi)\tau\bar{\nu}$, for the most general dimension-six effective Hamiltonian, which includes (axial)vector, (pseudo)scalar and tensor operators for both the left- and right-handed leptonic currents. The rich dynamical information embodied in the coefficients of these angular distributions could

be, in principle, experimentally accessed. From these distributions, we have constructed different observables and have analysed their predicted values within the NP scenarios emerging from our fits. In the next few paragraphs, we briefly summarize the key findings of our analysis.

NP contributions have been assumed to be present only in operators involving charged leptons of the third generation, which is well justified since potential NP effects in $b \to c\,\ell\,\bar{\nu}$ transitions ($\ell = e, \mu$) are known to be negligible [253]. The NP couplings have been also assumed to be real, due to the absence of any evidence of CP violation in these channels. After investigating the separate impact of individual Wilson coefficients, we have performed multi-dimensional fits to the data within eleven different scenarios. The first and the second case include all five RHN operators with and without a SM-like NP contribution, respectively, whereas the remaining scenarios correspond to 'simplified models' obtained by integrating a single mediator above the EW scale: namely, a scalar boson Φ, a vector boson V^μ, two scalar leptoquarks S_1 and $\tilde{R}_2$, and two vector leptoquarks U_1^μ and $\tilde{V}_2^\mu$. In those cases where the tree-level exchange of a mediator generates both ν_L and ν_R operators, we have further analysed two model variants with and without the ν_L contributions.

Among all scenarios analysed, the vector boson V^μ (*Scenario 3*) seems to be the preferred option, in terms of the pulls from the SM hypothesis, as shown in Table 8.11. The next two possibilities are the scalar leptoquark S_1 (*Scenario 7*) and the vector leptoquark U_1^μ (*Scenario 5*), switching on the RHN couplings only, which can also provide good agreement to the data. However, it is important to note that none of these three possibilities can generate values of the longitudinal D^* polarization within its current 1σ experimental range; they can only reach agreement with the $\bar{F}_L^{D^*}$ measurement at the 2σ level. Interestingly, the $\bar{F}_L^{D^*}$ data can only be explained at 1σ in very few cases, namely, with all RHN operators plus the SM-like contribution (*Scenario 1*), or with a scalar boson Φ, switching on both ν_L and ν_R operators (*Scenario 4b*) and with a relaxed upper limit of 30% on $\mathcal{B}(B_c \to \tau\bar{\nu})$. However, these scenarios are not the best choices in explaining the $\mathcal{R}_{D^{(*)}}$ measurements in terms of pull, as reflected in Table 8.11. Nevertheless, they do reduce

the $\mathcal{R}_{D^{(*)}}$ deviation significantly, and bear very important information about simultaneous agreement of all observables considered in this work. Due to the large uncertainty of the current $\bar{\mathcal{P}}_\tau^{D^*}$ measurement, all scenarios are compatible (within $\pm 1\sigma$) with it. The $\mathcal{R}_D$ measurement is also easily accommodated in all the NP scenarios that we have analysed.

Measurements of additional observables such as polarizations and angular distributions could help to to disentangle the dynamical origin of the current anomalies. In particular, we have displayed the information contained in the three-body and four-body angular distributions of $B \to D\tau\bar{\nu}$ and $B \to D^*(\to D\pi)\tau\bar{\nu}$, respectively, and their sensitivity to the different NP scenarios analysed. The experimental measurement of these distributions is of course very challenging because of the presence of undetected neutrinos, and one would need to further analyse the decay products of the tau in order to recover the accessible information.

8.4 Final remarks

In this chapter we have performed several fits to the relevant Wilson coefficients involving $b \to c\tau\bar{\nu}$ transitions. Such transitions have been measured at several observables, being the most relevant ones the ratios $\mathcal{R}_{D^{(*)}}$. These ratios are relevant for two reasons. First of all they are extremely clean observables, since both the CKM element V_{cb} and many FFs parameters cancel. Furthermore, their experimental measurements present deviations with respect to the SM related to LFUV that could be interpreted as NP. These anomalies have driven attention since they were first measured in 2012, and the subsequent measurements, performed by different collaborations, have confirmed them. Even though the experimental central values are getting closer to the SM expectations, the improvement in the theoretical predictions keeps the discrepancy above 3σ.

Our first work consisted in a global fit with a minimal set of assumptions: real Wilson coefficients, there are no light RHN and EWSB is linearly realized. We analyzed all the relevant data at the time and found that, while the preferred solution was a global modification of the SM (*i.e.* a non-zero value of C_{LL}^V while the rest of Wilson coefficients

are 0), it was difficult to accommodate all the experimental data within their 1σ range. Motivated by this fact, we relaxed one of our conditions and added the Wilson coefficient C_{RL}^{V}. The only solutions that improved the situation with this new Wilson coefficient corresponded to fine-tuned minima and therefore did not provide a suitable explanation.

The second work on these anomalies described here corresponds to relaxing another of the assumptions. Now RHN were included in the fit, increasing the number of (real) Wilson coefficients from five to ten. Being impossible to fit all the parameters at the same time, we worked on several scenarios, corresponding to the integration of a single NP mediator. Even though several scenarios improved the situation with respect to the SM case, just a few scenarios were able to reproduce all the experimental information within their 1σ uncertainty.

For both situations (with and without RHNs), we presented several predictions for observables involving $b \to c$ transitions. These observables are of great relevance: even though they have not been measured yet they could help us to disentangle different solutions in the future. These measurements together with the forthcoming new data on the $\mathcal{R}_{D^{(*)}}$ ratios and the improvement in the theoretical calculations will help us to understand better these anomalies.

The situation of these anomalies will be clarified in the future, when more experimental information will be available. Despite the fact that the numerical input used in these works may become obsolete, the framework developed here will be easily adapted to study new results. Furthermore, the effort made to predict several observables can be used as a guide to understand which measurements will be the most relevant to uncover the pattern of NP.

Chapter 9

Fits to electroweak couplings of the top and bottom quarks

The LHC has suceeded in confirming the particle content predicted by the SM. In the last years, a broad range of production and decay channels have been measured to characterize the interactions among all the particles of the model and to search for deviations with respect to the predicted couplings. In this chapter we will focus on the EW couplings of the third generation of quarks, which are specially relevant in many extensions of the SM such as composite Higgs models or extra dimensions scenarios [341, 342].

Since setting limits on the top-quark couplings has not been possible with previous electron-positron colliders, the LHC measurements analyzed in this work provide the first constraints on top EW couplings. Here we aim to set constraints on these couplings by including information provided by ATLAS and CMS for collisions at a center of mass energy of 13 TeV of the associated production $t\bar{t}X$ (with $X = Z, W, \gamma, H$), single top production in the t channel, Wt associated production and tZq production as well as the W helicity fraction in top-quark decays.

Since top and bottom quarks belong to the same $SU(2)_L$ doublet, their couplings are related [343, 344] and one needs to consider also bottom-quark operators. To constrain

them, it is useful to consider measurements by LEP and SLC, in particular precise measurements at the Z pole of the ratio R_b and the b-quark asymmetry parameter $\mathcal{A}_b$.

The effect of NP at high scales in these observables can be parametrized by an EFT containing a subset of ten (CP-conserving) operators. These operators can be constrained performing a global fit and taking into account the experimental information of the LHC and LEP/SLC simultaneously. Fits have been performed using the `HEPfit` tool described in Chapter 5 with the `NPSMEFT6dtopquark` model class. The resulting bounds can be interpreted in terms of NP models in which these operators play the most relevant role. One can also combine these constraints with the limits for other operators (obtained from different analyses) and reduce the parameter space of models with larger sets of operators.

In the following years, bounds on the Wilson coefficients are expected to become more stringent. The LHC program expects to sharpen the limits on these operators considerably in the high-luminosity LHC (HL-LHC) [345]. Further, future e^+e^- colliders (either linear colliders as the International Lineal Collider (ILC) [346] and the Compact Linear Collider (CLIC) [347] or circular colliders as FCCee [348] and CEPC [349]) operating at energies above the top-quark production threshold will give rise to important bounds for top-related operators. Operation above this threshold is part of the initial state of the CLIC project [350] and later stages of FCCee and CEPC. In this chapter we will define some well-motivated scenarios to set prospects on the constraints that could be obtained in these future experiments.

This represents the most complete characterization of the EW couplings of top and bottom quarks up to date. Our fit yields more stringent constraints than previous works [351–353]. We also present the first comparison between the HL-LHC and the ILC potential for precision measurements that constrain the top and bottom-quark EW couplings.

The rest of the chapter is organized as follows. In Section 9.1 the effective Lagrangian containing dimension-six operators is defined, and the fit procedure is briefly explained. The observables used in the fit and their sensitivity to the effective operators are described in Section 9.2. Constraints of the current LHC and LEP/SLC data are summarized in Section 9.3, while prospects for future colliders are displayed in Section 9.4. This section

is divided into prospects for the HL-LHC and the different energy stages of the ILC, extending the basis from ten to seventeen operators in the last case. In Section 9.5 the fit results for the top-quark Yukawa coupling are described in detail both for the LHC-LEP/SLC data and for future colliders. The conclusions of the work are summarized in Section 9.6. This chapter is based in Ref. [354].

9.1 EFT and fit set-up

9.1.1 Operator basis

Let us consider the effective Lagrangian,

$$\mathcal{L}_{\text{eff}} = \mathcal{L}_{\text{SM}} + \left(\frac{1}{\Lambda^2} \sum_i C_i \mathcal{O}_i + \text{h.c.} \right) + \mathscr{O}\left(\Lambda^{-4}\right), \tag{9.1.1}$$

where $\mathcal{L}_{\text{SM}}$ contains the dimension-4 operators of the SM and $\mathcal{O}_i$ are gauge-invariant dimension-six operators suppressed by the NP scale Λ^{-2}. Operators of odd dimension will lead to baryon or lepton number violation and therefore are ignored. In this work, terms suppressed by Λ^{-4} arising from two insertions of the Λ^{-2} terms and from the interference between two dimension-six operators with the SM part are also considered. Dimension-eight operators, suppressed by Λ^{-4} are not included. For typical values of the Wilson coefficients, $C_i \sim 1$ and considering that the NP scale will exceed several TeV, the expansion parameters of our theory, C_i/Λ^2 are expected to give a well-behaved perturbative series. Therefore, the non-inclusion of dimension-eight operators will not spoil the validity of the theory. In some special cases, this truncation requires a more careful treatment. A summary of the physical situations in which dimension-eight operators can be relevant, while the EFT expansion is convergent, is summarized in Ref. [355]. They include (approximate) symmetries of the low-energy theory that suppress dimension-four and dimension-six operators, processes where the scattering amplitude vanishes without any symmetry reason, approximate selection rules enhancing the contribution of dimension-eight operators or fine-tuned situations in which the dimension-six operators are much

smaller than the dimension-eight ones. To check this assumption, we will perform our fits with and without considering these Λ^{-4} terms and the results will be compared.[1] This will be studied with more detail in Section 9.3.

In this analysis we do not consider the full set of dimension-six operator involving a top and bottom quark, but we consider the operators relevant for the study of our observables. Further, we will restrict the analysis to CP-conserving coefficients, so imaginary parts are ignored. Studies dedicated to setting constraints on these complex phases at colliders can be found in Refs. [357, 358] and from low-energy probes in Ref. [359].

The relevant operators defined in the Warsaw basis [290, 360, 361] are,

$$\begin{aligned}
\mathcal{O}^1_{\varphi Q} &\equiv \tfrac{y_t^2}{2}\bar{\boldsymbol{q}}\gamma^\mu \boldsymbol{q}\varphi^\dagger i\overleftrightarrow{D}_\mu\varphi, \\
\mathcal{O}^3_{\varphi Q} &\equiv \tfrac{y_t^2}{2}\bar{\boldsymbol{q}}\tau^I\gamma^\mu \boldsymbol{q}\varphi^\dagger i\overleftrightarrow{D}^I_\mu\varphi, \\
\mathcal{O}_{\varphi u} &\equiv \tfrac{y_t^2}{2}\bar{\boldsymbol{u}}\gamma^\mu \boldsymbol{u}\varphi^\dagger i\overleftrightarrow{D}_\mu\varphi, \\
\mathcal{O}_{\varphi d} &\equiv \tfrac{y_t^2}{2}\bar{\boldsymbol{d}}\gamma^\mu \boldsymbol{d}\varphi^\dagger i\overleftrightarrow{D}_\mu\varphi, \\
\mathcal{O}_{\varphi ud} &\equiv \tfrac{y_t^2}{2}\bar{\boldsymbol{u}}\gamma^\mu \boldsymbol{d}\varphi^T\epsilon i D_\mu\varphi,
\end{aligned}
\qquad
\begin{aligned}
\mathcal{O}_{uW} &\equiv y_t g_W \bar{\boldsymbol{q}}\tau^I\sigma^{\mu\nu}\boldsymbol{u}\epsilon\varphi^* W^I_{\mu\nu}, \\
\mathcal{O}_{dW} &\equiv y_t g_W \bar{\boldsymbol{q}}\tau^I\sigma^{\mu\nu}\boldsymbol{d}\varphi W^I_{\mu\nu}, \\
\mathcal{O}_{uB} &\equiv y_t g_Y \bar{\boldsymbol{q}}\sigma^{\mu\nu}\boldsymbol{u}\epsilon\varphi^* B_{\mu\nu}, \\
\mathcal{O}_{dB} &\equiv y_t g_Y \bar{\boldsymbol{q}}\sigma^{\mu\nu}\boldsymbol{d}\varphi B_{\mu\nu},
\end{aligned}
\qquad
\begin{aligned}
\mathcal{O}_{u\varphi} &\equiv \bar{\boldsymbol{q}}\boldsymbol{u}\epsilon\varphi^*\,\varphi^\dagger\varphi, \\
\mathcal{O}_{d\varphi} &\equiv \bar{\boldsymbol{q}}\boldsymbol{d}\epsilon\varphi^*\,\varphi^\dagger\varphi.
\end{aligned}
\tag{9.1.2}$$

where $\boldsymbol{q} \equiv (u_L, V_{\rm CKM} d_L)$, $\boldsymbol{u} \equiv u_R$, $\boldsymbol{d} \equiv d_R$ and $\epsilon \equiv \left(\begin{smallmatrix} 0 & 1 \\ -1 & 0 \end{smallmatrix}\right)$ acts on $SU(2)_L$ indices.

The operators $\mathcal{O}^1_{\varphi Q}$ and $\mathcal{O}^3_{\varphi Q}$ modify the left-handed couplings between the Z boson and the top/bottom quarks,

$$\delta g_L^t = -\left(C^1_{\varphi Q} - C^3_{\varphi Q}\right)\frac{m_t^2}{\Lambda^2}, \qquad \delta g_L^b = -\left(C^1_{\varphi Q} + C^3_{\varphi Q}\right)\frac{m_t^2}{\Lambda^2}. \tag{9.1.3}$$

A simultaneous fit of the $\mathcal{O}^1_{\varphi Q}$ and $\mathcal{O}^3_{\varphi Q}$ Wilson coefficients is motivated by the purpose of constraining these couplings. The right-handed couplings are modified by the coefficients $C_{\varphi u}$ and $C_{\varphi d}$,

$$\delta g_R^t = -C_{\varphi u}\frac{m_t^2}{\Lambda^2}, \qquad \delta g_R^b = -C_{\varphi d}\frac{m_t^2}{\Lambda^2}. \tag{9.1.4}$$

The operators $\mathcal{O}_{uW}, \mathcal{O}_{dW}, \mathcal{O}_{uB}, \mathcal{O}_{dB}$ are the EW dipole operators. $\mathcal{O}_{uW}$ and $\mathcal{O}_{uB}$ ($\mathcal{O}_{dW}$ and $\mathcal{O}_{dB}$) give rise to tensor couplings between the photons and the Z bosons to the

[1] This procedure is the one proposed by the LHC TOP Working Group [356].

up (down) quarks and induce anomalous dipole moments of the top (bottom) quarks. The $\mathcal{O}^3_{\varphi Q}$ and $\mathcal{O}_{uW}$ operators modify the charged-current interaction of the top quark with a W boson and a left-handed b quark. Similarly, $\mathcal{O}_{\varphi ud}$ and $\mathcal{O}_{dW}$ give rise to the interaction between a W boson, a top quark and a right-handed bottom quark.

Finally, the operators $\mathcal{O}_{u\varphi}$ and $\mathcal{O}_{d\varphi}$ shift the Yukawa couplings of up/down quarks. Shifts in the top-quark Yukawa couplings related to $\mathcal{O}_{u\varphi}$ will be of special relevance and are studied in detail in Section 9.5. A full study of this operator should include Higgs production and decay rates. Therefore, our EW EFT should be combined with a Higgs EFT. However, this analysis is beyond the scope of this work. The observables studied here are insensitive to $O_{d\varphi}$, so this operator is ignored in the analysis.

The chromo-magnetic operators $\mathcal{O}_{uG} \equiv y_t g_s \bar{q}\sigma^{\mu\nu} u \epsilon \varphi^* G_{\mu\nu}$ and $\mathcal{O}_{dG} \equiv y_t g_s \bar{q}\sigma^{\mu\nu} d \epsilon \varphi^* G_{\mu\nu}$, or the four-fermion operators of the $q\bar{q}t\bar{t}$ type are not considered here. The 4-fermion operators could be constrained by $pp \to t\bar{t}/b\bar{b}$ observables and top/bottom production. In particular, contributions to the associated production $pp \to t\bar{t}X$ considered here, could be sizeable and play an important role in probing all combinations of $q\bar{q}t\bar{t}$ operators efficiently. Consequently, the validity of our EFT is restricted to BSM models where these operators are subleading.

In the following we will focus on the third generation of quarks. Therefore, the operators will be labelled as $\mathcal{O}_{tW}, \mathcal{O}_{bW}, \mathcal{O}_{tB}, \mathcal{O}_{bB}, \mathcal{O}_{t\varphi}, \mathcal{O}_{b\varphi}$ and $\mathcal{O}_{\varphi tb}$. The Wilson coefficients are normalized to the TeV scale.

9.1.2 Fit set-up and implementation

The dependence of the observables of the fit with the Wilson coefficients is calculated at leading order (LO) with the Monte Carlo generator `MG5_aMC@NLO` [362]. For most of the operators the `TEFT_EW` UFO model [363] is used, with the exception of $C_{t\varphi}$ generated

with the `dim6top` UFO model [356], and (C_{bW}, C_{bB}) generated with the `SMEFTsim` UFO model [364]. The following input parameters are used,

$$\begin{array}{llllll} \alpha & = 1/127.9\,, & m_Z & = 91.1876 \text{ GeV}\,, & m_b & = 0 \text{ GeV}\,, \\ G_F & = 1.16637 \times 10^{-5} \text{ GeV}^{-2}\,, & m_H & = 125 \text{ GeV}\,, & m_t & = 172.5 \text{ GeV}\,. \end{array}$$

The dependence of the observables "obs" on the Wilson coefficients implemented in the fit can be parametrized as,

$$\text{obs} = \text{obs}_{\text{SM}} + \frac{1}{\Lambda^2}\sum_i C_i \text{obs}_i + \frac{1}{\Lambda^4}\sum_j \sum_k C_j C_k \text{obs}_{jk} + \mathcal{O}(\Lambda^{-4})\,, \tag{9.1.5}$$

where obs_{SM} are the SM part of these observabes, *i.e.* with all the Wilson coefficients set to zero. The second terms, suppressed by Λ^{-2} come from the interference between the SM and a dimension-six operator. Terms suppressed by Λ^{-4} come either from the square of the amplitudes with one insertion of a dimension-six operator or from the interference of amplitudes involving two of these insertions with the SM. Terms suppressed by Λ^{-4} corresponding to dimension-eight operators are not considered. The explicit dependence of all the observables with the Wilson coefficients can be found in Appendix A of Ref. [354].

For several observables the Λ^{-2} terms of Eq. (9.1.5) are suppressed, so Λ^{-4} play a crucial role to set constraints on our coefficients and the EFT is not valid in full generality. This suppression appears for different reasons:

- **$\sigma^{\mu\nu} q_\nu$ structure:** The $\sigma^{\mu\nu} q_\nu$ structure present in associated production $pp \to t\bar{t}X$ with top-quark dipole operators involves the momentum of a photon or a Z boson that tends to be soft and therefore is suppressed [363]. The validity of the fit is recovered for C_{tW} and C_{tB} if the charged-current interaction $e^+e^- \to t\bar{t}$ is included, as in future linear colliders.

- **Operators suppressed by the bottom mass:** The operators $\mathcal{O}_{bW}, \mathcal{O}_{\varphi tb}$ induce a $\bar{t}bW$ vertex involving a right-handed bottom quark. $\mathcal{O}_{bB}$ also generates a chirality flipping $b\bar{b}$ dipole interaction. In the $m_b = 0$ approximation adopted here, the

dependence on the Λ^{-2} terms vanishes, and Λ^{-4} terms present a strong dependence. Even after the ILC programme, a strong dependence on the Λ^{-4} terms remains.

The fits are implemented in the `HEPfit` package [92, 93]. Details on this open-code source as well as the implementation of the model can be found in Chapter 5.

The results of this chapter have been verified with an independent fitting code based on the *Minuit* minimization package in ROOT [365]. Results for individual limits agree to the 1% level. For the comparison of the global limits we perform an ad-hoc fit in which we reduce the number of parameters and observables. In this case the results agree to 10%. In general we find `HEPfit` is more robust when dealing with several local minima, so all final results are obtained using it. Results are given as intervals on the operator coefficients with a given posterior probability, typically 68%.

9.2 Observables included in the fits

Here we collect the observables used for the fits. A summary of these observables can be found in Table 9.1. Measurements of LHC (ATLAS and CMS) correspond to a center of mass energy of $\sqrt{s} = 13$ TeV and an integrated luminosity of 36 fb^{-1}. Since measurements from different collaborations have not been combined yet and this combination will require an harmonization of the definition of systematics errors, we take the most precise measurement for each observable. Measurements of the same observables at 8 TeV are not included, with the exception of the W boson helicity fractions in top decays, not available at 13 TeV.

LEP and SLC measurements of R_b and A_{FBLR}^{bb} at the Z pole have been combined in the EW fit of Ref. [366]. This fit correlates the measurements of several quantities and reports a complete covariance matrix.

Correlation among different measurements can be relevant in our fits due to systematic uncertainties. Theory predictions are also correlated through the parton density functions and the similarity of the matrix elements of the several associated production processes. The full correlation matrix has been included for the LEP/SLC measurements, and has

a negligible effect in our results. The inclusion of an ad-hoc 50% correlation between the results of an associated top production has been also checked, and this has a minor effect. Consequently, these correlations are ignored.

Process	Observable	$\sqrt{s}$	$\int \mathcal{L}$	SM	Ref.
$pp \to t\bar{t}H$	cross section	13 TeV	36 fb^{-1}	-	[367]
$pp \to t\bar{t}Z/W$	cross section	13 TeV	36 fb^{-1}	[363]	[368]
$pp \to t\bar{t}\gamma$	fid. x-sec.	13 TeV	36 fb^{-1}	[363]	[369]
single-top (t-ch)	cross section	13 TeV	36 fb^{-1}	-	[370]
single-top (Wt)	cross section	13 TeV	36 fb^{-1}	-	[371]
single-top (tZq)	cross section	13 TeV	36 fb^{-1}	[372]	[373]
$t \to W^+b$	F_0, F_L	8 TeV	20 fb^{-1}	[374]	[375]
$e^-e^+ \to b\bar{b}$	R_b , A_{FBLR}^{bb}	$\sim$ 91 GeV	202.1 pb^{-1}	-	[366]

Table 9.1: Measurements included in the EFT fit of the top and bottom-quark EW sector. For each measurement, the process, the measured observable, the center of mass energy and the integrated luminosity are listed. The last column shows the references for the measurement that is included in the fit.

The observables included in our fit are the following:

Top-quark neutral current interactions

- ***pp* $\to$ *t$\bar{t}$h* production:** The production of a Higgs boson in association with a top-quark pair was observed by ATLAS and CMS in 2018 [367, 376]. Shifts in the top-

quark Yukawa coupling and therefore in the Wilson coefficient $C_{t\varphi}$ have sensitivity to this observable.

- ***pp* → *ttZ/W* production:** The associated production of top quarks with a Z boson gives access to all operators that modify the coupling of the top quark with neutral EW gauge bosons and is therefore a key channel in a combined fit [363]. The ATLAS and CMS measurements of the inclusive cross section using 36 fb^{-1} of data at 13 TeV have reached a precision of approximately 15-20% [368, 377]. The results on $pp \to t\bar{t}W$ production are also included in the fit. A recent preliminary result [378], with an integrated luminosity of 8 fb^{-1} and a relative uncertainty of less than 10%, is not included.

- ***pp* → *ttγ* production:** The rate of $pp \to t\bar{t}\gamma$ depends on the C_{tW} and C_{tB} coefficients of EW dipole operators. ATLAS has published a measurement of the $pp \to t\bar{t}\gamma$ fiducial cross-section [369] at $\sqrt{s} = 13$ TeV.

- ***pp* → *tZq* production:** Single top-quark production in association with a Z boson has been observed by ATLAS and CMS in $pp \to tZq$ with a precision of approximately 15-35% [379, 380].

The neutral-current pair production process $q\bar{q} \to Z/\gamma \to t\bar{t}$ is overwhelmed by the QCD process and has not been isolated. This contribution to the inclusive $pp \to t\bar{t}$ process leads to a dependence of the rate on the EW operators considered, but in practice this contribution can be ignored so we do not include it in our fits.

Top-quark charged current interactions

- **Top-quark decay, *t* → *Wb*:** The $t\bar{b}W$ vertex is accesible thorugh the $t \to Wb$ decay, which has a branching ratio close to the 100%. For this decay, helicity fractions are predicted with excellent precision [374] and have been measured by ATLAS and CMS at center of mass energies of $\sqrt{s} = 7$ and 8 TeV with a precision of several percent [375, 381–383]. The combination of theoretical and experimental

information converts these observables in sensitive probes to new physics affecting the $t\bar{b}W$ vertex [357]. Helicity fractions at 8 TeV (F_L and F_0) are included and tightly constrain the Wilson coefficient C_{tW}.

- **Single top production:** The t-channel process of single top-quark production has a sizeable contribution with a precision better than 10 % at $\sqrt{s} = 13$ TeV [370, 383]. ATLAS and CMS have also published precise measurements of the rate for the Wt associated production channel [371, 384].

Bottom-quark production

- $\boldsymbol{e^+e^- \to b\bar{b}}$ **production:** LEP and SLC measurements of bottom-quark pair production provide very powerful constraints and complement the top quark production measurements that allow to constrain $C^3_{\varphi Q}$ and $C^1_{\varphi Q}$ in a global fit [344]. The combination of top-quark production observables with R_b and A^{bb}_{FBLR} at the Z pole [366] yield into strong constraints for both operators [344] .

The $pp \to b\bar{b}Z/\gamma$ associated production, measured at the LHC and Tevatron provide information about the $b\bar{b}Z$ and $b\bar{b}\gamma$ vertices. This has been measured by ATLAS and CMS in early LHC runs [385, 386]. Constraints derived from here are considerably weaker than the ones coming from LEP and SLC measurements and therefore are ignored.

9.2.1 Sensitivity to coefficients

The set of observables summarized in Table 9.1 provides sensitivity to the operators of Eq. (9.1.2). The associated production of top quarks with Z bosons measured at the LHC is sensitive to all five top-quark operators and provides relevant constraints. Associated production with a photon gives access to the dipole operators C_{tW} and C_{tB}. Charged-current processes such as $t\bar{t}W$ production, EW single top-quark production and top-quark decay are sensitive to $C_{tW}, C^3_{\varphi Q}, C^1_{\varphi Q}$ and $C_{\varphi tb}$. Finally, results on $e^+e^- \to b\bar{b}$ production constrain $C^1_{\varphi Q}$ and $C^3_{\varphi Q}$ and pure bottom-quark operators.

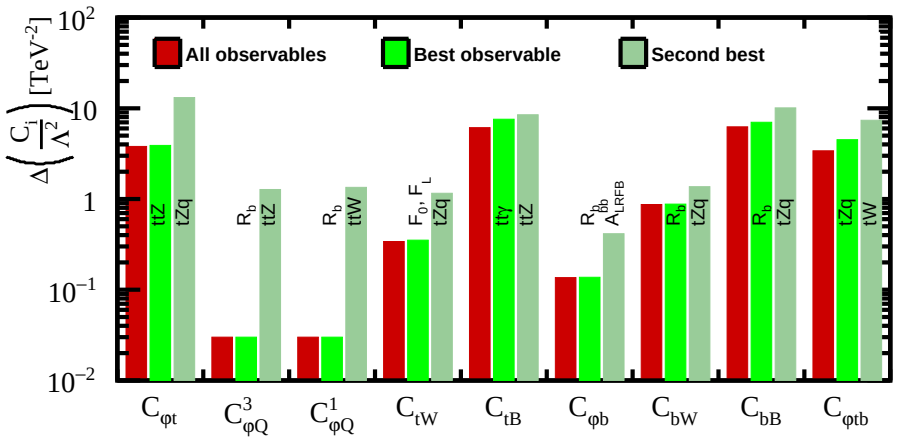

Figure 9.1: Results of single-parameter individual fits to the Wilson coefficients of the dimension-six operators introduced in Section 9.1. For each operator the 1σ uncertainty is shown. The three bars correspond to the result of the combined fit using all data (red), to the constraint obtained from the most sensitive single measurement (light green), and to that of the second-best measurement (greyish green).

The sensitivity of the observables to the different operators is summarized in Fig. 9.1. The first bar (in red) displays the individual limit on a given Wilson coefficients for a fit with all the data presented in Table 9.1. The second and third bars (in light and greyish green) show constraints obtained from the first and second most sensitive observables for that Wilson coefficient. One can note that there is a strong hierarchy in the sensitivity of the measurements for most of the operators. The most sensitive observables give bounds that are 2-5 times stronger than the second best. The coefficients $C^1_{\varphi Q}$ and $C^3_{\varphi Q}$ are strongly constrained by R_b, 30 times better than for the next most sensitive observables $t\bar{t}Z$ and $t\bar{t}W$. For C_{tB}, both the associated production of $t\bar{t}Z$ and $t\bar{t}\gamma$ have a similar sensitivity. The combination of these two observables yields into significantly better bounds than limits from the individual observables. In the case of $C_{\varphi tb}$, the different single top-quark measurements provide similar sensitivity. The helicity fractions of the W boson in top-

quark decay provide a strong limit on C_{tW} that is not affected by other observables significantly.

There are few observables that are sensitive to a larger set of Wilson coefficients: R_b can constrain five different operators in a stringent way and $t\bar{t}Z$ and tZq are also sensitive to several operators.

9.3 Present constraints

In this section we present a ten-parameter global fit to the experimental observables of LHC and LEP of Section 9.2. The obtained 68% probability bounds are summarized in the left panel of Fig. 9.2 and in Table 9.2. The correlation among the different parameters can be seen in the right panel of Fig. 9.2. Global or marginalized limits where all the coefficients are varied simultaneously are denoted with blue solid lines and individual limits with red dashed lines.

In general, one can note that individual limits yield tighter bounds than limits from a combined fit, but a global fit still gives relevant constraints. The Wilson coefficient C_{tW}/Λ^2 is strongly constrained, both in an individual and in a global fit. As it can be seen from Fig. 9.1, several observables have similar sensitivity for the coefficients C_{tB}/Λ^2 and $C_{\varphi t}/\Lambda^2$, so the bounds are not degraded very much when we compare individual and global limits.

For those operators that affect bottom-quark production in e^+e^- collisions, the individual limits from the Z-pole measurements are very tight. Therefore, several observables have to be used to disentangle the contributions of different operators. Given the large hierarchy in sensitivities observed in Fig. 9.1 the global limits are typically much weaker than the individual ones. Even so, tight constraints of order 1 TeV^{-2} are obtained for $C^1_{\varphi Q}/\Lambda^2$, $C^3_{\varphi Q}/\Lambda^2$ and $C_{\varphi b}/\Lambda^2$.

The results of our global fit give stronger results than previous works. In particular the inclusion of the Z-pole measurements leads to considerably stronger constraints than the ones obtained in Ref. [353].

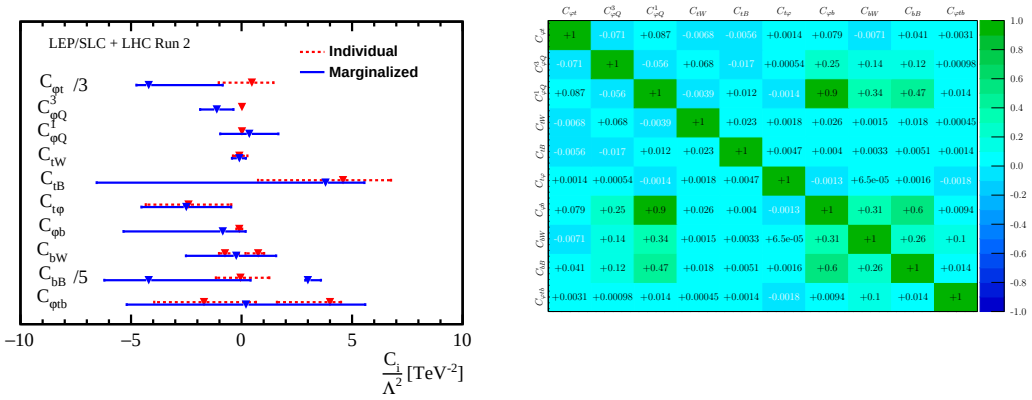

Figure 9.2: The 68% probability intervals (left panel) and correlation matrix (right panel) for the Wilson coefficients of the ten effective operators that modify the EW couplings of top and bottom quarks derived from a fit of the data included in Table 9.1. The correlation matrix in `HEPfit` is calculated following Ref. [88]. Detailed information about the correlation between the parameters and the complete covariance matrix of the fit are given in Appendix C.1 of Ref. [354]. Global (marginalized) limits obtained in the fit are shown as blue (red) bars. The local minima of the χ^2 are shown as triangles.

The results summarized in the left column of Table 9.2 and Fig. 9.2, corresponding to a nominal fit including Λ^{-2} and Λ^{-4} terms, show two different allowed regions, almost symmetric around the SM limit, *i.e.* $C_i = 0$, for three Wilson coefficients. This can be understood by looking at the parametrization of the observables in Eq. (9.1.5), that includes Λ^{-2} and Λ^{-4} terms. The two allowed regions for $C_{bW}/\Lambda^2, C_{bB}/\Lambda^2$ and $C_{\varphi tb}/\Lambda^2$ are a consequence of the Λ^{-4} terms. In Table 9.2, the results of a fit with only quadratic terms and a fit with both Λ^{-2} and the Λ^{-4} terms are compared. In the dependence of $t\bar{t}X$ on C_{tB}, the Λ^{-2} term is suppressed and Λ^{-4} term dominates. Therefore, if one drops the Λ^{-4} term in this observable the limit is degraded. The same does not happen for C_{tW}, dominated by the helicity fractions in top-quark decay and single-top production cross section. For the Wilson operators C_{bW}, C_{bB} and $C_{\varphi tb}$, the Λ^{-2} term vanishes in the $m_b = 0$ approximation used here, so no limits can be obtained only from the Λ^{-2} terms and Λ^{-4} parts are needed. The correlation among the different observables propagates

	Λ^{-2} and Λ^{-4} terms	Λ^{-2} term only
$C_{\varphi t}/\Lambda^2$	$(-16, -2.4)$	$(-2.1, +4.5)$
$C^3_{\varphi Q}/\Lambda^2$	$(-1.9, -0.4)$	$(-0.7, +0.5)$
$C^1_{\varphi Q}/\Lambda^2$	$(-1, +1.7)$	$(-0.6, +0.7)$
C_{tW}/Λ^2	$(-0.4, +0.2)$	$(-0.42, +0.24)$
C_{tB}/Λ^2	$(-6.8, +5.6)$	$(-9.6, +38.4)$
$C_{t\varphi}/\Lambda^2$	$(-4.6, -0.4)$	$(-4.42, 0)$
$C_{\varphi b}/\Lambda^2$	$(-5.4, +0.2)$	$(-0.6, +0.2)$
C_{bW}/Λ^2	$(-2.6, +2.1)$	—
C_{bB}/Λ^2	$(-31.2, +2.4)$, $(+14.4, +18)$	—
$C_{\varphi tb}/\Lambda^2$	$(-5.2, 5.6)$	—

Table 9.2: The 68% probability intervals on the dimension-six operator coefficients in units of TeV^{-2}. These results are obtained with a fit to LHC and LEP/SLC data for two parametrizations of the dependence of the observables on dimension-six operator coefficients. The first column lists the results from the fit based on the nominal parametrization, which includes terms proportional to Λ^{-2} and Λ^{-4}. The second column is obtained with a fit based on a parametrization that only includes Λ^{-2} terms. The coefficient $C_{t\varphi}$ is marginalized over in the fit, but discussed separately in Section 9.5.

this effect to the other observables. If the fit is repeated excluding $\mathcal{O}_{bW}, \mathcal{O}_{bB}$ and $\mathcal{O}_{\varphi tb}$ the fits with and without including Λ^{-4} terms are very similar except for C_{tB} and $C_{\varphi t}$.

The importance of the Λ^{-4} terms indicates that the expansion of the EFT should be carefully verified. When these results are applied to a concrete BSM model, the ignored dimension-eight operators need to be subdominant in comparison with the dimension-six ones.

9.4 Future colliders prospects

9.4.1 High-luminosity phase of the LHC

At this point, the ATLAS and CMS experiments have collected a total of 140 fb^{-1} of pp collisions at a center of mass energy of $\sqrt{s} = 13$ TeV in Run 2 and the LHC is currently in a long shut-down (LS2) stage. After the LS2, that will finish in March 2021, the LHC Run 3 is expected to deliver a total of 300 fb^{-1} at $\sqrt{s} = 14$ TeV. Between 2025 and the middle of 2027 the LHC will be upgraded at the long shut-down 3 (LS3) and detectors will allow operation of five to seven times the nominal LHC luminosity. This is known as the HL-LHC and will bring a total integrated luminosity of 3 ab^{-1} by 2037.

The expected precision for the SM measurements at the HL-LHC is presented in a series of *Yellow Reports*. The chapter on top-quark physics [387] does not provide a quantitavive basis for the measurements included in our study. Therefore, we adopt two simple scenarios to present prospects on future measurements based on the HL-LHC Higgs chapter of the Yellow report [388]. *Scenario 1 (S1)* envisages that the statistical uncertainty scales with the inverse square root of the integrated luminosity, while systematics uncertainties in measurements and predictions do not change. *Scenario 2 (S2)* envisages an improvement of a factor of two for the theory uncertainty, while the statistical uncertainty and the experimental systematic uncertainty scale with the inverse square root of the integrated luminosity. For the observables included in this analysis, it implies a reduction of the statistical uncertainty by a factor of 6-10. At that point, comparison with the SM is limited by the theory uncertainty, that has a minor improvement.

The production of a top quark in association with a gauge boson plays and important role in the fit. In these observables, the theoretical and experimental uncertainties are both of a 10%. In *S2* the experimental uncertainties are expected to reduce significantly and therefore the limitation at the end of the HL-LHC phase will come from the theoretical determination. The improvement by a factor of two in these theoretical determinations,

assumed in *S2*, could be achieved by improving the QCD description from NLO to NNLO, which seems feasible on the time scale of the HL-LHC programme.

More precise measurements of differential observables are expected to improve the fit substantially. In the current data set, the precision is limited for rare processes, but with a hundred-fold increase in the data sample, differential analyses at the HL-LHC are expected to provide powerful constraints [389, 390]. As it was studied at [354], this is particularly important for the top dipole operators, that will improve substantially from higher transverse momenta of the photon in $pp \to t\bar{t}\gamma$ differential cross sections, even exceeding the prospects of *S2*.

The constraints expected in *S2* from the W-boson helicity fraction measurements in top decays are probably overoptimistic. Unlike in other observables, the theoretical uncertainty for this observable is significatively below the experimental precision, so that it does not limit the precision for this projection and *S2* is found to be optimistic in comparison with other works, as the one of Ref. [357]. In practise, the effect of an overestimation in this observable is limited, since these observables are most relevant to constrain C_{tW}/Λ^2, that is already sensitive to other measurements. Even if measurements in top-quark decays are less precise than the expectations in *S2*, other measurements (such as single top-quark production with a Z boson) can take over its role in the global fit. Therefore, an overestimation in the precision of these observables will not affect significantly the results of the fit for the HL-LHC that will be presented in Section 9.4.3.

9.4.2 Future e^+e^- collider: ILC

To study the prospects of future e^+e^- colliders we will focus in the ILC. A future CLIC collider at its initial stage $\sqrt{s} = 380$ GeV [347, 350, 391] is found to be very similar for the relevant two-fermion operators, when rescaled by the appropriate integrated luminosity [342].

At an electron-positron collider, the production of a bottom and top-quark pair through the exchange of a photon or a Z-boson will be among the dominant processes. Therefore,

a high-energy e^+e^- collider is the perfect laboratory to study $Z/\gamma b\bar{b}$ and $Z/\gamma t\bar{t}$ vertices. Single top-quark production could also bring valuable constraining power [392], but no quantitative prospects are currently available, so it is ignored in this work.

These colliders could help us to access to both the bottom and top-quark couplings, depending on their center of mass energy. For the top to be produced, the center of mass energy needs to be above the production threshold, *i.e.* two times the top mass. Only above these energies top-quark operators could be constrained. Let's consider three stages of an e^+e^- collider like the ILC:

- **ILC at $\sqrt{s} = 250$ GeV and 2000 fb^{-1}:** This scenario was studied in [351, 393]. These studies considered measurements of the cross section and forward-backward asymmetries, where the e^+e^- beams are polarized with $\pm 80\%$ and $\pm 30\%$. Luminosity is divided equally among the left-right and right-left configurations. The authors of [351,393] performed full simulations that include the SM background and jet simulations. We adopt the framework of [393], that includes statistical and systematic uncertainties.

- **ILC at $\sqrt{s} = 500$ GeV and 4 ab^{-1}:** For this scenario we adopt an acceptance times efficiency of 25% and an integrated luminosity of 4 ab^{-1} as it was done in Ref. [393]. An e^+e^- collider at this center of mass energy will also set bounds on top couplings. Being polarized, the γ and Z vertices could be distinguished [394, 395], and therefore C_{tb} and C_{tW} could be simultaneously constrained. Projections on $e^+e^- \to t\bar{t}$ are based on optimal observables as described in [344]. These observables are optimized to exploit the $bW^+\bar{b}W^-$ differential information (in the narrow top-quark width approximation). This provides strong constraints for the Wilson coefficients $C_{\varphi t}, \left(C^1_{\varphi Q} - C^3_{\varphi Q}\right), C_{tW}$ and C_{tB}. Ref. [344] showed that at least two center of mass energies are needed to constraint all the two-fermion and four-fermion operators simultaneously. The experimental uncertainties are studied in full simulation in Ref. [350, 394]. Statistical uncertainties are estimated, including the relevant branching ratios for the lepton+jets final state, the effect of the luminosity spectrum

and a $t\bar{t}$ reconstruction efficiency of 50%. This yields an effective efficiency of 10% that multiplies the $e^+e^- \to t\bar{t}$ cross-section (see Ref. [344] for more details).

- **ILC at $\sqrt{s} = 1000$ GeV and 8 ab^{-1}:** With a linear collider operating at 1000 GeV and making use of the other two energy stages additional four-fermion operators can be constrained. This will be done in Section 9.4.4.

9.4.3 Global fit on prospects

Several global fits for the scenarios presented in Sections 9.4.1 and 9.4.2 are summarized in Fig. 9.3. The uncertainty in the Wilson coefficients $\Delta C_i/\Lambda^2$, estimated as half the 68% probability interval, is shown here. Different colour bars represent the different scenarios, as the plot legend shows: the first (dark brown) column corresponds to the current LEP/SLC + Run 2 data, the second and third columns (brown and red) are the *S1* and *S2* scenarios described in Section 9.4.1. The last two columns (dark and light green) describe the ILC prospects at $\sqrt{s} = 250$ GeV and $\sqrt{s} = 500$ GeV, respectively. Solid lines show the individual constraints, when a single operator is fitted each time, and the full bars correspond to ten-parameter fits. Full covariance matrices for all the fits are provided in Appendix C.2 of Ref. [354]. The top-Yukawa coupling $C_{t\varphi}$ is of special interest and will be described in detail in Section 9.5.

For the different prospects, the central value of all the experimental observables are set to their SM prediction. The conservative scenario *S1* only improves the situation marginally. For *S2* almost all the limits are tighter than for the LHC+LEP/SLC fit. The Wilson coefficient C_{tb} remains poorly constrained, due the limited sensitivity of the LHC observables. It could be improved with differential $t\bar{t}\gamma$ measurements [396]. For the top-quark sector one finds that the individual and marginalized limits are very similar. Since most top-quark operators are constrained from several observables, the correlation among them is limited. The same is not true for the bottom sector, where the bounds are dominated by R_b and therefore the coefficients are considerably correlated. This also explains the difference between the individual and marginalized bounds.

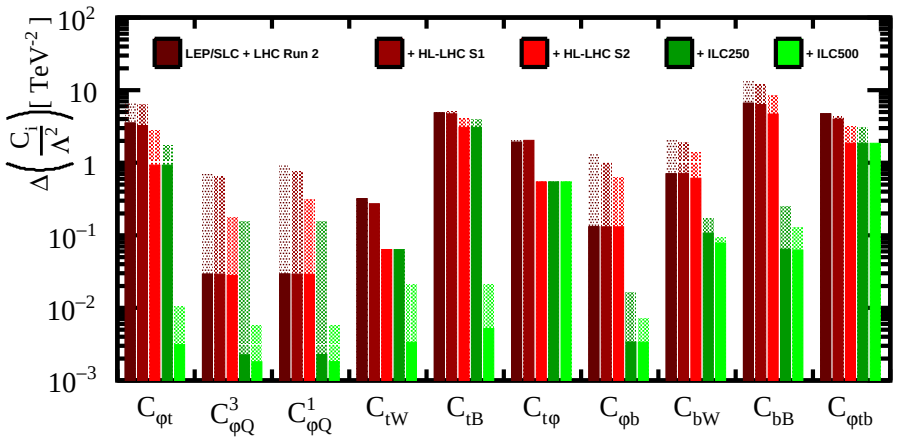

Figure 9.3: Prospects for the precision of the Wilson coefficients in future high-luminosity operation of the LHC and at a high-energy e^+e^- collider. Assumptions on the operating scenarios and details of the uncertainty estimates are given in the text. The solid section of the bars represents the individual constraints, where each parameter is fitted in isolation, the full length indicates the marginalized constraints in the ten-parameter fits. The complete covariance matrices of the fits that are presented in this figure are available in Appendix C.2 of Ref. [354].

Future linear colliders could also improve the bounds significantly. At an ILC operating at 250 GeV, bottom-antibottom pairs can be produced which can help to improve the bottom-quark operator constraints by an order of magnitude. Since top pair production is not accessible at these energies, top operators only improve through their correlation with the bottom ones.

Adding a second energy state at $\sqrt{s} = 500$ GeV, the bottom operators have a similar sensitivity as at the $\sqrt{s} = 250$ GeV stage, since $b\bar{b}$ production decreases with the center of mass energy. Adding $e^+e^- \to t\bar{t}$ data, improves the top operator bounds by one or two orders of magnitude. The direct access to the $Z/\gamma t\bar{t}$ vertices yields into tight constraints. This situation can be seen at the left column of Table 9.3. The Wilson coefficients $C^1_{\varphi Q}/\Lambda^2$ and $C^3_{\varphi Q}/\Lambda^2$ are expected to improve by one order of magnitude, giving strong limits to

the top and bottom production couplings $\left(C^1_{\varphi Q} \pm C^3_{\varphi Q}\right)$. Finally the degeneracy of the LHC/LEP fit of Section 9.3 is broken.

	10-parameter fit ILC250 + ILC500	17-parameter fit + ILC1000
$C_{\varphi t}/\Lambda^2$	0.01	0.09
$C^3_{\varphi Q}/\Lambda^2$	0.005	0.04
$C^1_{\varphi Q}/\Lambda^2$	0.005	0.04
C_{tW}/Λ^2	0.02	0.014
C_{tB}/Λ^2	0.02	0.015
$C_{t\varphi}/\Lambda^2$	0.54	0.54
$C_{\varphi b}/\Lambda^2$	0.007	0.008
C_{bW}/Λ^2	0.09	0.17
C_{bB}/Λ^2	0.13	0.17
$C_{\varphi tb}/\Lambda^2$	1.9	1.9
C_{eu}/Λ^2	—	0.0006
C_{ed}/Λ^2	—	0.0005
C_{eq}/Λ^2	—	0.0004
C_{lu}/Λ^2	—	0.0006
C_{ld}/Λ^2	—	0.0009
C^-_{lq}/Λ^2	—	0.0006
C^+_{lq}/Λ^2	—	0.0005

Table 9.3: The marginalized 68% probability bounds on the dimension-six operator coefficients in units of TeV^{-2}. The results in the first column are based on a ten-parameter fit on pseudo-data from two ILC runs, with an integrated luminosity of 2 ab^{-1} at 250 GeV and 4 ab^{-1} at $\sqrt{s} = 500$ GeV. These results are identical to those of the ILC500 entry in Fig. 9.3. The second column presents the results of the seventeen-parameter fit. It includes an additional run, with an integrated luminosity of 8 ab^{-1} at $\sqrt{s} = 1$ TeV and seven additional degrees of freedom corresponding to two-lepton-two-third-generation-quark operators.

Again, the validity of our fits has to be checked carefully, since dimension-eight operators are ignored. Once we move to scenarios giving tighter constraints, we expect the

validity to increase. At the HL-LHC scenario the tension between the Λ^{-2} and Λ^{-4} decreases significantly. Most of the observables give better constraints (up to three times better) for the Λ^{-2} terms, due to the fact that observables depend on less parameters because the Λ^{-4} terms vanish for C_{bW}, C_{bB} and $C_{\varphi tb}$ in the $m_b \to 0$ limit. However, the Λ^{-4} terms still play an important role in C_{tB}, since the linear term is suppressed, as we mentioned in Section 9.2. High precision e^+e^- collisions improve the bounds by at least one order of magnitude, and bring most of the operators to a range where the EFT expansion is valid in full generality. The difference between the nominal fit and the fit based in Λ^{-2} terms is reduced to less than a 20%.

9.4.4 Four-fermion operators of the form $e^+e^-Q^+Q^-$

Here we will consider the complete set of CP-conserving dimension-six operators that affect the top and bottom-quark EW couplings.

The two-lepton-two-quark operators contributing to $e^+e^-t\bar{t}$ and $e^+e^-b\bar{b}$ (also $\nu e^- t\bar{b}$) are,

$$\begin{array}{lllll} O_{lq}^1 & \equiv \frac{1}{2} & \bar{q}\gamma_\mu q & \bar{l}\gamma^\mu l, & \\ O_{lq}^3 & \equiv \frac{1}{2} & \bar{q}\tau^I\gamma_\mu q & \bar{l}\tau^I\gamma^\mu l, & \\ O_{lu} & \equiv \frac{1}{2} & \bar{u}\gamma_\mu u & \bar{l}\gamma^\mu l, & O_{lequ}^T \equiv \bar{q}\sigma^{\mu\nu}u \quad \epsilon\bar{l}\sigma_{\mu\nu}e, \\ O_{ld} & \equiv \frac{1}{2} & \bar{d}\gamma_\mu d & \bar{l}\gamma^\mu l, & O_{lequ}^S \equiv \bar{q}u \quad \epsilon\,\bar{l}e, \\ O_{eq} & \equiv \frac{1}{2} & \bar{q}\gamma_\mu q & \bar{e}\gamma^\mu e, & O_{ledq} \equiv \bar{d}q \quad \bar{l}e, \\ O_{eu} & \equiv \frac{1}{2} & \bar{u}\gamma_\mu u & \bar{e}\gamma^\mu e, & \\ O_{ed} & \equiv \frac{1}{2} & \bar{d}\gamma_\mu d & \bar{e}\gamma^\mu e, & \end{array} \tag{9.4.6}$$

where $l \equiv (V_{\rm PMNS}\nu_L, e_L)^T$, $e \equiv e_R$, and $V_{\rm PMNS}$ is the Pontecorvo-Maki-Nakagawa-Sakata [397–399] matrix. We define $O_{lq}^+ \equiv O_{lq}^1 + O_{lq}^3$ which mediates $b\bar{b}$ production and $O_{lq}^- \equiv O_{lq}^1 - O_{lq}^3$ for $t\bar{t}$ production in e^+e^- collisions.

The seven operators in the left column of Eq.(9.4.6) have vector Lorentz structures similar to SM gauge interactions. The three further scalar and tensor operators of the second colun have non-standard Lorentz structures and can effectively be constrained with specialized observables [344] and runs with left-left or right-right beam polarization [400]. In the following, we therefore focus on the seven vector operators.

The primary handle to constrain 2 and 4-fermion operators in a global fit is their energy dependence. While the sensitivity for the 4-fermions operators grows strongly with the energy, it is flat for the two-fermion ones. At hadron colliders, 4-fermions operators can be constrained by the differential analyses of the $pp \to t\bar{t}e^+e^-$ process versus the invariant mass and the transverse momentum of the e^+e^- system [363]. The fit can disentangle the contributions from the photon, the Z-boson and the contact interactions. No such analysis has been made public so far.

A linear e^+e^- collider with several energy states can set bounds to the four-fermion operators. A detailed analysis with the basis of ten operators of Section 9.1 was done in Ref. [344]. Stringent bounds were obtained when at least two energy states were considered.

In this work we extend the basis of ten Wilson operators with the seven additional operators of the form $e^+e^-Q^+Q^-$ of Eq. (9.4.6). To constrain them, we project prospects for masurements at $\sqrt{s} = 1$ TeV with an integrated luminosity of 8 ab^{-1}. This stage is added to the previous ones (HL-LHC+ILC250+ILC500). For the top-quark operators we again adopt the projections of Ref. [344]. For bottom-quark operators, statistical uncertainties on the cross-section and A_{FB} are propagated, assuming a conservative acceptance times selection efficiency of 10%.

The marginalized results of this fit at a 68% probability are summarized in the right panel of Table 9.3. These results can be compared to the ten-parameter fit of the ILC500 at the right column of Table 9.3 and the light green bands of Fig. 9.3.

The fit yields into excellent limits for the four-fermion operators, below 10^{-3} TeV^{-2}. These bounds agree with those of Ref. [344] when the larger integrated luminosity in the 1 TeV scenario is accounted for. The bounds on the dipole operators are similar to the ten-parameter fit: for the top-dipole operators, C_{tW} and C_{tB} the bounds slightly improve, as the sensitivity increases with the center of mass energy. Bounds on C_{bW} come from the cross section and A_{FB} measurements. As it has been mentioned, the sensitivity of $b\bar{b}$ production decays with $\sqrt{s}$, so we do not find an improvement with respect to ILC500, but constraints become weaker, as additional $e^+e^-b\bar{b}$ degrees of freedom are introduced.

The main consequence of introducing the ILC1000 stage is that the bounds for the two-fermion operators that modify the left-handed couplings for the top and bottom-quarks to the Z bosons and the right-handed coupling of the top quark to the Z boson ($C_{\varphi t}/\Lambda^2, C_{\varphi Q}^{1,3}/\Lambda^2$) are degraded by a factor of eight.

Therefore, and EFT fit including all the dimension-six operators affecting the top and bottom EW couplings is feasible provided data is collected at two sufficiently distinct centre of mass energies above the top-quark pair production threshold.

9.5 The top-Yukawa coupling

9.5.1 Direct and indirect constraints

The top Yukawa coupling is one of the most intriguing parameters of the LHC. With a numerical value close to 1, it is the largest Yukawa coupling of the model and it is sensitive to many NP models, such as the 2HDM of Chapter 2 or composite Higgs models [401]. Therefore, a precise and robust measurement of this coupling is one of the main targets for future collider experiments in the next years.

$t\bar{t}H$ production and decay give a direct constrain for these couplings. Other channels such as $gg \to H, H \to Z\gamma$ and $H \to \gamma\gamma$ are sensitive to the top Yukawa coupling and can set indirect constraints on it. However, even if top loops dominate in the processes, the effective couplings to the gluon and the photon can also receive contributions from new particles. In the κ formalism employed in early Higgs fits, contributions other than the top are assumed to be zero. This, combined with the universality assumption $\kappa_u = \kappa_c = \kappa_t$ yield into a fit value from Run 1 of $\kappa_t = 1.40^{+0.24}_{-0.21}$ [358]. Significant sharper results can be obtained from Run 2 measurements [402, 403]. When these results are combined in a global fit these bounds weaken considerably.

An e^+e^- collider below the $t\bar{t}H$ production threshold provide additional information of these indirect bounds. Besides the processes mentioned above, the precise determination of the $H \to c\bar{c}$ decay yields into a tight bound in the κ framework with $\kappa_u = \kappa_c =$

κ_t. Measurements of the Hgg and $H\gamma\gamma$ couplings with 1% precision after 2 ab^{-1} at $\sqrt{s} = 250$ GeV [404] can also be used to set bounds on the top Yukawa coupling. A global EFT fit is performed in Ref. [405], analyzing the indirect sensitivity of Higgs and diboson measurements to the EW top-quark Yukawa coupling. It is found that differential measurements are crucial to disentangle the different tree-level and loop contributions and therefore set bounds on the top Yukawa coupling.

Several attempts have been done to disentangle the contributions of different operators to the $gg \to H$ and $H \to \gamma\gamma$ rates (see Ref. [406] and references therein) with additional probes, such as boosted Higgs+jet production, di-Higgs boson production and off-shell Higgs production. None of these seem sufficiently sensitive to lift the degeneracy between the operator that modifies the top-quark Yukawa coupling and operators representing Hgg and $H\gamma\gamma$ contact interactions. Therefore we focus on the direct bounds that can be obtained from the $t\bar{t}H$ couplings.

9.5.2 Associated $t\bar{t}H$ production at the LHC

The associated $pp \to t\bar{t}H$ production at the LHC [367] brings a direct probe of the $t\bar{t}H$ interaction. The parameter μ_{ttH}, defined as the ratio between the measured cross section and the SM one, has an experimental precision of 20%, while the theoretical NLO QCD SM precision is of 8%. Our ten-parameter fit of Section 9.3 contains the measurement of the $pp \to t\bar{t}H$ cross section. Performing a single-parameter fit, we obtain the 68% probability region,

$$C_{t\varphi}/\Lambda^2 \in [-4.4, 0]\,\text{TeV}^{-2} \qquad \text{(individual)}. \tag{9.5.7}$$

A second minimum, far from the SM limit is found, as a consequence of the Λ^{-4} terms. Here we only analyze the closest minimum to the SM. Repeating the fit including the ten parameters, the result is slightly weaker,

$$C_{t\varphi}/\Lambda^2 \in [-4.6, 0.1]\,\text{TeV}^{-2} \qquad \text{(marginalized)}. \tag{9.5.8}$$

Being close to the individual fit, this indicates that the constraint from $t\bar{t}H$ is very robust. Other operators entering in this observables such as gg-initial production are subdominant with respect to $q\bar{q}$ initial production. The correlation between $C_{t\varphi}$ and these observables ($C_{tW}, C^{1,3}_{\varphi Q}, C_{tB}$ and C_{bW}) is smaller than 0.1%.

9.5.3 Prospects on the top Yukawa coupling

The fit is repeated with the projections expected for the HL-LHC. Here we focus in *S2* described in Section 9.4.1 with 3 ab^{-1} and $\sqrt{s} = 14$ TeV. The statistical uncertainty of $t\bar{t}H$ is now negligible and the total uncertainty is dominated by the theoretical one (which now is reduced to 4%). The precision improves considerably and the 68% probability limits are reduced,

$$C_{t\varphi}/\Lambda^2 \in [-0.55, 0.55]\,\text{TeV}^{-2} \qquad \text{(HL-LHC marginalized)}, \tag{9.5.9}$$

in agreement with [388].

The ILC needs operation above the $t\bar{t}H$ threshold to be able to access the top Yukawa coupling directly. The cross section is expected to increase sharply around $\sqrt{s} = 500$ GeV. The unpolarized cross section reaches a maximum of 2 fb^{-1} at $\sqrt{s} \approx 800$ GeV. Below the $t\bar{t}H$ threshold, the $t\bar{t}$ production rate is two orders of magnitude higher than the $t\bar{t}H$ one, and forms the most relevant background for $H \to b\bar{b}$. The cross section of the irreducible $t\bar{t}b\bar{b}$ background, either from associated $t\bar{t}Z$ production or a hard gluon splitting to a $b\bar{b}$ pair, is similar to that of the signal.

Full simulation studies [350,407–410] have been performed, with center of mass energies from 500 GeV to several TeVs. Realistic descriptions of $t\bar{t}$ and $t\bar{t}Z$ backgrounds, of the detector response and jet clustering have been included.

Projections of the nominal ILC program [400] with 4 ab^{-1} and $\sqrt{s} = 500$ GeV are presented in Ref. [411]. An uncertainity of 13% is expected on the $t\bar{t}H$ cross section, limited by the statistics. As the nominal ILC energy is very close to the $t\bar{t}H$ production threshold, operating at a slightly higher energy of 550 GeV enhances the cross section

by a factor of four and the Yukawa coupling by a factor of two, for the same integrated luminosity [411].

Our projections for 1 TeV are based in the analysis of Ref. [407] of $t\bar{t}H$ production followed by the decay $H \to b\bar{b}$. The expected uncertainty on the $t\bar{t}H$ cross section for an integrated luminosity of 8 ab^{-1} is of 3.2%, obtained by scaling the signal and background yields with a flat luminosity factor.

To match the statistical precision, the systematic uncertainties must be controlled to a challenging level. At 1 TeV, the signal efficiency and background yield must be known to approximately 1%, which seems feasible with data-driven estimation in control regions. The theory uncertainty in the cross section at $\sqrt{s} = 1$ TeV must be reduced to the level of 1-2%, a factor two with respect to currently available calculations [412]. On the other hand, it is likely that the analysis can be further improved, by reoptimizing the selection, with the inclusion of other Higgs decay channels and of the τ-lepton plus jets final state. Significant additional improvements are possible with improved jet clustering algorithms and the use of kinematic fits.

9.5.4 Summary of the top Yukawa coupling

A summary of the different bounds on $C_{t\varphi}/\Lambda^2$ can be seen in Table 9.4. For comparison with other works, recall the relation of these coefficient with the Yukawa coupling:

$$\delta y_t = -\frac{C_{t\varphi} v^2}{\Lambda^2} \,. \tag{9.5.10}$$

The first four columns of Table 9.4 correspond to the different ten-parameter fits described in the text. The last column shows the seventeen-parameter fit of HL-LHC+ILC250 +ILC500+ILC1000 of the end of Section 9.4.2. For $C_{t\varphi}/\Lambda^2$ the 68% probability regions are shown. In the last line the relative uncertainty on the top-Yukawa coupling is displayed in %. Both the individual and marginalized bounds are shown for each case.

The HL-LHC results of Table 9.4 agree with the projections of Ref. [388]. By construction, the ILC results agree with the summary of the Higgs/EW group for the 2020

scenario	LHC Run 2 +LEP/SLC	HL-LHC S2 +LEP/SLC	ILC500	ILC550	ILC500 +ILC1000
$\sqrt{s}$, $\int \mathcal{L}$	13 TeV, 36 fb^{-1}	14 TeV, 3 ab^{-1}	500 GeV, 4 ab^{-1}	550 GeV, 4 ab^{-1}	+1 TeV, +8 ab^{-1}
68% probability interval for the effective operator coefficient $C_{t\varphi}/\Lambda^2$ [TeV^{-2}]					
individual	$[-4.4, +0.0]$	$[-0.55, +0.55]$	$[-1.06, +1.06]$	$[-0.50, 0.50]$	$[-0.27, +0.27]$
marginalized	$[-4.6, -0.2]$	$[-0.55, +0.55]$	$[-1.07, +1.07]$	$[-0.52, +0.52]$	$[-0.32, +0.32]$
corresponding relative uncertainty on the top-quark Yukawa coupling $\Delta y_t/y_t$ [%]					
individual	13.2	3.3	6.4	3.0	1.62
marginalized	13.2	3.3	6.4	3.1	1.96

Table 9.4: The 68% probability intervals for $C_{t\varphi}/\Lambda^2$ and the corresponding precision on the top-quark Yukawa coupling. The results of the first four columns correspond to the ten-parameter fit that we used to obtain the results of Fig. 9.3. The results for the scenario with ILC runs at two different center of mass energies in the last column were obtained with the extended seventeen-parameter fit presented in Section 9.4.4.

update of the European strategy for particle physics in Ref. [413]. The results for operation at 550 GeV and 1 TeV extend the study to higher energies. In all the cases, the marginal and individual limits are very close, which means that other operators modifying the top-quark EW dipole operators do not affect the top Yukawa coupling considerably. However, it should be kept in mind that operators that affect QCD interactions like C_{tG} and four fermions ($q\bar{q}t\bar{t}$) are not included in the fits. These operators can be constrained using differential $t\bar{t}$ cross sections. A recent global fit of the top-quark sector on LHC data [353] finds, however, that the marginalized limit on $C_{t\varphi}$ is approximately a factor 10 weaker than the individual limit, due to strong correlations between operator coefficients. The addition of Tevatron results or future differential measurements could help reducing this degeneracy. It is nevertheless likely that a combination of $pp \to t\bar{t}$ and $pp \to t\bar{t}X$ measurements could be needed to constrain simultaneously all $q\bar{q}t\bar{t}$ operators. In this respect, the extraction of the top-quark Yukawa coupling at future lepton colliders so far seems more robust.

At a future e^+e^- collider, we indeed find that the contamination of both four-fermion and two-fermion operators in $e^-e^+ \to t\bar{t}H$ is limited due to the very tight constraints on their coefficients deriving from $e^-e^+ \to t\,\bar{t}$ production. Even in the most challenging

case, the ILC scenario at 1 TeV with a precision on the top-quark Yukawa coupling of 1.6% and sixteen competing operator coefficients, the marginalized bound is only about 20% weaker than the individual bound. The extraction of the top-quark Yukawa is then very clean in this case. We also note that the measurement of $e^-e^+ \to t\bar{t}H$ in addition to $e^-e^+ \to t\,\bar{t}$ does not improve significantly the constraints on operators other than the top-quark Yukawa one. Only a 14% improvement is observed on C_{tW}.

The results of Table 9.4 demonstrate that the bounds on the Wilson coefficient $C_{t\varphi}/\Lambda^2$ that shifts the top-quark Yukawa coupling from measurements of the $t\bar{t}H$ production are robust in the presence of the operators that affect the top and bottom-quark EW couplings. A precise measurement of this rate is therefore an ideal complement to more indirect bounds from $gg \to H$ production and the $H \to \gamma\gamma$, $H \to gg$ and $H \to Z\gamma$ decays.

9.6 Conclusions

In this work we have performed a global fit to the relevant EFT operators to constrain the top and bottom EW couplings. The relevant subset of ten effective operators are isolated and several observables are expressed in terms of them. LHC data on top production in association with a weak boson, single top-quark production and the W-helicity fraction in top-quark decay are combined with LEP/SLC bottom-quark measurements at the Z pole to perform a global fit. Terms suppressed by Λ^{-4} arising from two insertion of dimension-six operators are included in the fit, but pure dimension-eight operators contributing to the same order are omitted. The inclusion of Λ^{-4} terms is necessary to constraint several operators, since Λ^{-2} terms are suppressed in several observables. Thus, the validity of the EFT expansion has to be checked carefully while studying a concrete BSM model. The 68% probability intervals of the LHC+LEP/SLC fit can be seen in Table 9.2. Bounds below 1 TeV^{-2} can be found for C_{tW}/Λ^2. Tight bounds are also found for $C_{\varphi Q}^{1,3}/\Lambda^2$, the Wilson coefficients that modify the top and bottom-quark right-handed couplings to the Z boson. From the fit results, one can see how the combination of LEP/SLC and LHC data has the power to disentangle the operators affecting top and bottom quarks. The

study of the sensitivity of the different observables, as well as the comparison between the individual and the marginalized limits show that the observables considered are a suitable choice. Our fit results provide stronger bounds than previous works.

Projections on the constraints that could be obtained by future colliders have been also studied. The high-luminosity phase of the LHC is studied through two different scenarios. At the conservative scenario *S1* (statistical uncertainty scales with the inverse square root of the integrated luminosity and systematic uncertainties in measurements and predictions do not change) the bounds on the Wilson coefficients only improve slightly. For *S2* (SM theoretical predictions improved by a factor of two and experimental systematics evolve with luminosity in the same way as statistical uncertainties) the bounds of all the Wilson coefficients but C_{tB} become tighter.

At a linear e^+e^- collider operating at $\sqrt{s} = 250$ GeV the bounds of all the bottom operators are reduced by an order of magnitude. At this energy, the top production threshold has not been reached, so top operators only improve through the correlation between them and bottom operators. Adding a second energy state at 500 GeV, top operators are accessible, and therefore their bounds are reduced by one or two orders of magnitude. A third energy stage $\sqrt{s} = 1000$ GeV will allow to constraint seven additional operators of the form $e^+e^-Q^+Q^-$. The limits on these four-fermions operators (normalized to Λ^2) are really good, below 10^{-3} TeV^{-2}. Some of the other limits, such as for C_{bW} suffer from the inclusion of additional operators but in general the fit improves and allows to constraint simultaneously the 17 operators.

Finally, the top-quark Yukawa coupling has been studied in detail. Fits from the LHC/LEP-SLC data allow to constraint the $C_{t\varphi}$ operator. Values of the Wilson coefficient that modify the right-handed coupling between a top quark and the Z boson of $C_i/\Lambda^2 \sim 10^1$ TeV^{-2} are still allowed. The similarity between the individual and marginalized fit shows that $t\bar{t}H$ is indeed a good choice to constrain this coefficient. At the HL-LHC this bound will improve significantly and at the ILC the bounds will improve even more.

The EW couplings of the third-generation quarks form one of the uncharted corners of the SM. These couplings are a sensitive probe of broad classes of NP models. It is

therefore very exciting to see meaningful bounds in a multi-parameter fit on LEP/SLC and LHC data. Further progress at the LHC, and especially at a future electron-positron collider can probe subtle contributions from physics beyond the SM at scales well beyond the direct reach of the collider.

Chapter 10

Resum de la tesi

El Model Estàndard (SM per les seues sigles en anglés) de física de partícules ens proporciona la descripció més adient de l'estructura de la matèria i les seues interaccions. Aquest model va ser desenvolupat durant la segona meitat del segle XX, gràcies tant a les contribucions teòriques, com als resultats experimentals a acceleradors de partícules. El descobriment del bosó de Higgs l'any 2012 va representar una confirmació crucial del model i va iniciar una època d'exploració i recerca al LHC. Malgrat l'èxit del SM com a una teoria efectiva a baixes energies, alguns aspectes teòrics i experimentals indiquen que aquesta no pot ser la teoria definitiva. En aquesta tesi hem seguit algunes de les direccions que semblen indicar desviacions respecte del SM. El SM es descriu breument al Capítol 1.

10.1 Objectius assolits

L'extensió més senzilla del SM és el model de N doblets de Higgs (NHDM per les seues sigles en anglés), descrita al Capítol 2. A aquest model, el contingut de partícules del SM s'estén afegint N doblets escalars amb els mateixos nombres quàntics que el doblet de Higgs. Com a conseqüència, apareixen interaccions de Yukawa que no són diagonals a l'espai de sabor, donant lloc a corrents neutres amb canvi de sabor, molt suprimides fenomenologicament. Per evitar aquests corrents i així reproduir les observacions exper-

imentals, imposem alineament a l'espai de sabor, donant lloc als models coneguts com a models alineats o models amb N doblets de Higgs alineats (ANHDM). L'alineament de sabor s'imposa a ordre més baix en teoria de pertorbacions o *ordre arbre* (*tree-level* en anglés) però es veu trencat per les correccions quàntiques a ordres superiors, donant lloc a termes no diagonals. Aquestes contribucions han d'estar prou suprimides per a reproduir les dades experimentals. Això s'estudia amb detall al Capítol 6, trobant que els models alineats estan fenomenològicament permesos. Per al nomenat estudi s'inclouen diferents observables de sabor, com ara $B_s \to \mu^+\mu^-$, la mescla de mesons neutres i restriccions provinents del decaïment radiatiu $\bar{B} \to X_s\gamma$. A més, al Capítol 7 es realitza un ajust bayesià global a un model alineat amb $N = 2$ doblets en el límit en el qual la càrrega CP es conserva, el model de dos doblets de Higgs alineats (A2HDM per les seues sigles en anglés). L'ajust combina diferents restriccions teòriques, observables electrofebles, de sabor i relacionats amb el Higgs, com les cerques directes o les *Higgs signal strengths*. L'ajust s'ha realitzat amb el codi obert `HEPfit`, descrit al Capítol 5.

La següent desviació del SM estudiada són les conegudes com a anomalies de B carregades (*charged B-anomalies* en anglés). Aquestes anomalies són desviacions respecte de les prediccions del SM en mesures experimentals que contenen transicions del quark *fons* (*bottom* en anglés) al quark *encant* (*charm* en anglés), mesurades per diversos experiments i en diferents observables, sent els més rellevants les ràtios $\mathcal{R}_D$ i $\mathcal{R}_{D^*}$. Després de presentar els observables d'interés al Capítol 4, mostrem diferents ajusts globals al Capítol 8. Els ajusts s'han realitzat a partir del formalisme de teories efectives (EFTs), introduïdes al Capítol 3. Als primers ajusts treballem amb un Hamiltonià efectiu que conté tots els operadors de dimensió sis rellevants, amb un conjunt mínim d'assumpcions: la nova física està present sols a la tercera generació de leptons, prenem el límit en el qual la càrrega CP es conserva i per tant els coeficients de Wilson són reals, la ruptura de simetria electrofeble es realitza de manera lineal i no hi ha neutrins lleugers amb quiralitat dextrogira (*right-handed neutrinos*). Al mateix capítol relaxem alguna d'aquestes assumpcions. En primer lloc, repetim els ajustos afegint l'operador que apareix a conseqüència de no imposar una ruptura de simetria lineal $\left(C_{RL}^V\right)$ i després, ampliem la base d'operadors per a contenir

neutrins amb quiralitat dextrogira (augmentant el nombre d'operadors fins a deu). En tots els casos estudiem els resultats obtinguts, la seua relació amb partícules mediadores de nova física pesades i les implicacions dels resultats en diferents observables que podrien ser mesurats experimentalment en el futur pròxim. Per a realitzar aquesta anàlisi s'ha emprat el formalisme d'helicitats.

Per últim, s'han estudiat els acoblaments electrofebles dels quarks *cim* (*top* en anglés) i fons. Aquests acoblaments són d'especial importància per la seua sensibilitat a la presència de nova física. Emprant el ja mencionat codi `HEPfit`, i considerant resultats experimentals del LHC i LEP/SLC, s'ha realitzat un ajust als operadors de dimensió sis rellevants. A més, s'han establert perspectives sobre les cotes que es podran obtenir a futurs acceleradors, com ara la fase d'alta lluminositat del LHC (HL-LHC) o el col·lisionador lineal ILC. L'acoblament de Yukawa del quark cim és d'especial interés i ha estat estudiat en detall, establint límits al nivell de l'u per cent.

10.2 Metodologia

La metodologia emprada a aquesta tesi es pot trobar als Capítols 1, 3 i 5. A continuació es presenta un breu resum dels mètodes i tècniques aplicades.

10.2.1 El Model Estàndard

Com ja hem mencionat, el SM descriu les partícules elementals i les seues interaccions [1–4]. Es basa en principis de simetria, de manera que el contingut de matèria del model es pot classificar en *fermions (quarks i leptons)* amb espín 1/2 i *bosons* amb espín 0 (*bosó de Higgs*) o espín 1 (*bosons febles, $W^{\pm}$ i Z^0, fotons γ i gluons g*). El SM és una teoria local o de gauge sota el grup $SU(3)_C \otimes SU(2)_L \otimes U(1)_Y$, i per tant la natura de les interaccions fortes, febles i electromagnètiques està relacionada amb els principis de simetria del grup.

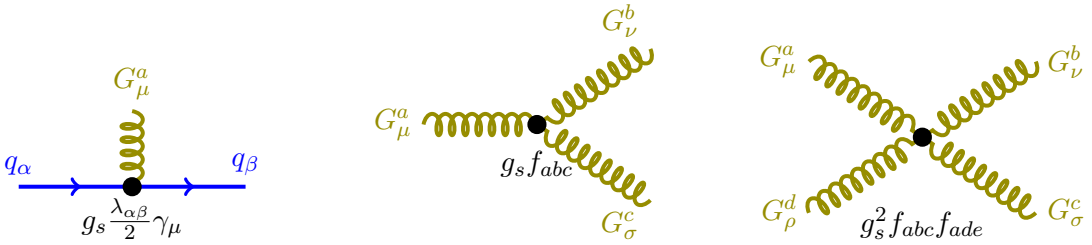

Figure 10.1: Vèrtexs d'interacció cúbics i quàrtics del Lagrangià de QCD. Els gluons i els quarks estan representats com a línies verdes i blaves respectivament.

10.2.2 QCD i unificiació electrofeble

La primera peça del SM és la cromodinàmica quàntica (QCD per les seues sigles en anglés), una teoria no Abeliana basada en grup $SU(3)_C$ i que descriu la interacció entre els quarks i els bosons del grup, els gluons [8–11]. Els quarks poden tindre sis sabors diferents (*dalt, baix, estrany, encant, fons* i *cim*) i $N_C = 3$ càrregues de color.

Els gluons, G^μ_a amb càrrega de color a apareixen a conseqüència del requeriment de què el Lagrangià de QCD siga invariant sota transformacions de $SU(3)_C$ locals. Com la invariància gauge prohibeix un terme de massa pels gluons, aquests romandran com a partícules d'espín 1 sense massa. La transformació sota el grup de simetria també determina les interaccions entre les diferents partícules del model, resumides a la Fig. 10.1

Les interaccions febles venen descrites pel Model Estàndard Electrofeble (EWSM per les seues sigles en anglés), basada en el grup de simetria $G = SU(2)_L \otimes U(1)_Y$ [1–3]. L'EWSM conté camps amb quiralitat dextrogira i levogira, que interaccionen a través de mediadors amb espín 1: els *fotons* sense massa γ, i els *bosons febles* massius, $W^\pm$ i Z^0.

El sector fermiònic del SM conté tres famílies de quarks i leptons, que tan sols es diferencien per les seues masses i nombres quàntics de sabor,

$$\textit{1era generació:} \begin{bmatrix} \nu_e & u \\ e^- & d' \end{bmatrix}, \qquad \textit{2na generació:} \begin{bmatrix} \nu_\mu & c \\ \mu^- & s' \end{bmatrix}, \qquad \textit{3era generació:} \begin{bmatrix} \nu_\tau & t \\ \tau^- & b' \end{bmatrix}.$$

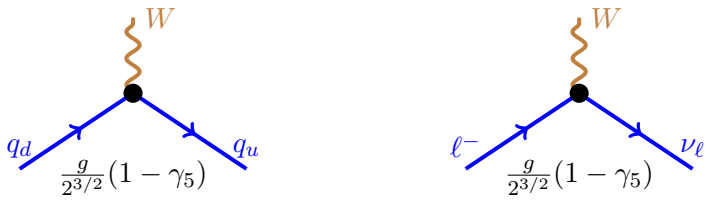

Figure 10.2: Vèrtexs de la interacció de corrents carregats per a quarks (panel de l'esquerra) i leptons (panel de la dreta). Els fermions i els bosons estan descrits per línies sòlides blaves i línies ondulants marrons respectivament.

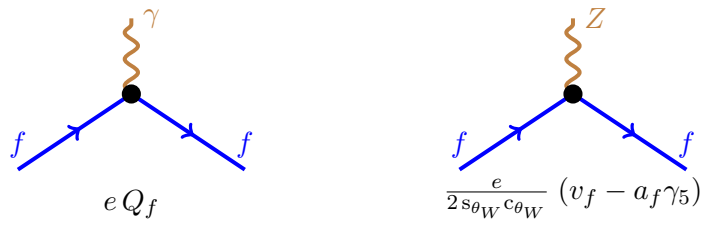

Figure 10.3: Vèrtexs d'interacció dels corrents neutres per quarks (panel de l'esquerra) i leptons (panel de la dreta). Els fermions i els bosons estan descrits per línies sòlides blaves i línies ondulants marrons respectivament.

En aquesta notació la columna de l'esquerra de cada matriu representa el sector leptònic de cada generació. El primer element són els *neutrins* i el segon els *leptons carregats*. La columna de la dreta representa el sector quark amb els *quarks dalt* com a primer element i els *quarks baix* com a segons. Els fermions de cada columna i cada generació pertanyen al mateix doblet de $SU(2)_L$.

D'una manera similar a QCD, imposant que el Lagrangià de la nostra teoria siga invariant sota el grup de simetria G, apareixen els quatre bosons vectorials sense massa que interaccionen amb els fermions de la teoria. La interacció entre dos fermions de diferent càrrega i un bosó carregat, denominada *interacció de corrents carregats*, es pot veure esquematitzada a la Fig. 10.2. La interacció entre dos fermions amb càrregues oposades i un bosó neutre dóna lloc als *corrents neutres* de la Fig. 10.3. A més també

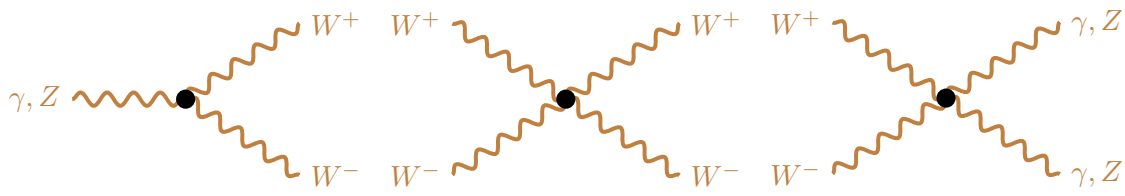

Figure 10.4: Vèrtexs d'auto-interacció entre els bosons de gauge. Els bosons estan representats com a línies ondulants marrons.

apareixen auto-interaccions entre els diferents bosons de la teoria (Fig. 10.4).

10.2.2.1 Ruptura espontània de simetria i el bosó de Higgs

Mentre que bosons $W^{\pm}$ i Z^0 són descrits a l'EWSM com a partícules amb massa nul·la, les nostres observacions experimentals ens les mostren com a partícules massives. El procés conegut com a *ruptura espontània de simetria* (SSB en anglés) és capaç de generar les masses de les partícules a l'hora que les simetries de la teoria es mantenen. La idea bàsica d'aquest procés és que part de les simetries no són respectades pel buit físic i per tant, pels estats obtinguts una volta el buit és excitat. Al SM el SSB s'implementa a través del *mecanisme de Higgs*, introduint el camp de Higgs que en interaccionar amb els bosons $W^{\pm}$ i Z^0 genera les masses d'aquestes partícules.

El camp de Higgs s'introdueix a la teoria com un doblet de $SU(2)_L$, la qual cosa permet construir nous termes que seran invariants sota les nostres simetries. En concret, es generen termes d'interacció entre el doblet de Higgs, un fermió i el seu antifermió. Aquests termes d'interacció són a priori no diagonals, però gràcies a les propietats de simetria es poden realitzar transformacions sota els camps, donant com a resultat estructures diagonals que podem identificar amb les masses dels fermions. Donat que els quarks dalt i baix estan relacionats (pertanyen al mateix doblet de $SU(2)_L$), aquestes transformacions no són independents i una transformació addicional és necessària. Els corrents carregats no són invariants sota aquesta transformació addicional, generant un canvi de sabor als corrents

neutres, parametritzada amb una matriu no diagonal, la matriu de Cabibbo-Kobayashi-Maskawa (CKM).

10.2.3 Teories de camps efectives

Les teories de camps efectius ens proporcionen una descripció més senzilla d'una teoria física, de manera que aquesta és equivalent a l'escala d'energies a la qual estem treballant. Les EFTs són molt útils per a descriure problemes físics que involucren diferents escales d'energia. La idea bàsica es basa en el *teorema del desacoblament* [38] que ens diu que la dinàmica d'un sistema a energies baixes no pot dependre dels detalls a altes energies. Per tant, emprant els graus de llibertat adients a la nostra escala d'energies podem donar una descripció de la natura simplificada. El SM és un exemple de la gran utilitat de les teories efectives. El fet que el SM alhora ens descriga la realitat amb una gran precisió i que algunes observacions ens indiquen que una teoria més general ha d'existir, fan del SM una teoria efectiva aplicable a energies baixes. A més, al SM podem identificar la nova física a partir de desviacions dels paràmetres mesurats, accessibles a través d'experiments de precisió.

L'ingredient principal d'una teoria de camps efectiva és el *Lagrangià efectiu*, expressat com una suma d'operadors locals,

$$\mathcal{L}_{\text{eff}} = \sum_{i,j} \frac{c_i^{(j)}}{\Lambda^{d_i-4}} \mathcal{O}_i^{(j)} = \sum_{i,j} C_i^{(j)} \mathcal{O}_i^{(j)} \,, \tag{10.2.1}$$

on $\mathcal{O}_i^{(j)}$ són els *operadors* de dimensió d_i, construïts dels camps lleugers i $C_i^{(j)}$ són els *coeficients de Wilson*, que contenen informació dels acoblaments dels graus de llibertat pesats. Λ és l'escala on els graus de llibertat passats són rellevants, és a dir, l'escala de nova física.

Depenent de la dimensió dels operadors, aquests es classifiquen en *operadors rellevants* ($d_i < 4$, importants a energies baixes), *operadors marginals* ($d_i = 4$, independents de E/Λ) i *operadors irrellevants* ($d_i > 4$, suprimits a energies baixes). $\mathcal{L}_{\text{eff}}$ conté un nombre infinit de termes (potències en Λ), i típicament es trunca a una dimensió N.

Els operadors reben correccions d'ordres superiors, de manera que els operadors d'igual dimensió es mesclen entre ells. Les correccions quàntiques i la seua dependència en l'escala estan incloses en els coeficients de Wilson, de manera que $\mathcal{L}_{\text{eff}}$ és independent de l'escala. La dependència dels coeficients en l'escala és expressada per les equacions del grup de renormalització (RGEs en anglés),

$$\mathcal{C}_i^{(j)}(\mu) = \sum_{a,k} \mathbf{U}_{ia} \exp\left\{ \int_{\alpha(\mu_0)}^{\alpha(\mu)} \frac{d\alpha}{\alpha} \frac{\gamma_{\mathcal{O},a}^{(j)}(\alpha)}{\beta(\alpha)} \right\} \left(\left(\mathbf{U}^{(j)} \right)^{-1} \right)_{ak} \mathcal{C}_k^{(j)}(\mu_0)\,. \tag{10.2.2}$$

10.2.4 `HEPfit`

El codi obert `HEPfit`, descrit al Capítol 5, és una ferramenta general dissenyada per a combinar restriccions directes i indirectes a EFTs o extensions particulars del SM. A més, ofereix la possibilitat de mostrejar l'espai de paràmetres emprant un Markov Chain Monte Carlo (MCMC) implementat a la llibreria `BAT` [88–90]. Està escrit en `C++` i paral·lelitzat amb Message Passing Interface (MPI) [91]. `HEPfit` està publicat sota la GNU General Public License, així que les contribucions dels usuaris són possibles i benvolgudes. Els observables inclosos es poden classificar com a teòrics, observables electrofebles de precisió, observables de Higgs o de sabor. Estan calculats a diferents models, com ara el SM o el A2HDM.

`HEPfit` es basa en l'estadística bayesiana, pel que la probabilitat expressa un *grau de creença*. La *probabilitat posterior* es defineix a partir de teorema de Bayes [94],

$$P(\vec{x}|D) = \frac{P(D|\vec{x})P_0(\vec{x})}{\int P(D|\vec{x})P_0(\vec{x})\,d\vec{x}}\,, \tag{10.2.3}$$

on $\vec{x}$ són els paràmetres del model, D les dades i $P_0(\vec{x})$ és la *probabilitat prèvia*.

Les peces de `HEPfit` són les classes `Model` i `Observable`. Els models estenen la classe base de manera seqüencial, `QCD` ← `StandardModel` ← `GeneralTHDM`. Això facilita implementar extensions o modificacions de models, ja que sols els nous ingredients respecte del model anterior han de ser afegits.

A la tesi s'han estudiat dos models diferents. En primer lloc, la classe `GeneralTHDM` conté un A2HDM en el qual la simetria CP es conserva. Aquest model conté com a paràmetres els tres acoblaments de Yukawa, les masses dels nous escalars, els paràmetres del potencial i l'angle de mescla $\tilde{\alpha}$. Diferents observables teòrics (potencial acotat per baix i unitarietat pertorbativa de la matriu S), electrofebles (paràmetres STU i R_b), de sabor (paràmetres STU i R_b) i de Higgs estan implementats per a aquest model. A més, `NPSMEFT6dtopquark`, a la classe `NewPhyics` conté els operadors de dimensió sis rellevants per a l'estudi dels acoblaments electrofebles dels quarks cim i fons. Aquestes classes s'empren als Capítols 7 i 9.

10.3 Resultats i conclusions

A aquesta tesi s'han tractat d'explorar diverses direccions que serien fonamentals per a entendre la natura de les partícules fonamentals i les seues interaccions. A continuació, es presenten algunes conclusions obtingudes a partir dels treballs realitzats a aquesta tesi. Aquests treballs es poden trobar en detall als Capítols 6, 7, 8 i 9.

10.3.1 Alineament als models de N doblets de Higgs

Al Capítol 6 s'estudien les conseqüències que les correccions quàntiques impliquen per als ANHDM. L'alineament a l'espai de sabor a ordre arbre s'imposa a una escala d'energia determinada (típicament a una escala alta), i les correccions quàntiques i el "córrer" dels paràmetres (*running* en anglés) donen lloc a que apareguen termes no diagonals, que tindrien conseqüències fenomenològiques a baixes energies i serien susceptibles de ser observades als nostres experiments.

Després de calcular les RGEs que ens proporcionen el *running* d'aquests paràmetres en el cas més general possible, ens centrem en les conseqüències fenomenològiques d'aquesta ruptura de l'alineament per al model més senzill (A2HDM). Considerant els observables més restrictius ($B_s \to \mu^+\mu^-, B \to X_s\gamma$ i ΔM_{B_s}) hem investigat les cotes actuals al

paràmetre de desalineació $C_d(M_W)$, tenint en compte els límits correlacionats de ς_u, ς_d i $M_{H^\pm}$.

Trobem que, mentre que els acoblaments fermiònics estan molt restringits, la sensibilitat a $C_d(M_W)$ és molt menuda, mostrant la supressió fenomenològica que esperàvem. Amb $\Lambda_A \leq M_{\text{Planck}} \sim 10^9$ GeV, tenim $C_d(M_W) \leq 40$, i per tant, la hipòtesi d'alineament a l'espai de sabor a altes energies (Λ_A amb $C_d(\Lambda_A) = 0$) sobreviu els límits fenomenològics en tots els casos i el nostre model no queda descartat. Com que l'A2HDM és el model de multi-Higgs més restringit, les nostres conclusions són aplicables a models més generals, amb $N > 2$ doblets.

10.3.2 Ajust global al A2HDM

El Capítol 7 consisteix en un ajust global a l'A2HDM amb conservació de CP. L'ajust s'ha realitzat amb el codi obert `HEPfit` del Capítol 5 i representa l'ajust més general fins ara. Es consideren observables teòrics, els paràmetres electrofebles de precisió (STU i R_b), observables de sabor i de Higgs.

Depenent de la massa del nou escalar neutre amb càrrega CP parella del model, es poden donar dos escenaris. Al primer d'ells, l'escenari *lleuger*, el Higgs descobert pel LHC és el de menor massa. En aquest cas, trobem que masses lleugeres i diferències de masses menudes són afavorides per l'ajust. Els observables de Higgs (*Higgs signal strengths*) ens ajuden a restringir el valor de l'angle de mescla $\tilde{\alpha}$, donant restriccions importants als plans $\tilde{\alpha} - \varsigma_f$. És d'especial interés l'aparició de dues branques per als plans $\tilde{\alpha} - \varsigma_d$ i $\tilde{\alpha} - \varsigma_\ell$, corresponent al que anomenem com a branca positiva ($y^H_{d,\ell} \approx 1$) i negativa $y^h_{d,\ell} \approx -1$). La combinació d'aquestes restriccions amb la resta d'observables ens permet restringir el valor de l'angle de mescla $\tilde{\alpha}$,

$$\begin{aligned} -0.015 \;&\leq \tilde{\alpha} \leq\; 0.013 \qquad \text{probabilitat del } 68\%, \\ -0.04 \;&\leq \tilde{\alpha} \leq\; 0.04 \qquad \text{probabilitat del } 95.5\%, \end{aligned} \tag{10.3.4}$$

i els paràmetres d'alineament (Fig. 10.5).

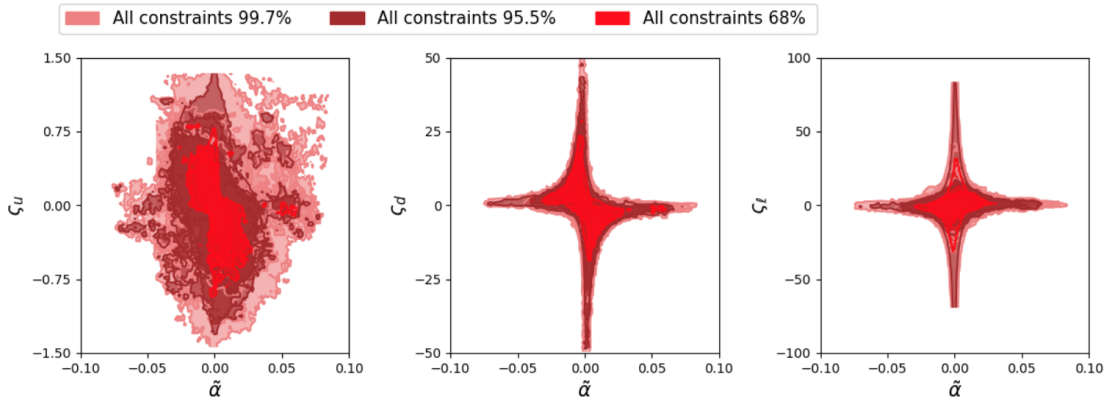

Figure 10.5: Restriccions als plans $\tilde{\alpha} - \varsigma_f$ a partir d'un ajust global amb una probabilitat del 68% (roig fosc), 95.5% (marró) and 99.7% (roig clar).

A l'escenari *pesat*, el Higgs amb massa al voltant de 125 GeV és el més pesat del model. A aquest cas, les masses dels escalars restants estan restringides a ser menors que 700 GeV. Les restriccions en els paràmetres d'alineament i l'angle de mescla són semblants a les de l'escenari anterior, desplaçant l'angle $\tilde{\alpha} \to \tilde{\alpha} - \frac{\pi}{2}$.

En els dos escenaris és interessant destacar la dependència de la *probabilitat prèvia* de les distribucions de les masses. Dependent de l'ús de distribucions de probabilitat de massa lineals o quadràtics les regions de massa lleugeres estan prohibides o no a una probabilitat donada. Aquest tret de l'estadística bayesiana ha de ser tingut en compte quan s'observen les restriccions dels plans de les masses. Observant les dues possibilitats interpretem que els resultats dels ajustos afavoreixen masses grans i diferències de masses menudes, independentment de les distribucions de *probabilitat prèvia*.

10.3.3 Ajusts a les transicions $b \to c$

Les desviacions experimentals als observables que involucren transicions $b \to c$ han atret l'atenció de la comunitat els últims anys. Sent mesurades a diferents observables i per diferents col·laboracions experimentals, aquestes anomalies es poden interpretar com a un

senyal de nova física. Com que aquesta nova física sembla afectar sols a la tercera generació de leptons, es pot relacionar amb violació de la universalitat leptònica.

Per tal d'entendre aquestes anomalies de B vam treballar en el formalisme de les teories efectives, realitzant ajusts globals i considerant els operadors de dimensió sis rellevants. A diferència d'altres treballs hem considerat les distribucions de q^2, mesurades per Belle i BaBar, i l'efecte de l'observable de la mesura de Belle $\bar{F}_L^{D^*}$.

Al nostre primer treball vam considerar un conjunt mínim d'assumpcions: la nova física sols està present a la tercera generació de leptons, els coeficients de Wilson són reals, no hi ha neutrins lleugers i la ruptura de simetria és lineal.

Si l'ajust es realitza sense tindre en compte $\bar{F}_L^{D^*}$, es troben tres mínims. El mínim global té un excel·lent valor del χ^2 i és compatible amb una modificació global del SM ($\chi^2_{\text{Min 1}} - \chi^2_{\text{SM}} = 1.4$). Els mínims locals presenten valors més grans del χ^2 i desviacions majors respecte del SM. Una vegada afegit $\bar{F}_L^{D^*}$, els ajusts mostren que la solució preferida encara és una modificació global del SM, però no és possible reproduir totes les mesures experimentals simultàniament a 1σ. Motivats per aquesta aparent incompatibilitat, vam relaxar la nostra assumpció sobre la ruptura de simetria lineal. En aquest cas, si bé és cert que es poden trobar regions de l'espai de paràmetres que satisfan tots els resultats experimentals a 1σ, les regions són molt afinades (*fine-tuned*) i per tant no donen descripcions satisfactòries de la realitat.

Al nostre segon treball, vam explorar la generalització dels nostres ajusts afegint els operadors que apareixen en presència de neutrins amb quiralitat dextrogira. El fet de tindre un elevat nombre de paràmetres impossibilita fer un ajust general, considerant tots els coeficients de Wilson de manera simultània. Per això vam treballar en un conjunt d'escenaris motivats, quantificant la qualitat dels resultats amb diferents paràmetres estadístics (Pull, p-value).

En tots els casos s'han estudiat les implicacions que la mesura de nous observables podria tindre per discriminar els possibles escenaris.

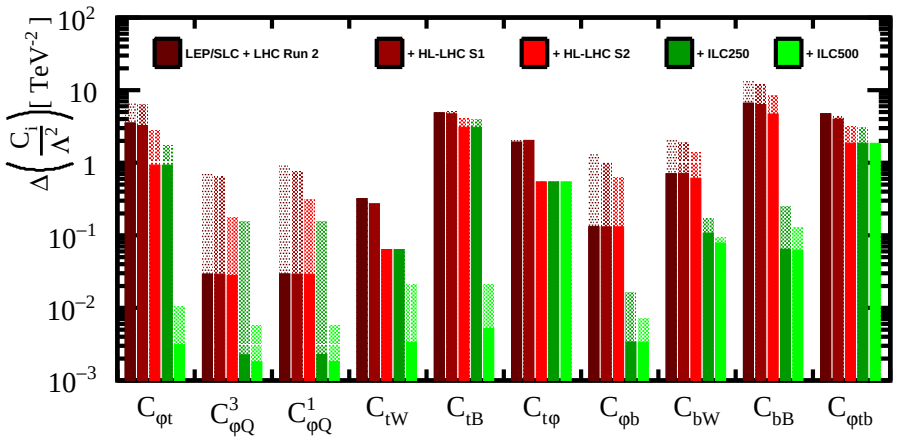

Figure 10.6: Resultats de l'ajust per als observables del LHC i LEP/SLC (marró clar) i perspectives per a la precisió dels coeficients de Wilson en el HL-LHC (marró fosc i roig) i futurs col·lisionadors e^+e^- (verd clar i fosc). Les barres sòlides indiquen cotes individuals i la barra completa els resultats dels ajusts globals (marginalitzats) amb deu paràmetres.

10.3.4 Ajusts electrofebles als quarks cim i fons

Al Capítol 9 hem realitzat un ajust global al subconjunt de deu operadors de dimensió sis rellevants per a acotar els acoblaments electrofebles dels quarks cim i fons. Les dades del LHC de producció del quark cim en associació amb un bosó feble, producció d'un únic quark cim (single-top) i fraccions d'helicitat del W en el decaïment del cim, es combinen amb els resultats de mesures del quark fons de LEP/SLC en el pol del Z. A l'ajust es tenen en compte els termes de dimensió Λ^{-4}, provinents de la interferència de dos operadors de dimensió sis, però s'ignoren els operadors de dimensió huit. Atés que a molts observables els termes lineals (amb un únic operador de dimensió sis) estan molt suprimits, aquest marc de treball és necessari per a poder realitzar el nostre ajust. Les conseqüències d'aquesta assumpció són estudiades en detall, i es fa un èmfasi en la validesa de l'ajust.

Es realitza un primer ajust a les dades actuals, obtenint cotes més fortes que treballs anteriors. Els resultats es poden trobar a la Fig. 10.6. A continuació, es presenten

escenari	LHC Run 2 +LEP/SLC	HL-LHC S2 +LEP/SLC	ILC500	ILC550	ILC500 +ILC1000
$\sqrt{s}$, $\int \mathcal{L}$	13 TeV, 36 fb^{-1}	14 TeV, 3 ab^{-1}	500 GeV, 4 ab^{-1}	550 GeV, 4 ab^{-1}	+1 TeV, +8 ab^{-1}
interval de probabilitat del 68% per al coeficient $C_{t\varphi}/\Lambda^2$ *[TeV*$^{-2}$*]*					
individual	$[-4.4, +0.0]$	$[-0.55, +0.55]$	$[-1.06, +1.06]$	$[-0.50, 0.50]$	$[-0.27, +0.27]$
marginalitzat	$[-4.6, -0.2]$	$[-0.55, +0.55]$	$[-1.07, +1.07]$	$[-0.52, +0.52]$	$[-0.32, +0.32]$
incertesa relativa en l'acoblament de Yukawa del quark cim, $\Delta y_t/y_t$ *[%]*					
individual	13.2	3.3	6.4	3.0	1.62
marginalitzat	13.2	3.3	6.4	3.1	1.96

Table 10.1: Intervals del 68% de probabilitat de $C_{t\varphi}/\Lambda^2$ i precisió corresponent per a l'acoblament e Yukawa del quark cim. Els resultats de l'última columna estan realitzats amb un ajust a desset paràmetres.

prediccions sobre les cotes que s'obtindran a futurs acceleradors, com ara a la fase d'alta lluminositat del LHC o a un accelerador lineal com l'ILC (Fig. 10.6) . A aquest últim cas s'estén la base d'operadors per contenir set operadors addicionals amb estructura de dos quarks i dos leptons.

Finalment, l'acoblament de Yukawa del quark cim s'estudia en detall. De l'ajust a les dades del LHC i LEP/SLC s'obtenen cotes de l'ordre de 10^1 TeV^{-2}. També es mostra com aquesta cota milloraria a futurs acceleradors. Aquests resultats estan resumits a la Taula 10.1.

Appendix A

Form factors for $B \to D^{(*)}$ transitions

The FFs $F_0(q^2)$, $F_1(q^2)$ and $F_T(q^2)$ appearing in the $B \to D$ matrix elements are defined,

$$\begin{aligned} F_1(q^2) &= \frac{1}{2\sqrt{m_B m_D}} \left[(m_B + m_D)\, h_+(q^2) - (m_B - m_D)\, h_-(q^2) \right], \\ F_0(q^2) &= \frac{1}{2\sqrt{m_B m_D}} \left[\frac{(m_B + m_D)^2 - q^2}{m_B + m_D}\, h_+(q^2) - \frac{(m_B - m_D)^2 - q^2}{m_B - m_D}\, h_-(q^2) \right], \\ F_T(q^2) &= \frac{m_B + m_D}{2\sqrt{m_B m_D}}\, h_T(q^2), \end{aligned} \tag{A.0.1}$$

while the $B \to D^*$ helicity amplitudes involve the following FFs for vector, axial and pseudoscalar currents,

$$\begin{aligned} V(q^2) &= \frac{m_B + m_{D^*}}{2\sqrt{m_B m_{D^*}}}\, h_V(q^2), \\ A_1(q^2) &= \frac{(m_B + m_{D^*})^2 - q^2}{2\sqrt{m_B m_{D^*}}(m_B + m_{D^*})}\, h_{A_1}(q^2), \\ A_2(q^2) &= \frac{m_B + m_{D^*}}{2\sqrt{m_B m_{D^*}}} \left[h_{A_3}(q^2) + \frac{m_{D^*}}{m_B} h_{A_2}(q^2) \right], \end{aligned} \tag{A.0.2}$$

$$\begin{aligned} A_0(q^2) &= \frac{1}{2\sqrt{m_B m_{D^*}}} \left[\frac{(m_B + m_{D^*})^2 - q^2}{2m_{D^*}}\, h_{A_1}(q^2) - \frac{m_B^2 - m_{D^*}^2 + q^2}{2m_B}\, h_{A_2}(q^2) \right. \\ &\qquad \left. - \frac{m_B^2 - m_{D^*}^2 - q^2}{2m_{D^*}}\, h_{A_3}(q^2) \right], \end{aligned} \tag{A.0.3}$$

and for the tensor matrix elements,

$$\begin{aligned}
T_1(q^2) &= \frac{1}{2\sqrt{m_B m_{D^*}}}\left[(m_B + m_{D^*})\, h_{T_1}(q^2) - (m_B - m_{D^*})\, h_{T_2}(q^2)\right], \\
T_2(q^2) &= \frac{1}{2\sqrt{m_B m_{D^*}}}\left[\frac{(m_B + m_{D^*})^2 - q^2}{m_B + m_{D^*}}\, h_{T_1}(q^2) - \frac{(m_B - m_{D^*})^2 - q^2}{m_B - m_{D^*}}\, h_{T_2}(q^2)\right], \qquad \text{(A.0.4)} \\
T_3(q^2) &= \frac{1}{2\sqrt{m_B m_{D^*}}}\left[(m_B - m_{D^*})\, h_{T_1}(q^2) - (m_B + m_{D^*})\, h_{T_2}(q^2) - 2\,\frac{m_B^2 - m_{D^*}^2}{m_B}\, h_{T_3}(q^2)\right].
\end{aligned}$$

The reduced functions $\hat{h}_i(q^2) = h_i(q^2)/\xi(q^2)$ take the form [60]

$$\begin{aligned}
\hat{h}_+ &= 1 + \hat{\alpha}_s\left[C_{V_1} + \frac{\omega+1}{2}\,(C_{V_2} + C_{V_3})\right] + (\varepsilon_c + \varepsilon_b)\,\hat{L}_1\,, \\
\hat{h}_- &= \hat{\alpha}_s\,\frac{\omega+1}{2}\,(C_{V_2} - C_{V_3}) + (\varepsilon_c - \varepsilon_b)\,\hat{L}_4\,, \\
\hat{h}_T &= 1 + \hat{\alpha}_s\,(C_{T_1} - C_{T_2} + C_{T_3}) + (\varepsilon_c + \varepsilon_b)\left(\hat{L}_1 - \hat{L}_4\right), \qquad \text{(A.0.5)}
\end{aligned}$$

for $B \to D$, and

$$\begin{aligned}
\hat{h}_V &= 1 + \hat{\alpha}_s C_{V_1} + \varepsilon_c\left(\hat{L}_2 - \hat{L}_5\right) + \varepsilon_b\left(\hat{L}_1 - \hat{L}_4\right), \\
\hat{h}_{A_1} &= 1 + \hat{\alpha}_s C_{A_1} + \varepsilon_c\left(\hat{L}_2 - \hat{L}_5\,\frac{\omega-1}{\omega+1}\right) + \varepsilon_b\left(\hat{L}_1 - \hat{L}_4\,\frac{\omega-1}{\omega+1}\right), \\
\hat{h}_{A_2} &= \hat{\alpha}_s C_{A_2} + \varepsilon_c\left(\hat{L}_3 + \hat{L}_6\right), \\
\hat{h}_{A_3} &= 1 + \hat{\alpha}_s\,(C_{A_1} + C_{A_3}) + \varepsilon_c\left(\hat{L}_2 - \hat{L}_3 + \hat{L}_6 - \hat{L}_5\right) + \varepsilon_b\left(\hat{L}_1 - \hat{L}_4\right), \\
\hat{h}_{T_1} &= 1 + \hat{\alpha}_s\left[C_{T_1} + \frac{\omega-1}{2}\,(C_{T_2} - C_{T_3})\right] + \varepsilon_c\hat{L}_2 + \varepsilon_b\hat{L}_1\,, \\
\hat{h}_{T_2} &= \hat{\alpha}_s\,\frac{\omega+1}{2}\,(C_{T_2} + C_{T_3}) + \varepsilon_c\hat{L}_5 - \varepsilon_b\hat{L}_4\,, \\
\hat{h}_{T_3} &= \hat{\alpha}_s C_{T_2} + \varepsilon_c\left(\hat{L}_6 - \hat{L}_3\right), \qquad \text{(A.0.6)}
\end{aligned}$$

for $B \to D^*$. The explicit expressions of the $\omega(q^2)$-dependent factors $\hat{L}_{1\ldots6}$ and the $\mathcal{O}(\alpha_s)$ corrections C_i can be found in Ref. [60]. Note that corrections of order $\Lambda_{\rm QCD}^2/m_c^2$ are included via the subleading Isgur-Wise functions $l_{1,2}(\omega)$. The detailed parametrization of the different FFs can be found in Ref. [60, 253].

The FF parameters can be seen in Table 8.2 of Chapter 8. The correlation between these parameters is given in Table A.1.

	ρ^2	c	d	$\chi_2(1)$	$\chi_2(1)'$	$\chi_3(1)'$	$\eta(1)$	$\eta(1)'$	$l_1(1)$	$l_2(1)$
ρ^2	1									
c	0.82	1								
d	-0.57	-0.91	1							
$\chi_2(1)$	-0.29	-0.22	0.13	1						
$\chi_2(1)'$	0.01	0.13	-0.13	0.00	1					
$\chi_3(1)'$	0.89	0.75	-0.51	0.00	-0.01	1				
$\eta(1)$	0.09	0.13	-0.14	-0.01	0.01	0.01	1			
$\eta(1)'$	-0.08	0.04	-0.08	0.03	0.00	-0.07	0.28	1		
$l_1(1)$	- 0.03	0.01	-0.05	0.00	0.00	0.01	0.34	-0.15	1	
$l_2(1)$	-0.01	0.00	0.00	0.00	-0.01	-0.01	0.00	0.00	0.01	1

Table A.1: Correlation matrix of the inputs in Table 8.2, used to determine the form factors in the HQET parametrization.

Appendix B

Kinematics for semileptonic decays

In this appendix we give the explicit form of the helicity spinors and 4-vectors needed to calculate $M \to M'\ell\bar{\nu}$ transitions with the helicity formalism [53, 79].

B.1 V^* rest frame

The spinors describing leptons (antileptons) of helicity $\pm\frac{1}{2}$, in the V^* rest frame, are:

$$
\begin{aligned}
u(p,+) &= \begin{bmatrix} \sqrt{E_\ell - |\vec{p}|}\cos\frac{\theta_\ell}{2} \\ \sqrt{E_\ell - |\vec{p}|}\sin\frac{\theta_\ell}{2}\mathrm{e}^{i\phi_\ell} \\ \sqrt{E_\ell + |\vec{p}|}\cos\frac{\theta_\ell}{2} \\ \sqrt{E_\ell + |\vec{p}|}\sin\frac{\theta_\ell}{2}\mathrm{e}^{i\phi_\ell} \end{bmatrix}, \qquad u(p,-) = \begin{bmatrix} -\sqrt{E_\ell + p}\sin\frac{\theta_\ell}{2}\mathrm{e}^{-i\phi_\ell} \\ \sqrt{E_\ell + |\vec{p}|}\cos\frac{\theta_\ell}{2} \\ -\sqrt{E_\ell - p}\sin\frac{\theta_\ell}{2}\mathrm{e}^{-i\phi_\ell} \\ \sqrt{E_\ell - |\vec{p}|}\cos\frac{\theta_\ell}{2} \end{bmatrix}, \\
v(p,+) &= \begin{bmatrix} -\sqrt{E_\nu - |\vec{p}|}\cos\frac{\theta_\ell}{2}\mathrm{e}^{-i\phi_\ell} \\ -\sqrt{E_\nu - |\vec{p}|}\sin\frac{\theta_\ell}{2} \\ \sqrt{E_\nu + |\vec{p}|}\cos\frac{\theta_\ell}{2}\mathrm{e}^{-i\phi_\ell} \\ \sqrt{E_\nu + |\vec{p}|}\sin\frac{\theta_\ell}{2} \end{bmatrix}, \qquad v(p,-) = \begin{bmatrix} -\sqrt{E_\nu + p}\sin\frac{\theta_\ell}{2} \\ \sqrt{E_\nu + |\vec{p}|}\cos\frac{\theta_\ell}{2}\mathrm{e}^{i\phi_\ell} \\ \sqrt{E_\nu - |\vec{p}|}\sin\frac{\theta_\ell}{2} \\ -\sqrt{E_\nu - |\vec{p}|}\cos\frac{\theta_\ell}{2}\mathrm{e}^{i\phi_\ell} \end{bmatrix},
\end{aligned}
\tag{B.1.1}
$$

where $\theta_{\ell,\nu}$ and $\phi_{\ell.\nu}$ are the polar and azimuthal angles of the lepton and the neutrino. These angles obey the relations $\theta_\nu = \pi - \theta_\ell$ and $\phi_\nu = \phi_\ell + \pi$. The 4-momenta of $M(p_M) \to M'\ell(p_\ell)\bar{\nu}(p_\nu)$ in the V^* rest frame, are given by,

$$
\begin{aligned}
p_M^\mu &= (E_M, 0, 0, |\vec{p}_M|)\,, \\
p_\ell^\mu &= \frac{q^2 - m_\ell^2}{2\sqrt{q^2}}\left(\frac{q^2 + m_\ell^2}{q^2 - m_\ell^2}, \sin\theta_\ell, 0, \cos\theta_\ell\right), \\
p_\nu^\mu &= \frac{q^2 - m_\ell^2}{2\sqrt{q^2}}\left(1, -\sin\theta_\ell, 0, -\cos\theta_\ell\right), \\
q^\mu &= \left(\sqrt{q^2}, 0, 0, 0\right),
\end{aligned}
\tag{B.1.2}
$$

The V^* polarization vectors read in this frame:

$$\begin{aligned}
\epsilon^{\mu}(q,\pm) &= \mp\frac{1}{\sqrt{2}}\,(0,1,\pm i,0)\,,\\
\epsilon^{\mu}(q,0) &= (0,0,0,-1)\,,\\
\epsilon^{\mu}(q,s) &= \frac{1}{\sqrt{q^2}}q^{\mu} = (1,0,0,0)\,.
\end{aligned}$$

B.2 M rest frame

In the M rest frame the z axis is aligned with the momentum of M'. The 4-momentum of M and M' are,

$$\begin{aligned}
p_M^{\mu} &= (m_M,0,0,0)\,,\\
p_{M'}^{\mu} &= (E_{M'},0,0,p_{M'})\,,
\end{aligned} \tag{B.2.3}$$

and the transfered momentum,

$$q^{\mu} = p_M^{\mu} - p_D^{\mu} = (m_M - E_D, 0, 0, -|\vec{p_D}|) = (q_0,0,0,-|\vec{p_D}|)\,. \tag{B.2.4}$$

The polarization vectors for V,

$$\begin{aligned}
\eta(p_D,\pm)^{\mu} &= \mp\frac{1}{\sqrt{2}}\,(0,1,\pm i,0)\,,\\
\eta(p_D,0)^{\mu} &= \frac{1}{m_D}\,(p_D,0,0,E_D)\ .
\end{aligned} \tag{B.2.5}$$

Appendix C

Propagation and decay of D^*

To compute the full four-body decay amplitude $B \to D^*\tau\bar{\nu} \to (D\pi)\,\tau\bar{\nu}$, we need to describe the propagation and the decay of the vector boson D^* to the $D\pi$ final state. The $D^* \to D\pi$ amplitude can be parametrized in the form

$$\mathcal{M}^{\lambda_{D^*}}_{D^*\to D\pi} \,=\, g_{D^*D\pi}\,\varepsilon_\mu(\lambda_{D^*})\,p_D^\mu\,, \tag{C.0.1}$$

with an effective coupling $g_{D^*D\pi}$ that can be determined from the total decay width,

$$\Gamma(D^* \to D\pi) \,=\, C\,\frac{\lambda^{3/2}(m^2_{D^*}, m^2_D, m^2_\pi)}{192\pi m^5_{D^*}}\,|g_{D^*D\pi}|^2\,, \tag{C.0.2}$$

where $C = 1,\ \frac{1}{2}$ for a final $\pi^\pm$, π^0, respectively. The dependence of the effective amplitude (C.0.1) on the momentum and polarization vectors fixes the angular structure of the three possible helicity amplitudes:

$$\mathcal{M}^0_{D^*\to D\pi} \,=\, -g_{D^*D\pi}\,|\vec{p}_D|\,\cos\theta_D \qquad \text{and} \qquad \mathcal{M}^{\pm1}_{D^*\to D\pi} \,=\, \pm\frac{1}{\sqrt{2}}\,g_{D^*D\pi}\,|\vec{p}_D|\,\sin\theta_D\,, \tag{C.0.3}$$

with $|\vec{p}_D| = \lambda^{1/2}(m^2_{D^*}, m^2_D, m^2_\pi)/(2m_{D^*})$ being the three-momentum of the D meson in the D^* rest frame.

The propagation of the D^* can be described through a Breit-Wigner function. Since the decay width of the D^* is much smaller than its mass, we can use the narrow-width

approximation,

$$\frac{1}{(m^2_{D\pi}-m^2_{D^*})^2+m^2_{D^*}\Gamma^2_{D^*}} \quad \xrightarrow{\Gamma_{D^*}\ll m_{D^*}} \quad \frac{\pi}{m_{D^*}\Gamma_{D^*}}\,\delta(m^2_{D\pi}-m^2_{D^*})\,, \tag{C.0.4}$$

and write the decay probability of the process $B\to(D\pi)\,\tau\bar{\nu}$ in the form

$$|\mathcal{M}[B\to(D\pi)\,\tau(\lambda_\tau)\,\nu_X]|^2 \;=\; \frac{1}{2}\,G_F^2\,|V_{cb}|^2\,\frac{\pi}{m_{D^*}\Gamma_{D^*}}\,\delta(m^2_{D\pi}-m^2_{D^*})\,\left|\sum_{\lambda_{D^*}}\mathcal{M}_X^{\lambda_{D^*},\lambda_\tau}\,\mathcal{M}^{\lambda_{D^*}}_{D^*\to D\pi}\right|^2 . \tag{C.0.5}$$

Notice that the dependence on $g_{D^*D\pi}$ cancels out from this expression. The interferences among the unobservable helicity amplitudes of the intermediate D^* meson generate the different dependences on θ_D, appearing in the four-body angular distribution listed in Eq. (4.3.36).

Appendix D

Hadronic matrix elements for meson mixing

The Wilson coefficients of the effective Hamiltonian (6.5.32) have been evaluated at the electroweak scale, $\mu_{tW} \sim \mathcal{O}(M_W, m_t, M_{H^\pm}, M_{\varphi_i^0})$, and need to be evolved down to the low-energy scales where the hadronic matrix elements of the corresponding quark operators are determined. In addition to the three scalar operators in Eq. (6.5.33), generated through φ_k^0-exchange between two $\mathcal{L}_{\rm FCNC}$ vertices, one must take also into account the leading contributions from 1-loop box diagrams with $W^\pm$ and/or $H^\pm$ propagators. Neglecting the light quark mass ($m_{d,s}$ for $B_{d,s}^0$ or m_d for K^0), these charged-current boxes contribute to $C_{1,ij}^{SRR}$ and to the SM operator [112]

$$\mathcal{O}_{ij}^{VLL} \,=\, (\bar{d}_{iL}\gamma_\mu d_{jL})(\bar{d}_{iL}\gamma^\mu d_{jL})\,. \tag{D.0.1}$$

Gluonic corrections give rise to the appearance of additional operators which mix under renormalization with the previous ones. In general, one must consider a basis of eight operators including the additional structures [414]:

$$\begin{aligned}
\mathcal{O}_{ij}^{VRR} \,&=\, (\bar{d}_{iR}\gamma_\mu d_{jR})(\bar{d}_{iR}\gamma^\mu d_{jR})\,, & \mathcal{O}_{1,ij}^{LR} \,&=\, (\bar{d}_{iL}\gamma_\mu d_{jL})(\bar{d}_{iR}\gamma^\mu d_{jR})\,, \\
\mathcal{O}_{2,ij}^{SLL} \,&=\, (\bar{d}_{iR}\sigma_{\mu\nu} d_{jL})(\bar{d}_{iR}\sigma^{\mu\nu} d_{jL})\,, & \mathcal{O}_{2,ij}^{SRR} \,&=\, (\bar{d}_{iL}\sigma_{\mu\nu} d_{jR})(\bar{d}_{iL}\sigma^{\mu\nu} d_{jR})\,,
\end{aligned} \tag{D.0.2}$$

with[1] $\sigma^{\mu\nu} \equiv \frac{i}{2}\,[\gamma^\mu, \gamma^\nu]$. The renormalization group evolution of this operator basis factorizes in five different sectors [414, 415]:

$$\begin{bmatrix} C^X_{1,ij}(\mu) \\ \\ C^X_{2,ij}(\mu) \end{bmatrix} = \begin{bmatrix} [\eta_{11}(\mu)]_X & [\eta_{12}(\mu)]_X \\ \\ [\eta_{21}(\mu)]_X & [\eta_{22}(\mu)]_X \end{bmatrix} \begin{bmatrix} C^X_{1,ij}(\mu_{tW}) \\ \\ C^X_{2,ij}(\mu_{tW}) \end{bmatrix}, \tag{D.0.3}$$

$$C^Y_{1,ij}(\mu) \;=\; [\eta(\mu)]_Y \;\, C^Y_{1,ij}(\mu_{tW})\,, \tag{D.0.4}$$

where $X = SRR, SLL, LR$ and $Y = VLL, VRR$. Next-to-leading-order expressions for the coefficients $[\eta_{kl}(\mu)]_X$ $(k,l = 1,2)$ and $[\eta(\mu)]_Y$ can be found in Refs. [414, 415] for the B^0_q and K^0 systems. Since in our case the initial conditions are only known at the lowest order, we have calculated the evolution with leading-order anomalous dimensions and two-loop running for the strong coupling α_s.

The hadronic matrix elements of the $\Delta F = 2$ four-quark operators can be expressed as:

$$\langle \bar{M}^0 |\, \mathcal{O}^{VZZ}_{1,ij} \,| M^0 \rangle \;=\; \frac{2}{3}\, f_M^2\, m_{M^0}^2\; B_1^{VZZ}(\mu)\,, \tag{D.0.5}$$

$$\langle \bar{M}^0 |\, \mathcal{O}^{LR}_{1,ij} \,| M^0 \rangle \;=\; -\frac{1}{3}\left(\frac{f_M\, m_{M^0}^2}{m_i(\mu) + m_j(\mu)}\right)^2 B_1^{LR}(\mu)\,, \tag{D.0.6}$$

$$\langle \bar{M}^0 |\, \mathcal{O}^{LR}_{2,ij} \,| M^0 \rangle \;=\; \frac{1}{2}\left(\frac{f_M\, m_{M^0}^2}{m_i(\mu) + m_j(\mu)}\right)^2 B_2^{LR}(\mu)\,, \tag{D.0.7}$$

$$\langle \bar{M}^0 |\, \mathcal{O}^{SZZ}_{1,ij} \,| M^0 \rangle \;=\; -\frac{5}{12}\left(\frac{f_M\, m_{M^0}^2}{m_i(\mu) + m_j(\mu)}\right)^2 B_1^{SZZ}(\mu)\,, \tag{D.0.8}$$

$$\langle \bar{M}^0 |\, \mathcal{O}^{ZZ}_{2,ij} \,| M^0 \rangle \;=\; \left(\frac{f_M\, m_{M^0}^2}{m_i(\mu) + m_j(\mu)}\right)^2 B_2^{SZZ}(\mu)\,, \tag{D.0.9}$$

where $Z = L, R$ denotes the two different operator chiralities, $m_{i,j}(\mu)$ are the relevant running quark masses and the $B_i(\mu)$ factors parametrize the deviations from the naive vacuum-insertion approximation. These parameters have been calculated by the ETM

[1] Notice that Refs. [414, 415] adopt a non-conventional definition of $\sigma^{\mu\nu}$, without the factor 'i', and have then the opposite sign for the operators $\mathcal{O}^{SRR}_{2,ij}$.

$i=$	1	2	3	4	5
$f_{B_d}\sqrt{B_i^{B_d}}$	174 ± 8 MeV	160 ± 8 MeV	177 ± 17 MeV	185 ± 9 MeV	229 ± 14 MeV
$f_{B_s}\sqrt{B_i^{B_s}}$	211 ± 8 MeV	195 ± 7 MeV	215 ± 17MeV	220 ± 9 MeV	285 ± 14 MeV
B_i^K	$0.506 \pm 0.017 \pm 0.003$	$0.46 \pm 0.01 \pm 0.03$	$0.79 \pm 0.02 \pm 0.05$	$0.78 \pm 0.02 \pm 0.04$	$0.49 \pm 0.03 \pm 0.03$

Table D.1: Lattice determinations of $f_M\sqrt{B_i^M}$ ($M = B_d^0, B_s^0$) [416] and B_i^K ($M = K^0$) [417], in the $\overline{\text{MS}}$ scheme. The B_q^0 parameters are given at $\mu = m_b$, while the K^0 values refer to $\mu = 3$ GeV.

lattice collaboration, employing the ratio method approach on $N_f = 2$ ensembles for B_d^0 and B_s^0 [416], and simulations with $N_f = 2+1+1$ dynamical sea quarks for K^0 [417]. The ETM results are given in a different operator basis; the connection reads:

$$B_1^{VZZ}(\mu) = B_1(\mu)\,, \qquad B_1^{LR}(\mu) = B_5(\mu)\,, \qquad B_2^{LR}(\mu) = B_4(\mu)\,,$$

$$B_1^{SZZ}(\mu) = B_2(\mu)\,, \qquad B_2^{SZZ}(\mu) = \frac{5}{3}\,B_2(\mu) - \frac{2}{3}\,B_3(\mu)\,. \tag{D.0.10}$$

The numerical values of the B_i parameters are compiled in Table D.1.

The observables relevant for our phenomenological analyses are

$$\Delta m_{B_q^0} = \frac{1}{m_{B_q^0}}\,\left|\langle B_q^0|\,\mathcal{H}_{\text{eff}}\,|\bar{B}_q^0\rangle\right|\,, \qquad \varepsilon_K = k_\epsilon\,\frac{\mathrm{e}^{i\phi_\epsilon}}{\sqrt{2}}\,\frac{\mathcal{I}\text{m}\left(\langle K^0|\,\mathcal{H}_{\text{eff}}\,|\bar{K}^0\rangle\right)}{2m_K\,\Delta m_K}\,, \tag{D.0.11}$$

where $\phi_\epsilon \approx \tan^{-1}\left[2(m_{K_L} - m_{K_S})/(\Gamma_{K_S} - \Gamma_{K_L})\right] = (43.52 \pm 0.05)^\circ$ is the so-called super-weak phase [73] and $k_\epsilon \approx 0.94 \pm 0.02$ accounts for small long-distance corrections [418]. We do not extract new-physics constraints from Δm_K because the kaon mass difference receives large long-distance contributions that introduce sizeable theoretical uncertainties.

Appendix E

Warsaw basis and UV Lagrangian

The operators describing the SMEFT in the Warsaw basis are given by [289, 290],

$$\begin{aligned}
\mathcal{O}_{lq}^{(3)} &= \left(\bar{\ell}\gamma_\mu\tau^I\ell\right)\left(\bar{q}\gamma^\mu\tau^I q\right), \\
\mathcal{O}_{lequ}^{(1)} &= \left(\bar{\ell}^j e\right)\varepsilon_{jk}\left(\bar{q}^k u\right), \\
\mathcal{O}_{ledq} &= \left(\bar{\ell}^j e\right)\left(\bar{d}q^j\right), \\
\mathcal{O}_{lequ}^{(3)} &= \left(\bar{\ell}^j\sigma_{\mu\nu}e\right)\varepsilon_{jk}\left(\bar{q}^k\sigma^{\mu\nu}u\right),
\end{aligned} \tag{E.0.1}$$

where τ^I are the Pauli matrices and ε_{jk} is the totally antisymmetric tensor with $\varepsilon_{12} = +1$. The fields q and ℓ are the quark and lepton $SU(2)_L$ doublets, respectively, and u, d, e are the right-handed $SU(2)_L$ singlets. Neglecting the small corrections proportional to the CKM factors V_{ub} and V_{cb}, the relevant contributions to the $b \to c\tau\nu$ transitions originate in the Wilson coefficients $[C_{lq}^{(3)}]_{3323} \equiv \tilde{C}_{LL}^V$, $[C_{lequ}^{(1)}]_{3332} \equiv \tilde{C}_{RL}^S$, $[C_{ledq}]_{3332} \equiv \tilde{C}_{LL}^S$ and $[C_{lequ}^{(3)}]_{3332} \equiv \tilde{C}_{LL}^T$, where $[C_X]_{ijkl}$ denotes the coefficient of the corresponding operator O_X with flavour indices i, j, k, l. The effective Lagrangian relevant for the description of the B anomalies is therefore given by

$$\mathcal{L}_{\text{SMEFT}} \supset \frac{1}{\Lambda_{\text{NP}}^2}\left(\tilde{C}_{LL}^V\,[\mathcal{O}_{lq}^{(3)}]_{3323} + \tilde{C}_{RL}^S\,[\mathcal{O}_{lequ}^{(1)}]_{3332} + \tilde{C}_{LL}^S\,[\mathcal{O}_{ledq}]_{3332} + \tilde{C}_{LL}^T\,[\mathcal{O}_{lequ}^{(3)}]_{3332}\right). \tag{E.0.2}$$

Notice that there is a correspondence between the effective operators at the SMEFT basis with those at the WET basis, according to:

$$\mathcal{O}_{lq}^{(3)} \leftrightarrow \mathcal{O}_{LL}^{V}\,, \qquad \mathcal{O}_{lequ}^{(1)} \leftrightarrow \mathcal{O}_{RL}^{S}\,, \qquad \mathcal{O}_{ledq} \leftrightarrow \mathcal{O}_{LL}^{S}\,, \qquad \mathcal{O}_{lequ}^{(3)} \leftrightarrow \mathcal{O}_{LL}^{T}\,, \tag{E.0.3}$$

which allow us to use the notation $\tilde{C}_i$ for the Wilson coefficients at the SMEFT basis, with the aim of making the discussion more intuitive for the reader.

Possible new mediators contributing to the effective Hamiltonian of Eq. (8.2.13) and their relative effective Lagrangian are summarized in Table E.1.

Spin	NP mediator	Contribution	Relevant effective Lagrangian (+ h.c.)
0	$(\bar{3},1,1/3)\sim\phi$	$\mathcal{O}_{LL}^{V}$	$\propto\frac{1}{2M_\phi^2}(\overline{d_L}\gamma_\mu u_L)(\overline{\nu_L}\gamma^\mu e_L)$
		$\mathcal{O}_{LL}^{S}$, $\mathcal{O}_{LL}^{T}$	$\propto\frac{1}{M_\phi^2}\left[(\overline{u_R}d_L)(\overline{e_R}\nu_L)-\frac{1}{4}(\overline{u_R}\sigma_{\mu\nu}d_L)(\overline{e_R}\sigma^{\mu\nu}\nu_L)\right]$
	$(3,2,7/6)\sim\left(\phi_{5/3},\phi_{2/3}\right)$	$\mathcal{O}_{LL}^{S}$, $\mathcal{O}_{LL}^{T}$	$\propto\frac{1}{M_{\phi_{2/3}}^2}\left[(\overline{e_R}\nu_L)(\overline{u_R}d_L)+\frac{1}{4}(\overline{e_R}\sigma_{\mu\nu}\nu_L)(\overline{u_R}\sigma^{\mu\nu}d_L)\right]$
	$(\bar{3},3,1/3)\sim(\phi_{4/3},\phi_{1/3},\phi_{-2/3})$	$\mathcal{O}_{LL}^{V}$	$\propto\frac{1}{M_{\phi_{1/3}}^2}(\overline{d_L}\gamma_\mu u_L)(\overline{\nu_L}\gamma^\mu e_L)$
	$(1,2,1/2)\sim(h_2^+,h_2^0)$	$\mathcal{O}_{RL}^{S}$	$\propto\frac{1}{M_{h_2^+}^2}(\overline{u_L}d_R)(\overline{e_R}\nu_L)$
		$\mathcal{O}_{LL}^{S}$	$\propto\frac{1}{M_{h_2^+}^2}(\overline{u_R}d_L)(\overline{e_R}\nu_L)$
1	$(\bar{3},2,5/6)\sim(\phi_{4/3}^\mu,\phi_{1/3}^\mu)$	$\mathcal{O}_{RL}^{S}$	$\propto\frac{1}{M_{\phi_{-1/3}}^2}(\overline{e_R}\nu_L)(\overline{u_L}d_R)$
	$(3,1,2/3)\sim\phi^\mu$	$\mathcal{O}_{LL}^{V}$	$\propto\frac{1}{M_\phi^2}(\overline{u_L}\gamma_\mu d_L)(\overline{e_L}\gamma^\mu\nu_L)$
		$\mathcal{O}_{RL}^{S}$	$\propto\frac{1}{M_\phi^2}(\overline{u_L}d_R)(\overline{e_R}\nu_L)$
	$(3,3,2/3)\sim(\phi_{5/3}^\mu,\phi_{2/3}^\mu,\phi_{-1/3}^\mu)$	$\mathcal{O}_{LL}^{V}$	$\propto\frac{1}{M_{\phi_{2/3}}^2}(\overline{\nu_L}\gamma_\mu e_L)(\overline{d_L}\gamma^\mu u_L)$
	$(1,3,0)\sim(W_+'^\mu,W_0'^\mu,W_-'^\mu)$	$\mathcal{O}_{LL}^{V}$	$\frac{1}{M_{W_+'}^2}(\overline{e_L}\gamma_\mu\nu_L)(\overline{u_L}\gamma^\mu d_L)$

Table E.1: Possible fields contributing to the effective Hamiltonian of Eq. (8.2.13), at dimension 6: leptoquarks are denoted by ϕ and a second Higgs doublet as h_2. Their quantum numbers ($SU(3)$, $SU(2)$, $U(1)_Y$), contribution to the EFT operators and their relevant effective Lagrangian after integrating them out are described for each new field. Their $SU(2)$ decomposition is explicitly shown after the "$\sim$".

Appendix F

Data compilation for the A2HDM fit

The following tables detail the collider data sources employed in our global fit. Table F.1 compiles the LHC and Tevatron data sources on Higgs signal strengths. The information on heavy scalar searches at the LHC is collected in Tables F.2, F.3, F.4 and F.5. These searches are applied either to the neutral scalars $\varphi_i^0 = H, A$ or to the charged Higgs boson, $H^\pm$. Table F.2 contains information about $\varphi_i^0 = H, A$ decaying into fermions, $\gamma\gamma$ and $Z\gamma$. In Table F.3 the final channel is either WW, ZZ or $VV = ZZ, WW$. Information about a neutral scalar decaying into the SM Higgs boson is summarized in Table F.4. Finally direct searches related to the charged Higgs boson are displayed in Table F.5. Parenthesis indicate an specific final state and square brackets that limits are quoted on the primary final state, measured through the second final state.

Channel	$b\bar{b}$	$\gamma\gamma$	$\mu^+\mu^-$	$\tau^+\tau^-$	WW	$Z\gamma$	ZZ
ggF_8		[419, 420]	[421]	[422, 423]	[424–426]	[427, 428]	[429, 430]
ggF_{13}		[431, 432]	[433, 434]	[435, 436]	[437–439]	[440, 441]	[442–444]
VBF_8		[419, 420]	[421]	[422, 423]	[424–426]	[427]	[429, 430]
VBF_{13}	[445, 446]	[431, 432]	[433, 434]	[435, 436]	[437–439]	-	[442–444]
VH_8	[447, 448]	[419, 420]	[421]	[422]	[424–426]	[427]	[429, 430]
VH_{13}	[449, 450]	[431, 432]	[433, 434]	[435, 451]	[437–439]		[442–444]
ttH_8	[452, 453]	[419, 420]	[421]			[427]	[429, 430]
ttH_{13}	[454–456]	[431, 432]	[433, 434]		[439]		[442–444]
VH_2	[457, 458]						
ttH_2	[457, 458]						

Table F.1: Higgs signal strengths input used in the fit, for different production and decay channels, at energies of $\sqrt{s} = 7, 8$ TeV (ATLAS and CMS, Run I), $\sqrt{s} = 13$ TeV (ATLAS and CMS, Run II) and $\sqrt{s} = 2$ TeV (D0 and CDF collaborations).

Label	**Channel**	**Experiment**	**Mass range [TeV]**	$\mathcal{L}$ [$\mathbf{fb}^{-1}$]
A_{13t}^{tt}	$tt \to \varphi_i^0 \to tt$	ATLAS [459]	[0.4;1]	36.1
A_{13b}^{tt}	$bb \to \varphi_i^0 \to tt$	ATLAS [460]	[0.4;1]	13.2
C_{8b}^{bb}	$bb \to \varphi_i^0 \to bb$	CMS [461]	[0.1;0.9]	19.7
C_{8}^{bb}	$gg \to \varphi_i^0 \to bb$	CMS [462]	[0.33;1.2]	19.7
C_{13}^{bb}	$pp \to \varphi_i^0 \to bb$	CMS [463]	[0.55;1.2]	2.69
C_{13b}^{bb}	$bb \to \varphi_i^0 \to bb$	CMS [464]	[0.3;1.3]	35.7
$A_{8}^{\tau\tau}$	$gg \to \varphi_i^0 \to \tau\tau$	ATLAS [465]	[0.09;1]	20
$C_{8}^{\tau\tau}$		CMS [466]	[0.09;1]	19.7
$A_{8b}^{\tau\tau}$	$bb \to \varphi_i^0 \to \tau\tau$	ATLAS [465]	[0.09;1]	20
$C_{8b}^{\tau\tau}$		CMS [466]	[0.09;1]	19.7
$A_{13}^{\tau\tau}$	$gg \to \varphi_i^0 \to \tau\tau$	ATLAS [467]	[0.2;2.25]	36.1
$C_{13}^{\tau\tau}$		CMS [468]	[0.09;3.2]	35.9
$A_{13b}^{\tau\tau}$	$bb \to \varphi_i^0 \to \tau\tau$	ATLAS [467]	[0.2;2.25]	36.1
$C_{13b}^{\tau\tau}$		CMS [468]	[0.09;3.2]	35.9
$A_{8}^{\gamma\gamma}$	$gg \to \varphi_i^0 \to \gamma\gamma$	ATLAS [469]	[0.065;0.6]	20.3
$A_{13}^{\gamma\gamma}$	$pp \to \varphi_i^0 \to \gamma\gamma$	ATLAS [470]	[0.2;2.7]	36.7
$C_{13}^{\gamma\gamma}$	$gg \to \varphi_i^0 \to \gamma\gamma$	CMS [471]	[0.5;4]	35.9
$A_{8}^{Z\gamma}$	$pp \to \varphi_i^0 \to Z\gamma \to (\ell\ell)\gamma$	ATLAS [472]	[0.2;1.6]	20.3
$C_{8}^{Z\gamma}$		CMS [473]	[0.2;1.2]	19.7
$A_{13}^{\ell\ell\gamma}$	$gg \to \varphi_i^0 \to Z\gamma[\to (\ell\ell)\gamma]$	ATLAS [440]	[0.25;2.4]	36.1
$A_{13}^{qq\gamma}$	$gg \to \varphi_i^0 \to Z\gamma[\to (qq)\gamma]$	ATLAS [474]	[1;6.8]	36.1
$C_{8+13}^{Z\gamma}$	$gg \to \varphi_i^0 \to Z\gamma$	CMS [475]	[0.35;4]	35.9

Table F.2: Direct searches for neutral heavy scalars, $\varphi_i^0 = H, A$, with quarks, leptons ($\ell = e, \mu$), photons and $Z\gamma$ final states.

Label	**Channel**	**Experiment**	**Mass range [TeV]**	$\mathcal{L}$ [fb^{-1}]
A_8^{ZZ}	$gg \to \varphi_i^0 \to ZZ$	ATLAS [476]	[0.14;1]	20.3
A_{8V}^{ZZ}	$VV \to \varphi_i^0 \to ZZ$	ATLAS [476]	[0.14;1]	20.3
$A_{13}^{2\ell 2L}$	$gg \to \varphi_i^0 \to ZZ[\to (\ell\ell)(\ell\ell,\nu\nu)]$	ATLAS [477]	[0.2;1.2]	36.1
$A_{13V}^{2\ell 2L}$	$VV \to \varphi_i^0 \to ZZ[\to (\ell\ell)(\ell\ell,\nu\nu)]$	ATLAS [477]	[0.2;1.2]	36.1
A_{13}^{2L2q}	$gg \to \varphi_i^0 \to ZZ[\to (\ell\ell,\nu\nu)(qq)]$	ATLAS [478]	[0.3;3]	36.1
A_{13V}^{2L2q}	$VV \to \varphi_i^0 \to ZZ[\to (\ell\ell,\nu\nu)(qq)]$	ATLAS [478]	[0.3;3]	36.1
$C_{13}^{2\ell 2X}$	$pp \to \varphi_i^0 \to ZZ[\to (\ell\ell)(qq,\nu\nu,\ell\ell)]$	CMS [479]	[0.13;3]	35.9
$C_{13}^{2q2\nu}$	$pp \to \varphi_i^0 \to ZZ[\to (qq)(\nu\nu)]$	CMS [480]	[1;4]	35.9
A_8^{WW}	$gg \to \varphi_i^0 \to WW$	ATLAS [481]	[0.3;1.5]	20.3
A_{8V}^{WW}	$VV \to \varphi_i^0 \to WW$	ATLAS [481]	[0.3;1.5]	20.3
$A_{13}^{2(\ell\nu)}$	$gg \to \varphi_i^0 \to WW[\to (e\nu)(\mu\nu)]$	ATLAS [482]	[0.2;4]	36.1
$A_{13V}^{2(\ell\nu)}$	$VV \to \varphi_i^0 \to WW[\to (e\nu)(\mu\nu)]$	ATLAS [482]	[0.2;3]	36.1
$C_{13}^{2(\ell\nu)}$	$(gg{+}VV) \to \varphi_i^0 \to WW \to (\ell\nu)(\ell\nu)$	CMS [483]	[0.2;1]	2.3
$A_{13}^{\ell\nu 2q}$	$gg \to \varphi_i^0 \to WW[\to (\ell\nu)(qq)]$	ATLAS [484]	[0.3;3]	36.1
$A_{13V}^{\ell\nu 2q}$	$VV \to \varphi_i^0 \to WW[\to (\ell\nu)(qq)]$	ATLAS [484]	[0.3;3]	36.1
$C_{13}^{\ell\nu 2q}$	$pp \to \varphi_i^0 \to WW[\to (\ell\nu)(qq)]$	CMS [485]	[1;4.4]	35.9
C_8^{VV}	$pp \to \varphi_i^0 \to VV$	CMS [486]	[0.145;1]	24.8
A_{13}^{4q}	$pp \to \varphi_i^0 \to VV[\to (qq)(qq)]$	ATLAS [487]	[1.2;3]	36.7

Table F.3: Direct searches for neutral heavy scalars, $\varphi_i^0 = H, A$, with vector-boson final states. $V = W, Z$, $\ell = e, \mu$.

Label	Channel	Experiment	Mass range [TeV]	$\mathcal{L}$ [fb^{-1}]
A_8^{hh}	$gg \to \varphi_i^0 \to hh$	ATLAS [488]	[0.26;1]	20.3
C_8^{4b}	$pp \to \varphi_i^0 \to hh \to (bb)(bb)$	CMS [489]	[0.27;1.1]	17.9
$C_8^{2\gamma 2b}$	$pp \to \varphi_i^0 \to hh \to (bb)(\gamma\gamma)$	CMS [490]	[0.260;1.1]	19.7
$C_{8g}^{2b2\tau}$	$gg \to \varphi_i^0 \to hh \to (bb)(\tau\tau)$	CMS [491]	[0.26;0.35]	19.7
$C_8^{2b2\tau}$	$pp \to \varphi_i^0 \to hh[\to (bb)(\tau\tau)]$	CMS [492]	[0.35;1]	18.3
A_{13}^{4b}	$pp \to \varphi_i^0 \to hh \to (bb)(bb)$	ATLAS [493]	[0.26;3]	36.1
$C_{13,1}^{4b}$		CMS [494]	[0.26;1.2]	35.9
$C_{13,2}^{4b}$		CMS [495]	[1.2;3]	35.9
$A_{13}^{2\gamma 2b}$	$pp \to \varphi_i^0 \to hh[\to (bb)(\gamma\gamma)]$	ATLAS [496]	[0.26;1]	36.1
$C_{13}^{2\gamma 2b}$	$pp \to \varphi_i^0 \to hh \to (bb)(\gamma\gamma)$	CMS [497]	[0.25;0.9]	35.9
$A_{13}^{2b2\tau}$	$pp \to \varphi_i^0 \to hh \to (bb)(\tau\tau)$	ATLAS [498]	[0.26;1]	36.1
$C_{13,1}^{2b2\tau}$		CMS [499]	[0.25;0.9]	35.9
$C_{13,2}^{2b2\tau}$	$pp \to \varphi_i^0 \to hh[\to (bb)(\tau\tau)]$	CMS [500]	[0.9;4]	35.9
C_{13}^{2b2V}	$pp \to \varphi_i^0 \to hh \to (bb)(VV \to \ell\nu\ell\nu)$	CMS [501]	[0.26;0.9]	35.9
A_{13}^{2b2W}	$pp \to \varphi_i^0 \to hh[\to (bb)(WW)]$	ATLAS [502]	[0.5;3]	36.1
$A_{13}^{2\gamma 2W}$	$gg \to \varphi_i^0 \to hh \to (\gamma\gamma)(WW)$	ATLAS [503]	[0.26;0.5]	36.1
A_8^{bbZ}	$gg \to \varphi_i^0 \to hZ \to (bb)Z$	ATLAS [504]	[0.22;1]	20.3
$C_8^{2b2\ell}$	$gg \to \varphi_i^0 \to hZ \to (bb)(\ell\ell)$	CMS [505]	[0.225;0.6]	19.7
$A_8^{\tau\tau Z}$	$gg \to \varphi_i^0 \to hZ \to (\tau\tau)Z$	ATLAS [504]	[0.22;1]	20.3
$C_8^{2\tau 2\ell}$	$gg \to \varphi_i^0 \to hZ \to (\tau\tau)(\ell\ell)$	CMS [491]	[0.22;0.35]	19.7
A_{13}^{bbZ}	$gg \to \varphi_i^0 \to hZ \to (bb)Z$	ATLAS [506]	[0.2;2]	36.1
$C_{13,1}^{bbZ}$		CMS [507]	[0.22;0.8]	35.9
$C_{13,2}^{bbZ}$		CMS [508]	[0.8;2]	35.9
A_{13b}^{bbZ}	$bb \to \varphi_i^0 \to hZ \to (bb)Z$	ATLAS [506]	[0.2;2]	36.1
$C_{13b,1}^{bbZ}$		CMS [507]	[0.22;0.8]	35.9
$C_{13b,2}^{bbZ}$		CMS [508]	[0.8;2]	35.9
$C_{8,1}^{\varphi_2 Z}$	$pp \to \varphi_3 \to \varphi_2 Z \to (bb)(\ell\ell)$	CMS [509]	[0.04;1]	19.8
$C_{8,2}^{\varphi_2 Z}$	$pp \to \varphi_3 \to \varphi_2 Z \to (\tau\tau)(\ell\ell)$	CMS [509]	[0.05;1]	19.8
$A_{13}^{\varphi Z}$	$gg \to \varphi_3 \to \varphi_2 Z \to (bb)Z$	ATLAS [510]	[0.13;0.8]	36.1
$A_{13b}^{\varphi Z}$	$bb \to \varphi_3 \to \varphi_2 Z \to (bb)Z$	ATLAS [510]	[0.13;0.8]	36.1

Table F.4: Direct searches for neutral heavy scalars, $\varphi_i^0 = H, A$, with final states including the SM Higgs boson or other neutral scalars. φ_3 denotes the heaviest scalar, $V = W, Z$, $\ell = e, \mu$.

Label	**Channel**	**Experiment**	**Mass range [TeV]**	$\mathcal{L}$ [$\mathbf{fb}^{-1}$]
$A_8^{\tau\nu}$	$pp \to H^\pm \to \tau^\pm\nu$	ATLAS [511]	[0.18;1]	19.5
$C_8^{\tau\nu}$	$pp \to H^+ \to \tau^+\nu$	CMS [512]	[0.18;0.6]	19.7
$A_{13}^{\tau\nu}$	$pp \to H^\pm \to \tau^\pm\nu$	ATLAS [513]	[0.09;2]	36.1
$C_{13}^{\tau\nu}$		CMS [514]	[0.18;3]	12.9
A_8^{tb}	$pp \to H^\pm \to tb$	ATLAS [515]	[0.2;0.6]	20.3
C_8^{tb}	$pp \to H^+ \to t\bar{b}$	CMS [512]	[0.18;0.6]	19.7
A_{13}^{tb}	$pp \to H^\pm \to tb$	ATLAS [516]	[0.2;2]	36.1

Table F.5: Direct searches for charged scalars.

Acknowledgements

Vull agrair-li al meu director de tesi, Toni Pich, la seua gran ajuda i paciència amb mi durant aquests anys. Gràcies per mostrar-me una visió tan clara de la investigació i de la física de partícules. Also, thanks a lot to Otto Eberhardt for his huge help during his time in Valencia and for introducing me to the nice topic of `HEPfit`. Thanks to Ayan Paul for his help with the last fits of my thesis.

Gràcies també als meus companys d'*Escuadrón IFIC* pels dinars, les birres i les sobretaules al sol. En especial als meus companys de despatx Félix, Fernando i Víctor, per fer del lloc de treball un lloc tan agradable. Adrià, Clara, Martí i Víctor, estic molt orgullosa dels projectes que vam fer junts, perquè tot és més fàcil quan treballes amb els teus amics. Un especial agraïment a Héctor, una espècie de mentor durant la meua etapa doctorat. Gràcies per aguantar les meues paranoies i ratllades (a voltes les teues també) i per tota la teua ajuda durant aquest temps, estic desitjant que puga'm fer algun projecte conjunt. I en últim lloc, però no menys important a Clara, perquè em costa imaginar haver tingut una germana de doctorat millor. Encara que alguns moments hagen sigut dur sé que ens enduem moltes coses bones.

Fora de l'IFIC moltes gràcies als meus pares, Laura i Eduardo, i al meu germà Hugo per tot el vostre suport. Als *Mofers* per tots els moments d'aquest any, pels viatges, els festivals, les birres i sobre tot per aguantar-me. I per últim, als meus companys de pis Clara, Iker, Martí i la nostra gateta Emmy per ser la meua segona família aquests anys. Veig impossible estar més a gust convivint en un grup de persones que amb vosaltres. Gràcies per crear un espai on cuidar-nos entre totes. També gràcies a la resta de *Pisiers*

Mario, Sílvia, Núria, Víctor i Andreu per tots els dinarots, dards, partides de frontó i sobretot per totes les converses i reflexions.

Gràcies!

Bibliography

[1] S. L. Glashow, "Partial Symmetries of Weak Interactions," *Nucl. Phys.* **22** (1961) 579–588.

[2] S. Weinberg, "A Model of Leptons," *Phys. Rev. Lett.* **19** (1967) 1264–1266.

[3] A. Salam, "Weak and Electromagnetic Interactions," *Conf. Proc.* **C680519** (1968) 367–377.

[4] S. L. Glashow, J. Iliopoulos, and L. Maiani, "Weak Interactions with Lepton-Hadron Symmetry," *Phys. Rev.* **D2** (1970) 1285–1292.

[5] A. Pich, "The Standard Model of Electroweak Interactions," in *2010 European School of High Energy Physics*, pp. 1–50. 1, 2012. `arXiv:1201.0537 [hep-ph]`.

[6] M. Herrero, "The Standard model," *NATO Sci. Ser. C* **534** (1999) 1–59, `arXiv:hep-ph/9812242 [hep-ph]`.

[7] A. Pich, "Aspects of quantum chromodynamics," in *Proceedings, Summer School in Particle Physics: Trieste, Italy, June 21-July 9, 1999*, pp. 53–102. 1999. `arXiv:hep-ph/0001118 [hep-ph]`.

[8] D. J. Gross and F. Wilczek, "Ultraviolet Behavior of Nonabelian Gauge Theories," *Phys. Rev. Lett.* **30** (1973) 1343–1346. [,271(1973)].

[9] S. Weinberg, "Nonabelian Gauge Theories of the Strong Interactions," *Phys. Rev. Lett.* **31** (1973) 494–497.

[10] H. Fritzsch, M. Gell-Mann, and H. Leutwyler, "Advantages of the Color Octet Gluon Picture," *Phys. Lett.* **47B** (1973) 365–368.

[11] H. D. Politzer, "Reliable Perturbative Results for Strong Interactions?," *Phys. Rev. Lett.* **30** (1973) 1346–1349. [,274(1973)].

[12] P. W. Higgs, "Broken Symmetries and the Masses of Gauge Bosons," *Phys. Rev. Lett.* **13** (1964) 508–509. [,160(1964)].

[13] F. Englert and R. Brout, "Broken Symmetry and the Mass of Gauge Vector Mesons," *Phys. Rev. Lett.* **13** (1964) 321–323. [,157(1964)].

[14] G. S. Guralnik, C. R. Hagen, and T. W. B. Kibble, "Global Conservation Laws and Massless Particles," *Phys. Rev. Lett.* **13** (1964) 585–587. [,162(1964)].

[15] T. W. B. Kibble, "Symmetry breaking in nonAbelian gauge theories," *Phys. Rev.* **155** (1967) 1554–1561. [,165(1967)].

[16] J. Goldstone, A. Salam, and S. Weinberg, "Broken Symmetries," *Phys. Rev.* **127** (1962) 965–970.

[17] J. Goldstone, "Field Theories with Superconductor Solutions," *Nuovo Cim.* **19** (1961) 154–164.

[18] **ATLAS** Collaboration, G. Aad *et al.*, "Observation of a new particle in the search for the Standard Model Higgs boson with the ATLAS detector at the LHC," *Phys. Lett.* **B716** (2012) 1–29, `arXiv:1207.7214 [hep-ex]`.

[19] **CMS** Collaboration, S. Chatrchyan *et al.*, "Observation of a New Boson at a Mass of 125 GeV with the CMS Experiment at the LHC," *Phys. Lett.* **B716** (2012) 30–61, `arXiv:1207.7235 [hep-ex]`.

[20] A. Pich, "Electroweak Symmetry Breaking and the Higgs Boson," *Acta Phys. Polon.* **B47** (2016) 151, `arXiv:1512.08749 [hep-ph]`.

[21] T. Robens and T. Stefaniak, "Status of the Higgs Singlet Extension of the Standard Model after LHC Run 1," *Eur. Phys. J.* **C75** (2015) 104, arXiv:1501.02234 [hep-ph].

[22] N. Cabibbo, "Unitary Symmetry and Leptonic Decays," *Phys. Rev. Lett.* **10** (1963) 531–533. [,648(1963)].

[23] M. Kobayashi and T. Maskawa, "CP Violation in the Renormalizable Theory of Weak Interaction," *Prog. Theor. Phys.* **49** (1973) 652–657.

[24] A. Pich and P. Tuzon, "Yukawa Alignment in the Two-Higgs-Doublet Model," *Phys. Rev.* **D80** (2009) 091702, arXiv:0908.1554 [hep-ph].

[25] A. Pich, "Flavour constraints on multi-Higgs-doublet models: Yukawa alignment," *Nucl. Phys. Proc. Suppl.* **209** (2010) 182–187, arXiv:1010.5217 [hep-ph].

[26] S. Weinberg, "Gauge Theory of CP Violation," *Phys. Rev. Lett.* **37** (1976) 657.

[27] H. E. Haber, G. L. Kane, and T. Sterling, "The Fermion Mass Scale and Possible Effects of Higgs Bosons on Experimental Observables," *Nucl. Phys.* **B161** (1979) 493–532.

[28] L. J. Hall and M. B. Wise, "FLAVOR CHANGING HIGGS - BOSON COUPLINGS," *Nucl. Phys.* **B187** (1981) 397–408.

[29] J. F. Donoghue and L. F. Li, "Properties of Charged Higgs Bosons," *Phys. Rev.* **D19** (1979) 945.

[30] V. D. Barger, J. L. Hewett, and R. J. N. Phillips, "New Constraints on the Charged Higgs Sector in Two Higgs Doublet Models," *Phys. Rev.* **D41** (1990) 3421–3441.

[31] N. G. Deshpande and E. Ma, "Pattern of Symmetry Breaking with Two Higgs Doublets," *Phys. Rev.* **D18** (1978) 2574.

[32] H. Georgi, "Effective field theory," *Ann. Rev. Nucl. Part. Sci.* **43** (1993) 209–252.

[33] J. Wudka, "Electroweak effective Lagrangians," *Int. J. Mod. Phys.* **A9** (1994) 2301–2362, arXiv:hep-ph/9406205 [hep-ph].

[34] A. V. Manohar, "Effective field theories," *Lect. Notes Phys.* **479** (1997) 311–362, arXiv:hep-ph/9606222 [hep-ph].

[35] A. Pich, "Effective field theory: Course," in *Probing the standard model of particle interactions. Proceedings, Summer School in Theoretical Physics, NATO Advanced Study Institute, 68th session, Les Houches, France, July 28-September 5, 1997. Pt. 1, 2*, pp. 949–1049. 1998. arXiv:hep-ph/9806303 [hep-ph].

[36] A. J. Buras, "Weak Hamiltonian, CP violation and rare decays," in *Probing the standard model of particle interactions. Proceedings, Summer School in Theoretical Physics, NATO Advanced Study Institute, 68th session, Les Houches, France, July 28-September 5, 1997. Pt. 1, 2*, pp. 281–539. 1998. arXiv:hep-ph/9806471 [hep-ph].

[37] M. Neubert, "Les Houches Lectures on Renormalization Theory and Effective Field Theories," in *Les Houches summer school: EFT in Particle Physics and Cosmology Les Houches, Chamonix Valley, France, July 3-28, 2017*. 2019. arXiv:1901.06573 [hep-ph].

[38] T. Appelquist and J. Carazzone, "Infrared Singularities and Massive Fields," *Phys. Rev.* **D11** (1975) 2856.

[39] V. Ilisie, *Concepts in Quantum Field Theory*. UNITEXT for Physics. Springer, 2016.

[40] V. A. Mitsou, "Overview of searches for dark matter at the LHC," *J. Phys. Conf. Ser.* **651** no. 1, (2015) 012023, arXiv:1402.3673 [hep-ex].

[41] M. Klasen, M. Pohl, and G. Sigl, "Indirect and direct search for dark matter," *Prog. Part. Nucl. Phys.* **85** (2015) 1–32, arXiv:1507.03800 [hep-ph].

[42] S. Rappoccio, "The experimental status of direct searches for exotic physics beyond the standard model at the Large Hadron Collider," *Rev. Phys.* **4** (2019) 100027, arXiv:1810.10579 [hep-ex].

[43] A. Canepa, "Searches for Supersymmetry at the Large Hadron Collider," *Rev. Phys.* **4** (2019) 100033.

[44] P. Gambino, M. Jung, and S. Schacht, "The V_{cb} puzzle: An update," *Phys. Lett. B* **795** (2019) 386–390, arXiv:1905.08209 [hep-ph].

[45] S. Descotes-Genon, J. Matias, M. Ramon, and J. Virto, "Implications from clean observables for the binned analysis of $B- > K*\mu^+\mu^-$ at large recoil," *JHEP* **01** (2013) 048, arXiv:1207.2753 [hep-ph].

[46] S. Descotes-Genon, L. Hofer, J. Matias, and J. Virto, "On the impact of power corrections in the prediction of $B \to K^*\mu^+\mu^-$ observables," *JHEP* **12** (2014) 125, arXiv:1407.8526 [hep-ph].

[47] W. Altmannshofer and D. M. Straub, "New physics in $b \to s$ transitions after LHC run 1," *Eur. Phys. J. C* **75** no. 8, (2015) 382, arXiv:1411.3161 [hep-ph].

[48] **HFLAV** Collaboration, Y. S. Amhis *et al.*, "Averages of b-hadron, c-hadron, and τ-lepton properties as of 2018," arXiv:1909.12524 [hep-ex].

[49] **Flavour Lattice Averaging Group** Collaboration, S. Aoki *et al.*, "FLAG Review 2019," *Eur. Phys. J. C* **80** no. 2, (2020) 113, arXiv:1902.08191 [hep-lat].

[50] **HPQCD** Collaboration, B. Colquhoun, C. Davies, R. Dowdall, J. Kettle, J. Koponen, G. Lepage, and A. Lytle, "B-meson decay constants: a more complete picture from full lattice QCD," *Phys. Rev. D* **91** no. 11, (2015) 114509, arXiv:1503.05762 [hep-lat].

[51] Y. Sakaki, M. Tanaka, A. Tayduganov, and R. Watanabe, "Testing leptoquark models in $\bar{B} \to D^{(*)}\tau\bar{\nu}$," *Phys. Rev. D* **88** no. 9, (2013) 094012, arXiv:1309.0301 [hep-ph].

[52] C. Murgui, A. Peñuelas, M. Jung, and A. Pich, "Global fit to $b \to c\tau\nu$ transitions," *JHEP* **09** (2019) 103, arXiv:1904.09311 [hep-ph].

[53] K. Hagiwara, A. D. Martin, and M. Wade, "EXCLUSIVE SEMILEPTONIC B MESON DECAYS," *Nucl. Phys. B* **327** (1989) 569–594.

[54] K. Hagiwara, A. D. Martin, and M. F. Wade, "The Semileptonic Decays $B \to M\tau\nu$ as a Probe of Hadron Dynamics," *Z. Phys.* **C46** (1990) 299.

[55] J. G. Korner and G. A. Schuler, "Exclusive Semileptonic Heavy Meson Decays Including Lepton Mass Effects," *Z. Phys.* **C46** (1990) 93.

[56] A. Pich, "Flavour Anomalies," *PoS* **LHCP2019** (2019) 078, arXiv:1911.06211 [hep-ph].

[57] S. Kumbhakar, A. K. Alok, D. Kumar, and S. Uma Sankar, "New Physics solutions for $b \to c\,\tau\,\bar{\nu}$ anomalies after Moriond 2019," in *Workshop on Frontiers in High Energy Physics 2019*. 1, 2020. arXiv:2001.06344 [hep-ph].

[58] **ATLAS, CMS, LHCb** Collaboration, E. Graverini, "Flavour anomalies: a review," *J. Phys. Conf. Ser.* **1137** no. 1, (2019) 012025, arXiv:1807.11373 [hep-ex].

[59] D. Bigi and P. Gambino, "Revisiting $B \to D\ell\nu$," *Phys. Rev.* **D94** no. 9, (2016) 094008, arXiv:1606.08030 [hep-ph].

[60] F. U. Bernlochner, Z. Ligeti, M. Papucci, and D. J. Robinson, "Combined analysis of semileptonic B decays to D and D^*: $R(D^{(*)})$, $|V_{cb}|$, and new physics," *Phys. Rev.* **D95** no. 11, (2017) 115008, arXiv:1703.05330 [hep-ph]. [erratum: Phys. Rev.D97,no.5,059902(2018)].

[61] D. Bigi, P. Gambino, and S. Schacht, "$R(D^*)$, $|V_{cb}|$, and the Heavy Quark Symmetry relations between form factors," *JHEP* **11** (2017) 061, arXiv:1707.09509 [hep-ph].

[62] S. Jaiswal, S. Nandi, and S. K. Patra, "Extraction of $|V_{cb}|$ from $B \to D^{(*)}\ell\nu_\ell$ and the Standard Model predictions of $R(D^{(*)})$," *JHEP* **12** (2017) 060, arXiv:1707.09977 [hep-ph].

[63] **BaBar** Collaboration, J. P. Lees *et al.*, "Evidence for an excess of $\bar{B} \to D^{(*)}\tau^-\bar{\nu}_\tau$ decays," *Phys. Rev. Lett.* **109** (2012) 101802, arXiv:1205.5442 [hep-ex].

[64] **BaBar** Collaboration, J. P. Lees *et al.*, "Measurement of an Excess of $\bar{B} \to D^{(*)}\tau^-\bar{\nu}_\tau$ Decays and Implications for Charged Higgs Bosons," *Phys. Rev.* **D88** no. 7, (2013) 072012, arXiv:1303.0571 [hep-ex].

[65] **Belle** Collaboration, M. Huschle *et al.*, "Measurement of the branching ratio of $\bar{B} \to D^{(*)}\tau^-\bar{\nu}_\tau$ relative to $\bar{B} \to D^{(*)}\ell^-\bar{\nu}_\ell$ decays with hadronic tagging at Belle," *Phys. Rev.* **D92** no. 7, (2015) 072014, arXiv:1507.03233 [hep-ex].

[66] **Belle** Collaboration, S. Hirose *et al.*, "Measurement of the τ lepton polarization and $R(D^*)$ in the decay $\bar{B} \to D^*\tau^-\bar{\nu}_\tau$," *Phys. Rev. Lett.* **118** no. 21, (2017) 211801, arXiv:1612.00529 [hep-ex].

[67] **Belle** Collaboration, A. Abdesselam *et al.*, "Measurement of $\mathcal{R}(D)$ and $\mathcal{R}(D^*)$ with a semileptonic tagging method," arXiv:1904.08794 [hep-ex].

[68] **LHCb** Collaboration, R. Aaij *et al.*, "Measurement of the ratio of branching fractions $\mathcal{B}(\bar{B}^0 \to D^{*+}\tau^-\bar{\nu}_\tau)/\mathcal{B}(\bar{B}^0 \to D^{*+}\mu^-\bar{\nu}_\mu)$," *Phys. Rev. Lett.* **115** no. 11, (2015) 111803, arXiv:1506.08614 [hep-ex]. [Erratum: Phys. Rev. Lett.115,no.15,159901(2015)].

[69] **LHCb** Collaboration, R. Aaij *et al.*, "Measurement of the ratio of the $B^0 \to D^{*-}\tau^+\nu_\tau$ and $B^0 \to D^{*-}\mu^+\nu_\mu$ branching fractions using three-prong

τ-lepton decays," *Phys. Rev. Lett.* **120** no. 17, (2018) 171802, arXiv:1708.08856 [hep-ex].

[70] R. Alonso, B. Grinstein, and J. Martin Camalich, "Lifetime of B_c^- Constrains Explanations for Anomalies in $B \to D^{(*)}\tau\nu$," *Phys. Rev. Lett.* **118** no. 8, (2017) 081802, arXiv:1611.06676 [hep-ph].

[71] **Belle** Collaboration, A. Abdesselam *et al.*, "Measurement of the D^{*-} polarization in the decay $B^0 \to D^{*-}\tau^+\nu_\tau$," in *10th International Workshop on the CKM Unitarity Triangle*. 3, 2019. arXiv:1903.03102 [hep-ex].

[72] **LHCb** Collaboration, R. Aaij *et al.*, "Measurement of the ratio of branching fractions $\mathcal{B}(B_c^+ \to J/\psi\tau^+\nu_\tau)/\mathcal{B}(B_c^+ \to J/\psi\mu^+\nu_\mu)$," *Phys. Rev. Lett.* **120** no. 12, (2018) 121801, arXiv:1711.05623 [hep-ex].

[73] **Particle Data Group** Collaboration, C. Patrignani *et al.*, "Review of Particle Physics," *Chin. Phys.* **C40** no. 10, (2016) 100001.

[74] M. Freytsis, Z. Ligeti, and J. T. Ruderman, "Flavor models for $\bar{B} \to D^{(*)}\tau\bar{\nu}$," *Phys. Rev. D* **92** no. 5, (2015) 054018, arXiv:1506.08896 [hep-ph].

[75] **Particle Data Group** Collaboration, M. Tanabashi *et al.*, "Review of Particle Physics," *Phys. Rev. D* **98** no. 3, (2018) 030001.

[76] F. U. Bernlochner, Z. Ligeti, and S. Turczyk, "A Proposal to solve some puzzles in semileptonic B decays," *Phys. Rev. D* **85** (2012) 094033, arXiv:1202.1834 [hep-ph].

[77] **Heavy Flavor Averaging Group (HFAG)** Collaboration, Y. Amhis *et al.*, "Averages of b-hadron, c-hadron, and τ-lepton properties as of summer 2014," arXiv:1412.7515 [hep-ex].

[78] A. K. Leibovich, Z. Ligeti, I. W. Stewart, and M. B. Wise, "Semileptonic B decays to excited charmed mesons," *Phys. Rev. D* **57** (1998) 308–330, arXiv:hep-ph/9705467.

[79] D. Be$\check{}$ cirević, M. Fedele, I. Ni$\check{}$ sandžić, and A. Tayduganov, "Lepton Flavor Universality tests through angular observables of $\overline{B} \to D^{(*)}\ell\overline{\nu}$ decay modes," arXiv:1907.02257 [hep-ph].

[80] P. Asadi, M. R. Buckley, and D. Shih, "Asymmetry Observables and the Origin of $R_{D^{(*)}}$ Anomalies," *Phys. Rev. D* **99** no. 3, (2019) 035015, arXiv:1810.06597 [hep-ph].

[81] M. Duraisamy and A. Datta, "The Full $B \to D^*\tau^-\bar{\nu_\tau}$ Angular Distribution and CP violating Triple Products," *JHEP* **09** (2013) 059, arXiv:1302.7031 [hep-ph].

[82] M. Duraisamy, P. Sharma, and A. Datta, "Azimuthal $B \to D^*\tau^-\bar{\nu_\tau}$ angular distribution with tensor operators," *Phys. Rev. D* **90** no. 7, (2014) 074013, arXiv:1405.3719 [hep-ph].

[83] D. Becirevic, S. Fajfer, I. Nisandzic, and A. Tayduganov, "Angular distributions of $\bar{B} \to D^{(*)}\ell\bar{\nu}_\ell$ decays and search of New Physics," *Nucl. Phys. B* **946** (2019) 114707, arXiv:1602.03030 [hep-ph].

[84] R. Alonso, A. Kobach, and J. Martin Camalich, "New physics in the kinematic distributions of $\bar{B} \to D^{(*)}\tau^-(\to \ell^-\bar{\nu}_\ell\nu_\tau)\bar{\nu}_\tau$," *Phys. Rev. D* **94** no. 9, (2016) 094021, arXiv:1602.07671 [hep-ph].

[85] Z. Ligeti, M. Papucci, and D. J. Robinson, "New Physics in the Visible Final States of $B \to D^{(*)}\tau\nu$," *JHEP* **01** (2017) 083, arXiv:1610.02045 [hep-ph].

[86] D. Hill, M. John, W. Ke, and A. Poluektov, "Model-independent method for measuring the angular coefficients of $B^0 \to D^{*-}\tau^+\nu_\tau$ decays," *JHEP* **11** (2019) 133, arXiv:1908.04643 [hep-ph].

[87] J. Aebischer, T. Kuhr, and K. Lieret, "Clustering of $\bar{B} \to D^{(*)}\tau^-\bar{\nu}_\tau$ kinematic distributions with ClusterKinG," *JHEP* **04** (2020) 007, arXiv:1909.11088 [hep-ph].

[88] A. Caldwell, D. Kollar, and K. Kroninger, "BAT: The Bayesian Analysis Toolkit," *Comput. Phys. Commun.* **180** (2009) 2197–2209, arXiv:0808.2552 [physics.data-an].

[89] A. C. Caldwell, D. Kollar, and K. Kroninger, "BAT: The Bayesian analysis toolkit," *J. Phys. Conf. Ser.* **219** (2010) 032013.

[90] F. Beaujean, A. Caldwell, D. Kollar, and K. Kroninger, "BAT: The Bayesian analysis toolkit," *J. Phys. Conf. Ser.* **331** (2011) 072040.

[91] W. Gropp, *MPI (Message Passing Interface)*. Springer US, Boston, MA, 2011. https://doi.org/10.1007/978-0-387-09766-4_222.

[92] **HEPfit** Collaboration. https://hepfit.roma1.infn.it.

[93] J. De Blas *et al.*, "HEPfit: a Code for the Combination of Indirect and Direct Constraints on High Energy Physics Models," *Eur. Phys. J. C* **80** no. 5, (2020) 456, arXiv:1910.14012 [hep-ph].

[94] M. G. Kendall, A. Stuart, and J. K. Ord, *Kendall's Advanced Theory of Statistics*. Oxford University Press, Inc., USA, 1987.

[95] R. D. Morey, J.-W. Romeijn, and J. N. Rouder, "The philosophy of bayes factors and the quantification of statistical evidence," *Journal of Mathematical Psychology* **72** (2016) 6 – 18. http://www.sciencedirect.com/science/article/pii/S0022249615000723. Bayes Factors for Testing Hypotheses in Psychological Research: Practical Relevance and New Developments.

[96] S. P. Brooks and A. Gelman, "General methods for monitoring convergence of iterative simulations," *Journal of Computational and Graphical Statistics* **7** no. 4, (1998) 434–455, https://www.tandfonline.com/doi/pdf/10.1080/10618600.1998.10474787. https://www.tandfonline.com/doi/abs/10.1080/10618600.1998.10474787.

[97] A. Gelman and D. B. Rubin, "Inference from iterative simulation using multiple sequences," *Statist. Sci.* **7** no. 4, (11, 1992) 457–472. https://doi.org/10.1214/ss/1177011136.

[98] A. Pich, "Flavour Physics and CP Violation," in *Proceedings, 6th CERN - Latin-American School of High-Energy Physics (CLASHEP 2011): Natal, Brazil , March 23 - April 5, 2011*, pp. 119–144. 2013. arXiv:1112.4094 [hep-ph].

[99] G. C. Branco, P. M. Ferreira, L. Lavoura, M. N. Rebelo, M. Sher, and J. P. Silva, "Theory and phenomenology of two-Higgs-doublet models," *Phys. Rept.* **516** (2012) 1–102, arXiv:1106.0034 [hep-ph].

[100] J. F. Gunion, H. E. Haber, G. L. Kane, and S. Dawson, "The Higgs Hunter's Guide," *Front. Phys.* **80** (2000) 1–404.

[101] I. P. Ivanov, "Building and testing models with extended Higgs sectors," *Prog. Part. Nucl. Phys.* **95** (2017) 160–208, arXiv:1702.03776 [hep-ph].

[102] Y. Grossman, "Phenomenology of models with more than two Higgs doublets," *Nucl. Phys.* **B426** (1994) 355–384, arXiv:hep-ph/9401311 [hep-ph].

[103] A. G. Akeroyd and W. J. Stirling, "Light charged Higgs scalars at high-energy e+ e- colliders," *Nucl. Phys.* **B447** (1995) 3–17.

[104] A. G. Akeroyd, "Nonminimal neutral Higgs bosons at LEP-2," *Phys. Lett.* **B377** (1996) 95–101, arXiv:hep-ph/9603445 [hep-ph].

[105] E. Ma, "Utility of a Special Second Scalar Doublet," *Mod. Phys. Lett.* **A23** (2008) 647–652, arXiv:0802.2917 [hep-ph].

[106] M. Aoki, S. Kanemura, K. Tsumura, and K. Yagyu, "Models of Yukawa interaction in the two Higgs doublet model, and their collider phenomenology," *Phys. Rev.* **D80** (2009) 015017, arXiv:0902.4665 [hep-ph].

[107] S. L. Glashow and S. Weinberg, "Natural Conservation Laws for Neutral Currents," *Phys. Rev.* **D15** (1977) 1958.

[108] E. A. Paschos, "Diagonal Neutral Currents," *Phys. Rev.* **D15** (1977) 1966.

[109] J. M. Alves, F. J. Botella, G. C. Branco, F. Cornet-Gomez, and M. Nebot, "Controlled Flavour Changing Neutral Couplings in Two Higgs Doublet Models," *Eur. Phys. J. C* **77** no. 9, (2017) 585, arXiv:1703.03796 [hep-ph].

[110] A. V. Manohar and M. B. Wise, "Flavor changing neutral currents, an extended scalar sector, and the Higgs production rate at the CERN LHC," *Phys. Rev.* **D74** (2006) 035009, arXiv:hep-ph/0606172 [hep-ph].

[111] P. M. Ferreira, L. Lavoura, and J. P. Silva, "Renormalization-group constraints on Yukawa alignment in multi-Higgs-doublet models," *Phys. Lett.* **B688** (2010) 341–344, arXiv:1001.2561 [hep-ph].

[112] M. Jung, A. Pich, and P. Tuzon, "Charged-Higgs phenomenology in the Aligned two-Higgs-doublet model," *JHEP* **11** (2010) 003, arXiv:1006.0470 [hep-ph].

[113] F. J. Botella, G. C. Branco, A. M. Coutinho, M. N. Rebelo, and J. I. Silva-Marcos, "Natural Quasi-Alignment with two Higgs Doublets and RGE Stability," *Eur. Phys. J.* **C75** (2015) 286, arXiv:1501.07435 [hep-ph].

[114] R. S. Chivukula and H. Georgi, "Composite Technicolor Standard Model," *Phys. Lett.* **B188** (1987) 99–104.

[115] G. D'Ambrosio, G. F. Giudice, G. Isidori, and A. Strumia, "Minimal flavor violation: An Effective field theory approach," *Nucl. Phys.* **B645** (2002) 155–187, arXiv:hep-ph/0207036 [hep-ph].

[116] C. B. Braeuninger, A. Ibarra, and C. Simonetto, "Radiatively induced flavour violation in the general two-Higgs doublet model with Yukawa alignment," *Phys. Lett.* **B692** (2010) 189–195, arXiv:1005.5706 [hep-ph].

[117] J. Bijnens, J. Lu, and J. Rathsman, "Constraining General Two Higgs Doublet Models by the Evolution of Yukawa Couplings," *JHEP* **05** (2012) 118, arXiv:1111.5760 [hep-ph].

[118] X.-Q. Li, J. Lu, and A. Pich, "$B^0_{s,d} \to \ell^+\ell^-$ Decays in the Aligned Two-Higgs-Doublet Model," *JHEP* **06** (2014) 022, arXiv:1404.5865 [hep-ph].

[119] G. Abbas, A. Celis, X.-Q. Li, J. Lu, and A. Pich, "Flavour-changing top decays in the aligned two-Higgs-doublet model," *JHEP* **06** (2015) 005, arXiv:1503.06423 [hep-ph].

[120] S. Gori, H. E. Haber, and E. Santos, "High scale flavor alignment in two-Higgs doublet models and its phenomenology," *JHEP* **06** (2017) 110, arXiv:1703.05873 [hep-ph].

[121] M. Jung, A. Pich, and P. Tuzon, "The B -> Xs gamma Rate and CP Asymmetry within the Aligned Two-Higgs-Doublet Model," *Phys. Rev.* **D83** (2011) 074011, arXiv:1011.5154 [hep-ph].

[122] M. Jung, X.-Q. Li, and A. Pich, "Exclusive radiative B-meson decays within the aligned two-Higgs-doublet model," *JHEP* **10** (2012) 063, arXiv:1208.1251 [hep-ph].

[123] A. Celis, V. Ilisie, and A. Pich, "LHC constraints on two-Higgs doublet models," *JHEP* **07** (2013) 053, arXiv:1302.4022 [hep-ph].

[124] A. Celis, V. Ilisie, and A. Pich, "Towards a general analysis of LHC data within two-Higgs-doublet models," *JHEP* **12** (2013) 095, arXiv:1310.7941 [hep-ph].

[125] V. Ilisie and A. Pich, "Low-mass fermiophobic charged Higgs phenomenology in two-Higgs-doublet models," *JHEP* **09** (2014) 089, arXiv:1405.6639 [hep-ph].

[126] M. Jung and A. Pich, "Electric Dipole Moments in Two-Higgs-Doublet Models," *JHEP* **04** (2014) 076, arXiv:1308.6283 [hep-ph].

[127] V. Ilisie, "New Barr-Zee contributions to $(\mathbf{g}-\mathbf{2})_\mu$ in two-Higgs-doublet models," *JHEP* **04** (2015) 077, arXiv:1502.04199 [hep-ph].

[128] A. Cherchiglia, P. Kneschke, D. Stöckinger, and H. Stöckinger-Kim, "The muon magnetic moment in the 2HDM: complete two-loop result," *JHEP* **01** (2017) 007, arXiv:1607.06292 [hep-ph].

[129] Q. Chang, P.-F. Li, and X.-Q. Li, "B_s^0 – $\bar{B}_s^0$ mixing within minimal flavor-violating two-Higgs-doublet models," *Eur. Phys. J.* **C75** no. 12, (2015) 594, arXiv:1505.03650 [hep-ph].

[130] Q.-Y. Hu, X.-Q. Li, and Y.-D. Yang, "$B^0 \to K^{*0}\mu^+\mu^-$ decay in the Aligned Two-Higgs-Doublet Model," *Eur. Phys. J. C* **77** no. 3, (2017) 190, arXiv:1612.08867 [hep-ph].

[131] Q.-Y. Hu, X.-Q. Li, and Y.-D. Yang, "The $\Lambda_b \to \Lambda(\to p\pi^-)\mu^+\mu^-$ decay in the aligned two-Higgs-doublet model," *Eur. Phys. J.* **C77** no. 4, (2017) 228, arXiv:1701.04029 [hep-ph].

[132] N. Cho, X.-q. Li, F. Su, and X. Zhang, "$K^0 - \overline{K}^0$ mixing in the minimal flavor-violating two-Higgs-doublet models," *Adv. High Energy Phys.* **2017** (2017) 2863647, arXiv:1705.07638 [hep-ph].

[133] W. Altmannshofer, S. Gori, and G. D. Kribs, "A Minimal Flavor Violating 2HDM at the LHC," *Phys. Rev.* **D86** (2012) 115009, arXiv:1210.2465 [hep-ph].

[134] Y. Bai, V. Barger, L. L. Everett, and G. Shaughnessy, "General two Higgs doublet model (2HDM-G) and Large Hadron Collider data," *Phys. Rev.* **D87** (2013) 115013, arXiv:1210.4922 [hep-ph].

[135] L. Duarte, G. A. González-Sprinberg, and J. Vidal, "Top quark anomalous tensor couplings in the two-Higgs-doublet models," *JHEP* **11** (2013) 114, arXiv:1308.3652 [hep-ph].

[136] C. Ayala, G. A. González-Sprinberg, R. Martinez, and J. Vidal, "The top right coupling in the aligned two-Higgs-doublet model," *JHEP* **03** (2017) 128, arXiv:1611.07756 [hep-ph].

[137] T. Han, S. K. Kang, and J. Sayre, "Muon $g-2$ in the aligned two Higgs doublet model," *JHEP* **02** (2016) 097, arXiv:1511.05162 [hep-ph].

[138] T. Enomoto and R. Watanabe, "Flavor constraints on the Two Higgs Doublet Models of Z_2 symmetric and aligned types," *JHEP* **05** (2016) 002, arXiv:1511.05066 [hep-ph].

[139] N. Mileo, K. Kiers, and A. Szynkman, "Probing sensitivity to charged scalars through partial differential widths: $\tau \to K\pi\pi\nu_\tau$ decays," *Phys. Rev.* **D91** no. 7, (2015) 073006, arXiv:1410.1909 [hep-ph].

[140] L. Wang and X.-F. Han, "Status of the aligned two-Higgs-doublet model confronted with the Higgs data," *JHEP* **04** (2014) 128, arXiv:1312.4759 [hep-ph].

[141] A. G. Akeroyd, S. Moretti, and J. Hernandez-Sanchez, "Light charged Higgs bosons decaying to charm and bottom quarks in models with two or more Higgs doublets," *Phys. Rev.* **D85** (2012) 115002, arXiv:1203.5769 [hep-ph].

[142] G. Cree and H. E. Logan, "Yukawa alignment from natural flavor conservation," *Phys. Rev.* **D84** (2011) 055021, arXiv:1106.4039 [hep-ph].

[143] H. Serodio, "Yukawa Alignment in a Multi Higgs Doublet Model: An effective approach," *Phys. Lett.* **B700** (2011) 133–138, arXiv:1104.2545 [hep-ph].

[144] D. López-Val, T. Plehn, and M. Rauch, "Measuring extended Higgs sectors as a consistent free couplings model," *JHEP* **10** (2013) 134, arXiv:1308.1979 [hep-ph].

[145] **Belle** Collaboration, Y. Sato *et al.*, "Measurement of the branching ratio of $\bar{B}^0 \to D^{*+}\tau^-\bar{\nu}_\tau$ relative to $\bar{B}^0 \to D^{*+}\ell^-\bar{\nu}_\ell$ decays with a semileptonic tagging method," *Phys. Rev.* **D94** no. 7, (2016) 072007, arXiv:1607.07923 [hep-ex].

[146] **Belle** Collaboration, S. Hirose *et al.*, "Measurement of the τ lepton polarization and $R(D^*)$ in the decay $\bar{B} \to D^*\tau^-\bar{\nu}_\tau$ with one-prong hadronic τ decays at Belle," *Phys. Rev.* **D97** no. 1, (2018) 012004, arXiv:1709.00129 [hep-ex].

[147] **LHCb** Collaboration, R. Aaij *et al.*, "Test of Lepton Flavor Universality by the measurement of the $B^0 \to D^{*-}\tau^+\nu_\tau$ branching fraction using three-prong τ decays," *Phys. Rev. D* **97** no. 7, (2018) 072013, arXiv:1711.02505 [hep-ex].

[148] F. Mahmoudi and O. Stal, "Flavor constraints on the two-Higgs-doublet model with general Yukawa couplings," *Phys. Rev.* **D81** (2010) 035016, arXiv:0907.1791 [hep-ph].

[149] A. Celis, M. Jung, X.-Q. Li, and A. Pich, "Sensitivity to charged scalars in $\boldsymbol{B \to D^{(*)}\tau\nu_\tau}$ and $\boldsymbol{B \to \tau\nu_\tau}$ decays," *JHEP* **01** (2013) 054, arXiv:1210.8443 [hep-ph].

[150] A. Celis, M. Jung, X.-Q. Li, and A. Pich, "Scalar contributions to $b \to c(u)\tau\nu$ transitions," *Phys. Lett.* **B771** (2017) 168–179, arXiv:1612.07757 [hep-ph].

[151] A. Crivellin, A. Kokulu, and C. Greub, "Flavor-phenomenology of two-Higgs-doublet models with generic Yukawa structure," *Phys. Rev.* **D87** no. 9, (2013) 094031, arXiv:1303.5877 [hep-ph].

[152] J. M. Cline, "Scalar doublet models confront τ and b anomalies," *Phys. Rev.* **D93** no. 7, (2016) 075017, arXiv:1512.02210 [hep-ph].

[153] A. J. Buras, M. V. Carlucci, S. Gori, and G. Isidori, "Higgs-mediated FCNCs: Natural Flavour Conservation vs. Minimal Flavour Violation," *JHEP* **10** (2010) 009, arXiv:1005.5310 [hep-ph].

[154] A. Dery, A. Efrati, G. Hiller, Y. Hochberg, and Y. Nir, "Higgs couplings to fermions: 2HDM with MFV," *JHEP* **08** (2013) 006, arXiv:1304.6727 [hep-ph].

[155] Y. H. Ahn and C.-H. Chen, "New charged Higgs effects on $\Gamma_{K_{e2}}/\Gamma_{K_2}$, f_{D_s} and $\mathcal{B}(B^+ \to \tau^+\nu)$ in the Two-Higgs-Doublet model," *Phys. Lett.* **B690** (2010) 57–61, arXiv:1002.4216 [hep-ph].

[156] A. Peñuelas and A. Pich, "Flavour alignment in multi-Higgs-doublet models," *JHEP* **12** (2017) 084, arXiv:1710.02040 [hep-ph].

[157] G. Cvetic, S. S. Hwang, and C. S. Kim, "One loop renormalization group equations of the general framework with two Higgs doublets," *Int. J. Mod. Phys.* **A14** (1999) 769–798, arXiv:hep-ph/9706323 [hep-ph].

[158] G. Cvetic, C. S. Kim, and S. S. Hwang, "Higgs mediated flavor changing neutral currents in the general framework with two Higgs doublets: An RGE analysis," *Phys. Rev.* **D58** (1998) 116003, arXiv:hep-ph/9806282 [hep-ph].

[159] W. Grimus and L. Lavoura, "Renormalization of the neutrino mass operators in the multi-Higgs-doublet standard model," *Eur. Phys. J.* **C39** (2005) 219–227, arXiv:hep-ph/0409231 [hep-ph].

[160] **ATLAS, CMS** Collaboration, G. Aad *et al.*, "Combined Measurement of the Higgs Boson Mass in pp Collisions at $\sqrt{s} = 7$ and 8 TeV with the ATLAS and CMS Experiments," *Phys. Rev. Lett.* **114** (2015) 191803, arXiv:1503.07589 [hep-ex].

[161] I. de Medeiros Varzielas, "Family symmetries and alignment in multi-Higgs doublet models," *Phys. Lett.* **B701** (2011) 597–600, arXiv:1104.2601 [hep-ph].

[162] A. Celis, J. Fuentes-Martín, and H. Serôdio, "Effective Aligned 2HDM with a DFSZ-like invisible axion," *Phys. Lett.* **B737** (2014) 185–190, arXiv:1407.0971 [hep-ph].

[163] S. Knapen and D. J. Robinson, "Disentangling Mass and Mixing Hierarchies," *Phys. Rev. Lett.* **115** no. 16, (2015) 161803, arXiv:1507.00009 [hep-ph].

[164] **LEP Higgs Working Group for Higgs boson searches, ALEPH, DELPHI, L3, OPAL** Collaboration, "Search for charged Higgs bosons: Preliminary combined results using LEP data collected at energies up to 209-GeV," in *Lepton and photon interactions at high energies. Proceedings, 20th International Symposium, LP 2001, Rome, Italy, July 23-28, 2001.* 2001. arXiv:hep-ex/0107031 [hep-ex]. http://weblib.cern.ch/abstract?CERN-L3-NOTE-2689.

[165] M. E. Peskin and T. Takeuchi, "A New constraint on a strongly interacting Higgs sector," *Phys. Rev. Lett.* **65** (1990) 964–967.

[166] S. Kanemura and K. Yagyu, "Unitarity bound in the most general two Higgs doublet model," *Phys. Lett.* **B751** (2015) 289–296, arXiv:1509.06060 [hep-ph].

[167] **Gfitter Group** Collaboration, M. Baak, J. Cúth, J. Haller, A. Hoecker, R. Kogler, K. Mönig, M. Schott, and J. Stelzer, "The global electroweak fit at NNLO and prospects for the LHC and ILC," *Eur. Phys. J.* **C74** (2014) 3046, arXiv:1407.3792 [hep-ph].

[168] J. C. Hardy and I. S. Towner, "Superallowed $0^+ \to 0^+$ nuclear β decays: 2014 critical survey, with precise results for V_{ud} and CKM unitarity," *Phys. Rev.* **C91** no. 2, (2015) 025501, arXiv:1411.5987 [nucl-ex].

[169] J. Fuster, A. Irles, D. Melini, P. Uwer, and M. Vos, "Extracting the top-quark running mass using $t\bar{t}$ + 1-jet events produced at the Large Hadron Collider," *Eur. Phys. J.* **C77** no. 11, (2017) 794, arXiv:1704.00540 [hep-ph].

[170] **ATLAS** Collaboration, G. Aad *et al.*, "Determination of the top-quark pole mass using $t\bar{t}$ + 1-jet events collected with the ATLAS experiment in 7 TeV pp collisions," *JHEP* **10** (2015) 121, arXiv:1507.01769 [hep-ex].

[171] **LHCb** Collaboration, R. Aaij *et al.*, "Measurement of the $B_s^0 \to \mu^+\mu^-$ branching fraction and effective lifetime and search for $B^0 \to \mu^+\mu^-$ decays," *Phys. Rev. Lett.* **118** no. 19, (2017) 191801, arXiv:1703.05747 [hep-ex].

[172] P. Arnan, D. Bečirević, F. Mescia, and O. Sumensari, "Two Higgs doublet models and $b \to s$ exclusive decays," *Eur. Phys. J.* **C77** no. 11, (2017) 796, arXiv:1703.03426 [hep-ph].

[173] M. Misiak and M. Steinhauser, "NNLO QCD corrections to the anti-B —> X(s) gamma matrix elements using interpolation in m(c)," *Nucl. Phys.* **B764** (2007) 62–82, arXiv:hep-ph/0609241 [hep-ph].

[174] T. Hermann, M. Misiak, and M. Steinhauser, "$\bar{B} \to X_s\gamma$ in the Two Higgs Doublet Model up to Next-to-Next-to-Leading Order in QCD," *JHEP* **11** (2012) 036, arXiv:1208.2788 [hep-ph].

[175] C. Bobeth, M. Misiak, and J. Urban, "Matching conditions for $b \to s\gamma$ and $b \to sgluon$ in extensions of the standard model," *Nucl. Phys.* **B567** (2000) 153–185, arXiv:hep-ph/9904413 [hep-ph].

[176] M. Misiak *et al.*, "Estimate of $\mathcal{B}(\bar{B} \to X_s\gamma)$ at $O(\alpha_s^2)$," *Phys. Rev. Lett.* **98** (2007) 022002, arXiv:hep-ph/0609232 [hep-ph].

[177] C.-Y. Chen and S. Dawson, "Exploring Two Higgs Doublet Models Through Higgs Production," *Phys. Rev. D* **87** (2013) 055016, arXiv:1301.0309 [hep-ph].

[178] C.-W. Chiang and K. Yagyu, "Implications of Higgs boson search data on the two-Higgs doublet models with a softly broken Z_2 symmetry," *JHEP* **07** (2013) 160, arXiv:1303.0168 [hep-ph].

[179] B. Grinstein and P. Uttayarat, "Carving Out Parameter Space in Type-II Two Higgs Doublets Model," *JHEP* **06** (2013) 094, arXiv:1304.0028 [hep-ph]. [Erratum: JHEP 09, 110 (2013)].

[180] A. Barroso, P. Ferreira, R. Santos, M. Sher, and J. P. Silva, "2HDM at the LHC - the story so far," in *1st Toyama International Workshop on Higgs as a Probe of New Physics 2013*. 4, 2013. arXiv:1304.5225 [hep-ph].

[181] D. Xu *et al.*, "Discovery of the broad-lined Type Ic SN 2013cq associated with the very energetic GRB 130427A," *Astrophys. J.* **776** (2013) 98, arXiv:1305.6832 [astro-ph.HE].

[182] O. Eberhardt, U. Nierste, and M. Wiebusch, "Status of the two-Higgs-doublet model of type II," *JHEP* **07** (2013) 118, arXiv:1305.1649 [hep-ph].

[183] S. Chang, S. K. Kang, J.-P. Lee, K. Y. Lee, S. C. Park, and J. Song, "Two Higgs doublet models for the LHC Higgs boson data at $\sqrt{s} = 7$ and 8 TeV," *JHEP* **09** (2014) 101, arXiv:1310.3374 [hep-ph].

[184] J. Baglio, O. Eberhardt, U. Nierste, and M. Wiebusch, "Benchmarks for Higgs Pair Production and Heavy Higgs boson Searches in the Two-Higgs-Doublet Model of Type II," *Phys. Rev. D* **90** no. 1, (2014) 015008, arXiv:1403.1264 [hep-ph].

[185] S. Inoue, M. J. Ramsey-Musolf, and Y. Zhang, "CP-violating phenomenology of flavor conserving two Higgs doublet models," *Phys. Rev. D* **89** no. 11, (2014) 115023, arXiv:1403.4257 [hep-ph].

[186] S. Kanemura, K. Tsumura, K. Yagyu, and H. Yokoya, "Fingerprinting nonminimal Higgs sectors," *Phys. Rev. D* **90** (2014) 075001, arXiv:1406.3294 [hep-ph].

[187] P. Ferreira, R. Guedes, J. F. Gunion, H. E. Haber, M. O. P. Sampaio, and R. Santos, "The Wrong Sign limit in the 2HDM," in *2nd Large Hadron Collider Physics Conference*. 10, 2014. arXiv:1410.1926 [hep-ph].

[188] B. Dumont, *Higgs, supersymmetry and dark matter after Run I of the LHC*. PhD thesis, Grenoble U., Cham, 2014. arXiv:1411.3465 [hep-ph].

[189] J. Bernon, J. F. Gunion, Y. Jiang, and S. Kraml, "Light Higgs bosons in Two-Higgs-Doublet Models," *Phys. Rev. D* **91** no. 7, (2015) 075019, arXiv:1412.3385 [hep-ph].

[190] D. Chowdhury and O. Eberhardt, "Global fits of the two-loop renormalized Two-Higgs-Doublet model with soft Z_2 breaking," *JHEP* **11** (2015) 052, arXiv:1503.08216 [hep-ph].

[191] N. Craig, F. D'Eramo, P. Draper, S. Thomas, and H. Zhang, "The Hunt for the Rest of the Higgs Bosons," *JHEP* **06** (2015) 137, arXiv:1504.04630 [hep-ph].

[192] J. Bernon, J. F. Gunion, H. E. Haber, Y. Jiang, and S. Kraml, "Scrutinizing the alignment limit in two-Higgs-doublet models: m_h=125 GeV," *Phys. Rev. D* **92** no. 7, (2015) 075004, arXiv:1507.00933 [hep-ph].

[193] J. Bernon, J. F. Gunion, H. E. Haber, Y. Jiang, and S. Kraml, "Scrutinizing the alignment limit in two-Higgs-doublet models. II. m_H=125 GeV," *Phys. Rev. D* **93** no. 3, (2016) 035027, arXiv:1511.03682 [hep-ph].

[194] V. Cacchio, D. Chowdhury, O. Eberhardt, and C. W. Murphy, "Next-to-leading order unitarity fits in Two-Higgs-Doublet models with soft $\mathbb{Z}_2$ breaking," *JHEP* **11** (2016) 026, arXiv:1609.01290 [hep-ph].

[195] H. Bélusca-Maïto, A. Falkowski, D. Fontes, J. C. Romão, and J. P. Silva, "Higgs EFT for 2HDM and beyond," *Eur. Phys. J. C* **77** no. 3, (2017) 176, arXiv:1611.01112 [hep-ph].

[196] O. Eberhardt, "Current status of Two-Higgs-Doublet models with a softly broken $\mathbb{Z}_2$ symmetry," *PoS* **ICHEP2018** (2019) 457, arXiv:1809.04851 [hep-ph].

[197] D. Chowdhury and O. Eberhardt, "Update of Global Two-Higgs-Doublet Model Fits," *JHEP* **05** (2018) 161, arXiv:1711.02095 [hep-ph].

[198] O. Eberhardt, "Two-Higgs-doublet model fits with HEPfit," in *2017 European Physical Society Conference on High Energy Physics*. 9, 2017. arXiv:1709.09414 [hep-ph].

[199] O. Eberhardt, "Fitting the Two-Loop Renormalized Two-Higgs-Doublet Model," *PoS* **PLANCK2015** (2015) 040, arXiv:1510.05966 [hep-ph].

[200] O. Eberhardt, "Fitting the Two-Higgs-Doublet model of type II," in *49th Rencontres de Moriond on Electroweak Interactions and Unified Theories*, pp. 523–526. 2014. arXiv:1405.3181 [hep-ph].

[201] J. F. Gunion and H. E. Haber, "The CP conserving two Higgs doublet model: The Approach to the decoupling limit," *Phys. Rev. D* **67** (2003) 075019, arXiv:hep-ph/0207010.

[202] P. Ferreira, R. Santos, and A. Barroso, "Stability of the tree-level vacuum in two Higgs doublet models against charge or CP spontaneous violation," *Phys. Lett. B* **603** (2004) 219–229, arXiv:hep-ph/0406231. [Erratum: Phys.Lett.B 629, 114–114 (2005)].

[203] I. Ginzburg and I. Ivanov, "Tree-level unitarity constraints in the most general 2HDM," *Phys. Rev. D* **72** (2005) 115010, arXiv:hep-ph/0508020.

[204] M. E. Peskin and T. Takeuchi, "Estimation of oblique electroweak corrections," *Phys. Rev. D* **46** (1992) 381–409.

[205] H. E. Haber and D. O'Neil, "Basis-independent methods for the two-Higgs-doublet model III: The CP-conserving limit, custodial symmetry, and the oblique parameters S, T, U," *Phys. Rev. D* **83** (2011) 055017, arXiv:1011.6188 [hep-ph].

[206] W. Hollik, "Nonstandard Higgs Bosons in SU(2) X U(1) Radiative Corrections," *Z. Phys. C* **32** (1986) 291.

[207] W. Hollik, "Radiative Corrections With Two Higgs Doublets at LEP / SLC and HERA," *Z. Phys. C* **37** (1988) 569.

[208] J. Bernabeu, A. Pich, and A. Santamaria, "Gamma (Z —> B anti-B): A Signature of Hard Mass Terms for a Heavy Top," *Phys. Lett. B* **200** (1988) 569–574.

[209] J. Bernabeu, A. Pich, and A. Santamaria, "Top quark mass from radiative corrections to the Z —> b anti-b decay," *Nucl. Phys. B* **363** (1991) 326–344.

[210] H. E. Haber and H. E. Logan, "Radiative corrections to the Z b anti-b vertex and constraints on extended Higgs sectors," *Phys. Rev. D* **62** (2000) 015011, arXiv:hep-ph/9909335.

[211] G. Degrassi and P. Slavich, "QCD Corrections in two-Higgs-doublet extensions of the Standard Model with Minimal Flavor Violation," *Phys. Rev. D* **81** (2010) 075001, arXiv:1002.1071 [hep-ph].

[212] J. de Blas, M. Ciuchini, E. Franco, S. Mishima, M. Pierini, L. Reina, and L. Silvestrini, "Electroweak precision observables and Higgs-boson signal strengths in the Standard Model and beyond: present and future," *JHEP* **12** (2016) 135, arXiv:1608.01509 [hep-ph].

[213] M. Misiak *et al.*, "Updated NNLO QCD predictions for the weak radiative B-meson decays," *Phys. Rev. Lett.* **114** no. 22, (2015) 221801, arXiv:1503.01789 [hep-ph].

[214] A. Cherchiglia, D. Stöckinger, and H. Stöckinger-Kim, "Muon g-2 in the 2HDM: maximum results and detailed phenomenology," *Phys. Rev. D* **98** (2018) 035001, arXiv:1711.11567 [hep-ph].

[215] L. Wang, J. M. Yang, M. Zhang, and Y. Zhang, "Revisiting lepton-specific 2HDM in light of muon g-2 anomaly," *Phys. Lett. B* **788** (2019) 519–529, arXiv:1809.05857 [hep-ph].

[216] S. Bifani, S. Descotes-Genon, A. Romero Vidal, and M.-H. Schune, "Review of Lepton Universality tests in B decays," *J. Phys. G* **46** no. 2, (2019) 023001, arXiv:1809.06229 [hep-ex].

[217] K. Cheung, Z.-R. Huang, H.-D. Li, C.-D. Lü, Y.-N. Mao, and R.-Y. Tang, "Revisit to the $b \to c\tau\nu$ transition: in and beyond the SM," arXiv:2002.07272 [hep-ph].

[218] S. Kumbhakar, A. K. Alok, D. Kumar, and S. U. Sankar, "A global fit to $b \to c\tau\bar{\nu}$ anomalies after Moriond 2019," in *2019 European Physical Society Conference on High Energy Physics*. 9, 2019. arXiv:1909.02840 [hep-ph].

[219] **HFLAV** Collaboration, Y. Amhis *et al.*, "Averages of b-hadron, c-hadron, and τ-lepton properties as of summer 2016," *Eur. Phys. J.* **C77** no. 12, (2017) 895, arXiv:1612.07233 [hep-ex].

[220] S. Aoki *et al.*, "Review of lattice results concerning low-energy particle physics," *Eur. Phys. J.* **C77** no. 2, (2017) 112, arXiv:1607.00299 [hep-lat].

[221] A. Anisimov, I. Narodetsky, C. Semay, and B. Silvestre-Brac, "The B_c meson lifetime in the light front constituent quark model," *Phys. Lett. B* **452** (1999) 129–136, arXiv:hep-ph/9812514.

[222] V. Kiselev, "Exclusive decays and lifetime of B_c meson in QCD sum rules," arXiv:hep-ph/0211021.

[223] M. A. Ivanov, J. G. Korner, and P. Santorelli, "Exclusive semileptonic and nonleptonic decays of the B_c meson," *Phys. Rev. D* **73** (2006) 054024, arXiv:hep-ph/0602050.

[224] E. Hernandez, J. Nieves, and J. Verde-Velasco, "Study of exclusive semileptonic and non-leptonic decays of B_c - in a nonrelativistic quark model," *Phys. Rev. D* **74** (2006) 074008, arXiv:hep-ph/0607150.

[225] T. Huang and F. Zuo, "Semileptonic B_c decays and charmonium distribution amplitude," *Eur. Phys. J. C* **51** (2007) 833–839, arXiv:hep-ph/0702147.

[226] W. Wang, Y.-L. Shen, and C.-D. Lu, "Covariant Light-Front Approach for B(c) transition form factors," *Phys. Rev. D* **79** (2009) 054012, arXiv:0811.3748 [hep-ph].

[227] A. Issadykov and M. A. Ivanov, "The decays $B_c \to J/\psi + \bar{\ell}\nu_\ell$ and $B_c \to J/\psi + \pi(K)$ in covariant confined quark model," *Phys. Lett. B* **783** (2018) 178–182, arXiv:1804.00472 [hep-ph].

[228] W.-F. Wang, Y.-Y. Fan, and Z.-J. Xiao, "Semileptonic decays $B_c \to (\eta_c, J/\Psi) l\nu$ in the perturbative QCD approach," *Chin. Phys. C* **37** (2013) 093102, arXiv:1212.5903 [hep-ph].

[229] X.-Q. Hu, S.-P. Jin, and Z.-J. Xiao, "Semileptonic decays $B_c \to (\eta_c, J/\psi) l\bar{\nu}_l$ in the "PQCD + Lattice" approach," *Chin. Phys. C* **44** no. 2, (2020) 023104, arXiv:1904.07530 [hep-ph].

[230] D. Leljak, B. Melic, and M. Patra, "On lepton flavour universality in semileptonic $B_c \to \eta_c$, J/ψ decays," *JHEP* **05** (2019) 094, arXiv:1901.08368 [hep-ph].

[231] K. Azizi, Y. Sarac, and H. Sundu, "Lepton flavor universality violation in semileptonic tree level weak transitions," *Phys. Rev. D* **99** no. 11, (2019) 113004, arXiv:1904.08267 [hep-ph].

[232] C.-T. Tran, M. A. Ivanov, J. G. Körner, and P. Santorelli, "Implications of new physics in the decays $B_c \to (J/\psi, \eta_c)\tau\nu$," *Phys. Rev. D* **97** no. 5, (2018) 054014, arXiv:1801.06927 [hep-ph].

[233] S. de Boer, T. Kitahara, and I. Nisandzic, "Soft-Photon Corrections to $\bar{B} \to D\tau^-\bar{\nu}_\tau$ Relative to $\bar{B} \to D\mu^-\bar{\nu}_\mu$," *Phys. Rev. Lett.* **120** no. 26, (2018) 261804, arXiv:1803.05881 [hep-ph].

[234] S. Calí, S. Klaver, M. Rotondo, and B. Sciascia, "Impacts of radiative corrections on measurements of lepton flavour universality in $B \to D\ell\nu_\ell$ decays," *Eur. Phys. J. C* **79** no. 9, (2019) 744, arXiv:1905.02702 [hep-ph].

[235] D. Becirevic and N. Kosnik, "Soft photons in semileptonic B —> D decays," *Acta Phys. Polon. Supp.* **3** (2010) 207–214, arXiv:0910.5031 [hep-ph].

[236] D. Atwood and W. J. Marciano, "Radiative Corrections and Semileptonic B Decays," *Phys. Rev. D* **41** (1990) 1736.

[237] Y. Sakaki, M. Tanaka, A. Tayduganov, and R. Watanabe, "Probing New Physics with q^2 distributions in $\bar{B} \to D^{(*)}\tau\bar{\nu}$," *Phys. Rev. D* **91** no. 11, (2015) 114028, arXiv:1412.3761 [hep-ph].

[238] S. Bhattacharya, S. Nandi, and S. K. Patra, "Looking for possible new physics in $B \to D^{(*)}\tau\nu_\tau$ in light of recent data," *Phys. Rev. D* **95** no. 7, (2017) 075012, arXiv:1611.04605 [hep-ph].

[239] A. Datta, M. Duraisamy, and D. Ghosh, "Diagnosing New Physics in $b \to c\,\tau\,\nu_\tau$ decays in the light of the recent BaBar result," *Phys. Rev. D* **86** (2012) 034027, arXiv:1206.3760 [hep-ph].

[240] M. Duraisamy and A. Datta, "The Full $B \to D^*\tau^-\bar{\nu_\tau}$ Angular Distribution and CP violating Triple Products," *JHEP* **09** (2013) 059, arXiv:1302.7031 [hep-ph].

[241] R. Dutta, A. Bhol, and A. K. Giri, "Effective theory approach to new physics in b $\to$ u and b $\to$ c leptonic and semileptonic decays," *Phys. Rev. D* **88** no. 11, (2013) 114023, arXiv:1307.6653 [hep-ph].

[242] R. Alonso, B. Grinstein, and J. Martin Camalich, "Lepton universality violation and lepton flavor conservation in B-meson decays," *JHEP* **10** (2015) 184, arXiv:1505.05164 [hep-ph].

[243] D. Boubaa, S. Khalil, and S. Moretti, "Alleviating the $\bar{B} \to D\tau\nu$ and $\bar{B} \to D^*\tau\nu_\tau$ puzzle in the MSSM," *Int. J. Mod. Phys. A* **34** no. 32, (2019) 1950209, arXiv:1604.03416 [hep-ph].

[244] D. Bardhan, P. Byakti, and D. Ghosh, "A closer look at the R_D and R_{D^*} anomalies," *JHEP* **01** (2017) 125, arXiv:1610.03038 [hep-ph].

[245] D. Choudhury, A. Kundu, S. Nandi, and S. K. Patra, "Unified resolution of the $R(D)$ and $R(D^*)$ anomalies and the lepton flavor violating decay $h \to \mu\tau$," *Phys. Rev. D* **95** no. 3, (2017) 035021, arXiv:1612.03517 [hep-ph].

[246] A. K. Alok, D. Kumar, S. Kumbhakar, and S. U. Sankar, "D^* polarization as a probe to discriminate new physics in $\bar{B} \to D^*\tau\bar{\nu}$," *Phys. Rev. D* **95** no. 11, (2017) 115038, arXiv:1606.03164 [hep-ph].

[247] A. K. Alok, D. Kumar, J. Kumar, S. Kumbhakar, and S. U. Sankar, "New physics solutions for R_D and R_{D^*}," *JHEP* **09** (2018) 152, arXiv:1710.04127 [hep-ph].

[248] B. Capdevila, A. Crivellin, S. Descotes-Genon, L. Hofer, and J. Matias, "Searching for New Physics with $b \to s\tau^+\tau^-$ processes," *Phys. Rev. Lett.* **120** no. 18, (2018) 181802, arXiv:1712.01919 [hep-ph].

[249] W. Altmannshofer, P. Bhupal Dev, and A. Soni, "$R_{D^{(*)}}$ anomaly: A possible hint for natural supersymmetry with R-parity violation," *Phys. Rev. D* **96** no. 9, (2017) 095010, arXiv:1704.06659 [hep-ph].

[250] D. Buttazzo, A. Greljo, G. Isidori, and D. Marzocca, "B-physics anomalies: a guide to combined explanations," *JHEP* **11** (2017) 044, arXiv:1706.07808 [hep-ph].

[251] Y. Cai, J. Gargalionis, M. A. Schmidt, and R. R. Volkas, "Reconsidering the One Leptoquark solution: flavor anomalies and neutrino mass," *JHEP* **10** (2017) 047, arXiv:1704.05849 [hep-ph].

[252] A. Crivellin, D. Müller, and T. Ota, "Simultaneous explanation of $R(D^{(*)})$ and $b \to s\mu^+\mu^-$: the last scalar leptoquarks standing," *JHEP* **09** (2017) 040, arXiv:1703.09226 [hep-ph].

[253] M. Jung and D. M. Straub, "Constraining new physics in $b \to c\ell\nu$ transitions," *JHEP* **01** (2019) 009, arXiv:1801.01112 [hep-ph].

[254] A. Biswas, D. K. Ghosh, S. K. Patra, and A. Shaw, "$b \to c\ell\nu$ anomalies in light of extended scalar sectors," *Int. J. Mod. Phys. A* **34** no. 21, (2019) 1950112, arXiv:1801.03375 [hep-ph].

[255] A. Azatov, D. Bardhan, D. Ghosh, F. Sgarlata, and E. Venturini, "Anatomy of $b \to c\tau\nu$ anomalies," *JHEP* **11** (2018) 187, arXiv:1805.03209 [hep-ph].

[256] Q.-Y. Hu, X.-Q. Li, and Y.-D. Yang, "$b \to c\tau\nu$ transitions in the standard model effective field theory," *Eur. Phys. J. C* **79** no. 3, (2019) 264, arXiv:1810.04939 [hep-ph].

[257] A. Angelescu, D. Beˇ cirević, D. Faroughy, and O. Sumensari, "Closing the window on single leptoquark solutions to the B-physics anomalies," *JHEP* **10** (2018) 183, arXiv:1808.08179 [hep-ph].

[258] J. Aebischer, J. Kumar, P. Stangl, and D. M. Straub, "A Global Likelihood for Precision Constraints and Flavour Anomalies," *Eur. Phys. J. C* **79** no. 6, (2019) 509, arXiv:1810.07698 [hep-ph].

[259] M. Blanke, A. Crivellin, S. de Boer, T. Kitahara, M. Moscati, U. Nierste, and I. Niˇ sandžić, "Impact of polarization observables and $B_c \to \tau\nu$ on new physics explanations of the $b \to c\tau\nu$ anomaly," *Phys. Rev. D* **99** no. 7, (2019) 075006, arXiv:1811.09603 [hep-ph].

[260] S. Bhattacharya, S. Nandi, and S. Kumar Patra, "$b \to c\tau\nu_\tau$ Decays: a catalogue to compare, constrain, and correlate new physics effects," *Eur. Phys. J. C* **79** no. 3, (2019) 268, arXiv:1805.08222 [hep-ph].

[261] R. Dutta and A. Bhol, "$B_c \to (J/\psi,\, \eta_c)\tau\nu$ semileptonic decays within the standard model and beyond," *Phys. Rev. D* **96** no. 7, (2017) 076001, arXiv:1701.08598 [hep-ph].

[262] R. Dutta, "$\Lambda_b \to (\Lambda_c,\, p)\, \tau\, \nu$ decays within standard model and beyond," *Phys. Rev. D* **93** no. 5, (2016) 054003, arXiv:1512.04034 [hep-ph].

[263] Z.-R. Huang, Y. Li, C.-D. Lu, M. A. Paracha, and C. Wang, "Footprints of New Physics in $b \to c\tau\nu$ Transitions," *Phys. Rev. D* **98** no. 9, (2018) 095018, arXiv:1808.03565 [hep-ph].

[264] K. Azizi and J. Süngü, "Semileptonic $\Lambda_b \to \Lambda_c \ell \bar{\nu}_\ell$ Transition in Full QCD," *Phys. Rev. D* **97** no. 7, (2018) 074007, arXiv:1803.02085 [hep-ph].

[265] R. Mandal, C. Murgui, A. Peñuelas, and A. Pich, "The role of right-handed neutrinos in $b \to c\tau\bar{\nu}$ anomalies," arXiv:2004.06726 [hep-ph].

[266] **MILC** Collaboration, J. A. Bailey *et al.*, "B→ $D\ell\nu$form factors at nonzero recoil and $|V_{cb}|$ from 2+1-flavor lattice QCD," *Phys. Rev. D* **92** no. 3, (2015) 034506, arXiv:1503.07237 [hep-lat].

[267] D. Bigi, P. Gambino, and S. Schacht, "A fresh look at the determination of $|V_{cb}|$ from $B \to D^* \ell\nu$," *Phys. Lett.* **B769** (2017) 441–445, arXiv:1703.06124 [hep-ph].

[268] F. U. Bernlochner, Z. Ligeti, M. Papucci, and D. J. Robinson, "Tensions and correlations in $|V_{cb}|$ determinations," *Phys. Rev.* **D96** no. 9, (2017) 091503, arXiv:1708.07134 [hep-ph].

[269] B. Grinstein and A. Kobach, "Model-Independent Extraction of $|V_{cb}|$ from $\bar{B} \to D^* \ell \overline{\nu}$," *Phys. Lett.* **B771** (2017) 359–364, arXiv:1703.08170 [hep-ph].

[270] I. Caprini, L. Lellouch, and M. Neubert, "Dispersive bounds on the shape of anti-B —> D(*) lepton anti-neutrino form-factors," *Nucl. Phys. B* **530** (1998) 153–181, arXiv:hep-ph/9712417.

[271] C. Boyd, B. Grinstein, and R. F. Lebed, "Constraints on form-factors for exclusive semileptonic heavy to light meson decays," *Phys. Rev. Lett.* **74** (1995) 4603–4606, arXiv:hep-ph/9412324.

[272] C. Boyd, B. Grinstein, and R. F. Lebed, "Model independent determinations of anti-B —> D (lepton), D* (lepton) anti-neutrino form-factors," *Nucl. Phys. B* **461** (1996) 493–511, arXiv:hep-ph/9508211.

[273] C. Boyd, B. Grinstein, and R. F. Lebed, "Precision corrections to dispersive bounds on form-factors," *Phys. Rev. D* **56** (1997) 6895–6911, arXiv:hep-ph/9705252.

[274] M. Neubert, "Heavy quark symmetry," *Phys. Rept.* **245** (1994) 259–396, arXiv:hep-ph/9306320.

[275] A. V. Manohar and M. B. Wise, *Heavy quark physics*, vol. 10. 2000.

[276] N. Isgur and M. B. Wise, "WEAK TRANSITION FORM-FACTORS BETWEEN HEAVY MESONS," *Phys. Lett. B* **237** (1990) 527–530.

[277] C. Bourrely, B. Machet, and E. de Rafael, "Semileptonic Decays of Pseudoscalar Particles ($M \to M' \ell \nu_\ell$) and Short Distance Behavior of Quantum Chromodynamics," *Nucl. Phys. B* **189** (1981) 157–181.

[278] M. Bordone, M. Jung, and D. van Dyk, "Theory determination of $\bar{B} \to D^{(*)}\ell^-\bar{\nu}$ form factors at $\mathcal{O}(1/m_c^2)$," *Eur. Phys. J. C* **80** no. 2, (2020) 74, arXiv:1908.09398 [hep-ph].

[279] **HPQCD** Collaboration, H. Na, C. M. Bouchard, G. P. Lepage, C. Monahan, and J. Shigemitsu, "$B \to Dl\nu$ form factors at nonzero recoil and extraction of $|V_{cb}|$," *Phys. Rev. D* **92** no. 5, (2015) 054510, arXiv:1505.03925 [hep-lat]. [Erratum: Phys.Rev.D 93, 119906 (2016)].

[280] **Fermilab Lattice, MILC** Collaboration, J. A. Bailey *et al.*, "Update of $|V_{cb}|$ from the $\bar{B} \to D^*\ell\bar{\nu}$ form factor at zero recoil with three-flavor lattice QCD," *Phys. Rev. D* **89** no. 11, (2014) 114504, arXiv:1403.0635 [hep-lat].

[281] **HPQCD** Collaboration, J. Harrison, C. Davies, and M. Wingate, "Lattice QCD calculation of the $B_{(s)} \to D^*_{(s)}\ell\nu$ form factors at zero recoil and implications for $|V_{cb}|$," *Phys. Rev. D* **97** no. 5, (2018) 054502, arXiv:1711.11013 [hep-lat].

[282] S. Faller, A. Khodjamirian, C. Klein, and T. Mannel, "B —> D(*) Form Factors from QCD Light-Cone Sum Rules," *Eur. Phys. J. C* **60** (2009) 603–615, arXiv:0809.0222 [hep-ph].

[283] M. Neubert, Z. Ligeti, and Y. Nir, "QCD sum rule analysis of the subleading Isgur-Wise form-factor Chi-2 (v v-prime)," *Phys. Lett. B* **301** (1993) 101–107, arXiv:hep-ph/9209271.

[284] M. Neubert, Z. Ligeti, and Y. Nir, "The Subleading Isgur-Wise form-factor chi(3) (v, v-prime) to order alpha-s in QCD sum rules," *Phys. Rev. D* **47** (1993) 5060–5066, arXiv:hep-ph/9212266.

[285] Z. Ligeti, Y. Nir, and M. Neubert, "The Subleading Isgur-Wise form-factor Xi-3 (v - v-prime) and its implications for the decays anti-B —> D* lepton anti-neutrino," *Phys. Rev. D* **49** (1994) 1302–1309, arXiv:hep-ph/9305304.

[286] V. Cirigliano, J. Jenkins, and M. Gonzalez-Alonso, "Semileptonic decays of light quarks beyond the Standard Model," *Nucl. Phys. B* **830** (2010) 95–115, arXiv:0908.1754 [hep-ph].

[287] R. Alonso, B. Grinstein, and J. Martin Camalich, "$SU(2) \times U(1)$ gauge invariance and the shape of new physics in rare B decays," *Phys. Rev. Lett.* **113** (2014) 241802, arXiv:1407.7044 [hep-ph].

[288] O. Catà and M. Jung, "Signatures of a nonstandard Higgs boson from flavor physics," *Phys. Rev. D* **92** no. 5, (2015) 055018, arXiv:1505.05804 [hep-ph].

[289] W. Buchmuller and D. Wyler, "Effective Lagrangian Analysis of New Interactions and Flavor Conservation," *Nucl. Phys. B* **268** (1986) 621–653.

[290] B. Grzadkowski, M. Iskrzynski, M. Misiak, and J. Rosiek, "Dimension-Six Terms in the Standard Model Lagrangian," *JHEP* **10** (2010) 085, arXiv:1008.4884 [hep-ph].

[291] D. Beˇ cirević, I. Dorˇ sner, S. Fajfer, N. Koˇ snik, D. A. Faroughy, and O. Sumensari, "Scalar leptoquarks from grand unified theories to accommodate the B-physics anomalies," *Phys. Rev. D* **98** no. 5, (2018) 055003, arXiv:1806.05689 [hep-ph].

[292] B. Bhattacharya, A. Datta, S. Kamali, and D. London, "CP Violation in $\bar{B}^0 \to D^{*+}\mu^-\bar{\nu}_\mu$," *JHEP* **05** (2019) 191, arXiv:1903.02567 [hep-ph].

[293] W. Dekens, J. de Vries, M. Jung, and K. Vos, "The phenomenology of electric dipole moments in models of scalar leptoquarks," *JHEP* **01** (2019) 069, arXiv:1809.09114 [hep-ph].

[294] M. Beneke and G. Buchalla, "The B_c Meson Lifetime," *Phys. Rev.* **D53** (1996) 4991–5000, arXiv:hep-ph/9601249 [hep-ph].

[295] A. G. Akeroyd and C.-H. Chen, "Constraint on the branching ratio of $B_c \to \tau\bar{\nu}$ from LEP1 and consequences for $R(D^{(*)})$ anomaly," *Phys. Rev.* **D96** no. 7, (2017) 075011, arXiv:1708.04072 [hep-ph].

[296] S. Fajfer, J. F. Kamenik, and I. Nisandzic, "On the $B \to D^*\tau\bar{\nu}_\tau$ Sensitivity to New Physics," *Phys. Rev. D* **85** (2012) 094025, arXiv:1203.2654 [hep-ph].

[297] G. Buchalla, A. J. Buras, and M. E. Lautenbacher, "Weak decays beyond leading logarithms," *Rev. Mod. Phys.* **68** (1996) 1125–1144, arXiv:hep-ph/9512380.

[298] J. Aebischer, M. Fael, C. Greub, and J. Virto, "B physics Beyond the Standard Model at One Loop: Complete Renormalization Group Evolution below the Electroweak Scale," *JHEP* **09** (2017) 158, arXiv:1704.06639 [hep-ph].

[299] E. E. Jenkins, A. V. Manohar, and P. Stoffer, "Low-Energy Effective Field Theory below the Electroweak Scale: Operators and Matching," *JHEP* **03** (2018) 016, arXiv:1709.04486 [hep-ph].

[300] E. E. Jenkins, A. V. Manohar, and P. Stoffer, "Low-Energy Effective Field Theory below the Electroweak Scale: Anomalous Dimensions," *JHEP* **01** (2018) 084, arXiv:1711.05270 [hep-ph].

[301] F. Feruglio, "The Chiral approach to the electroweak interactions," *Int. J. Mod. Phys. A* **8** (1993) 4937–4972, arXiv:hep-ph/9301281.

[302] A. Pich, "Effective Field Theory with Nambu-Goldstone Modes," in *Les Houches summer school: EFT in Particle Physics and Cosmology*. 4, 2018. arXiv:1804.05664 [hep-ph].

[303] J. Aebischer, A. Crivellin, M. Fael, and C. Greub, "Matching of gauge invariant dimension-six operators for $b \to s$ and $b \to c$ transitions," *JHEP* **05** (2016) 037, arXiv:1512.02830 [hep-ph].

[304] J. Aebischer, J. Kumar, and D. M. Straub, "Wilson: a Python package for the running and matching of Wilson coefficients above and below the electroweak scale," *Eur. Phys. J. C* **78** no. 12, (2018) 1026, arXiv:1804.05033 [hep-ph].

[305] G. Buchalla and O. Cata, "Effective Theory of a Dynamically Broken Electroweak Standard Model at NLO," *JHEP* **07** (2012) 101, arXiv:1203.6510 [hep-ph].

[306] G. Buchalla, O. Catà, and C. Krause, "Complete Electroweak Chiral Lagrangian with a Light Higgs at NLO," *Nucl. Phys. B* **880** (2014) 552–573, arXiv:1307.5017 [hep-ph]. [Erratum: Nucl.Phys.B 913, 475–478 (2016)].

[307] E. E. Jenkins, A. V. Manohar, and M. Trott, "Renormalization Group Evolution of the Standard Model Dimension Six Operators I: Formalism and lambda Dependence," *JHEP* **10** (2013) 087, arXiv:1308.2627 [hep-ph].

[308] E. E. Jenkins, A. V. Manohar, and M. Trott, "Renormalization Group Evolution of the Standard Model Dimension Six Operators II: Yukawa Dependence," *JHEP* **01** (2014) 035, arXiv:1310.4838 [hep-ph].

[309] R. Alonso, E. E. Jenkins, A. V. Manohar, and M. Trott, "Renormalization Group Evolution of the Standard Model Dimension Six Operators III: Gauge Coupling Dependence and Phenomenology," *JHEP* **04** (2014) 159, arXiv:1312.2014 [hep-ph].

[310] M. González-Alonso, J. Martin Camalich, and K. Mimouni, "Renormalization-group evolution of new physics contributions to (semi)leptonic meson decays," *Phys. Lett. B* **772** (2017) 777–785, arXiv:1706.00410 [hep-ph].

[311] A. J. Buras and M. Jung, "Analytic inclusion of the scale dependence of the anomalous dimension matrix in Standard Model Effective Theory," *JHEP* **06** (2018) 067, arXiv:1804.05852 [hep-ph].

[312] D. A. Faroughy, A. Greljo, and J. F. Kamenik, "Confronting lepton flavor universality violation in B decays with high-p_T tau lepton searches at LHC," *Phys. Lett. B* **764** (2017) 126–134, arXiv:1609.07138 [hep-ph].

[313] F. Feruglio, P. Paradisi, and O. Sumensari, "Implications of scalar and tensor explanations of $R_{D^{(*)}}$," *JHEP* **11** (2018) 191, arXiv:1806.10155 [hep-ph].

[314] A. Greljo, J. Martin Camalich, and J. D. Ruiz-Álvarez, "Mono-τ Signatures at the LHC Constrain Explanations of B-decay Anomalies," *Phys. Rev. Lett.* **122** no. 13, (2019) 131803, arXiv:1811.07920 [hep-ph].

[315] **ATLAS** Collaboration, The ATLAS collaboration, "Search for a new heavy gauge boson resonance decaying into a lepton and missing transverse momentum in 79.8 fb^{-1} of pp collisions at $\sqrt{s} = 13$ TeV with the ATLAS experiment,".

[316] S. Iguro, T. Kitahara, Y. Omura, R. Watanabe, and K. Yamamoto, "D* polarization vs. $R_{D^{(*)}}$ anomalies in the leptoquark models," *JHEP* **02** (2019) 194, arXiv:1811.08899 [hep-ph].

[317] P. Asadi, M. R. Buckley, and D. Shih, "It's all right(-handed neutrinos): a new W' model for the $R_{D^{(*)}}$ anomaly," *JHEP* **09** (2018) 010, arXiv:1804.04135 [hep-ph].

[318] A. Greljo, D. J. Robinson, B. Shakya, and J. Zupan, "$R(D^{"}(*))$ from W' and right-handed neutrinos," *JHEP* **09** (2018) 169, arXiv:1804.04642 [hep-ph].

[319] D. J. Robinson, B. Shakya, and J. Zupan, "Right-handed neutrinos and $R(D^{"}(*))$," *JHEP* **02** (2019) 119, arXiv:1807.04753 [hep-ph].

[320] **Belle, Belle-II** Collaboration, K. Adamczyk, "Semitauonic B decays at Belle/Belle II," in *10th International Workshop on the CKM Unitarity Triangle*. 1, 2019. arXiv:1901.06380 [hep-ex].

[321] W. Detmold, C. Lehner, and S. Meinel, "$\Lambda_b \to p\ell^-\bar{\nu}_\ell$ and $\Lambda_b \to \Lambda_c\ell^-\bar{\nu}_\ell$ form factors from lattice QCD with relativistic heavy quarks," *Phys. Rev. D* **92** no. 3, (2015) 034503, arXiv:1503.01421 [hep-lat].

[322] A. Datta, S. Kamali, S. Meinel, and A. Rashed, "Phenomenology of $\Lambda_b \to \Lambda_c\tau\overline{\nu}_\tau$ using lattice QCD calculations," *JHEP* **08** (2017) 131, arXiv:1702.02243 [hep-ph].

[323] J. Harrison, C. T. Davies, and A. Lytle, "$B_c \to J/\psi$ Form Factors for the full q^2 range from Lattice QCD," *PoS* **Beauty2019** (2020) 059, arXiv:2007.06957 [hep-lat].

[324] **LATTICE-HPQCD** Collaboration, J. Harrison, C. T. Davies, and A. Lytle, "$R(J/\psi)$ and $B_c^- \to J/\psi\ell^-\overline{\nu}_\ell$ Lepton Flavor Universality Violating Observables from Lattice QCD," arXiv:2007.06956 [hep-lat].

[325] R. Watanabe, "New Physics effect on $B_c \to J/\psi\tau\bar{\nu}$ in relation to the $R_{D^{(*)}}$ anomaly," *Phys. Lett. B* **776** (2018) 5–9, arXiv:1709.08644 [hep-ph].

[326] **BaBar** Collaboration, B. Aubert *et al.*, "Measurements of the Semileptonic Decays anti-B —> D l anti-nu and anti-B —> D* l anti-nu Using a Global Fit to D X l anti-nu Final States," *Phys. Rev. D* **79** (2009) 012002, arXiv:0809.0828 [hep-ex].

[327] A. Azatov, D. Barducci, D. Ghosh, D. Marzocca, and L. Ubaldi, "Combined explanations of B-physics anomalies: the sterile neutrino solution," *JHEP* **10** (2018) 092, arXiv:1807.10745 [hep-ph].

[328] J. Heeck and D. Teresi, "Pati-Salam explanations of the B-meson anomalies," *JHEP* **12** (2018) 103, arXiv:1808.07492 [hep-ph].

[329] K. S. Babu, B. Dutta, and R. N. Mohapatra, "A theory of $R(D^*, \mathrm{D})$ anomaly with right-handed currents," *JHEP* **01** (2019) 168, arXiv:1811.04496 [hep-ph].

[330] D. Bardhan and D. Ghosh, "B -meson charged current anomalies: The post-Moriond 2019 status," *Phys. Rev.* **D100** no. 1, (2019) 011701, arXiv:1904.10432 [hep-ph].

[331] R.-X. Shi, L.-S. Geng, B. Grinstein, S. Jäger, and J. Martin Camalich, "Revisiting the new-physics interpretation of the $b \to c\tau\nu$ data," *JHEP* **12** (2019) 065, arXiv:1905.08498 [hep-ph].

[332] J. D. Gómez, N. Quintero, and E. Rojas, "Charged current $b \to c\tau\bar{\nu}_\tau$ anomalies in a general W' boson scenario," *Phys. Rev.* **D100** no. 9, (2019) 093003, arXiv:1907.08357 [hep-ph].

[333] B. Capdevila, U. Laa, and G. Valencia, "Anatomy of a six-parameter fit to the $b \to s\ell^+\ell^-$ anomalies," *Eur. Phys. J. C* **79** no. 6, (2019) 462, arXiv:1811.10793 [hep-ph].

[334] J. C. Pati and A. Salam, "Lepton Number as the Fourth Color," *Phys. Rev. D* **10** (1974) 275–289. [Erratum: Phys.Rev.D 11, 703–703 (1975)].

[335] R. Barbieri, G. Isidori, A. Pattori, and F. Senia, "Anomalies in B-decays and $U(2)$ flavour symmetry," *Eur. Phys. J.* **C76** no. 2, (2016) 67, arXiv:1512.01560 [hep-ph].

[336] L. Di Luzio, A. Greljo, and M. Nardecchia, "Gauge leptoquark as the origin of B-physics anomalies," *Phys. Rev.* **D96** no. 11, (2017) 115011, arXiv:1708.08450 [hep-ph].

[337] M. Bordone, C. Cornella, J. Fuentes-Martin, and G. Isidori, "A three-site gauge model for flavor hierarchies and flavor anomalies," *Phys. Lett.* **B779** (2018) 317–323, arXiv:1712.01368 [hep-ph].

[338] M. Blanke and A. Crivellin, "B Meson Anomalies in a Pati-Salam Model within the Randall-Sundrum Background," *Phys. Rev. Lett.* **121** no. 1, (2018) 011801, arXiv:1801.07256 [hep-ph].

[339] L. Calibbi, A. Crivellin, and T. Li, "Model of vector leptoquarks in view of the B-physics anomalies," *Phys. Rev. D* **98** no. 11, (2018) 115002, arXiv:1709.00692 [hep-ph].

[340] M. Algueró, S. Descotes-Genon, J. Matias, and M. Novoa-Brunet, "Symmetries in $B \to D^* \ell \nu$ angular observables," *JHEP* **06** (2020) 156, arXiv:2003.02533 [hep-ph].

[341] F. Richard, "Present and future constraints on top EW couplings," arXiv:1403.2893 [hep-ph].

[342] G. Durieux and O. Matsedonskyi, "The top-quark window on compositeness at future lepton colliders," *JHEP* **01** (2019) 072, arXiv:1807.10273 [hep-ph].

[343] C. Englert and M. Russell, "Top quark electroweak couplings at future lepton colliders," *Eur. Phys. J. C* **77** no. 8, (2017) 535, arXiv:1704.01782 [hep-ph].

[344] G. Durieux, M. Perelló, M. Vos, and C. Zhang, "Global and optimal probes for the top-quark effective field theory at future lepton colliders," *JHEP* **10** (2018) 168, arXiv:1807.02121 [hep-ph].

[345] M. L. Mangano *et al.*, "Physics at a 100 TeV pp Collider: Standard Model Processes," *CERN Yellow Report* no. 3, (2017) 1–254, arXiv:1607.01831 [hep-ph].

[346] P. Bambade *et al.*, "The International Linear Collider: A Global Project," arXiv:1903.01629 [hep-ex].

[347] **CLICdp, CLIC** Collaboration, T. Charles *et al.*, "The Compact Linear Collider (CLIC) - 2018 Summary Report," *CERN Yellow Rep. Monogr.* **1802** (2018) 1–98, arXiv:1812.06018 [physics.acc-ph].

[348] **FCC** Collaboration, A. Abada *et al.*, "FCC-ee: The Lepton Collider: Future Circular Collider Conceptual Design Report Volume 2," *Eur. Phys. J. ST* **228** no. 2, (2019) 261–623.

[349] **CEPC Study Group** Collaboration, "CEPC Conceptual Design Report: Volume 1 - Accelerator," arXiv:1809.00285 [physics.acc-ph].

[350] **CLICdp** Collaboration, H. Abramowicz *et al.*, "Top-Quark Physics at the CLIC Electron-Positron Linear Collider," *JHEP* **11** (2019) 003, arXiv:1807.02441 [hep-ex].

[351] A. Buckley, C. Englert, J. Ferrando, D. J. Miller, L. Moore, M. Russell, and C. D. White, "Global fit of top quark effective theory to data," *Phys. Rev. D* **92** no. 9, (2015) 091501, arXiv:1506.08845 [hep-ph].

[352] M. de Beurs, E. Laenen, M. Vreeswijk, and E. Vryonidou, "Effective operators in t-channel single top production and decay," *Eur. Phys. J. C* **78** no. 11, (2018) 919, arXiv:1807.03576 [hep-ph].

[353] N. P. Hartland, F. Maltoni, E. R. Nocera, J. Rojo, E. Slade, E. Vryonidou, and C. Zhang, "A Monte Carlo global analysis of the Standard Model Effective Field Theory: the top quark sector," *JHEP* **04** (2019) 100, arXiv:1901.05965 [hep-ph].

[354] G. Durieux, A. Irles, V. Miralles, A. Peñuelas, R. Pöschl, M. Perelló, and M. Vos, "The electro-weak couplings of the top and bottom quarks – global fit and future prospects," *JHEP* **12** (2019) 098, arXiv:1907.10619 [hep-ph].

[355] R. Contino, A. Falkowski, F. Goertz, C. Grojean, and F. Riva, "On the Validity of the Effective Field Theory Approach to SM Precision Tests," *JHEP* **07** (2016) 144, arXiv:1604.06444 [hep-ph].

[356] D. Barducci *et al.*, "Interpreting top-quark LHC measurements in the standard-model effective field theory," arXiv:1802.07237 [hep-ph].

[357] J. Birman, F. Déliot, M. Fiolhais, A. Onofre, and C. Pease, "New limits on anomalous contributions to the Wtb vertex," *Phys. Rev. D* **93** no. 11, (2016) 113021, arXiv:1605.02679 [hep-ph].

[358] W. Bernreuther, L. Chen, I. García, M. Perelló, R. Poeschl, F. Richard, E. Ros, and M. Vos, "CP-violating top quark couplings at future linear e^+e^- colliders," *Eur. Phys. J. C* **78** no. 2, (2018) 155, arXiv:1710.06737 [hep-ex].

[359] V. Cirigliano, W. Dekens, J. de Vries, and E. Mereghetti, "Is there room for CP violation in the top-Higgs sector?," *Phys. Rev. D* **94** no. 1, (2016) 016002, arXiv:1603.03049 [hep-ph].

[360] J. Aguilar-Saavedra, "A Minimal set of top anomalous couplings," *Nucl. Phys. B* **812** (2009) 181–204, arXiv:0811.3842 [hep-ph].

[361] C. Zhang and S. Willenbrock, "Effective-Field-Theory Approach to Top-Quark Production and Decay," *Phys. Rev. D* **83** (2011) 034006, arXiv:1008.3869 [hep-ph].

[362] J. Alwall, R. Frederix, S. Frixione, V. Hirschi, F. Maltoni, O. Mattelaer, H. S. Shao, T. Stelzer, P. Torrielli, and M. Zaro, "The automated computation of tree-level and next-to-leading order differential cross sections, and their matching to parton shower simulations," *JHEP* **07** (2014) 079, arXiv:1405.0301 [hep-ph].

[363] O. Bessidskaia Bylund, F. Maltoni, I. Tsinikos, E. Vryonidou, and C. Zhang, "Probing top quark neutral couplings in the Standard Model Effective Field Theory at NLO in QCD," *JHEP* **05** (2016) 052, arXiv:1601.08193 [hep-ph].

[364] I. Brivio, Y. Jiang, and M. Trott, "The SMEFTsim package, theory and tools," *JHEP* **12** (2017) 070, arXiv:1709.06492 [hep-ph].

[365] F. James and M. Winkler, "MINUIT User's Guide," *https://inspirehep.net/record/1258345* (2004) .

[366] **ALEPH, DELPHI, L3, OPAL, SLD, LEP Electroweak Working Group, SLD Electroweak Group, SLD Heavy Flavour Group** Collaboration, S. Schael *et al.*, "Precision electroweak measurements on the Z resonance," *Phys. Rept.* **427** (2006) 257–454, arXiv:hep-ex/0509008.

[367] **ATLAS** Collaboration, M. Aaboud *et al.*, "Observation of Higgs boson production in association with a top quark pair at the LHC with the ATLAS detector," *Phys. Lett. B* **784** (2018) 173–191, arXiv:1806.00425 [hep-ex].

[368] **ATLAS** Collaboration, M. Aaboud *et al.*, "Measurement of the $t\bar{t}Z$ and $t\bar{t}W$ cross sections in proton-proton collisions at $\sqrt{s} = 13$ TeV with the ATLAS detector," *Phys. Rev. D* **99** no. 7, (2019) 072009, arXiv:1901.03584 [hep-ex].

[369] **ATLAS** Collaboration, M. Aaboud *et al.*, "Measurements of inclusive and differential fiducial cross-sections of $t\bar{t}\gamma$ production in leptonic final states at $\sqrt{s} = 13$ TeV in ATLAS," *Eur. Phys. J. C* **79** no. 5, (2019) 382, arXiv:1812.01697 [hep-ex].

[370] **CMS** Collaboration, A. M. Sirunyan *et al.*, "Measurement of the single top quark and antiquark production cross sections in the t channel and their ratio in proton-proton collisions at $\sqrt{s} = 13$ TeV," *Phys. Lett. B* **800** (2020) 135042, arXiv:1812.10514 [hep-ex].

[371] **CMS** Collaboration, A. M. Sirunyan *et al.*, "Measurement of the production cross section for single top quarks in association with W bosons in proton-proton collisions at $\sqrt{s} = 13$ TeV," *JHEP* **10** (2018) 117, arXiv:1805.07399 [hep-ex].

[372] **CMS** Collaboration, A. M. Sirunyan *et al.*, "Measurement of the associated production of a single top quark and a Z boson in pp collisions at $\sqrt{s} = 13$ TeV," *Phys. Lett. B* **779** (2018) 358–384, arXiv:1712.02825 [hep-ex].

[373] **CMS** Collaboration, "First constraints on invisible Higgs boson decays using $\mathrm{t\bar{t}H}$ production at $\sqrt{s} = 13$ TeV,".

[374] A. Czarnecki, J. G. Korner, and J. H. Piclum, "Helicity fractions of W bosons from top quark decays at NNLO in QCD," *Phys. Rev. D* **81** (2010) 111503, arXiv:1005.2625 [hep-ph].

[375] **ATLAS** Collaboration, M. Aaboud *et al.*, "Measurement of the W boson polarisation in $t\bar{t}$ events from pp collisions at $\sqrt{s} = 8$ TeV in the lepton + jets channel with ATLAS," *Eur. Phys. J. C* **77** no. 4, (2017) 264, arXiv:1612.02577 [hep-ex]. [Erratum: Eur.Phys.J.C 79, 19 (2019)].

[376] **CMS** Collaboration, A. M. Sirunyan *et al.*, "Observation of $\mathrm{t\bar{t}H}$ production," *Phys. Rev. Lett.* **120** no. 23, (2018) 231801, arXiv:1804.02610 [hep-ex].

[377] **CMS** Collaboration, A. M. Sirunyan *et al.*, "Measurement of the cross section for top quark pair production in association with a W or Z boson in proton-proton collisions at $\sqrt{s} = 13$ TeV," *JHEP* **08** (2018) 011, arXiv:1711.02547 [hep-ex].

[378] **CMS** Collaboration, "Measurement of top quark pair production in association with a Z boson in proton-proton collisions at $\sqrt{s} = 13$ TeV,".

[379] **CMS** Collaboration, A. M. Sirunyan *et al.*, "Observation of Single Top Quark Production in Association with a Z Boson in Proton-Proton Collisions at $\sqrt{s}$ =13 TeV," *Phys. Rev. Lett.* **122** no. 13, (2019) 132003, arXiv:1812.05900 [hep-ex].

[380] **ATLAS** Collaboration, M. Aaboud *et al.*, "Measurement of the production cross-section of a single top quark in association with a Z boson in proton–proton collisions at 13 TeV with the ATLAS detector," *Phys. Lett. B* **780** (2018) 557–577, arXiv:1710.03659 [hep-ex].

[381] **CMS** Collaboration, V. Khachatryan *et al.*, "Measurement of the W boson helicity fractions in the decays of top quark pairs to lepton + jets final states produced in pp collisions at $\sqrt{s} = 8$TeV," *Phys. Lett. B* **762** (2016) 512–534, arXiv:1605.09047 [hep-ex].

[382] **CMS** Collaboration, S. Chatrchyan *et al.*, "Measurement of the W-Boson Helicity in Top-Quark decays from $t\bar{t}$ Production in Lepton + Jets Events in pp Collisions at $\sqrt{s} = 7$ TeV," *JHEP* **10** (2013) 167, arXiv:1308.3879 [hep-ex].

[383] **ATLAS** Collaboration, G. Aad *et al.*, "Measurement of the W boson polarization in top quark decays with the ATLAS detector," *JHEP* **06** (2012) 088, arXiv:1205.2484 [hep-ex].

[384] **ATLAS** Collaboration, M. Aaboud *et al.*, "Measurement of the cross-section for producing a W boson in association with a single top quark in pp collisions at $\sqrt{s} = 13$ TeV with ATLAS," *JHEP* **01** (2018) 063, arXiv:1612.07231 [hep-ex].

[385] **ATLAS** Collaboration, G. Aad *et al.*, "Measurement of differential production cross-sections for a Z boson in association with b-jets in 7 TeV proton-proton collisions with the ATLAS detector," *JHEP* **10** (2014) 141, arXiv:1407.3643 [hep-ex].

[386] **CMS** Collaboration, S. Chatrchyan *et al.*, "Measurement of the Z/γ*+b-jet cross section in pp collisions at $\sqrt{s} = 7$ TeV," *JHEP* **06** (2012) 126, arXiv:1204.1643 [hep-ex].

[387] P. Azzi *et al.*, *Report from Working Group 1: Standard Model Physics at the HL-LHC and HE-LHC*, vol. 7, pp. 1–220. 12, 2019. arXiv:1902.04070 [hep-ph].

[388] M. Cepeda *et al.*, *Report from Working Group 2: Higgs Physics at the HL-LHC and HE-LHC*, vol. 7, pp. 221–584. 12, 2019. arXiv:1902.00134 [hep-ph].

[389] M. Schulze and Y. Soreq, "Pinning down electroweak dipole operators of the top quark," *Eur. Phys. J. C* **76** no. 8, (2016) 466, arXiv:1603.08911 [hep-ph].

[390] R. Röntsch and M. Schulze, "Constraining couplings of top quarks to the Z boson in $t\bar{t}$ + Z production at the LHC," *JHEP* **07** (2014) 091, arXiv:1404.1005 [hep-ph]. [Erratum: JHEP 09, 132 (2015)].

[391] **CLIC, CLICdp** Collaboration, M. J. Boland *et al.*, "Updated baseline for a staged Compact Linear Collider," `arXiv:1608.07537 [physics.acc-ph]`.

[392] J. Fuster, I. García, P. Gomis, M. Perelló, E. Ros, and M. Vos, "Study of single top production at high energy electron positron colliders," *Eur. Phys. J. C* **75** (2015) 223, `arXiv:1411.2355 [hep-ex]`.

[393] S. Bilokin, A. Irles, R. Pöschl, and F. Richard, "Measurement of b quark EW couplings at ILC250 with 2000 fb^{-1}," *In preparation* .

[394] M. Amjad *et al.*, "A precise characterisation of the top quark electro-weak vertices at the ILC," *Eur. Phys. J. C* **75** no. 10, (2015) 512, `arXiv:1505.06020 [hep-ex]`.

[395] J. Aguilar-Saavedra, M. Fiolhais, and A. Onofre, "Top Effective Operators at the ILC," *JHEP* **07** (2012) 180, `arXiv:1206.1033 [hep-ph]`.

[396] D. Gauthier, V. Miralles, M. Miralles, M. Moreno, A. Peñuelas, M. Perelló, Vos, and C. M, Zhang.

[397] B. Pontecorvo, "Mesonium and anti-mesonium," *Sov. Phys. JETP* **6** (1957) 429.

[398] Z. Maki, M. Nakagawa, and S. Sakata, "Remarks on the unified model of elementary particles," *Prog. Theor. Phys.* **28** (1962) 870–880.

[399] B. Pontecorvo, "Neutrino Experiments and the Problem of Conservation of Leptonic Charge," *Sov. Phys. JETP* **26** (1968) 984–988.

[400] T. Barklow, J. Brau, K. Fujii, J. Gao, J. List, N. Walker, and K. Yokoya, "ILC Operating Scenarios," `arXiv:1506.07830 [hep-ex]`.

[401] S. Dawson *et al.*, "Working Group Report: Higgs Boson," in *Community Summer Study 2013: Snowmass on the Mississippi*. 10, 2013. `arXiv:1310.8361 [hep-ex]`.

[402] **ATLAS** Collaboration, "Combined measurements of Higgs boson production and decay using up to 80 fb^{-1} of proton–proton collision data at $\sqrt{s} = 13$ TeV collected with the ATLAS experiment,".

[403] **CMS** Collaboration, A. M. Sirunyan *et al.*, "Combined measurements of Higgs boson couplings in proton–proton collisions at $\sqrt{s} = 13\,\text{TeV}$," *Eur. Phys. J. C* **79** no. 5, (2019) 421, arXiv:1809.10733 [hep-ex].

[404] S. Boselli, R. Hunter, and A. Mitov, "Prospects for the determination of the top-quark Yukawa coupling at future e^+e^- colliders," *J. Phys. G* **46** no. 9, (2019) 095005, arXiv:1805.12027 [hep-ph].

[405] G. Durieux, J. Gu, E. Vryonidou, and C. Zhang, "Probing top-quark couplings indirectly at Higgs factories," *Chin. Phys. C* **42** no. 12, (2018) 123107, arXiv:1809.03520 [hep-ph].

[406] A. Azatov, C. Grojean, A. Paul, and E. Salvioni, "Resolving gluon fusion loops at current and future hadron colliders," *JHEP* **09** (2016) 123, arXiv:1608.00977 [hep-ph].

[407] T. Price, P. Roloff, J. Strube, and T. Tanabe, "Full simulation study of the top Yukawa coupling at the ILC at $\sqrt{s} = 1$ TeV," *Eur. Phys. J. C* **75** no. 7, (2015) 309, arXiv:1409.7157 [hep-ex].

[408] R. Yonamine, K. Ikematsu, T. Tanabe, K. Fujii, Y. Kiyo, Y. Sumino, and H. Yokoya, "Measuring the top Yukawa coupling at the ILC at $\sqrt{s} = 500$ GeV," *Phys. Rev. D* **84** (2011) 014033, arXiv:1104.5132 [hep-ph].

[409] A. Gay, "Measurement of the top-Higgs Yukawa coupling at a Linear e+ e- Collider," *Eur. Phys. J. C* **49** (2007) 489–497, arXiv:hep-ph/0604034.

[410] A. Juste and G. Merino, "Top Higgs-Yukawa coupling measurement at a linear e+ e- collider," arXiv:hep-ph/9910301.

[411] K. Fujii *et al.*, "Physics Case for the International Linear Collider," arXiv:1506.05992 [hep-ex].

[412] B. Chokoufé Nejad, W. Kilian, J. M. Lindert, S. Pozzorini, J. Reuter, and C. Weiss, "NLO QCD predictions for off-shell $t\bar{t}$ and $t\bar{t}H$ production and decay at a linear collider," *JHEP* **12** (2016) 075, arXiv:1609.03390 [hep-ph].

[413] J. de Blas *et al.*, "Higgs Boson Studies at Future Particle Colliders," *JHEP* **01** (2020) 139, arXiv:1905.03764 [hep-ph].

[414] A. J. Buras, M. Misiak, and J. Urban, "Two loop QCD anomalous dimensions of flavor changing four quark operators within and beyond the standard model," *Nucl. Phys.* **B586** (2000) 397–426, arXiv:hep-ph/0005183 [hep-ph].

[415] A. J. Buras, S. Jager, and J. Urban, "Master formulae for Delta F=2 NLO QCD factors in the standard model and beyond," *Nucl. Phys.* **B605** (2001) 600–624, arXiv:hep-ph/0102316 [hep-ph].

[416] **ETM** Collaboration, N. Carrasco *et al.*, "B-physics from $N_f = 2$ tmQCD: the Standard Model and beyond," *JHEP* **03** (2014) 016, arXiv:1308.1851 [hep-lat].

[417] **ETM** Collaboration, N. Carrasco, P. Dimopoulos, R. Frezzotti, V. Lubicz, G. C. Rossi, S. Simula, and C. Tarantino, "ΔS=2 and ΔC=2 bag parameters in the standard model and beyond from N_f=2+1+1 twisted-mass lattice QCD," *Phys. Rev.* **D92** no. 3, (2015) 034516, arXiv:1505.06639 [hep-lat].

[418] A. J. Buras, D. Guadagnoli, and G. Isidori, "On ϵ_K Beyond Lowest Order in the Operator Product Expansion," *Phys. Lett. B* **688** (2010) 309–313, arXiv:1002.3612 [hep-ph].

[419] **ATLAS** Collaboration, G. Aad *et al.*, "Measurement of Higgs boson production in the diphoton decay channel in pp collisions at center-of-mass energies of 7 and 8 TeV with the ATLAS detector," *Phys. Rev.* **D90** no. 11, (2014) 112015, arXiv:1408.7084 [hep-ex].

[420] **CMS** Collaboration, V. Khachatryan *et al.*, "Observation of the diphoton decay of the Higgs boson and measurement of its properties," *Eur. Phys. J.* **C74** no. 10, (2014) 3076, arXiv:1407.0558 [hep-ex].

[421] **ATLAS, CMS** Collaboration, G. Aad *et al.*, "Measurements of the Higgs boson production and decay rates and constraints on its couplings from a combined ATLAS and CMS analysis of the LHC pp collision data at $\sqrt{s} = 7$ and 8 TeV," *JHEP* **08** (2016) 045, arXiv:1606.02266 [hep-ex].

[422] **ATLAS** Collaboration, G. Aad *et al.*, "Evidence for the Higgs-boson Yukawa coupling to tau leptons with the ATLAS detector," *JHEP* **04** (2015) 117, arXiv:1501.04943 [hep-ex].

[423] **CMS** Collaboration, S. Chatrchyan *et al.*, "Evidence for the 125 GeV Higgs boson decaying to a pair of τ leptons," *JHEP* **05** (2014) 104, arXiv:1401.5041 [hep-ex].

[424] **ATLAS** Collaboration, G. Aad *et al.*, "Observation and measurement of Higgs boson decays to WW* with the ATLAS detector," *Phys. Rev.* **D92** no. 1, (2015) 012006, arXiv:1412.2641 [hep-ex].

[425] **ATLAS** Collaboration, G. Aad *et al.*, "Study of (W/Z)H production and Higgs boson couplings using $H \to WW^*$ decays with the ATLAS detector," *JHEP* **08** (2015) 137, arXiv:1506.06641 [hep-ex].

[426] **CMS** Collaboration, S. Chatrchyan *et al.*, "Measurement of Higgs boson production and properties in the WW decay channel with leptonic final states," *JHEP* **01** (2014) 096, arXiv:1312.1129 [hep-ex].

[427] **ATLAS** Collaboration, G. Aad *et al.*, "Measurements of the Higgs boson production and decay rates and coupling strengths using pp collision data at $\sqrt{s} = 7$ and 8 TeV in the ATLAS experiment," *Eur. Phys. J.* **C76** no. 1, (2016) 6, arXiv:1507.04548 [hep-ex].

[428] **CMS** Collaboration, S. Chatrchyan *et al.*, "Search for a Higgs boson decaying into a Z and a photon in pp collisions at sqrt(s) = 7 and 8 TeV," *Phys. Lett.* **B726** (2013) 587–609, arXiv:1307.5515 [hep-ex].

[429] **ATLAS** Collaboration, G. Aad *et al.*, "Measurements of Higgs boson production and couplings in the four-lepton channel in pp collisions at center-of-mass energies of 7 and 8 TeV with the ATLAS detector," *Phys. Rev.* **D91** no. 1, (2015) 012006, arXiv:1408.5191 [hep-ex].

[430] **CMS** Collaboration, V. Khachatryan *et al.*, "Precise determination of the mass of the Higgs boson and tests of compatibility of its couplings with the standard model predictions using proton collisions at 7 and 8 TeV," *Eur. Phys. J.* **C75** no. 5, (2015) 212, arXiv:1412.8662 [hep-ex].

[431] **CMS** Collaboration, A. M. Sirunyan *et al.*, "Measurements of Higgs boson properties in the diphoton decay channel in proton-proton collisions at $\sqrt{s} = 13$ TeV," arXiv:1804.02716 [hep-ex].

[432] **ATLAS** Collaboration, "Measurements of Higgs boson properties in the diphoton decay channel using 80 fb^{-1} of *pp* collision data at $\sqrt{s} = 13$ TeV with the ATLAS detector," Tech. Rep. ATLAS-CONF-2018-028, CERN, Geneva, Jul, 2018. http://cds.cern.ch/record/2628771.

[433] **ATLAS** Collaboration, T. A. collaboration, "A search for the rare decay of the Standard Model Higgs boson to dimuons in *pp* collisions at $\sqrt{s} = 13$ TeV with the ATLAS Detector,".

[434] **CMS** Collaboration, A. M. Sirunyan *et al.*, "Search for the Higgs boson decaying to two muons in proton-proton collisions at $\sqrt{s} = 13$ TeV," *Submitted to: Phys. Rev. Lett.* (2018) , arXiv:1807.06325 [hep-ex].

[435] **CMS** Collaboration, A. M. Sirunyan *et al.*, "Observation of the Higgs boson decay to a pair of τ leptons with the CMS detector," *Phys. Lett.* **B779** (2018) 283–316, arXiv:1708.00373 [hep-ex].

[436] **ATLAS** Collaboration, T. A. collaboration, "Cross-section measurements of the Higgs boson decaying to a pair of tau leptons in proton–proton collisions at $\sqrt{s} = 13$ TeV with the ATLAS detector,".

[437] **ATLAS** Collaboration, T. A. collaboration, "Measurements of the Higgs boson production cross section via Vector Boson Fusion and associated WH production in the $WW^* \to \ell\nu\ell\nu$ decay mode with the ATLAS detector at $\sqrt{s} = 13$ TeV,".

[438] **ATLAS** Collaboration, T. A. collaboration, "Measurement of gluon fusion and vector boson fusion Higgs boson production cross-sections in the $H \to WW^* \to e\nu\mu\nu$ decay channel in pp collisions at $\sqrt{s} = 13$ TeV with the ATLAS detector,".

[439] **CMS** Collaboration, A. M. Sirunyan *et al.*, "Measurements of properties of the Higgs boson decaying to a W boson pair in pp collisions at $\sqrt{s} = 13$ TeV," *Submitted to: Phys. Lett.* (2018) , arXiv:1806.05246 [hep-ex].

[440] **ATLAS** Collaboration, M. Aaboud *et al.*, "Searches for the $Z\gamma$ decay mode of the Higgs boson and for new high-mass resonances in pp collisions at $\sqrt{s} = 13$ TeV with the ATLAS detector," *JHEP* **10** (2017) 112, arXiv:1708.00212 [hep-ex].

[441] **CMS** Collaboration, A. M. Sirunyan *et al.*, "Search for the decay of a Higgs boson in the $\ell\ell\gamma$ channel in proton-proton collisions at $\sqrt{s} = 13$ TeV," *Submitted to: JHEP* (2018) , arXiv:1806.05996 [hep-ex].

[442] **ATLAS** Collaboration, T. A. collaboration, "Measurements of the Higgs boson production, fiducial and differential cross sections in the 4ℓ decay channel at $\sqrt{s} = 13$ TeV with the ATLAS detector,".

[443] **CMS** Collaboration, A. M. Sirunyan *et al.*, "Measurements of properties of the Higgs boson decaying into the four-lepton final state in pp collisions at $\sqrt{s} = 13$ TeV," *JHEP* **11** (2017) 047, arXiv:1706.09936 [hep-ex].

[444] **CMS** Collaboration, C. Collaboration, "Measurements of properties of the Higgs boson in the four-lepton final state at $\sqrt{s} = 13$ TeV,".

[445] **ATLAS** Collaboration, M. Aaboud *et al.*, "Search for Higgs bosons produced via vector-boson fusion and decaying into bottom quark pairs in $\sqrt{s} = 13$ TeV pp collisions with the ATLAS detector," *Phys. Rev.* **D98** no. 5, (2018) 052003, arXiv:1807.08639 [hep-ex].

[446] **CMS** Collaboration, C. Collaboration, "VBF H to bb using the 2015 data sample,".

[447] **ATLAS** Collaboration, G. Aad *et al.*, "Search for the $b\bar{b}$ decay of the Standard Model Higgs boson in associated $(W/Z)H$ production with the ATLAS detector," *JHEP* **01** (2015) 069, arXiv:1409.6212 [hep-ex].

[448] **CMS** Collaboration, S. Chatrchyan *et al.*, "Search for the standard model Higgs boson produced in association with a W or a Z boson and decaying to bottom quarks," *Phys. Rev.* **D89** no. 1, (2014) 012003, arXiv:1310.3687 [hep-ex].

[449] **ATLAS** Collaboration, T. A. collaboration, "Observation of $H \to b\bar{b}$ decays and VH production with the ATLAS detector,".

[450] **CMS** Collaboration, C. Collaboration, "Evidence for the decay of the Higgs Boson to Bottom Quarks,".

[451] **CMS** Collaboration, C. Collaboration, "Search for the standard model Higgs boson decaying to a pair of τ leptons and produced in association with a W or a Z boson in proton-proton collisions at $\sqrt{s} = 13$ TeV,".

[452] **CMS** Collaboration, V. Khachatryan *et al.*, "Search for the associated production of the Higgs boson with a top-quark pair," *JHEP* **09** (2014) 087, arXiv:1408.1682 [hep-ex]. [Erratum: JHEP10,106(2014)].

[453] **ATLAS** Collaboration, G. Aad *et al.*, "Search for the Standard Model Higgs boson produced in association with top quarks and decaying into $b\bar{b}$ in pp collisions at $\sqrt{s} = 8$ TeV with the ATLAS detector," *Eur. Phys. J.* **C75** no. 7, (2015) 349, arXiv:1503.05066 [hep-ex].

[454] **ATLAS** Collaboration, M. Aaboud *et al.*, "Search for the standard model Higgs boson produced in association with top quarks and decaying into a $b\bar{b}$ pair in *pp* collisions at $\sqrt{s} = 13$ TeV with the ATLAS detector," *Phys. Rev.* **D97** no. 7, (2018) 072016, arXiv:1712.08895 [hep-ex].

[455] **CMS** Collaboration, C. Collaboration, "Search for ttH production in the H-to-bb decay channel with leptonic tt decays in proton-proton collisions at sqrt(s) = 13 TeV with the CMS detector,".

[456] **CMS** Collaboration, A. M. Sirunyan *et al.*, "Search for $t\bar{t}H$ production in the all-jet final state in proton-proton collisions at $\sqrt{s} = 13$ TeV," *JHEP* **06** (2018) 101, arXiv:1803.06986 [hep-ex].

[457] **D0** Collaboration, V. M. Abazov *et al.*, "Combined search for the Higgs boson with the D0 experiment," *Phys. Rev.* **D88** no. 5, (2013) 052011, arXiv:1303.0823 [hep-ex].

[458] **CDF** Collaboration, T. Aaltonen *et al.*, "Combination fo Searches for the Higgs Boson Using the Full CDF Data Set," *Phys. Rev.* **D88** no. 5, (2013) 052013, arXiv:1301.6668 [hep-ex].

[459] **ATLAS** Collaboration, M. Aaboud *et al.*, "Search for new phenomena in events with same-charge leptons and *b*-jets in *pp* collisions at $\sqrt{s} = 13$ TeV with the ATLAS detector," arXiv:1807.11883 [hep-ex].

[460] **ATLAS** Collaboration, "Search for new phenomena in $t\bar{t}$ final states with additional heavy-flavour jets in pp collisions at $\sqrt{s} = 13$ TeV with the ATLAS detector," Tech. Rep. ATLAS-CONF-2016-104, CERN, Geneva, Sep, 2016. http://cds.cern.ch/record/2220371.

[461] **CMS** Collaboration, V. Khachatryan *et al.*, "Search for Neutral MSSM Higgs Bosons Decaying into A Pair of Bottom Quarks," *JHEP* **11** (2015) 071, arXiv:1506.08329 [hep-ex].

[462] **CMS** Collaboration, A. M. Sirunyan *et al.*, "Search for narrow resonances in the b-tagged dijet mass spectrum in proton-proton collisions at $\sqrt{s} = 8$ TeV," arXiv:1802.06149 [hep-ex].

[463] **CMS** Collaboration, "Search for a narrow heavy decaying to bottom quark pairs in the 13 TeV data sample," Tech. Rep. CMS-PAS-HIG-16-025, CERN, Geneva, 2016. http://cds.cern.ch/record/2204928.

[464] **CMS** Collaboration, A. M. Sirunyan *et al.*, "Search for beyond the standard model Higgs bosons decaying into a $\mathrm{b\bar{b}}$ pair in pp collisions at $\sqrt{s} = 13$ TeV," arXiv:1805.12191 [hep-ex].

[465] **ATLAS** Collaboration, G. Aad *et al.*, "Search for neutral Higgs bosons of the minimal supersymmetric standard model in pp collisions at $\sqrt{s} = 8$ TeV with the ATLAS detector," *JHEP* **11** (2014) 056, arXiv:1409.6064 [hep-ex].

[466] **CMS** Collaboration, "Search for additional neutral Higgs bosons decaying to a pair of tau leptons in pp collisions at $\sqrt{s} = 7$ and 8 TeV," Tech. Rep. CMS-PAS-HIG-14-029, CERN, Geneva, 2015. https://cds.cern.ch/record/2041463.

[467] **ATLAS** Collaboration, M. Aaboud *et al.*, "Search for additional heavy neutral Higgs and gauge bosons in the ditau final state produced in 36 fb^{-1} of pp collisions

at $\sqrt{s} = 13$ TeV with the ATLAS detector," *JHEP* **01** (2018) 055, arXiv:1709.07242 [hep-ex].

[468] **CMS** Collaboration, A. M. Sirunyan *et al.*, "Search for additional neutral MSSM Higgs bosons in the $\tau\tau$ final state in proton-proton collisions at $\sqrt{s} = 13$ TeV," arXiv:1803.06553 [hep-ex].

[469] **ATLAS** Collaboration, G. Aad *et al.*, "Search for Scalar Diphoton Resonances in the Mass Range $65 - 600$ GeV with the ATLAS Detector in pp Collision Data at $\sqrt{s} = 8\ TeV$," *Phys. Rev. Lett.* **113** no. 17, (2014) 171801, arXiv:1407.6583 [hep-ex].

[470] **ATLAS** Collaboration, M. Aaboud *et al.*, "Search for new phenomena in high-mass diphoton final states using 37 fb^{-1} of proton–proton collisions collected at $\sqrt{s} = 13$ TeV with the ATLAS detector," *Phys. Lett.* **B775** (2017) 105–125, arXiv:1707.04147 [hep-ex].

[471] **CMS** Collaboration, V. Khachatryan *et al.*, "Search for high-mass diphoton resonances in proton-proton collisions at 13 TeV and combination with 8 TeV search," *Phys. Lett.* **B767** (2017) 147–170, arXiv:1609.02507 [hep-ex].

[472] **ATLAS** Collaboration, G. Aad *et al.*, "Search for new resonances in $W\gamma$ and $Z\gamma$ final states in pp collisions at $\sqrt{s} = 8$ TeV with the ATLAS detector," *Phys. Lett.* **B738** (2014) 428–447, arXiv:1407.8150 [hep-ex].

[473] **CMS** Collaboration, "Search for scalar resonances in the 200–1200 GeV mass range decaying into a Z and a photon in pp collisions at $\sqrt{s} = 8$ TeV," Tech. Rep. CMS-PAS-HIG-16-014, CERN, Geneva, 2016. https://cds.cern.ch/record/2140286.

[474] **ATLAS** Collaboration, M. Aaboud *et al.*, "Search for heavy resonances decaying to a photon and a hadronically decaying $Z/W/H$ boson in pp collisions at $\sqrt{s} = 13$ TeV with the ATLAS detector," arXiv:1805.01908 [hep-ex].

[475] **CMS** Collaboration, A. M. Sirunyan *et al.*, "Search for Zγ resonances using leptonic and hadronic final states in proton-proton collisions at $\sqrt{s} = 13$ TeV," arXiv:1712.03143 [hep-ex].

[476] **ATLAS** Collaboration, G. Aad *et al.*, "Search for an additional, heavy Higgs boson in the $H \to ZZ$ decay channel at $\sqrt{s} = 8$ TeV in pp collision data with the ATLAS detector," *Eur. Phys. J.* **C76** no. 1, (2016) 45, arXiv:1507.05930 [hep-ex].

[477] **ATLAS** Collaboration, M. Aaboud *et al.*, "Search for heavy ZZ resonances in the $\ell^+\ell^-\ell^+\ell^-$ and $\ell^+\ell^-\nu\bar{\nu}$ final states using proton proton collisions at $\sqrt{s} = 13$ TeV with the ATLAS detector," arXiv:1712.06386 [hep-ex].

[478] **ATLAS** Collaboration, M. Aaboud *et al.*, "Searches for heavy ZZ and ZW resonances in the $\ell\ell qq$ and $\nu\nu qq$ final states in pp collisions at $\sqrt{s} = 13$ TeV with the ATLAS detector," arXiv:1708.09638 [hep-ex].

[479] **CMS** Collaboration, A. M. Sirunyan *et al.*, "Search for a new scalar resonance decaying to a pair of Z bosons in proton-proton collisions at $\sqrt{s} = 13$ TeV," arXiv:1804.01939 [hep-ex].

[480] **CMS** Collaboration, A. M. Sirunyan *et al.*, "Search for a heavy resonance decaying into a Z boson and a vector boson in the $\nu\overline{\nu}\mathrm{q}\overline{\mathrm{q}}$ final state," arXiv:1803.03838 [hep-ex].

[481] **ATLAS** Collaboration, G. Aad *et al.*, "Search for a high-mass Higgs boson decaying to a W boson pair in pp collisions at $\sqrt{s} = 8$ TeV with the ATLAS detector," *JHEP* **01** (2016) 032, arXiv:1509.00389 [hep-ex].

[482] **ATLAS** Collaboration, M. Aaboud *et al.*, "Search for heavy resonances decaying into WW in the $e\nu\mu\nu$ final state in pp collisions at $\sqrt{s} = 13$ TeV with the ATLAS detector," *Eur. Phys. J.* **C78** no. 1, (2018) 24, arXiv:1710.01123 [hep-ex].

[483] **CMS** Collaboration, "Search for high mass Higgs to WW with fully leptonic decays using 2015 data," Tech. Rep. CMS-PAS-HIG-16-023, CERN, Geneva, 2016. `http://cds.cern.ch/record/2205151`.

[484] **ATLAS** Collaboration, M. Aaboud *et al.*, "Search for WW/WZ resonance production in $\ell\nu qq$ final states in pp collisions at $\sqrt{s} = 13$ TeV with the ATLAS detector," `arXiv:1710.07235 [hep-ex]`.

[485] **CMS** Collaboration, A. M. Sirunyan *et al.*, "Search for a heavy resonance decaying to a pair of vector bosons in the lepton plus merged jet final state at $\sqrt{s} = 13$ TeV," `arXiv:1802.09407 [hep-ex]`.

[486] **CMS** Collaboration, V. Khachatryan *et al.*, "Search for a Higgs Boson in the Mass Range from 145 to 1000 GeV Decaying to a Pair of W or Z Bosons," *JHEP* **10** (2015) 144, `arXiv:1504.00936 [hep-ex]`.

[487] **ATLAS** Collaboration, M. Aaboud *et al.*, "Search for diboson resonances with boson-tagged jets in pp collisions at $\sqrt{s} = 13$ TeV with the ATLAS detector," *Phys. Lett.* **B777** (2018) 91–113, `arXiv:1708.04445 [hep-ex]`.

[488] **ATLAS** Collaboration, G. Aad *et al.*, "Searches for Higgs boson pair production in the $hh \to bb\tau\tau, \gamma\gamma WW^*, \gamma\gamma bb, bbbb$ channels with the ATLAS detector," *Phys. Rev.* **D92** no. 9, (2015) 092004, `arXiv:1509.04670 [hep-ex]`.

[489] **CMS** Collaboration, V. Khachatryan *et al.*, "Search for resonant pair production of Higgs bosons decaying to two bottom quark–antiquark pairs in proton–proton collisions at 8 TeV," *Phys. Lett.* **B749** (2015) 560–582, `arXiv:1503.04114 [hep-ex]`.

[490] **CMS** Collaboration, V. Khachatryan *et al.*, "Search for two Higgs bosons in final states containing two photons and two bottom quarks in proton-proton collisions at 8 TeV," *Phys. Rev.* **D94** no. 5, (2016) 052012, `arXiv:1603.06896 [hep-ex]`.

[491] **CMS** Collaboration, V. Khachatryan *et al.*, "Searches for a heavy scalar boson H decaying to a pair of 125 GeV Higgs bosons hh or for a heavy pseudoscalar boson A decaying to Zh, in the final states with $h \to \tau\tau$," *Phys. Lett.* **B755** (2016) 217–244, arXiv:1510.01181 [hep-ex].

[492] **CMS** Collaboration, A. M. Sirunyan *et al.*, "Search for Higgs boson pair production in the $bb\tau\tau$ final state in proton-proton collisions at $\sqrt{(s)} = 8$ TeV," *Phys. Rev.* **D96** no. 7, (2017) 072004, arXiv:1707.00350 [hep-ex].

[493] **ATLAS** Collaboration, M. Aaboud *et al.*, "Search for pair production of Higgs bosons in the $b\bar{b}b\bar{b}$ final state using proton-proton collisions at $\sqrt{s} = 13$ TeV with the ATLAS detector," arXiv:1804.06174 [hep-ex].

[494] **CMS** Collaboration, A. M. Sirunyan *et al.*, "Search for resonant pair production of Higgs bosons decaying to bottom quark-antiquark pairs in proton-proton collisions at 13 TeV," *Submitted to: JHEP* (2018) , arXiv:1806.03548 [hep-ex].

[495] **CMS** Collaboration, A. M. Sirunyan *et al.*, "Search for production of Higgs boson pairs in the four b quark final state using large-area jets in proton-proton collisions at $\sqrt{s} = 13$ TeV," arXiv:1808.01473 [hep-ex].

[496] **ATLAS** Collaboration, M. Aaboud *et al.*, "Search for Higgs boson pair production in the $\gamma\gamma b\bar{b}$ final state with 13 TeV pp collision data collected by the ATLAS experiment," arXiv:1807.04873 [hep-ex].

[497] **CMS** Collaboration, A. M. Sirunyan *et al.*, "Search for Higgs boson pair production in the $\gamma\gamma\mathrm{b\bar{b}}$ final state in pp collisions at $\sqrt{s} = 13$ TeV," arXiv:1806.00408 [hep-ex].

[498] **ATLAS** Collaboration, M. Aaboud *et al.*, "A search for resonant and non-resonant Higgs boson pair production in the $b\bar{b}\tau^+\tau^-$ decay channel in pp collisions at $\sqrt{s} = 13$ TeV with the ATLAS detector," arXiv:1808.00336 [hep-ex].

[499] **CMS** Collaboration, A. M. Sirunyan *et al.*, "Search for Higgs boson pair production in events with two bottom quarks and two tau leptons in proton-proton collisions at sqrt(s) = 13 TeV," `arXiv:1707.02909 [hep-ex]`.

[500] **CMS** Collaboration, A. M. Sirunyan *et al.*, "Search for heavy resonances decaying into two Higgs bosons or into a Higgs boson and a W or Z boson in proton-proton collisions at 13 TeV," `arXiv:1808.01365 [hep-ex]`.

[501] **CMS** Collaboration, A. M. Sirunyan *et al.*, "Search for resonant and nonresonant Higgs boson pair production in the bblnulnu final state in proton-proton collisions at sqrt(s) = 13 TeV," `arXiv:1708.04188 [hep-ex]`.

[502] **ATLAS** Collaboration, M. Aaboud *et al.*, "Search for Higgs boson pair production in the $b\bar{b}WW^*$ decay mode at $\sqrt{s} = 13$ TeV with the ATLAS detector," `arXiv:1811.04671 [hep-ex]`.

[503] **ATLAS** Collaboration, M. Aaboud *et al.*, "Search for Higgs boson pair production in the $\gamma\gamma WW^*$ channel using pp collision data recorded at $\sqrt{s} = 13$ TeV with the ATLAS detector," *Submitted to: Eur. Phys. J.* (2018) , `arXiv:1807.08567 [hep-ex]`.

[504] **ATLAS** Collaboration, G. Aad *et al.*, "Search for a CP-odd Higgs boson decaying to Zh in pp collisions at $\sqrt{s} = 8$ TeV with the ATLAS detector," *Phys. Lett.* **B744** (2015) 163–183, `arXiv:1502.04478 [hep-ex]`.

[505] **CMS** Collaboration, V. Khachatryan *et al.*, "Search for a pseudoscalar boson decaying into a Z boson and the 125 GeV Higgs boson in $\ell^+\ell^- b\bar{b}$ final states," *Phys. Lett.* **B748** (2015) 221–243, `arXiv:1504.04710 [hep-ex]`.

[506] **ATLAS** Collaboration, M. Aaboud *et al.*, "Search for heavy resonances decaying into a W or Z boson and a Higgs boson in final states with leptons and b-jets in 36 fb^{-1} of $\sqrt{s} = 13$ TeV pp collisions with the ATLAS detector," `arXiv:1712.06518 [hep-ex]`.

[507] **CMS** Collaboration, "Search for a heavy pseudoscalar boson decaying to a Z boson and a Higgs boson at sqrt(s)=13 TeV," Tech. Rep. CMS-PAS-HIG-18-005, CERN, Geneva, 2018. `http://cds.cern.ch/record/2628545`.

[508] **CMS** Collaboration, A. M. Sirunyan *et al.*, "Search for heavy resonances decaying into a vector boson and a Higgs boson in final states with charged leptons, neutrinos and b quarks at $\sqrt{s} = 13$ TeV," `arXiv:1807.02826 [hep-ex]`.

[509] **CMS** Collaboration, V. Khachatryan *et al.*, "Search for neutral resonances decaying into a Z boson and a pair of b jets or τ leptons," *Phys. Lett.* **B759** (2016) 369–394, `arXiv:1603.02991 [hep-ex]`.

[510] **ATLAS** Collaboration, M. Aaboud *et al.*, "Search for a heavy Higgs boson decaying into a Z boson and another heavy Higgs boson in the $\ell\ell bb$ final state in pp collisions at $\sqrt{s} = 13$ TeV with the ATLAS detector," *Phys. Lett.* **B783** (2018) 392–414, `arXiv:1804.01126 [hep-ex]`.

[511] **ATLAS** Collaboration, G. Aad *et al.*, "Search for charged Higgs bosons decaying via $H^{\pm} \to \tau^{\pm}\nu$ in fully hadronic final states using pp collision data at $\sqrt{s} = 8$ TeV with the ATLAS detector," *JHEP* **03** (2015) 088, `arXiv:1412.6663 [hep-ex]`.

[512] **CMS** Collaboration, V. Khachatryan *et al.*, "Search for a charged Higgs boson in pp collisions at $\sqrt{s} = 8$ TeV," *JHEP* **11** (2015) 018, `arXiv:1508.07774 [hep-ex]`.

[513] **ATLAS** Collaboration, M. Aaboud *et al.*, "Search for charged Higgs bosons decaying via $H^{\pm} \to \tau^{\pm}\nu_{\tau}$ in the τ+jets and τ+lepton final states with 36 fb^{-1} of pp collision data recorded at $\sqrt{s} = 13$ TeV with the ATLAS experiment," *Submitted to: JHEP* (2018) , `arXiv:1807.07915 [hep-ex]`.

[514] **CMS** Collaboration, "Search for charged Higgs bosons with the $H^{\pm} \to \tau^{\pm}\nu_{\tau}$ decay channel in the fully hadronic final state at $\sqrt{s} = 13$ TeV," Tech. Rep. CMS-PAS-HIG-16-031, CERN, Geneva, 2016. `https://cds.cern.ch/record/2223865`.

[515] **ATLAS** Collaboration, G. Aad *et al.*, "Search for charged Higgs bosons in the $H^{\pm} \to tb$ decay channel in pp collisions at $\sqrt{s} = 8$ TeV using the ATLAS detector," *JHEP* **03** (2016) 127, arXiv:1512.03704 [hep-ex].

[516] **ATLAS** Collaboration, M. Aaboud *et al.*, "Search for charged Higgs bosons decaying into top and bottom quarks at $\sqrt{s} = 13$ TeV with the ATLAS detector," arXiv:1808.03599 [hep-ex].